Diss. ETH No. 17790

Astrogeodetic Geoid and Isostatic Considerations in the North Aegean Sea, Greece

A dissertation submitted to the

ETH ZURICH

for the degree of

Doctor of Sciences

presented by

ANNA EVE SOMIESKI

Dipl. Ing., TU Dresden

born April 08, 1977

citizen of Germany

accepted on the recommendation of

Prof. Dr. H.-G. Kahle, examiner

Prof. Dr. I.N. Tziavos, co-examiner

Dr. B. Bürki, co-examiner

2008

Abstract

The present work is concerned with the enhancement, evaluation and deployment of the digital Zenith Camera DIADEM (Digital Astronomical Deflection Measuring System). DIADEM represents an important instrument of astrogeodesy and is applied for local geoid determinations by means of deflections of the vertical (ξ, η) (DOV). These components describe the difference between astronomical parameters (Φ, Λ) referring to the geoid and GPS-derived coordinates (φ, λ) referring to the ellipsoid.

The first part of the work deals with the enhancement of DIADEM aiming at the fully-automatic and economic determination of highly-precise DOV. The system is equipped with a CCD camera for the exposure of the zenithal star field, a GPS receiver providing epoch and position information and two types of inclination sensors controlling the vertical alignment of the Zenith Camera. Furthermore, the instrument possesses nine motors allowing for the steering of all necessary instrumental motions. The processes are controlled by two industrial PCs. A complex software package manages the data acquisition process comprising the leveling of the system, the adaption of the focus, the exposure of the images in two positions and the registration of corresponding exposure epochs and inclination data. A further software package allows for the subsequent data analysis in the field. The whole observation process including the data acquisition and analysis of 80-100 single solutions takes about 35-45 minutes per station.

In order to evaluate the field capability of DIADEM, several measuring campaigns were conducted in Switzerland, Portugal and Greece. They proved the extreme reliability of the system also under harsh conditions, such as in mountainous regions and at very low temperatures. An elaborate instrumental calibration and error analysis as well as comparison measurements with a second digital Zenith Camera (TZK2-D of University Hannover) demonstrated the high potential of DIADEM providing DOV with an accuracy of better than 0.15 arcsec.

The second part of the work describes the organization and realization of DIADEM measurements in the North Aegean Sea, Greece, as well as the thorough analysis of the DOV observed. Totally, 27 ξ- and η-components at several islands and along the coastline of the North Aegean Sea have been determined. The data analysis included the geophysical interpretation of the data as well as the final computation and evaluation of a local astrogeodetic geoid.

The research area has been chosen for two main reasons: Firstly, due to its location in the transition zone between the Eurasian and African plates, it forms a tectonically and seismically interesting region. It is dominated by the North Aegean Trough (NAT), which is considered to be a continuation of the seismically active North Anatolian Fault Zone. Secondly, the research area provides several data sets for comparison and validation, e.g. gravimetric and altimetric data as well as GPS-derived Sea Surface Heights (SSH).

For the geophysical interpretation, the DOV have been reduced for mass effects including a Digital Terrain Model, the isostasy model of Airy-Heiskanen and the Moho model of Tsokas and Hansen [1997]. The analysis of isostatic cogeoid revealed a mass excess along the NAT, hence indicating an isostatically overcompensated region. Furthermore, this supports the assumption of extensional tectonic processes being active in the North Aegean Sea. The interpretation of the Moho-reduced DOV indicated significant discrepancies of the Moho model concerning depth and location of local maxima and minima. The respective cogeoid revealed - similar to the isostatic cogeoid - a rising Moho along the NAT. This allows for the conclusion that the Moho model is too deep there.

The final geoid computation has been realized by applying the least-squares-collocation method to the residual DOV in a first step and by restoring the reduced mass effects in a second step. The Astro geoid and a combined geoid from DOV and SSH reflect well the topographic and bathymetric features of the research area. Especially, the mass deficit associated with the deep water of the NAT is indicated by a clear depression of the geoid. The geoid variations in NS-direction across the NAT amount up to 2.6 m. The combined geoid solution has been compared with altimetric and gravimetric geoid solutions available for the research area. Significant discrepancies in the existing geoid models have been detected. The new geoid reflects much better the shape and depth distribution of the NAT. In the marine area, the differences between the gravimetric geoid and the new model reach ± 3 m. These discrepancies can be mainly ascribed to the deficiency of marine gravity and altimetry data used for the computation of the gravimetric and altimetric geoid.

Zusammenfassung

Die vorliegende Arbeit befasst sich mit der Weiterentwicklung, der Evaluierung und dem Einsatz der digitalen Zenitkamera DIADEM (Digital Astronomical Deflection Measuring System), welche ein bedeutendes Instrument der Astrogeodäsie darstellt. Die Kamera dient der Bestimmung von Lotabweichungskomponenten (ξ, η) für die lokale Geoidbestimmung. Die Komponenten (ξ, η) repräsentieren den Unterschied zwischen den schwerefeldabhängigen astronomischen Parametern (Φ, Λ) und den mittels GPS bestimmten ellipsoidischen Koordinaten (φ, λ).

Der erste Teil der Arbeit beschäftigt sich mit der Weiterentwicklung des Messsystems, mit dem Ziel, eine vollautomatische und ökonomische Bestimmung hochpräziser Lotabweichungskomponenten zu ermöglichen. Die modernisierte Zenitkamera DIADEM verfügt über eine CCD-Kamera zur Aufnahme des zenitalen Sternfeldes, einen GPS-Empfänger zur Bestimmung der Belichtungsepochen und der Position, sowie zwei unterschiedliche Typen von Neigungssensoren zur Kontrolle der vertikalen Aufstellung des Instruments. Des weiteren besitzt DIADEM insgesamt neun Motoren, welche die Steuerung aller notwendigen Bewegungen des Instruments ermöglichen. Eine komplexe Software überwacht den Datenerfassungsprozess, welcher die Horizontierung, Fokussierung, Bildaufnahme sowie Registrierung der Belichtungsepochen und Neigungsdaten umfasst. Eine weitere Software ermöglicht die anschliessende Auswertung der Daten im Feld. Der gesamte Prozess, von der Datenerfassung mit 80-100 Einzellösungen bis zum Abschluss einer ersten Auswertung, dauert ca. 35-45 Minuten.

Zur Validierung der Feldtauglichkeit des Instruments wurden verschiedene Messkampagnen in der Schweiz, Portugal und Griechenland durchgeführt. Sie bewiesen die extreme Zuverlässigkeit des Instruments, selbst unter schwierigen Bedingungen, wie tiefe Temperaturen und unwegsames Gelände. Die ausführliche instrumentelle Kalibrierung und Fehleranalyse sowie Vergleichsmessungen mit einer zweiten digitalen Zenitkamera (TZK2-D) demonstrierten das hohe Genauigkeitspotential von DIADEM. Die Lotabweichungen können mit einer Genauigkeit von besser als 0.15 arcsec bestimmt werden.

Der zweite Teil der Arbeit befasst sich mit der Organisation und Durchführung von Beobachtungen mit DIADEM im Nordägäischen Meer, Griechenland, sowie der gründlichen Analyse der beobachteten Lotabweichungen. Insgesamt wurden 27 Lotabweichungen auf verschiedenen Inseln und entlang der Küste der Nordägäis bestimmt. Die Datenanalyse umfasst die geophysikalische Interpretation der Daten sowie die Berechnung und Validierung eines lokalen astrogeodätischen Geoids.

Das Messgebiet wurde aus zwei Gründen gewählt: Zum einen stellt es eine tektonisch und seismisch sehr interessante Region dar, da es sich in der Übergangszone zwischen der Eurasischen und Afrikanischen Platte befindet. Das Einsatzgebiet wird durch den Nordägäischen Graben (NAT) geprägt, welcher eine Fortsetzung der seismisch

aktiven Nordanatolischen Faltung darstellt. Zum anderen stehen im Gebiet unterschiedliche Datensätze zum Vergleich und zur Validierung der astronomischen Ergebnisse zur Verfügung, wie z.B. gravimetrische und altimetrische Daten sowie GPS-bestimmte Meeresoberflächen-Höhen.

Um eine geophysikalische Analyse der Lotabweichungen zu ermöglichen, wurden die Daten um Masseneinflüsse reduziert, welche mittels entsprechender Massenmodelle berechnet wurden. Dazu gehören ein digitales Geländemodell, das isostatische Modell von Airy-Heiskanen sowie das Moho-Modell von Tsokas and Hansen [1997]. Das isostatische Cogeoid zeigt einen Massenüberschuss entlang des Nordägäischen Grabens, was auf eine isostatisch überkompensierte Region hindeutet. Ausserdem kann auf extensionale tektonische Prozesse in der Region geschlossen werden. Die Interpretation der Moho-reduzierten Lotabweichungen ermöglichte die Detektion signifikanter Unterschiede gegenüber dem Moho-Modell, hauptsächlich hinsichtlich der Tiefenvariationen und der Lage lokaler Minima und Maxima. Das entsprechende Cogeoid zeigt - ähnlich wie das isostatische Cogeoid - eine Aufwölbung der Krusten-Mantel-Grenze (Moho) entlang des Nordägäischen Grabens. Das gibt den Hinweis, dass das Moho-Modell in dieser Region zu tief verläuft.

Die Berechnung des Geoids erfolgte durch Einführung der residualen Lotabweichungen in eine Kollokations-Software. Die eingangs reduzierten Masseneinflüsse wurden rechnerisch wieder berücksichtigt. Das Astro-Geoid sowie ein kombiniertes Geoid aus Lotabweichungen und Meeresoberflächen-Höhen spiegeln die topographischen und bathymetrischen Eigenschaften des Forschungsgebietes sehr gut wider. Besonders das durch das tiefe Wasser des Nordägäischen Grabens hervorgerufene Massendefizit wird durch eine deutliche Vertiefung des Geoids in diesem Gebiet reflektiert. Die Geoidhöhen-Variationen in NS-Richtung über den Graben betragen bis zu 2.6 m. Die kombinierte Geoidlösung wurde mit dem altimetrischen und gravimetrischen Geoid verglichen, welche im Einsatzgebiet zur Verfügung stehen. Es konnten signifikante Diskrepanzen der existierenden Geoidmodelle nachgewiesen werden. So spiegelt das neue Geoidmodell viel besser die typische Form und Massenverteilung des Nordägäischen Grabens wider. Im marinen Bereich betragen die Differenzen zwischen gravimetrischem Geoid und neuem Modell bis zu ± 3 m. Sie sind hauptsächlich auf einen Mangel an marinen gavimetrischen bzw. altimetrischen Daten für die Berechnung des gravimetrischen bzw. altimetrischen Geoids zurückzuführen.

Danksagung

Die Arbeit wurde am Geodäsie und Geodynamik Labor (GGL) der ETH Zürich durchgeführt. An dieser Stelle möchte ich mich bei allen Leuten bedanken, die mich während der Dissertation tatkräftig und hilfsbereit unterstützt haben:

* Prof. Dr. Hans-Gert Kahle, dem ich diese spannende Dissertation verdanke und auf dessen Unterstützung ich immer zählen konnte.
* Dr. Beat Bürki, der mir als mein Betreuer immer zur Seite stand und der hauptsächlich für den hohen technischen Entwicklungsstand der Zenitkamera verantwortlich ist. Unvergessen auch die zahlreich gemeinsam durchwachten Messnächte in der Schweiz, Portugal und Griechenland.
* Prof. Dr. Ilias N. Tziavos, dem ich besonders für seine Unterstützung während der Messkampagne und des anschliessenden einwöchigen Forschungsaufenthaltes in Griechenland danken möchte.
* Dr. Christian Hirt, dem ich aufgrund seiner immer hilfsbereiten und grosszügigen Unterstützung zu Dank verpflichtet bin. Seine Auswertesoftware AURIGA ermöglichte uns eine zügige und hochgenaue Auswertung der Zenitkamera-Aufnahmen. Dank seiner grossen wissenschaftlichen Neugierde konnte ich immer mit einem offenen Ohr in Diskussionen rechnen.
* Prof. Dr. Alain Geiger, auf dessen Hilfsbereitschaft und Diskussionsfreudigkeit ich in wissenschaftlichen Belangen immer rechnen konnte.
* Philippe Limpach, dem ich für die Bereitstellung seiner SSH-Daten zur Validierung des Astro-Geoids und zur Berechnung eines kombinierten Geoids danken möchte, sowie für seine Hilfe bei der Auswertung der GPS-Messungen.
* Paul Sorber, der bei Problemen elektronischer Natur immer grosse Hilfsbereitschaft zeigte.
* Michael Ganz, Stefan Münch, Claudia Röösli und Felix Bentz, die durch ihre Arbeiten am GGL zum instrumentellen und programmtechnischen Feinschliff des DIADEM Systems beigetragen haben. Besonders möchte ich mich hier bei Michael Ganz bedanken, dessen grosses Engagement bei der Arbeit mit der Zenitkamera wichtige Erkenntnisse ermöglicht hat.
* Georgios S. Vergos und Vassilios N. Grigoriadis, die mir während der Messkampagne in Griechenland eine grosse Hilfe waren und die Nächte unter dem griechischen Sternenhimmel mit mir gemeinsam durchwacht haben.
* Dr. Christine Hollenstein, die als langjährige Mitdoktorandin, Bürokollegin und gute Freundin einige Hochs und Tiefs miterlebt hat. Sie war mir auch in wissenschaftlichen Fragestellungen immer eine sehr gute Diskussionspartnerin.
* Dr. "Flip" Kehl, der bei jeglichen Problemen computertechnischer Natur ein sehr kompetenter Ansprechpartner war.

* Jrène Müller-Gantenbein, die stets ein offenes Ohr für kleinere und grössere Sorgen hatte.
* Und schliesslich dem gesamten GGL-Team, welches eine freundliche und kameradschaftliche Arbeitsatmosphäre ermöglichte.

Ein grosses Dankeschön geht an meine Eltern Sabine und Jens Müller und meinen Bruder Georg, die mich meinen Weg frei wählen liessen, und mich bei meinen Plänen immer unterstützt haben. Ganz besonders möchte ich meinem Mann Alexander danken. Auf seine Hilfe und Unterstützung konnte ich immer zählen, seine Liebe und Geduld sind ein fester Anker in meinem Leben. Ich freue mich sehr darauf, dass wir im Juli 2008 zu Dritt sein werden.

Contents

1 Introduction **1**
- 1.1 Rationale and Goals . . . 1
- 1.2 State of research . . . 3
  - 1.2.1 Astrogeodetic instruments . . . 3
  - 1.2.2 Geoid determination in Greece . . . 4
- 1.3 Structure of the thesis . . . 5

2 Basic knowledge **7**
- 2.1 Reference systems . . . 7
  - 2.1.1 Introduction . . . 7
  - 2.1.2 Celestial reference systems . . . 7
  - 2.1.3 Terrestrial reference systems . . . 8
  - 2.1.4 Orientation between terrestrial and celestial systems . . . 9
  - 2.1.5 Earth Orientation Parameters . . . 10
- 2.2 Star catalogs . . . 12
  - 2.2.1 Introduction . . . 12
  - 2.2.2 Tycho-2 catalog . . . 13
  - 2.2.3 UCAC catalog . . . 14
  - 2.2.4 Variations of star positions . . . 15
- 2.3 Time systems . . . 16
  - 2.3.1 Introduction . . . 16
  - 2.3.2 Important time systems for Zenith Camera observations . . . 17
- 2.4 Height systems . . . 19

3 Digital Astronomical Deflection Measuring System *DIADEM* **23**
- 3.1 Determination of deflections of the vertical . . . 23
- 3.2 Instrumental set-up . . . 25
  - 3.2.1 Introduction . . . 25
  - 3.2.2 Objective MIROTAR . . . 27
  - 3.2.3 CCD camera CHROMA C3 . . . 28
  - 3.2.4 Inclination sensors HRTM . . . 30
  - 3.2.5 Inclination sensors Zerotronics . . . 31
  - 3.2.6 GPS equipment . . . 32
  - 3.2.7 Control unit . . . 33
  - 3.2.8 Transportation . . . 34

4 Measuring procedure **37**
- 4.1 Data acquisition . . . 37
  - 4.1.1 Observation with DIADEM . . . 37
  - 4.1.2 Processing of inclination data . . . 40

4.2 Data analysis . . . 42
4.2.1 Introduction . . . 42
4.2.2 Image star field . . . 43
4.2.3 Reference star field . . . 44
4.2.4 Star identification . . . 45
4.2.5 Data reduction . . . 47
4.3 Corrections . . . 49
4.4 Calibrations . . . 51
4.4.1 Azimuth calibration . . . 51
4.4.2 Celestial calibration . . . 58
4.4.3 Shutter delay . . . 61
4.4.4 Focus-temperature-function . . . 67

5 Error analysis **73**
5.1 Introduction . . . 73
5.2 Determination of the rotational direction . . . 74
5.2.1 Astrometry . . . 74
5.2.2 Refraction . . . 79
5.3 Inclination measurements . . . 80
5.3.1 Sensor qualities . . . 80
5.3.2 Microseismics . . . 86
5.3.3 Azimuthal turning . . . 88
5.4 Epoch determination . . . 89
5.5 Azimuthal corrections . . . 90
5.6 Geodetic position . . . 90
5.7 Total error budget . . . 91

6 Field experiences **93**
6.1 Measurements in Switzerland 2003 . . . 93
6.2 Measurements in Portugal 2004 . . . 97
6.3 Measurements with two digital Zenith cameras in Switzerland 2005 . . . 99
6.4 Alptransit measurements in Switzerland 2005 . . . 103
6.5 Control measurements at Zurich . . . 105

7 Research area *North Aegean Sea* **111**
7.1 Introduction . . . 111
7.2 Domain characteristics . . . 112
7.2.1 Topography, bathymetry and geology . . . 112
7.2.2 Deformation field and active tectonics in the Aegean region . . . 114
7.3 Available data . . . 116
7.3.1 Earth Geopotential Model *EGM96* . . . 116
7.3.2 GRACE Gravity Model *GGM02* . . . 117
7.3.3 Gravimetric geoid *HGFFT98* . . . 118
7.3.4 Altimetric geoid . . . 119
7.4 Data acquisition . . . 121
7.4.1 Determination of deflections of the vertical . . . 121
7.4.2 Determination of Sea Surface Heights . . . 124

8 Mass reductions **129**
8.1 Introduction . . . 129
8.2 Computation of mass effects . . . 130
8.3 Topography from the NASA Shuttle Radar Topography Mission . . . 136
8.4 Isostasy . . . 137
8.4.1 Theory . . . 137
8.4.2 Airy-Heiskanen model . . . 138
8.5 Mohorovičić discontinuity . . . 139
8.5.1 Moho in Greece: a state of research . . . 139
8.5.2 Moho model applied for data reduction . . . 142
8.6 Reduced observations . . . 144
8.7 Additional investigations . . . 148
8.7.1 Dimension of the area of influence . . . 148
8.7.2 Comparison of different data reductions . . . 151
8.7.3 Impact of density variations . . . 154

9 Geoid determination **157**
9.1 Measuring methods . . . 157
9.1.1 Astrogeodetic method . . . 157
9.1.2 Gravimetric method . . . 158
9.1.3 Satellite missions . . . 160
9.1.4 Direct observation of geoid undulations . . . 160
9.2 Collocation . . . 161
9.2.1 Theoretical background . . . 161
9.2.2 Correlations between gravity field parameters . . . 164
9.2.3 Covariance function . . . 165
9.2.4 Covariance parameters . . . 166
9.3 Cogeoid and Geoid . . . 168
9.3.1 Theoretical background . . . 168
9.3.2 Interpretation of cogeoids . . . 169
9.3.3 Astro geoid . . . 174
9.3.4 DOVSSH07 geoid . . . 175
9.3.5 Validation of the DOVSSH07 geoid . . . 176
9.4 Additional investigations . . . 180
9.4.1 Impact of covariance parameters . . . 180
9.4.2 Error-variances-covariances . . . 182
9.4.3 Impact of Astro station distribution . . . 184
9.4.4 Cross-validation method . . . 190

10 Discussion and conclusions **195**

Bibliography **201**

A Mathematical background **209**
A.1 Variations of star positions . . . 209
A.2 Mass reduction . . . 210
A.3 Geoid determination . . . 212

Abbreviations

AIUB	Astronomical Institute of the University of Bern
AL	Azimuth calibration in combination with Lippmann inclination sensors
AURIGA	Automatic Real-Time Image Processing System for Geodetic Astronomy
AoI	Area of influence
AUTH	Aristotle University of Thessaloniki
AW	Azimuth calibration in combination with Wyler inclination sensors
BIH	Bureau International de l'Heure
CCD	Charge Coupled Device
CEP	Celestial Ephemeris Pole
CODE	Center for Orbit Determination
DGS	Department of Geodesy and Surveying
DIADEM	Digital Astronomical Deflection Measuring System
DLR	Deutsches Zentrum für Luft- und Raumfahrt
DOT	Dynamic Ocean Topography
DOV	Deflections of the Vertical
DOVSSH07	Combined geoid from Deflections of the Vertical and Sea Surface Heights
DTM	Digital Terrain Model
ECGN	European Combined Geodetic Network
EGM96	Earth Geopotential Model 1996
EOP	Earth Orientation Parameters
ERS1/2	European Remote Sensing Satellite
ESA	European Space Agency

ETH(Z)	Eidgenössische Technische Hochschule (Zürich)
EUREF	European Reference Frames
EUVN-DA	European Unified Vertical Network - Densification Action
FFT	Fast Fourier Transformation
FK5	Fundamentalkatalog No. 5
FOV	Field of view
GAST	Greenwich Apparent Sidereal Time
GGL	Geodesy and Geodynamics Laboratory
GGM02	GRACE Gravity Model
GMST	Greenwich Mean Sidereal Time
GPS(T)	Global Positioning System (Time)
GRS80	Geodetic Reference System 1980
GSC	Guide Star Catalog
IAU	International Astronomical Union
ICRF	International Celestial Reference Frame
ICRS	International Celestial Reference System
IERS	International Earth Rotation and Reference Systems Service
IfE	Institut für Erdmessung
IRP	IERS Reference Pole
ITRF	International Terrestrial Reference Frame
ITRS	International Terrestrial Reference System
LAST	Local Apparent Sidereal Time
LHN95	Landeshöhennetz
LLR	Lunar Laser Ranging
LMST	Local Mean Sidereal Time
LOD	Length of Day
mas	Milli-arcsecond
MDSST	Mean Dynamic Sea Surface Topography

MIMOS	Multiple Input - Multiple Output System
MJD	Modified Julian Date
MSWD	Multiple Source Werner Deconvolution
NASA	National Aeronautics and Space Administration
NAT	North Aegean Trough
NOVAS-C	Naval Observatory Vector Astrometry Subroutines - C
QE	Quantum efficiency
SLR	Satellite Laser Ranging
SSH	Sea Surface Heights
SST	Sea Surface Topography
TB	Topography/Bathymetry
TBAH	Topography/Bathymetry/Airy-Heiskanen
TBMoho	Topography/Bathymetry/Moho
TL	Tripod method in combination with Lippmann inclination sensors
TTL	Transistor-Transistor Logic
TW	Tripod method in combination with Wyler inclination sensors
TZK	Transportable Zenitkamera 1
TZK2-D	Digitale Transportable Zenitkamera 2
UCAC	US Naval Observatory CCD Astrograph Catalog
USNO	US Naval Observatory
UT	Universal Time
UTC	Universal Time Coordinated
VLBI	Very Long Baseline Interferometry
WGS84	World Geodetic System 1984

1 Introduction

1.1 Rationale and Goals

The determination of a precise and high-resolution geoid is subject of many research projects and the main concern of national surveying institutes. Especially in the last years, the theoretical and practical methods for geoid determination were strongly advanced, hence centupling the receivable accuracy within the last three decades. By now, an accuracy of a few "cm" and "mm" is reachable depending on time and effort.

The geoid as the equipotential surface coinciding with the mean sea level is an important reference surface for height systems. It is formed by the distribution of masses on and inside the earth. Density and mass variations in the earth's crust become noticeable in short wavelength signals, whereas deep-rooted structures inside the earth rather produce long wavelength signals. With the advent of satellite-based measuring techniques, it became mandatory to improve our knowledge about the earth's gravity field. The connection between GPS-based coordinates referring to a geometrically defined reference ellipsoid and terrestrial data referring to the geoid can only be achieved by considering the lateral changes of the equipotential surfaces of the earth's gravity field. The geoid is generally described in terms of geoid undulations with respect to the reference ellipsoid (e.g. WGS84). It shows strong undulations, with the most negative geoid height in the Indian Ocean (-106 m) and the most positive height over Indonesia and in the Northern Atlantic (85 m).

There exist various methods of geoid determination. Due to their sensitivity on gravity field variations some methods, as e.g. satellite missions, are more suitable to observe long wavelength structures of the geoid, while terrestrial methods rather detect short wavelength signals produced by the topography. A valuable terrestrial data set is formed by directions of the vertical representing the normal vectors to the geoid. They can be obtained by observations with a Zenith Camera, an important instrument of Astrogeodesy. By comparing the directions of the vertical, expressed by the astronomical parameters (Φ, Λ), with GPS-derived quantities (φ, λ), deflections of the vertical (DOV) can be derived. They are represented by a N-S-component ξ and a W-E-component η. Their knowledge is important for local precise geoid determinations, especially in mountainous areas such as the European Alps.

The present Ph.d.thesis can be split into two main parts:

* The first part of the work is concerned with the enhancement and validation of the modernized Zenith Camera, called **Digital Astronomical Deflection Measuring System (DIADEM)**. The astrogeodetic instrument follows a long tradition at the Geodesy and Geodynamics Laboratory (GGL) of ETH Zurich. Since 1983, it has been

frequently deployed in different countries, as e.g. in Switzerland, Portugal, Spain, German and Canada, hence contributing to national gravity field determinations. In order to upgrade the instrument to the state-of-the-art, it has been subject to several reconstruction works during the last years. The main important advancement comprised the implementation of digital photo technique using a CCD camera. In the frame of the project, DIADEM has been further advanced in terms of hardware and software developments aiming at the automation and real-time processing of Zenith Camera observations. The goal was to provide highly-precise DOV with an accuracy of better than 0.2 arcsec. The field capability of DIADEM concerning handling, economy and data quality has been proved by dedicated field campaigns, as e.g in the frame of the planned CHGeo2003 project (under the auspices of the Swiss Federal Office of Topography). Also comparison measurements with a second digital Zenith Camera, the TZK2-D, developed at the "Institut für Erdmessung" of the University of Hannover, have been conducted. They aimed at the validation of the accuracy potential of DIADEM and the investigation of error influences, as e.g. caused anomalous refraction. Furthermore, the instrument has been analyzed thoroughly with regard to instrumental and external errors.

* The first part of the work provided the conditions for the realization of the second part: the deployment of DIADEM in the North Aegean Sea, Greece. The campaign was a cooperation between the GGL and the Aristotle University of Thessaloniki (AUTH), Greece. The final goal was the computation of an astrogeodetic geoid as well as the geophysical interpretation of the data with focus on isostatic aspects. Due to the distinctive topographic, bathymetric and tectonic features of the project area, it forms an interesting domain for research. The Aegean Sea represents one of the tectonically and seismically most active regions in the world because of its location in the transition zone between Eurasian and African plate. The area of interest is situated within $38° < \varphi < 42°$ northern latitude and $22° < \lambda < 27°$ eastern longitude and covers the northern part of the Aegean Sea. The region is characterized by the North Aegean Trough (NAT), which is considered to be a continuation of the seismically active North Anatolian Fault Zone. It forms an elongate zone of deep water with a maximum depth of 1500 m. Existing local gravimetric and altimetric geoid models, calculated at the AUTH, show long wavelength errors due to the deficiency of marine data. Therefore, DOV have been observed at several islands and along the coastline of the North Aegean Sea. In the frame of another Ph.D. project at the GGL, parallel shipborne GPS and GPS buoy measurements have been performed aiming at the determination of Sea Surface Heights (SSH). Based on the DOV, the computation of a local astrogeodetic geoid has been realized. A second version of a geoid has been calculated by additionally introducing the SSH data. The combined geoid has been evaluated by comparing it to existing geoid models. Furthermore, the DOV have been interpreted thoroughly under isostatic aspects, especially with regard to the topography of the Moho discontinuity. Therefore, dedicated mass models as topography, isostasy and Moho models have been implemented into the process of data analysis. This allowed for conclusions about the quality of the used isostatic models and the Moho model, respectively, and, furthermore, it provided information about unconsidered masses and density anomalies inside the earth.

The goals can be summarized as follows:

Part 1 - Instrumentation:
a) Enhancement of DIADEM in terms of hard- and software
b) In-depth error investigation and calibration of the instrument
c) Verification of the field capability of DIADEM by dedicated field campaigns (e.g. CHGeo2003 project of swisstopo)
d) Parallel measurements with the digital Zenith Camera TZK2-D of Hannover
e) Evaluation of the accuracy potential of DIADEM

Part 2 - Field application:
a) Deployment of DIADEM in the North Aegean Sea, Greece
b) Reduction of the DOV by applying dedicated mass models
c) Computation of different cogeoid solutions and isostatic interpretation
d) Computation of an astrogeodetic geoid based on DOV
e) Computation of a combined geoid based on DOV and SSH
f) Evaluation of the final geoid by comparing it with other gravity field models

1.2 State of research

1.2.1 Astrogeodetic instruments

The main task of astrogeodesy is the determination of astronomical latitudes, longitudes and azimuths within an earth-fixed reference system by observing celestial objects (fixed stars, planets, sun and moon). The celestial objects are defined in a space-fixed reference system, which can be related to the earth-fixed system by considering effects as earth rotation, precession, nutation and polar motion. The directions derived by astrogeodetic observations provide the basis for the realization of diverse objectives, as e.g. the determination of the geoid by astronomical leveling, the determination of structures and densities inside the earth, the orientation and constraint of geodetic networks, the determination of fluctuations of the pole and in the earth's rotation as well as contributions to the definition of terrestrial and celestial reference systems. Typical instruments deployed are theodolites and tachymeters. Besides, there exist special astronomical and astrometric instruments based on visual, photographic or electro-optical principle. One of these special instruments is the Zenith Camera for the determination of deflections of the vertical.

In the seventies and eighties, photographic Zenith Cameras have been developed at several institutes in Europe. They have been successfully deployed for the determination of directions of the vertical. Hence, at the University of Hannover, the Transportable Zenith Cameras TZK1 and TZK2 have been designed providing directions of the vertical with an accuracy of about 0.5 arcsec (Gessler [1975], Wissel [1982], Wildermann [1988]). The successional instrument, the TZK3, has been developed in cooperation between the University of Hannover and the GGL of ETH Zurich, Switzerland (Bürki [1989]. The instrument is constructed in the same way as the TZK2, hence providing similar accuracies. Further developments have been carried out in Italy and Austria (Chesi

[1984]). In the eighties, Zenith Cameras represented one of the most economic instruments for an astrogeodetic determination of directions of the vertical. Nevertheless, the time need was relatively high, mainly caused by the laborious measuring of the analog photos. Due to an increasing availability of gravimetric and satellite data, the astrogeodetic method underwent a recession during the following years.

The advent of CCD technology opened a new field for astrogeodetic instruments, hence allowing for a digital data analysis in connection with a real-time provision of the results. Furthermore, CCD sensors provide a higher sensitivity than photo plates, which enables the observation of a significantly increased number of stars. These advantages caused the initiation of new research projects at several European institutes concerned with the implementation of CCD technology in astrogeodetic instruments:

* At the University of Munich, a CCD Zenith Camera has been designed providing directions of the vertical in connection with GPS-derived positions (Fosu [1999], Schöbel and Eissfeller [2000]). The internal accuracy has been indicated with 0.3 arcsec, however, the external accuracy is for a multiple worse.
* At the University of Vienna, a theodolite has been equipped with a high-resolution, though, not very light-sensitive CCD sensor. The internal accuracy obtainable ranges between 1 to 2 arcsec (Gerstbach [1999]).
* At the University of Hannover, the TZK2 has been upgraded to the TZK2-D using CCD technology and integrated GPS technique (Hirt [2004]). The obtained internal accuracy ranges between 0.1 and 0.3 arcsec. The external accuracy is denoted by about 0.1 arcsec.

At the GGL, intensive research at the field of astrogeodesy using digital technique has been conducted. Hence, a Leica tachymeter system, type TC1800, has been equipped with a CCD sensor. The system, called DAEDALUS, enables the automatic tracking of stars along the whole skyline measuring azimuths and zenithal angles of the stars. The obtainable accuracy for the resulting directions of the vertical is better than 1 arcsec. A lot of effort has been investigated in the enhancement of the analog TZK3. The new digital Zenith Camera DIADEM disposes of CCD and GPS technology as well as several servo motors for leveling, focussing and azimuthal turning. Therewith, it offers the possibility for a fully-automatic and completely PC-controlled observation. Furthermore, the close cooperation with the University of Hannover provides the possibility to use the software package AURIGA for a real-time analysis of the data in field. These conditions form the initial situation for the present Ph.d. project.

1.2.2 Geoid determination in Greece

From the early seventies on, systematic attempts for precise geoid determination have been carried out in the Hellenic area. Hence, Balodimos [1972] presented the first Hellenic geoid by using astrogeodetic-derived DOV, while Arabelos [1980] published a gravimetric solution some years later. Based on these spadeworks, Tziavos [1984] computed a combined geoid from astrogeodetic and gravimetric data. Almost at the same time, another geoid determination has been presented by Doufexopoulou-Patsada [1985] with emphasis on geophysical parameters related to the gravity field. A first comparison between the various geoid solutions in the Hellenic area has been performed

by Fotiou et al. [1986]. A still more detailed gravimetric geoid solution has been presented by Arabelos and Tziavos [1989]. In Arabelos and Tziavos [1990], a comparison between the gravimetric geoid for the southern Hellenic area and Geosat altimetry data has been conducted. The recent gravimetric geoid model HGFFT98 has been published by Tziavos and Andritsanos [1999]. It is based on an optimal combination of free-air gravity anomalies for the land area as well as gravity data for the marine area derived from altimetry and a digitization of sea gravity maps. Furthermore, information from a Digital Terrain Model with a resolution of 1 km and the geopotential model EGM96 have been implemented. A comparison of the HGFFT98 geoid with the current European Gravimetric Geoid 1997 (EGG97) showed differences of about 75 cm standard deviation. Another comparison in the marine area between HGFFT98 geoid heights and a number of SSH derived from the Topex/Poseidon mission revealed differences with a standard deviation of about 31 cm in the North Aegean Sea. A last evaluation in the continental area using GPS/leveling stations in northern Greece and in the central-western part of Greece revealed an accuracy of about 9 cm. With regard to these results, it has been concluded that further improvements of the Hellenic Geoid are necessary, mainly achievable by filling the major data gaps in the marine area (Tziavos and Andritsanos [1999]). Apart from the gravimetric geoid, an altimetric geoid has been computed for validation purposes (Tziavos et al. [2005]). It is based on the combination of altimetric data from the ER (European Remote) missions of ERS1/2 and TOPEX/Poseidon satellites. Also the EGM95 and bathymetric effects have been taken into account. A problem of the altimetric solution is caused by the fact that altimeter satellites are not able to measure over land, and that they also have problems receiving a signal over marine areas close to coastlines. Hence, especially in the North Aegean Sea, the coverage by altimetric data is very low due to the islands and the surrounding coastline to the west, north and east. This likewise demonstrates the need for additional marine data within the research area, which will be provided by the present Ph.d. project.

1.3 Structure of the thesis

Based on the goals of the project, the thesis is structured into 10 chapters. **Chapter 1** starts with an introduction into the rationale and goals of the project (1.1) and reflects the present state of research in the field of astrogeodetic instruments and geoid determination in the Hellenic area (1.2). **Chapter 2** provides basic skills (2) that are necessary in connection with the present work. It overviews geodetic fundamentals concerning reference systems (2.1), star catalogs (2.2), time scales (2.3) and height systems (2.4).

The first part of the project deals with the enhancement and validation of the Digital Astronomical Deflection System DIADEM: **Chapter 3** explains the principle of the determination of DOV (3.1) and provides a depiction of the technical features of DIADEM (3.2). **Chapter 4** outlines a measuring procedure with DIADEM comprising the process of data acquisition (4.1), data analysis (4.2), necessary corrections (4.3) and calibrations (4.4). **Chapter 5** discusses the main internal and external error sources affecting the determination of the rotational direction (5.2), inclination measurements (5.3), epoch determination (5.4), azimuthal corrections (5.5) and geodetic position (5.6). **Chapter 6** is finally concerned with the field applications performed during the last four project

years comprising observations in Switzerland (chapters 6.1, 6.3, 6.4) and Portugal (6.2). It also includes the discussion of the results of repeated observations with DIADEM at the reference station in Zurich (6.5).

The second part of the project refers to the deployment of DIADEM in the North Aegean Sea, Greece: **Chapter 7** introduces the topographic, bathymetric and tectonic features of the North Aegean Sea domain (7.2). Furthermore, it outlines the available geoid models in the Hellenic area (7.3). It also represents the data gathered during the campaign (7.4) including the DOV observed by DIADEM as well as the shipborne GPS data and GPS buoy measurements. **Chapter 8** is concerned with the reduction of the observed DOV in the frame of the Remove-Restore method applied. Therefore, the mathematical background for the computation of mass effects is explained (8.2). The mass models used like the Shuttle Radar Topography Mission model (8.3), different isostasy models (8.4) and the Moho model from the Aristotle University of Thessaloniki (8.5) are described thoroughly. The chapter finishes with the presentation and interpretation of the reduced DOV (8.6). **Chapter 9** attends to the computation of the geoid starting with a survey of different methods of geoid determination (9.1). The principle of least-squares-collocation is explained (9.2), and the computed cogeoid and geoid models are discussed and validated (9.3). **Chapter 10** finally summarizes and discusses the main results presented within this thesis and gives an outlook on potential future works to be done.

2 Basic knowledge

2.1 Reference systems

2.1.1 Introduction

In geodesy, there exist three classes of reference systems: space-fixed celestial systems, earth-fixed terrestrial systems and local or topocentric systems. This work focuses on celestial and terrestrial reference systems as the main important systems of astrogeodetic observations with a Zenith Camera. Celestial systems are extra-terrestrially determined and define the position of stars and their proper motions. Terrestrial systems are used for the definition of positions on earth and can be divided into gravity-field dependent (astronomical) and gravity-field independent (ellipsoidal) systems. It has to be differed between a *reference system* defining the origin, axes and constants of the coordinate system and a *reference frame* realizing the system by means of coordinates of objects and points (see e.g. Torge [2001], Rummel [2005] and Homepage of International Earth Rotation and Reference Systems Service IERS: http://www.iers.org/).

2.1.2 Celestial reference systems

International Celestial Reference System

In the past, space-fixed systems have been realized by methods of astronomy defining the coordinates of stars. Star catalogs like the FK5 or the Hipparcos catalog served as reference frames. Nowadays, a more precise realization of the celestial reference system is provided by the observation of so called extraterrestrial quasi-stellar radio sources (quasars) by means of VLBI (Very Long Baseline Interferometry). Quasars have the advantage that they do not show proper motions due to their great distances. Therefore, they can be regarded as space-fixed, hence coming close to an inertial system (no pseudo forces). The International Celestial Reference Frame (ICRF) contains fixed directions to about 608 extragalactic radio sources evenly distributed on the sky and determined with an accuracy of better than 0.3 mas. The axes of the International Celestial Reference System (ICRS) correspond to those formerly realized by the FK5 catalog at epoch J2000.0. The main important definitions concerning the ICRS can be found in Tab. 2.1.

Definition:	International Celestial Reference System ICRS
Realization:	International Celestial Reference Frame ICRF
Observation methods:	VLBI, HIPPARCOS and FK5 catalog
Reference:	600 quasars
Origin:	Barycenter of the solar system
Orientation:	
X-Y-plane:	Mean celestial equatorial plane at epoch J2000.0
X-axis:	Mean vernal equinox at epoch J2000.0
Z-axis:	ICRS Reference Pole at epoch J2000.0
Y-axis:	Completion of a right-hand system
Coordinates:	Equatorial coordinates: Right ascension α, Declination δ

Table 2.1: Details to the celestial reference system.

Equatorial coordinate system

The positions of stars are given in equatorial coordinates by means of right ascension α and declination δ. The definition of the equatorial coordinate system refers to the ICRS. The origin coincides with the geocenter, while the ICRS origin is normally defined in accordance with the mass center of the solar system (barycenter). Theoretically, the observed directions to the stars depend on the reference position (geocenter or barycenter), caused by parallax effects. However, because of the great distances of the stars, these differences can be neglected. The right ascension α is measured in the equatorial plane (X-Y-plane) referring to the vernal equinox (X-axis) and ranging from 0° to 360° or 0^h to 24^h, respectively. The declination δ is measured from the equatorial plane along the meridian of the star and ranges from -90° to 90° (Fig. 2.1).

2.1.3 Terrestrial reference systems

International Terrestrial Reference System

The International Terrestrial Reference System (ITRS) is a global, geocentric, cartesian and earth-fixed reference system. The main important definitions concerning the ITRS can be found in Tab. 2.2. Each point on earth is designated by a natural direction, the direction of the local plumb line standing orthogonally to the equipotential surfaces of the earth's gravity field. In ITRS, this direction is defined by the astronomical latitude Φ and longitude Λ (Fig. 2.1). The latitude Φ is counted from the equatorial plane (X-Y-plane) to the direction of the vertical ranging from -90° to 90°. The longitude Λ represents the angle between Greenwich and local meridian that runs through the direction of the vertical. It ranges from 0° to 360° or -180° to 180°, respectively. The ITRS is realized by the International Terrestrial Reference Frame (ITRF) by means of a list of station coordinates, velocities and corresponding accuracies. In former times, the station coordinates have been received from astronomical position determinations and geodetic networks. Today, more precise spatial methods, as e.g. VLBI, SLR, LLR and GPS are used for this purpose (Rummel [2005]).

Definition:	International Terrestrial Reference System ITRS
Realization:	International Terrestrial Reference Frame ITRF
Observation methods:	VLBI, SLR, LLR, GPS, DORIS
Reference:	Station coordinates, velocities
Origin:	Mass center of the earth (including atmosphere and oceans)
Orientation:	
X-Y-plane:	Earth's equatorial plane
X-axis:	Greenwich meridian
Z-axis:	IERS Reference Pole IRP
Y-axis:	Completion of a right-hand system
Coordinates:	Cartesian coordinates (X,Y,Z)

Table 2.2: Details to the terrestrial reference system.

Ellipsoidal coordinate system

The earth can be mathematically approximated by a spheroid, described by a 3D-cartesian coordinate system. The geodetic coordinates are represented by the latitude φ and longitude λ. The latitude φ is measured from the equatorial plane (X-Y-plane) to the ellipsoid normal in point P. The longitude λ is measured in the equatorial plane between the zero-meridian and the meridian through station P. The mean global ellipsoid (WGS84) agrees best-possible with the geoid and coincides with the ITRS axes and the geocenter. In contrast, conventional ellipsoids are normally shifted to the geocenter and rotated in comparison to the ITRS. They are adapted to the local gravity field, and their definition is subject of the national surveying institutions. The transformation between global and conventional ellipsoid can be realized via a 3D Helmert transformation (7 parameters) (Torge [2001]).

2.1.4 Orientation between terrestrial and celestial systems

The relative orientation between earth-fixed ITRS and space-fixed ICRS is defined by the Earth Orientation Parameters (EOP). They describe the variations of the earth's rotation around the Celestial Ephemeris Pole (CEP), which corresponds to the *instantaneous rotational axis of the earth*[1]. The EOP are determined permanently by the International Earth Rotation and Reference Systems Service (IERS) and are public accessible via internet (IERS homepage: http://hpiers.obspm.fr/). They comprise the following phenomena:

* Precession and Nutation: These effects cause variations of the instantaneous earth's rotational axis (CEP) in reference to the ICRS Reference Pole at epoch J2000.0. Hence, the CEP can not be considered as *space-fixed*.
* Earth's rotation: The daily rotation around the CEP is defined by the Greenwich Apparent Sidereal Time (GAST).

[1]The CEP corresponds to the instantaneous rotational axis of the earth except for short-periodic variations with amplitudes of less than 10 mas. For the analysis of the Zenith Camera observations, these deviations have been neglected (Hirt [2004]).

* Polar motion: The CEP moves relatively to the IERS Reference Pole (IRP) and can, therefore, not be considered as *earth-fixed*.

The effects are described in detail in chapter 2.1.5.

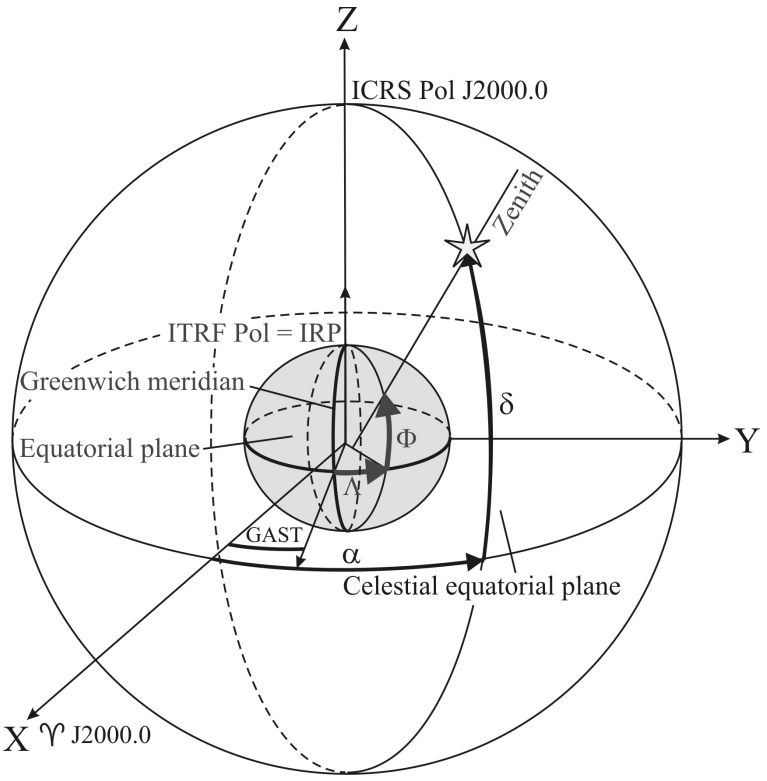

Figure 2.1: Depiction of space-fixed ICRS (black) with equatorial coordinates (α, δ), and earth-fixed ITRS (light-gray) with astronomical parameters (Φ, Λ). They are linked via Greenwich Apparent Sidereal Time GAST.

As for the analysis of Zenith Camera observations, the effects of *nutation* and *precession* are included in the computation of apparent star positions (chapter 2.2.4). The orientation angle GAST between ITRS and ICRS is considered within the process of the determination of the rotational direction (Φ_D, Λ_D) (chapter 4.2.5 and Fig. 4.4). The polar motion parameters (x_P, y_P) are applied as final corrections to (Φ_D, Λ_D) (chapter 4.3).

2.1.5 Earth Orientation Parameters

This chapter will provide a survey of the Earth Orientation Parameters (EOP) comprising the effects of precession, nutation, polar motion and earth rotation. More details concerning the EOP can be found in Sigl [1991], Seeber [2003], Torge [2003] as well as at the IERS homepage (http://www.iers.org/).

Precession and nutation

Sun, moon and other planets cause an attraction at the equator bulges. The resulting torsional moments try to turn the equatorial plane into the ecliptic, or in other words, to set up the axis of the earth. According to the gyroscopic laws, and as a result of the interaction between the described torsional moments with the earth's rotation, the rotational axis deviates orthogonally both to the rotational axis of the earth and the acting momentum. It describes a cone-shaped shell around the pole of ecliptic. This process is called *precession*. A complete circulation of the earth's axis lasts 25800 years (= 1 platonic year), the cone angle corresponds to two times of the ecliptic obliquity ($\varepsilon = 23.5°$). The main part of the precession (about 50 arcsec/yr) is caused by sun and moon (=lunisolar precession), a substantial smaller part (-0.12 arcsec/yr) is caused by other planets.

From the physical point of view, the *nutation* has its origin in the same phenomena as the precession, however, it is mainly caused by the attraction of the moon. As the moon's orbital plane is inclined by about 5.1° against the ecliptic, the varying declination of the moon causes an elliptically-shaped motion of the apparent earth's axis around a mean one, and, therewith linked, a libration of the apparent vernal equinox around a mean one. The sum of precession and nutation results in a wave-like motion of the earth's axis around the pole of ecliptic. Due to the described phenomena, the orientation of the instantaneous rotational axis of the earth (CEP) can not be considered as space-fixed. Therefore, the star positions (α, δ) have to be referenced to a certain equinox (mostly J2000.0) describing the orientation of the earth's axis at this epoch (=ICRS Reference Pole at epoch J2000.0).

The precession and nutation phenomena can be predicted by the precession-nutation-model of the International Astronomical Union (IAU 1980). The secular part (precession) is considered by the IAU precession model 1976 and the periodic part (nutation) by the IAU nutation model 1980. Both models are implemented in AURIGA (Hirt [2004]). By applying the IAU 1980 model, the instantaneous CEP can be computed in relation to the ICRS. However, due to the limited model accuracy, the CEP based on the IAU model and the true instantaneous CEP might differ for a few 0.01 arcsec. These time-dependent differences are published in terms of the parameters $(\delta\Delta\Psi, \delta\Delta\varepsilon)$ by the IERS. The IAU 1980 model in combination with these corrections allows for a consideration of the precession/nutation effects with an accuracy of better than 0.001 arcsec (McCarthy [1996]).

Polar motion

Polar motion is caused by the fact that the rotational axis of the earth does not coincide with the main axis of inertia, but rotates around it. In case the earth would be a rigid body, the motion could be described mathematically by means of the gyroscopic theory indicating a period of 305 days (=Euler period). However, due to the fact that the earth is elastic and reacts to gravitational forces induced by sun and moon, the direction of the main inertial axis is not constant. Hence, the period extends after Chandler up to 412 and 442 days, respectively. In consequence of seasonal relocations of air masses, the so called *Chandler wobble* is additionally superposed by a 365 days period. The amplitude of polar motion varies, with deviations of the instantaneous position of the pole from the long-term midpoint of $\leq$0.3 arcsec over one year (Torge [2001]). A further

part of the polar motion is caused by a shifting for about 0.1 m per year in direction to the 80th degree of western longitude (Kahle [2001]). Polar motion is expressed by the parameters (x_P, y_P) representing the difference between the CEP and the IERS Reference Pole IRP. They are determined and published by the IERS. For the correction of the polar motion effect see chapter 4.3.

Earth's rotation

Due to irregularities of the earth rotation, the rotational time systems GMST, GAST and UT1 are only computable based on observations (Hirt [2004]). The atomic time scale UTC agrees more or less with the earth rotation, the differences between UTC and UT1 are always $\leq 0.9s$ (see chapter 2.3.2). They are published in terms of the parameter $\Delta UT1$ by the IERS.

2.2 Star catalogs

2.2.1 Introduction

A star catalog is a table of stars comprising the equatorial coordinates of stars as well as proper motions, magnitudes, parallaxes and spectral properties (Zimmermann and Weigert [1995]). The task to be solved within the analysis of Zenith Camera observations is to extract the coordinates $(\alpha, \delta)_k$ of stars visible at the observation station at a determinated epoch. These stars have to be linked with the corresponding image coordinates $(x, y)_i$ of the stars exposed.

There exist catalogs of different accuracies and star densities, as e.g. the Hipparcos, Tycho-2, UCAC, GSC 1.1. and GSC 2.2 as well as the USNO-A and USNO-B catalogs, which have to fulfill several conditions within the frame of Zenith Camera observations (Hirt [2004]):

* Positions given in ICRS
* High star density up to a mag 14
* High position accuracies of $\leq$0.05 arcsec
* Indication of proper motions (see chapter 2.2.4) and magnitudes[2]

These conditions are fulfilled by the Tycho-2 and the UCAC catalog, which are described in chapters 2.2.2 and 2.2.3, respectively. The positions of the stars listed in a catalog are *mean positions*. Due to the fact that the stars are subject to different time-dependent phenomena (chapter 2.2.4), their positions have to be referenced to a certain *epoch* and *equinox*:

* The *epoch* defines the date and time, when the star position has been determined astrometrically (e.g. on a CCD). It forms the reference time for given proper motions. In order to ease the handling of a catalog, the stars are mostly transformed to a consistent epoch having regard to their proper motions. Both catalogs, the Tycho-2 and the UCAC, refer to the standard epoch J2000.0.

[2]Magnitudes form a logarithmic measure of received radiation (energy per second and unit of area) from a star. The lower the magnitude, the brighter the object.

* The determined star positions not only vary due to the proper motions of stars, but also due to variations of the celestial coordinate system (ICRS) as a result of precession and nutation (chapter 2.1.5). Therefore, the star positions are always referenced to a certain *equinox* of the coordinate system, which defines the spatial direction of the vernal equinox at a defined point of time. Mostly, the star catalogs refer to equinox J2000.0.

2.2.2 Tycho-2 catalog

The Tycho-2 catalog is an astrometric reference catalog containing positions and proper motions as well as two-color photometric data for the 2.5 million brightest stars of the whole sphere (Høg et al. [2000]). The Tycho-2 positions and magnitudes are based on precisely the same observations as the original Tycho catalog- They have been derived processing photon counts obtained from scans of the Tycho star mapper of the ESA Hipparcos satellite (observation period was from 1989.85 to 1993.21). However, the Tycho-2 catalog contains 2.5 times more stars than the first catalog and is slightly more precise, because of the use of more powerful data reduction technique. The precision of the positions is better than 0.1 arcsec depending on the magnitude. The proper motions indicate a precision of about 0.0025 arcsec/yr and have been derived from a comparison with the Astrograph catalog and 143 other ground-based astrometric catalogs, all reduced to the Hipparcos celestial coordinate system. The most important facts about the Tycho-2 catalog are provided in Tab. 2.3.

Mean satellite observation epoch	J1991.5
Standard epoch of the Tycho-2 catalog	J2000.0
Reference system	ICRS
Number of entries	2539913
Magnitude [mag] (approx. complete)	11.5
Astrometric standard errors:	
Stars mag < 9	≤ 0.007 arcsec
Stars $9 <$ mag < 12	≤ 0.07 arcsec
Stars $12 <$ mag < 14	≤ 0.1 arcsec
all stars, proper motions	0.0025 arcsec/yr
Photometric standard errors:	
Stars < 9 mag	0.013 mag
all stars	0.10 mag
Star density:	
Lat=0°	150 $stars/\deg^2$
Lat=±30°	50 stars $stars/\deg^2$
Lat=±90°	25 stars $stars/\deg^2$

Table 2.3: Tycho-2 catalog parameters (Høg et al. [2000]).

2.2.3 UCAC catalog

The second US Naval Observatory (USNO) CCD Astrograph Catalog, UCAC2, was released in 2003 July, obtained from terrestrial observations with the USNO 0.2 m Twin Astrograph. The instrument is equipped with a 16 MPixel CCD camera (Zacharias et al. [2004]). With the Astrograph, star fields of about 1 deg^2 can be covered. The catalog contains positions and proper motions for about 50 million objects (mostly stars). It covers the sky area from -90° to +40° declination extending to +52° in some areas. Depending on the magnitude, the precision of the positions is better than 0.07 arcsec with estimated systematic errors of maximum 0.01 arcsec. The proper motion errors amount to maximum 0.007 arcsec/yr, also for fainter stars up to mag 16. The UCAC2 provides about 30 times more $stars/\deg^2$ than the Tycho-2 catalog. It is a compiled catalog including Hipparcos and Tycho observational data as well as all ground-based catalogs used for the Tycho-2 proper motions (Zacharias et al. [2004]). The final catalog (UCAC3) is expected to be published in late 2008 (http://ad.usno.navy.mil/ucac/). The most important facts about the UCAC2 catalog are provided in Tab. 2.4.

Mean observation epoch	1998-2004
Standard epoch of the UCAC catalog	J2000.0
Reference system	ICRS
Number of entries	48330571
Magnitude [mag] (approx. complete)	16
Astrometric standard errors:	
Stars mag < 9	0.03-0.07 arcsec
Stars $9 <$ mag < 12	≤ 0.02 arcsec
Stars $12 <$ mag < 14	≤ 0.02 arcsec
all stars, proper motions	0.001-0.015 arcsec/yr
Average density	1360 $stars/\deg^2$

Table 2.4: UCAC catalog parameters.

The comparison of both catalogs, Tycho-2 and UCAC2, reveals that the Tycho-2 is indeed almost complete up to mag 11.5, however, it is incomplete within the relevant range of magnitude for Zenith Camera observations (mag 12-14). In contrast, the final version of the UCAC, the UCAC3[3], will provide an almost complete field up to mag 16. The Tycho-2 indicates very high precisions for stars up to mag 10 (0.02 arcsec), though, for higher magnitudes the catalog provides worse precisions than the UCAC (max. 0.1 arcsec vs. 0.02 arcsec). A disadvantage of the UCAC2 (implemented in AURIGA) is the fact that it does not cover the whole sphere. However, the implementation of the UCAC3 will compensate this disadvantage by providing stars for the whole sphere. Comparing the number of stars listed in Tycho-2 (2.5 million) and in UCAC (50 million), it is concluded by (Hirt [2004]) that the UCAC2 (and UCAC3 in future) provides an excellent reference for an analysis of Zenith Camera observations (Hirt [2004]). Due to the still lower coverage of the UCAC2, both catalogs, the Tycho-2 and the UCAC2, are implemented in AURIGA. Furthermore, this provides possibilities for comparisons and validations.

[3]The UCAC3 catalog is not published yet, but it is currently in process at the USNO

2.2.4 Variations of star positions

Star catalogs contain mean star positions $(\alpha, \delta)_0$, mostly referring to epoch J2000.0. They are subject to different time-dependent phenomena, which have to be taken into account for the analysis of Zenith Camera observations. This includes the effects of *proper motion* (effective changing of star positions), *precession* and *nutation* (shifting of coordinate systems), *refraction*, *daily* and *annual aberration* as well as *relativistic light diversion* (apparent changing of star positions). Due to the great distance of stars, the influence of geocentric and annual parallax is negligible.

The corrections for proper motion, precession, nutation, annual abberation and relativistic light diversion enable the transformation of *mean* into *apparent positions*, which refer to the *geocenter*. The corrections for daily abberation and refraction finally provide *topocentric* star positions as needed for the analysis of Zenith Camera observations. Thorough descriptions concerning the reduction of star positions with accuracies of better than 0.001 arcsec can be found in Kaplan et al. [1989] and Seidelmann [1992]. In AURIGA, the highly-precise algorithm of NOVAS-C software libraries from USNO (Bangert and Kaplan [1998]) are implemented (Hirt [2004]). The general formalism to transform mean into apparent positions is depicted in Appendix A.1, Eq. (A.1).

Proper motion. Due to their motions relative to each other, stars can not be considered as fixed objects in sphere. The spatial motion of a star in relation to the earth can be divided into two orthogonal components: the change of *distance*, which remains generally undiscovered, and the change of *direction*, which forms the observable part of proper motion. The observable proper motion of a star is mostly very small, the resulting variations of right ascension α and declination δ amount to a few 0.1 arcsec per year. To determine the proper motion of a star, the coordinates at two different epochs has to be computed (see Appendix A.1, Eq. (A.2), for strict formulas see Schödelbauer [2000]). As mentioned in chapter 2.2.1, both star catalogs implemented in AURIGA, the Tycho-2 and the UCAC, contain corresponding proper motions for each star registered. The respective accuracies are below 0.015 arcsec per year (see Tabs. 2.3 and 2.4) and, therefore, sufficient for a highly-precise reduction of star positions.

Precession and Nutation. The effects of precession and nutation are explained in chapter 2.1.5.

Daily and annual abberation. Due to the finite speed of light and the relative motion of the observer on earth, the effect of abberation causes apparent variations of star positions. Considering that the motion of the observer is composed of three components - (a) the earth's rotation, (b) the motion of the earth around the sun, and (c) the motion of the sun system relative to fixed stars - one has to differentiate between daily (a), annual (b) and secular (c) abberation (Sigl [1991]). For a star standing in zenith (as valid for Zenith Camera observations), the effect of *daily abberation* has merely an impact on the α-component. It causes a shifting for 0.32 arcsec in eastern direction (see Appendix A.1, Eqs. (A.3) to (A.5)). The *annual abberation* has the effect that the stars describe ellipses around the pole of ecliptic, with a semi-major axis of 20.495 arcsec (abberation constant) (see Appendix A.1, Eqs. (A.6)). The *secular abberation*, which can be associated with the movement of the solar system, is not available for astrometric measurements.

Relativistic light diversion. In the vicinity of strong gravity sources as the sun, a light beam is deflected in direction to the source. This effect (predicted by Einstein) causes a directional misalignment ΔE, which increases with decreasing elongation E (=angular separation) between sun and star. For very small E, ΔE reaches a maximum value of 1.75 arcsec. For Zenith Camera observations, the sun is generally beneath the horizon, hence the elongation between zenithal stars and sun amounts to about 90°. The misalignment ΔE amounts then to maximum 0.004 arcsec, and is, therefore, negligible for astrogeodetic observations into the zenith.

Refraction. The effect of atmospheric refraction is discussed separately in chapter 5.2.2.

Comprehensive descriptions of all phenomena can be found e.g. in Schödelbauer [2000], Sigl [1991] and Rummel [2005]. For detailed computation formulas concerning the consideration of the described phenomena within the analysis of Zenith Camera observations, please refer to Hirt [2004].

2.3 Time systems

2.3.1 Introduction

Time systems play an important role in geodesy, especially in the field of satellite geodesy and astronomical geodesy. In astronomical geodesy, they serve as information about the orientation between celestial and terrestrial reference system. Time scales describe periodic astronomical and physical phenomena, whereas the time interval between the phenomena define the *scale* and a dedicated multiple or fraction of the scale forms the *unit*. A generally accepted unit is the *second* providing the basis for higher units as days or years. The zero-point of a scale is defined e.g. by a certain astronomical event as the transit of a star across the meridian. The moment of an observation can be referenced to the zero-point of the scale, hence yielding the corresponding absolute time, called *epoch*. A natural unit is provided by the duration of the daily earth's rotation, e.g. in reference to the stars (sidereal time) or the sun (solar time). Due to irregularities in the earth's rotation (see chapter 2.1.5), these so called *rotational time systems* are not stable in time. However, many scientific or technical tasks require the definition of an uniform time scale. This demand is fulfilled by *atomic time systems* forming pure physically defined scales. The unit of these scales is the so called atomic second (SI second[4]). Over the years, the time systems show differences compared to each other, which can be attributed to irregularities and variations in the earth's rotation. They have to be determined by observations, which are performed by the IERS. Detailed explanations of time systems can be found e.g. in Sigl [1991], Seidelmann [1992], Seeber [2003] and Torge [2003].

[4]SI second: duration of 9192631770 periods of the radiation corresponding to the transition between the two hyperfine levels of the ground state of the cesium-133 atom

2.3.2 Important time systems for Zenith Camera observations

In order to establish the relation between astronomical coordinates (Φ, Λ) and equatorial coordinates (α, δ) (Eq. (3.2)), the respective exposure epoch determined by GPS has to be transformed into GAST. The necessary time systems and formulas for solving this task are depicted in Tab. 2.5. The time systems are shortly introduced within this chapter, for detailed information please refer to the literature mentioned in chapter 2.3.1.

Step	**Time systems + Parameters**	**Definition**	**Computation**
1	GPST	GPS Time	GPS-derived exposure epoch with DIADEM
2	UTC	Universal Time Coordinated	$UTC = GPST - 14\ s$
3	UT1	Universal Time 1	$UT1 = UTC + \Delta UT1$ $\Delta UT1 \leq 0.9\ s$
3.1	t	Julian centuries t elapsed between J2000.0 and computation epoch T_{UT1}	$t = \frac{T_{UT1} - 2451545.0}{36525}$
4	GMST	Greenwich Mean Sidereal Time	$GMST\ (at\ 0^h UT1) =$ $6^h 41^m 50.^s 5481 +$ $8640184.^s 812866 \cdot t +$ $0.093104 \cdot t^2 -$ $6.^s 2 \cdot 10^{-6} \cdot t^3$
4.1	TAI	International Atomic Time	$TAI = UTC + 33\ s$
4.2	TT	Terrestrial Time	$TT = TAI + 32.184\ s$
4.3	t	Julian centuries t elapsed between J2000.0 and computation epoch T_{TT}	$t = \frac{T_{TT} - 2451545.0}{36525}$
4.4	$\Delta\psi, \Delta\varepsilon, \varepsilon_0, \Omega$	Nutation parameters	IAU nutation model 1980 as function of t
4.5	Δm	Equation of Equinox	$\Delta m =$ $\Delta\psi \cdot \cos\varepsilon_0 +$ $0.“00264 \cdot \sin\Omega +$ $0.“000063 \cdot \sin 2\Omega$
5	GAST	Greenwich Apparent Sidereal Time	$GAST = GMST + \Delta m$

Table 2.5: Necessary transformations between GPST and GAST for the analysis of Zenith Camera observations. GPST: GPS Time, UTC: Universal Time Coordinated, UT1: Universal Time 1, GMST: Greenwich Mean Sidereal Time, TAI: International Atomic Time, TT: Terrestrial Time, GAST: Greenwich Apparent Sidereal Time, $\Delta\psi$: Nutation of the longitude of ecliptic, $\Delta\varepsilon$: Nutation of the obliquity of ecliptic, ε_0: Mean obliquity of ecliptic, Ω: Longitude of lunar node.

Rotational time systems

Sidereal time. A sidereal day is defined as the time interval between two transits of the vernal equinox across the observer's meridian. The Local Apparent Sidereal Time (LAST) corresponds to the observer's meridian and represents the hour angle of the apparent vernal equinox. A special meridian is formed by the Greenwich meridian, which serves as reference for GAST. The corresponding Local Mean Sidereal Time (LMST) and Greenwich Mean Sidereal Time (GMST) are obtained after accounting for effects of precession and nutation (see chapter 2.1.5). The difference between apparent and mean sidereal time is described by the "Equation of Equinox" (see steps 4.5 and 5 in Tab. 2.5).

Solar time. Due to practical needs, solar time is used in everyday life (Torge [2001]). A solar day represents the time interval between two sun transits across the observer's meridian. However, according to the fact that the revolution of the sun around the earth is a nonuniform process, a virtual mean sun is introduced moving evenly along the equator. The mean solar time UT0 (Universal Time) is defined as the time elapsed since the last transit of the mean sun across the Greenwich meridian plus 12 hours. This time scale is influenced by position-dependent variations (polar motion) of the apparent pole of rotation (CEP) compared to the defined mean pole (IRP). The reduction to the IRP yields a change of longitude and, hence, of time and results in the definition of UT1.

Both time scales, sidereal and solar time, are based on the earth's rotation. Therefore, the solar time can also be regarded as a special sidereal time. The sidereal and the solar day differ for about $3^m55.909^s$, as the earth moves forward for about $360°/365 \approx 1°$ per day on its orbit around the sun. Thus, 1 *mean sidereal day* corresponds to 1 *mean solar day* $- 3^m55.909^s$.

Atomic time systems

Universal Time Coordinated UTC. The various irregular fluctuations detected in the rotation of the earth yielded in 1972 the replacement of UT1 as the reference time scale by UTC. This time scale provides, on the one hand, the advantage of a strict and homogeneous measure, based on the atomic second (SI second). On the other hand, it is closely correlated with UT1. In order to ensure an agreement between physical and astronomical time scales, the difference UT1-UTC does, per definition, never exceed more than 0.9 second. This is realized by the introduction of so called leap seconds, which are regularly published by the IERS. The last additional second has been introduced on January 1st, 2006, at 0h UTC.

Global Positioning System Time GPST. For the Global Positioning System, the time scale GPST has been introduced differing from UTC for an integer number of seconds. Both times systems agree at January 5th, 1980. As no leap seconds are introduced in GPST, the difference between UTC-GPST increases by time (2008: GPST - UTC = 14 s). The actual relations are announced e.g. by the USNO.

International Atomic Time TAI. UTC is based on TAI, which is controlled by means of 250 globally distributed atomic clocks. The Bureau International des Poids et Mesures (BIPM) determines TAI from a weighted average of all clocks. The origin of TAI coincides with UT1 at January 1st, 0h. Due to the leap seconds regularly added to UTC, the

difference between TAI and UTC amounts to a varying integer number of seconds (2008: TAI - UTC = 33 s).

Model time systems

Terrestrial Time TT. TT is intimately connected with the atomic time systems and fulfills widely the condition of an inertial time. Its realization bases on TAI, which differs for a constant offset from TT (TT - TAI = 32.184 s). The scale TT is used for the calculation of the Julian date, which is a necessary argument for the IAU nutation and precession models, the calculation of the annual abberation and the relativistic light diversion.

Julian date. The astronomical standard epoch J2000.0 is equal to JD 2451545.0 in Julian days. Other epochs can be derived by simple algorithm, as e.g. described in Seidelmann [1992]. Some transformation formulas, e.g. between different time systems, need the Julian date of the observation/computation epoch T referring to the standard epoch J2000.0 and expressed in Julian centuries t (see steps 3.1 and 4.3 in Tab. 2.5).

2.4 Height systems

In Geodesy, a height is defined as a vertical distance between a point and a reference surface (geoid, quasigeoid or geodynamically defined reference ellipsoid). The height of the respective reference surface is fixed to a mean sea level, whereas each country uses different height systems and reference levels. Normally, one expects from heights that they are geometrical values, given in "Meter" (geometrical condition) and that no water is flowing between two points with identical heights, i.e. they feature the same gravitational potential (physical condition). However, due to gravity anomalies caused by inhomogeneities in the distribution of earth's masses, a height definition can not fulfill both conditions. This fact becomes obvious when leveling along different paths between two points yielding different height differences (theoretical closure error of leveling loops). It can be attributed to the condition that the heights are measured along non-parallel equipotential surfaces, but the differences are measured in "Meter". In order to obtain reasonable results, the consideration of the gravity field is required. Hence, two different classes of height systems have been established: *geometrical heights*, represented by ellipsoidal heights and *physical heights*, as e.g. formed by dynamic, orthometric and normal heights.

In order to understand the relation between them, the following theoretical background shall be provided (compare Fig. 2.2):

The potential W_P of a point P is the sum of the gravitational potential G_P depending on the mass distribution on and inside the earth and on the centrifugal potential C_P, caused by the earth's rotation (Schlatter [2007]): $W_P = G_P + C_P$. All points with a constant potential W define an equipotential surface, whereas the geoid represents a dedicated equipotential surface $W = W_0$ coinciding with the mean sea level. The geoid forms the main reference surface for physically defined height systems.

The reference for geometrically defined heights is represented by the mean earth ellipsoid GRS80 (Geodetic Reference System 1980), which indicates on its surface the same potential as the geoid ($U_0 = W_0$). Furthermore, it features the same angular velocity, total volume and center as the masses limited by the geoid. Similar as for the earth's gravity field, the earth ellipsoid indicates equipotential surfaces with a constant normal potential U.

The deviation of the geoid from the ellipsoid is indicated by the geoid undulation N. The potential W_P of a point P can now be split into the normal potential U_P, caused by the mean earth ellipsoid, and the anomalous potential T_P (sometimes also called *disturbing potential*), induced by irregularities in mass and density distributions: $W_P = U_P + T_P$. Due to the influence of the anomalous potential T_P, normal potential U_P and potential W_P of point P are not identical at the earth's surface. The equipotential surface of the earth ellipsoid with $U = W_P$ runs through a point Q, which differs from P ($U_Q = W_P$). The distance between both points is called *height anomaly* or *quasigeoid undulation* ζ. All points Q whose potential U_Q is identical with the potential W_P of the corresponding point P on the earth's surface form a further reference surface, the so called telluroid (Schlatter [2007]). The quasigeoid as another important reference surface yields from the adding of ζ to the ellipsoid.

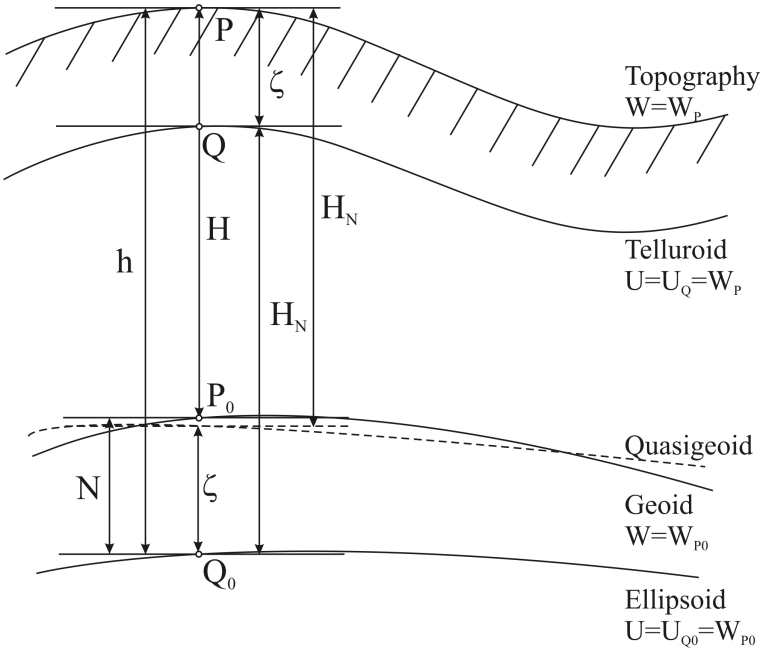

Figure 2.2: Depiction of different height systems referring to the geoid, telluroid, quasigeoid and ellipsoid. The according heights are: h = Ellipsoidal height, H_N = Normal height, H = Orthometric height, N = Geoid undulation, and ζ = Height anomaly = Quasigeoid undulation.

The height systems depicted in Fig. 2.2 are the following:

Orthometric heights H. Orthometric heights refer to the true gravity field of the earth. They describe the vertical distance between P_0 at the geoid and P at the surface and are measured along the curved plumb line through P.

Normal heights $\mathbf{H}_N$. Normal heights refer to the normal gravity field of the earth. They describe the height of P above the quasigeoid as well as the height difference between

Q at the telluroid and Q_0 at the ellipsoid. The differences "telluroid/surface" and "ellipsoid/quasigeoid", respectively, are called *height anomaly* or *quasigeoid undulation* ζ.

Ellipsoidal heights h. Ellipsoidal heights refer to a mathematically defined reference surface, e.g. the mean earth ellipsoid WGS84. They represent the vertical distance between P at the surface and Q_0 at the ellipsoid.

Ellipsoidal heights can be linked to the gravity field of the earth via orthometric heights H and normal heights H_N, respectively, by the following relations:

$$h = H + N = H_N + \zeta \tag{2.1}$$

Detailed descriptions of the common height systems used in geodesy can be found in Wirth [1990], Torge [2001] and Schlatter [2007].

3 Digital Astronomical Deflection Measuring System *DIADEM*

3.1 Determination of deflections of the vertical

The determination of deflections of the vertical (DOV) is based on the combination of a *Zenith Camera* with satellite-based methods like *GPS*. GPS provides the geometrically defined ellipsoidal latitude φ and longitude λ, which represent the normal vector referring to the ellipsoid. In contrast, Zenith Cameras determine the direction of the vertical referring to the geoid, which is expressed by the astronomical latitude Φ and longitude Λ. The difference between both vectors is called deflection of the vertical and is represented by the N-S-component ξ and the W-E-component η:

$$\xi = \Phi - \varphi \qquad \eta = (\Lambda - \lambda)\cos\varphi \tag{3.1}$$

The determination of the astronomical parameters (Φ, Λ) with a Zenith Camera is based on the idea to expose the zenithal star field by a CCD camera and to interpolate the direction of the instrument's axis into the star field. The celestial positions of the stars exposed are defined by equatorial coordinates (δ, α), obtainable from high-precision star catalogs as Tycho-2 (Høg et al. [2000]) and UCAC (Zacharias et al. [2004]) (chapter 2.2). They can be linked with the astronomical parameters (Φ, Λ) by the Greenwich Apparent Sidereal Time (GAST):

$$\Phi = \delta \qquad \Lambda = \alpha - GAST \tag{3.2}$$

Please note that the relation between Φ and δ is only valid for stars in zenith. Based on Eq. (3.2), the direction of the vertical could be easily determined, if a star was located directly in zenith and the sidereal time GAST was measured. However, this situation will hardly occur in reality.

Fig. 3.1 illustrates the two main reference systems: the equatorial reference system (ICRS, chapter 2.1.2), and the terrestrial reference system (ITRS, chapter 2.1.3). The equatorial system, a celestial space-fixed coordinate system, allows for the definition of the star positions by means of right ascension α and declination δ. The terrestrial system is an earth-fixed system, represented by the astronomical latitude Φ and longitude Λ. It is used to define the position of the observation point. Both systems refer to the equatorial plane and the rotational axis of the earth. They differ only by the apparent orientation angle of the earth θ (=GAST) at the observation epoch. The epoch of an

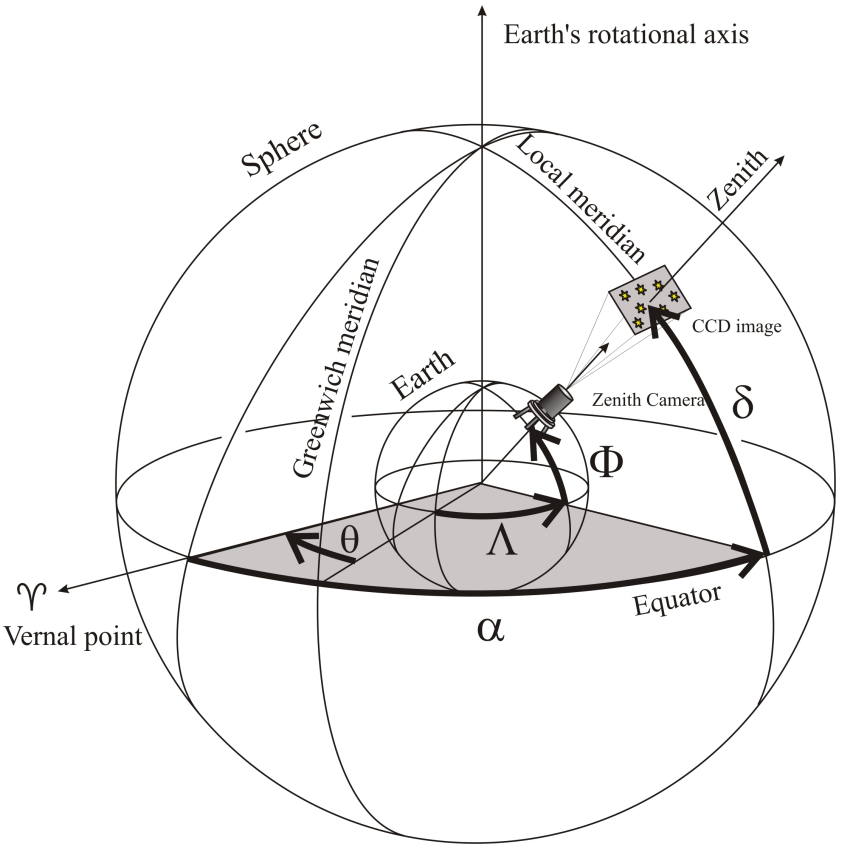

Figure 3.1: Main principle of the astrogeodetic determination of the direction of the vertical (Φ, Λ) (modified after Hirt and Bürki [2002]). The terrestrial (ITRS) and celestial reference system (ICRS) are depicted. The terrestrial system is simplified, since normally the direction of the vertical does not point directly to the earth's center (due to the flattening of the earth). However, this simplification is acceptable because of the infinite radius of the sphere. The link between astronomical coordinates (Φ, Λ) and equatorial coordinates (δ, α) is established by the orientation angle of the earth (GAST $= \theta$) at the observation epoch.

observation with DIADEM is provided by a GPS receiver implemented in the Zenith Camera system. The GPS time has to be converted into GAST by means of several time transformations. They are described in chapter 2.3.2.

For the final determination of DOV according to Eq. (3.1), the knowledge of ellipsoidal coordinates (φ, λ) is required. They are determined by additional differential GPS measurements at the observation point. The single-frequency GPS code-receiver implemented in DIADEM is not accurate enough for an appropriate determination of (φ, λ). A potential field of application of DOV (ξ, η) is the astrogeodetic geoid determination. The principle is depicted in Fig. 3.2 and explained in detail in chapter 9.1.1.

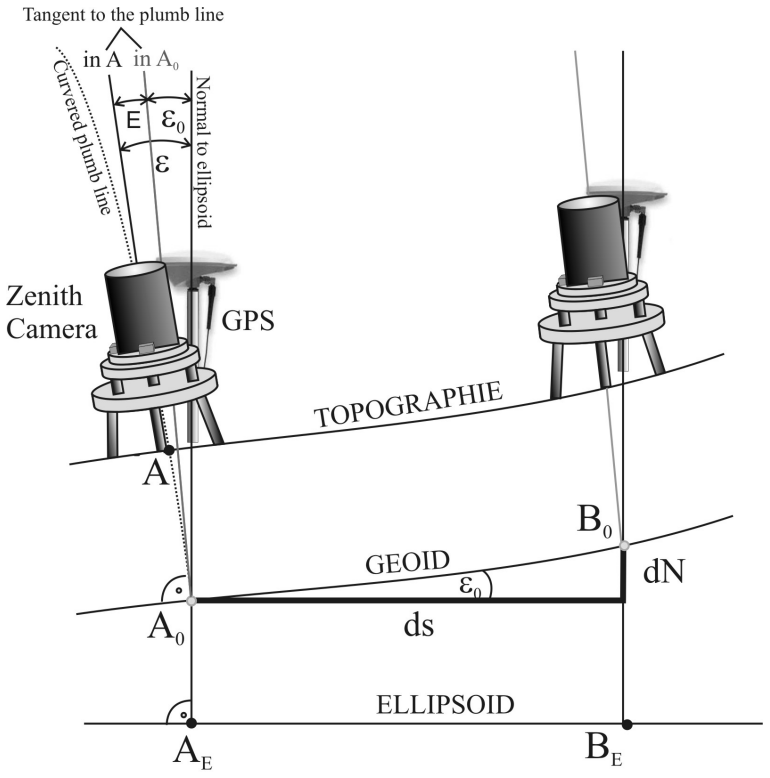

Figure 3.2: Determination of relative geoid undulations based on DOV (modified after Hirt [2004]). Due to the curvature of the local plumb line, the DOV observed at topography (ε) differ slightly from those referring directly to the geoid (ε_0). This difference is indicated by the angle E. The relative geoid undulation dN represents the change of the geoid between two stations A and B with the distance ds.

3.2 Instrumental set-up

3.2.1 Introduction

In order to upgrade the old analog Zenith Camera TZK3 of the GGL (Bürki [1989]) to the state-of-the-art, the instrument has been subject to extensive reconstruction works within the last four years. The main intention was the automation of the Zenith Camera for an efficient and PC-controlled deployment. The modernized instrument DIADEM (Digital Astronomical Deflection Measuring System) offers all requirements to perform automatic and real-time observations by using modern CCD technology and GPS equipment (Müller [2002], Müller et al. [2004]). Fig. 3.3 shows the main components of DIADEM. In general, the Zenith Camera is divided into two parts: a turnable superstructure and a fixed substructure. Both parts are separated by a special ball bearing.

The main components of the turnable superstructure are a highly light-sensitive objective (Zeiss Mirotar), a CCD camera for imaging stars as well as two different pairs of orthogonally mounted inclination sensors. They control the vertical alignment of the system. The CCD camera can be moved vertically along the optical axis by a servo motor,

hence enabling the automatic adaption of the temperature-dependent focus position. The superstructure can be rotated 180 degrees around the axis of the instrument. Hence, systematic errors caused by the eccentricity of the CCD sensor and the zero-point offset of the inclination sensors can be eliminated. The turning is realized by a servo motor (M4 in Fig. 3.4), which drives the superstructure by means of a gear belt. Position 1 is defined by a steal bolt, which is attached to the turnable part and an electromagnetic induction sensor, mounted on the fixed part. As soon as the turnable part passes over the steal bolt, the inductance changes and the motion stops.

The fixed substructure forms the basis of the system standing on three leveling screws. Each screw is connected with a servo motor (M1-M3 in Fig. 3.4), which allows for an automated vertical alignment of DIADEM into the local plumb line. Furthermore, a single-frequency GPS code-receiver is integrated in the Zenith Camera system providing highly precise epoch information and approximate ellipsoidal coordinates, respectively. Precise ellipsoidal coordinates have to be determined by additional differential GPS measurements.

The whole Zenith Camera is mounted on a tripod, which possesses three electric cylinders for leveling (Z1-Z3 in Fig. 3.4) and a servo motor for the azimuthal turning of the tripod platform (M5 in Fig. 3.4). All processes described are controlled by two appropriate industrial computers. In the following, the main components are presented in detail.

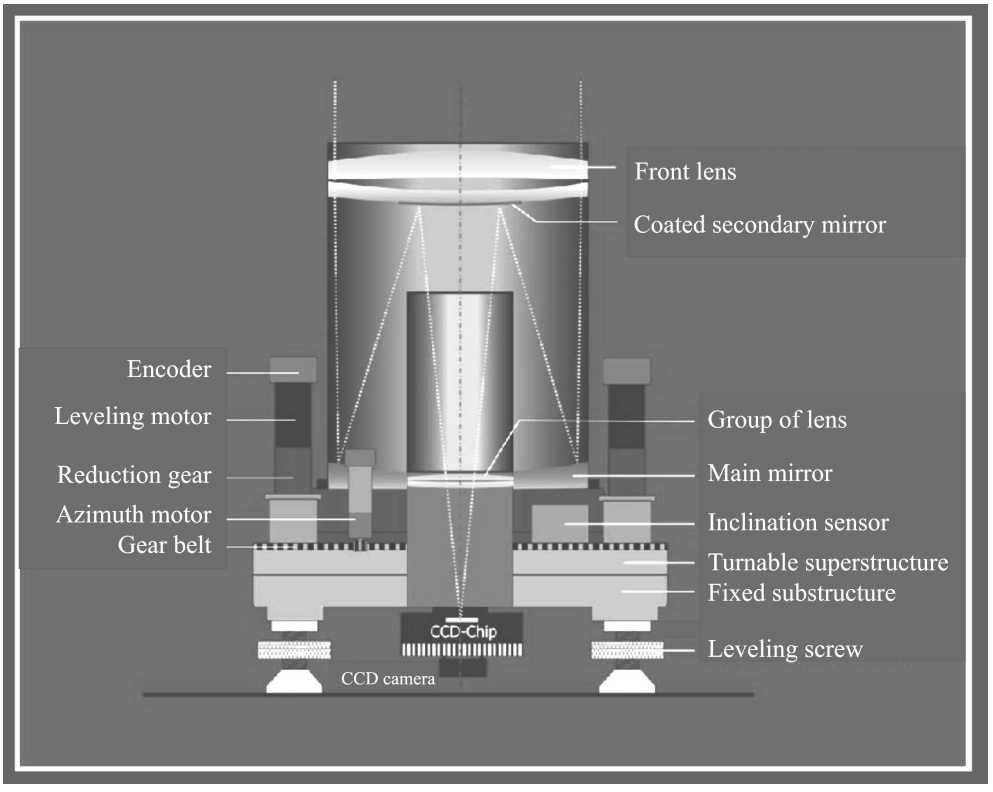

Figure 3.3: Main components of DIADEM (modified after B.Bürki, GGL).

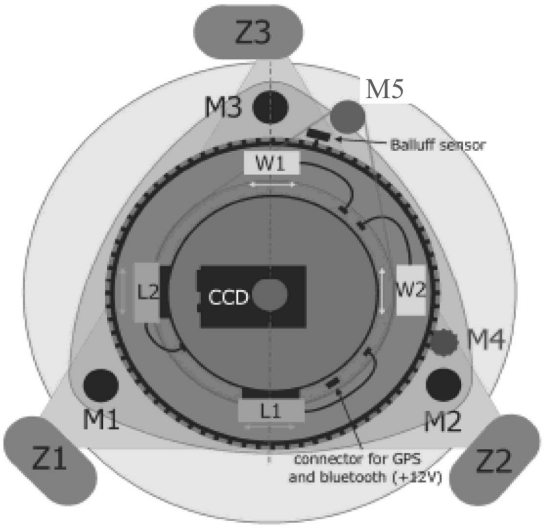

Figure 3.4: Topview on DIADEM. M1-M3: servo motors for leveling the superstructure, M4: motor for focussing, M5: motor for azimuthal turning, Z1-Z3: cylinder motors for leveling the tripod platform, W1/W2: Wyler inclination sensors, L1/L2: Lippmann inclination sensors.

3.2.2 Objective MIROTAR

The main optical component of DIADEM is the MIROTAR objective from Zeiss. It is a catadioptric system consisting of two mirrors (main and secondary mirror) and four lenses. The lenses allow for the correction of potential aberration effects caused by the mirrors. The use of two mirrors offers the possibility of a twice folded optical path, hence enabling at the same time a long focal length of 1020 mm and a short tube length of 328 mm. The aperture is 200 mm, with an effective focal-over-diameter-ratio of 1:5.6. The aperture angle of the objective amounts to 3.6°, which is not used to full capacity, because of the small CCD sensor surface (chapter 3.2.3). However, this has the advantage that the sensor and, therefore, the image plane is located close to the optical axis, hence avoiding distortion effects caused by the objective. A disadvantage of the objective is its temperature dependence, which causes changes of the focal length. The reason for this dependence is up to the materials used for the tube of the objective indicating high expansion coefficients. A special construction undertakes the task of an automatic adaption of the focus: A servo motor moves the CCD camera vertically via worm gear and drive belt. Hence, the CCD camera is moved along the optical axis aiming at the coincidence of CCD sensor and focal plane. The focal position is controlled by a digital caliper, a capacitive measuring system, which has been additionally attached to the CCD camera box. It measures the distance between CCD camera and a defined reference surface. The modeling of the focus-temperature-function is described in detail in chapter 4.4.4.

Figure 3.5: View into the MIROTAR objective of DIADEM.

3.2.3 CCD camera CHROMA C3

One of the first steps in the modernization of the Zenith Camera was the replacement of the analog photographic film by a CCD camera of type CHROMA C3 (manufactured by DTA, Italy, DTA [2008b]) (Figs. 3.6***a)*** and 3.6***b)***). The camera box is mounted beneath the Mirotar objective (Fig. 3.3) and connected with the focus adaption system. The CCD camera is thermo-electrically cooled to -40°C from ambient temperature, hence reducing the dark current. Furthermore, it indicates a fast image downloading rate (1.5 MPixel/s) and an excellent dynamic range (14 bit A/D converter, 16384 gray values) (DTA [2008a]). The electro-mechanical shutter provides opening times of minimum 10 ms up to 9999 s. The determination of the time-dependent shutter function is described in chapter 4.4.3. The integrated Kodak sensor KAF-6303E(LE), a full-frame image sensor, consists of 3072 x 2048 pixel, each with a square size of 9 μm (DTA [2008b]).

As already mentioned in chapter 3.2.2, the light-sensitive area of the CCD sensor does not cover the full range provided by the objective. The sensor size of 27.6 mm by 18.4 mm and the focus length of 1020 mm define an effective image section on sphere of 1.5° by 1°, which yields a field-of-view (FOV) of 1.5 $grad^2$. This is significantly less compared to about 13 $grad^2$ provided by the objective. However, due to the highly light-sensitive CCD sensor, the number of stars imaged is very high and amounts to about 200 stars in nights with an excellent seeing.

The CCD technique offers a significant increase of the magnitude of stars imaged. This value represents the measure of brightness of a celestial object as seen by an observer on

a) CCD camera box with ventilation (DTA [2008a]).

b) Interior view of the CCD camera. On the right side, the closed electro-mechanical shutter is visible. It covers the CCD sensor.

Figure 3.6: CCD camera CHROMA C3: box and interior view.

earth. While the analog photo technique allowed for a maximum magnitude of 10, the digital technique now enables the detection of stars with a magnitude of 14! For comparison only: the human eye is able to observe stars with a magnitude of 6, approximately referring to the maximum brightness of Uranus (5.5 mag).

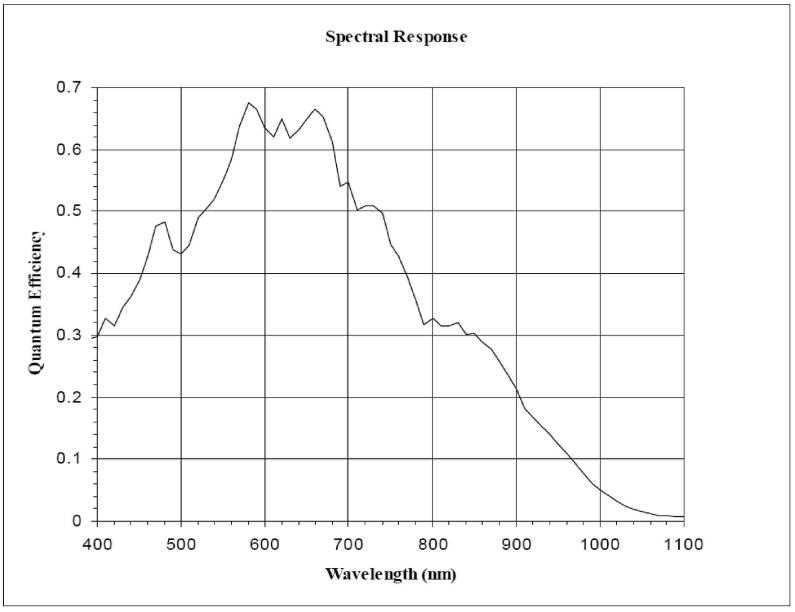

Figure 3.7: Quantum efficiency (QE) of the Kodak sensor integrated in the CHROMA C3 camera (DTA, Italy) (DTA [2008b]). The maximum QE is reached for a wavelength between 580 nm (yellow light) to 700 nm (red light).

The spectral sensitivity of the sensor ranges between 350 nm (ultraviolet) and 1000 nm (near infrared) (Fig. 3.7). The sensor features a high quantum efficiency (QE) over the whole spectral range. The QE factor represents the ratio of *registered photons* to

incoming photons per pixel and second. The highest sensivity is given between 580 nm and 700 nm, where about 65% of the incoming photons are registered. The exposure and read-out of the images as well as the cooling of the camera are controlled by a FDL-PCI card (=Facility Data Link - Peripheral Component Interconnect card), installed in the industrial PC.

3.2.4 Inclination sensors HRTM

Two High Resolution Tiltmeters (HRTM), manufactured by the German *Lippmann company for Geophysical Instruments*, are mounted orthogonally on the turnable part of the Zenith Camera (L1/L2 in Fig. 3.4). They control permanently the vertical alignment of the Zenith Camera, hence providing information for the final transformation of the rotational axis of the instrument into the direction of the vertical.

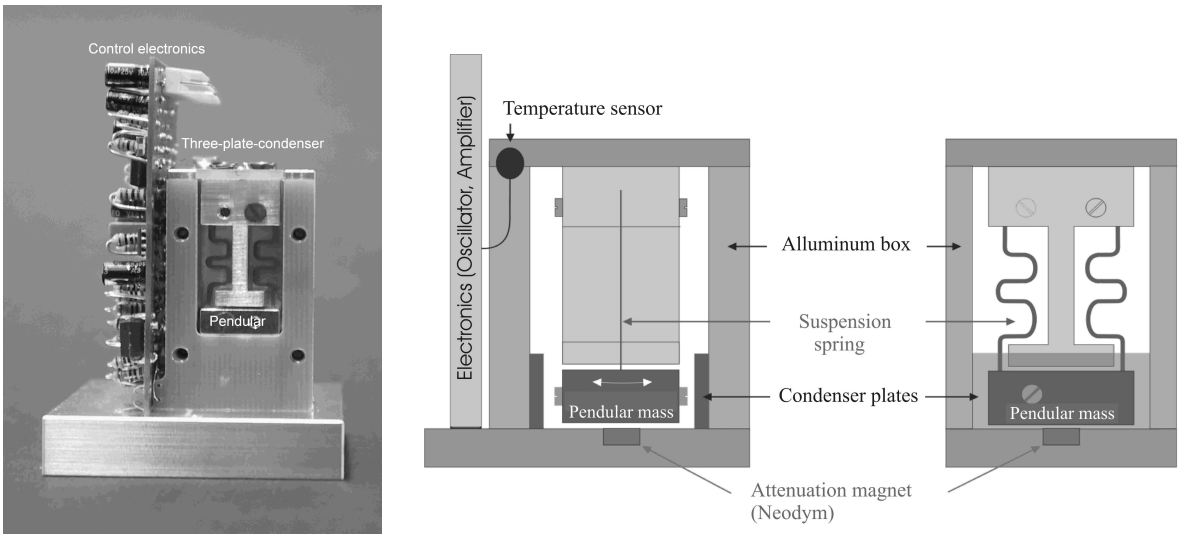

a) Interior view in direction of inclination measurement.

b) Schematical view. Right image: View in direction of inclination measurement.

Figure 3.8: High Resolution Tiltmeters: interior and schematical view.

The electronic pendular tiltmeters are constructed as three-panel-condenser (Figs. 3.8***a)*** and 3.8***b)***). The middle condenser panel assumes the function of a pendular. It is made of aluminum and fixed on a suspension spring from beryllium-bronce. Depending on the position of the pendular in reference to the frame, the capacities of the condensers change. The resulting analog voltage signal can be transformed into inclination data using the scale factor of 0.142 mrad/V specified by the Lippmann company (Lippmann [2005]). A DAQ board, implemented in the industrial PC, operates as 16-bit A/D converter. With a usable voltage of about ±8 V, it allows for a digitization interval of ±0.244 mV referring to about 0.007 arcsec. The effective measuring range amounts to ±200 arcsec. Within this range, the relation between voltage and inclination is linear. Additional to the inclination signal, the sensors provide additional voltage information, which can be transformed into sensor temperatures.

The space between the panels is filled with air. In contrast to a filling with depressant liquids, air enables a high temporal resolution. However, to avoid long reverberation

times (>2 s), an implemented permanent magnet mounted underneath the pendular induces eddy currents damping the pendular motions. The sampling rate is specified with 1000 Hz, hence providing inclination data with a very high temporal resolution. In order to keep the amount of data in an adequate frame, the sampling rate has been reduced for DIADEM observations.

For the protection of electronics and mechanics from external influences as humidity and touching, the sensor including the control electronics is placed inside a box with a size of 4 cm x 5 cm x 6 cm. A detailed analysis of the HRTM sensors can be found in chapter 5.3.

3.2.5 Inclination sensors Zerotronics

For redundant information, a second pair of inclination sensors is mounted orthogonally on the turnable part of DIADEM: the Zerotronic sensors manufactured by the swiss *Wyler company* (W1/W2 in Fig. 3.4). Similar to the HRTM sensors, the Zerotronics are electronic pendular systems, however, showing a different mechanical design (Fig. 3.9***a)***).

a) Interior view.

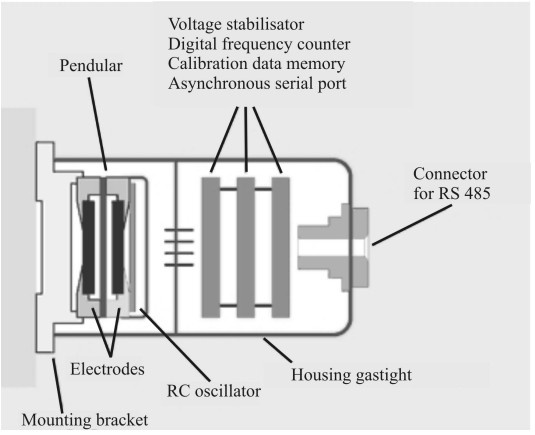

b) Schematical view (modified after Wyler [2007]).

Figure 3.9: Zerotronic sensors: interior and schematical view.

The pendular is suspended by three Archimedes helical springs and mounted between two electrodes (Fig. 3.9***b)***). Depending on the inclination of the sensor, the pendular swings out of its zero-position and causes a change of capacities between the pendular and the two electrodes. These capacities are transformed into different frequencies through the RC oscillator. The ratio of the two frequencies forms the primary signal for the detection of the required angle. The sensor box is hermetically encapsulated and filled with nitrogen. This avoids the influence of humidity changes on the measurements. Besides, the nitrogen serves as damping media between the electrodes. As the viscosity change of gas within a temperature range of -40° to +70° is considered to be minimal, the damping is virtually temperature-independent. The optimization of the damping is achieved by an adequate ratio between pendular surface and slot size of the Archimedes

spring. The mathematical damping is realized by an integration over time intervals (Wyler [2007]). The sensor features a measuring range of $\pm 1°$ and a digitalization interval of 0.1 arcsec, hence providing a ten times lower resolution than the HRTM. Also the temporal resolution is lower with a sampling rate of maximum 10 Hz. A parallel read-out of two inclination sensors further reduces the rate down to 5 Hz. Each sensor is mounted inside a metallic box with a size of 5 cm x 4 cm x 4.5 cm. A detailed analysis of the Zerotronic sensors can be found in chapter 5.3. Please note: Within this thesis, the HRTM and Zerotronic sensors are named *Lippmann sensors* and *Wyler sensors*, respectively.

3.2.6 GPS equipment

DIADEM is equipped with a civil GPS receiver, manufactured by the swiss company u-blox (u-blox AG [2003]). The GPS technique is necessary for two purposes: the determination of ellipsoidal coordinates and the provision of precise exposure epochs. Antenna and receiver are mounted eccentrically on the objective of the Zenith Camera (Fig. 3.10).

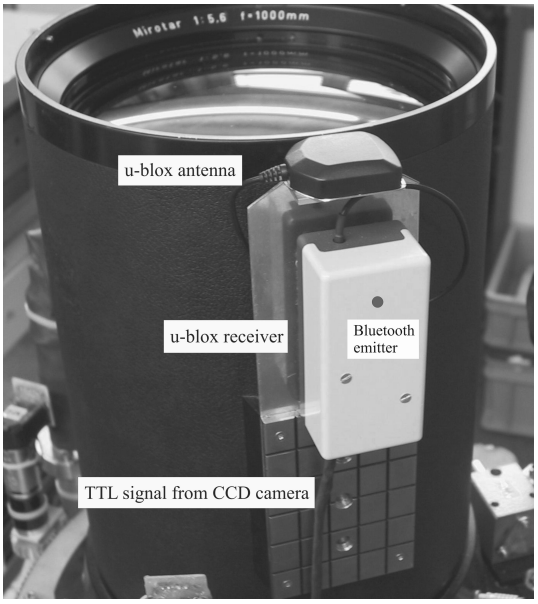

Figure 3.10: DIADEM with GPS antenna mounted on the objective. When turning DIADEM in different azimuthal directions, the ellipsoidal coordinates refer to different positions around the axis of the instrument. The mean of all values is finally centered on the rotational axis.

The distance to the center of the objective amounts to 15 cm. During an observation in different azimuthal directions, the ellipsoidal coordinates refer to different positions around the rotational axis, however, the average finally represents the position of the rotational axis. The single-frequency GPS code-receiver operating with C/A code communicates via Blue-tooth and a serial port adapter with the PC. The position accuracy of the raw navigation solution amounts to ± 3 m CEP[1] and improves to better

[1]CEP=Circular Error Probability: The radius of a horizontal circle, centered at the antenna's true position and containing 50% of the fixes

than 2 m CEP if operated in differential mode. However, these position accuracies are too low for the determination of highly-precise DOV as intended with DIADEM. Since the accuracy of the DOV directly depends on those of the geodetic position, the latter should be provided with an accuracy of better than 0.01 arcsec. This corresponds to a lateral displacement at the earth's surface of less than 30 cm. In order to enable the provision of the required accuracy, additional dual-frequency GPS measurements (e.g. with Trimble) in differential mode have to be performed (see chapter 5.6). The ellipsoidal coordinates provided by the u-blox GPS receiver can be used as approximate positions for the extraction of the reference star field from a star catalog. However, the most important task of the u-blox GPS receiver is the allocation of precise epoch information. It features a time-mark capability allowing to determine the corresponding epoch of an incoming TTL signal. Hence, the receiver provides the exact GPS time of the TTL signal (=epoch) emitted from the CCD camera in the moment of exposure. The time mark accuracy is with 0.2 ms relatively high. The epoch accuracy is mainly limited by the shutter characteristic. This problem is discussed in detail in chapter 4.4.3.

3.2.7 Control unit

The whole data acquisition process comprising leveling, focussing, exposure of images as well as registration of inclination data and exposure epochs is controlled by two industrial PCs of type Aaeon AEC-6910 Boxer (Fig. 3.11).

Figure 3.11: Industrial PC of type Aaeon AEC-6910 Boxer.

Boxer I contains an Intel Pentium M processor (1.6 GHz CPU) and Boxer II an Intel Celeron M processor (1.3 GHz CPU). Furthermore, both include a 80 GB hard disc and 512 MB memory. They are operated with 12 V DC, either provided by a car battery (12 V) or by a power supply via voltage transformation (input: 100-240 V AC, output: 12 V DC). Furthermore, the PCs are suitable for deployments under harsh conditions, as they feature anti-vibration and shock resistance abilities. Enhanced temperature specifications and humidity control provide reliability under extreme conditions and on unsteady roads. Boxer I contains only the FDL-PCI card of the CCD camera, while

in Boxer II the DAQ board for the two Lippmann sensors and the MOXA card are implemented. The MOXA card provides serial ports for all servo motors and the two Wyler sensors. The division on two PCs has the advantage that the registration of the inclination data is not intermitted by the exposure of the images, hence yielding a permanent inclination signal. The communication between both PCs is realized via local network. The data evaluated on PC-II are transfered to PC-I after finishing the acquisition process.

3.2.8 Transportation

There exist two possibilities of transportation: a trolley for local observations with short distances between the stations, as e.g. in case of geoid profile measurements, and a hanger for mobile measurements with greater distances between the stations. The first case is depicted in Fig. 3.12. There, the complete DIADEM system is mounted on a trolley. The tripod legs can be placed on the ground through three holes in the bottom of the trolley. When changing the station, the legs have to be moved in until the wooden ground plate, connected with the tripod legs, is seated on the bottom of the trolley.

The second possibility of transportation is provided by a hanger, which carries the complete DIADEM system (Fig. 3.13). The Zenith Camera is mounted in the rear of the hanger. The front part provides a small fold-out table and a seat bench for the observer. Like the trolley, the hanger's bottom features three holes for the tripod legs. They are huge enough to avoid a contact between legs and bottom, also under windy conditions. Hence, the system stands completely independent from the hanger.

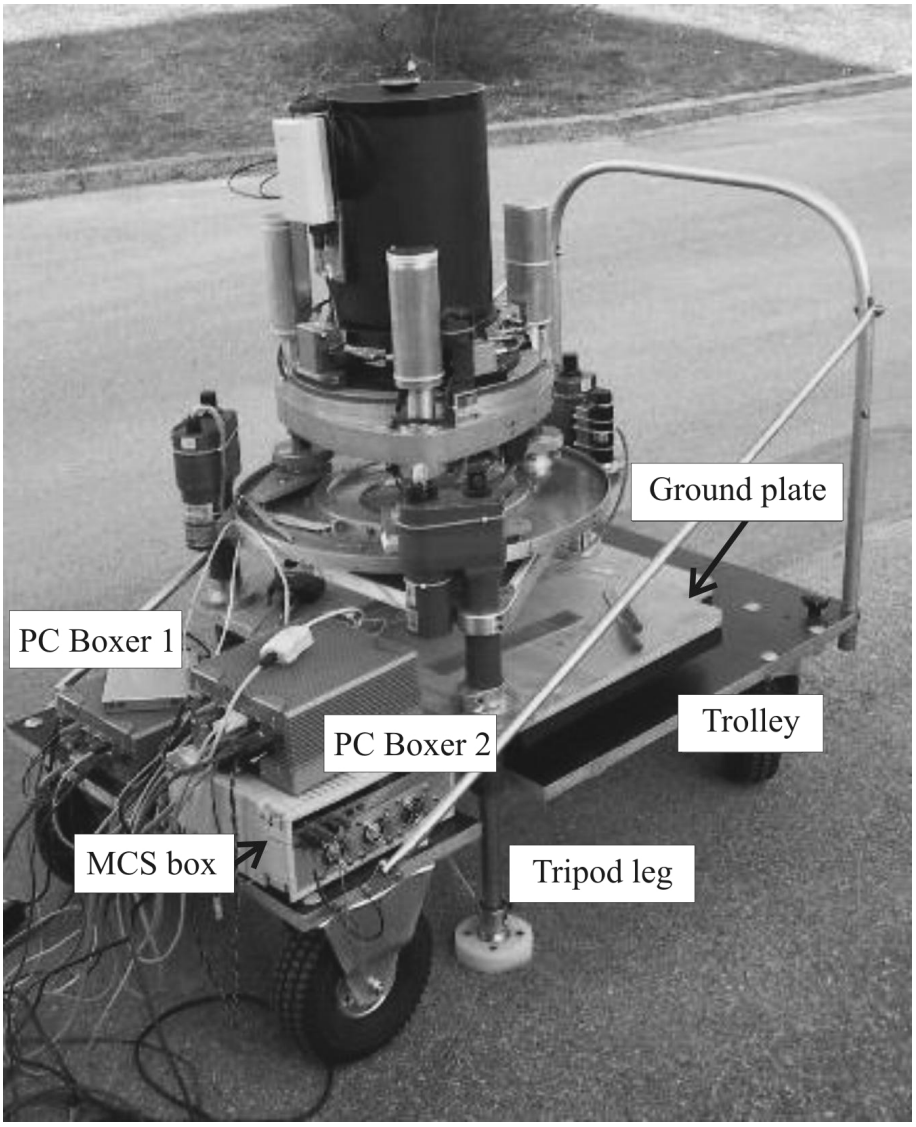

Figure 3.12: DIADEM mounted on the trolley. The tripod legs can be placed on the ground through three holes in the bottom of the trolley.

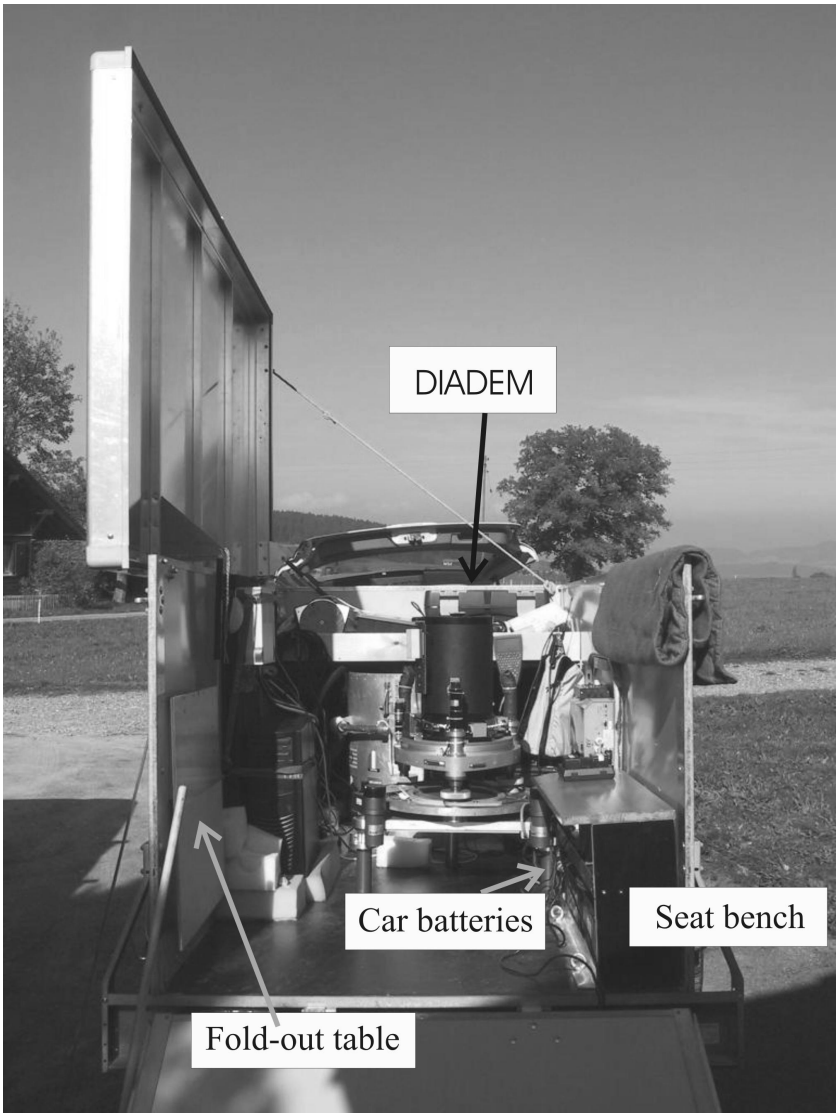

Figure 3.13: Installation of DIADEM on a hanger. In the rear, the Zenith Camera is visible. The front part is equipped with a small fold-out table and a seat for operating the system.

4 Measuring procedure

4.1 Data acquisition

4.1.1 Observation with DIADEM

An important goal related to the elaborate redesign of the Zenith Camera was the enabling of a fully-automatic deployment. Besides the described enhancement of the hardware (chapter 3.2), this included also the programming of a dedicated steering software. The programming language used is LABVIEW, a graphical development environment from National Instruments (http://www.ni.com/labview/). The data acquisition software comprises the leveling and focussing of the system, the exposure of images as well as the permanent registration of inclination data and exposure epochs per image. In order to allow for the determination of deflections of the vertical (DOV), also ellipsoidal coordinates have to be determined (see Eq. (3.1)).

Leveling

The determination of the direction of the vertical with a Zenith Camera is based on the condition that the optical axis of the system is oriented in direction to the zenith. Therefore, the system has to be leveled best-possible before starting an observation with DIADEM. This is realized by processing information from the inclination sensors mounted on the turnable superstructure. According to the measuring method defined (1: azimuth calibration, 2: tripod method; see details in chapter 4.4.1), either the fixed substructure of the Zenith Camera (1) or the tripod platform (2) have to be leveled. To enable the correction of a vertical misalignment, the inclination data are converted into servo motor pulses, which are sent to the respective motors steering either the leveling screws (1) or the tripod legs (2). Due to an existing zero-point offset of the inclination sensors, the leveling process has to be conducted in two opposite positions. Therefore, either the superstructure with the objective (1) or the tripod platform (2) have to be turned for 180°. The leveling process terminates, when the inclination of the system amounts to less than 5 arcsec in both positions (Müller [2002]). In order to allow for the correction of a residual misalignment, the inclination data have to be permanently registered during an observation.

Focussing

The quality of a photo largely depends on a proper focussing of the objects imaged. As the materials of the objective of DIADEM are temperature-dependent, the focus can not be considered as constant. Before and during an observation, the focus has to be controlled and adjusted. The relation between temperature and focal position is nearly linear (Röösli [2006]), hence allowing for an automatic correction of the focal position

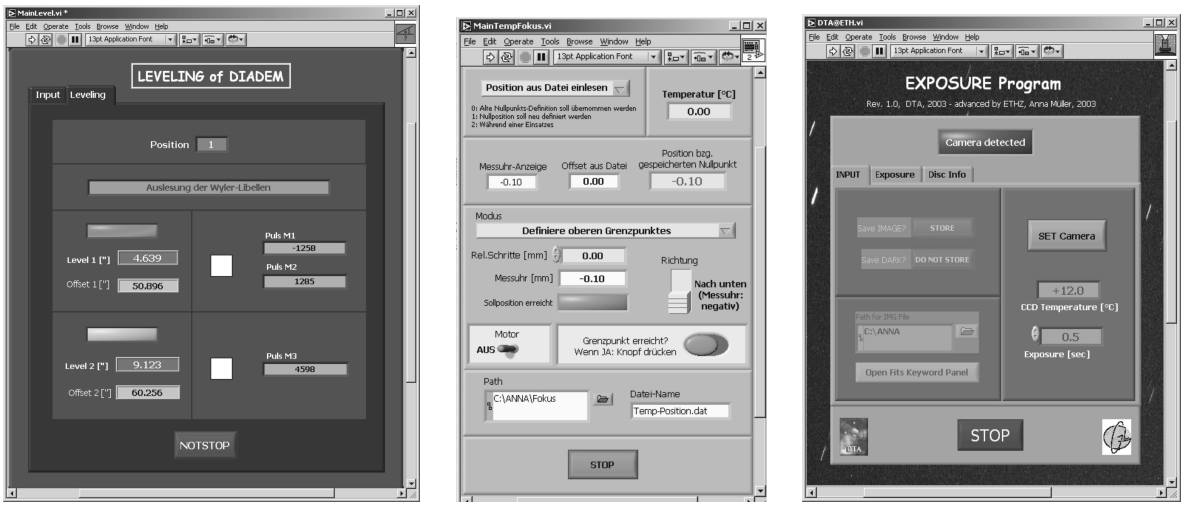

a) Leveling ***b)*** Focussing ***c)*** Exposuring

Figure 4.1: Data acquisition software written in LABVIEW.

depending on the temperature. Detailed results of the investigation are presented in chapter 4.4.4.

Registration of ellipsoidal coordinates

The knowledge of the geodetic position of DIADEM is required for two main purposes: a) to extract the equatorial coordinates of the observed stars from a star catalog (chapter 4.2.3) and b) to calculate final DOV (Eq. (3.1)). In order to obtain highly-precise DOV, the ellipsoidal coordinates (φ, λ) have to be provided with an accuracy better than 0.01 arcsec corresponding to a lateral displacement at the earth's surface of about 30 cm. This precision can not be assured by a single-frequency GPS code-receiver as implemented in the DIADEM system (chapter 3.2.6). Hence, an additional dual-frequency GPS receiver has to be deployed operating in differential mode and using corrections from a GPS reference station. During the campaign in Switzerland, the GPS measurements have been analyzed in real-time using carrier phase corrections provided via GSM by the Swiss Positioning Service (SWIPOS, Wild et al. [2004]). During the campaign in Greece, the GPS measurements have been analyzed in post-processing using information from different reference stations (see chapter 7.4.1).

Exposure of the image

After finishing the leveling and focussing of DIADEM, the process of data acquisition starts. The automatic routine comprises the exposure of images as well as the registration of corresponding exposure epochs and inclination data. The exposure epochs are provided by the GPS receiver mounted on the Zenith Camera system. It receives a TTL signal, emitted by the CCD camera in the moment of exposure. A constant time factor is added to the exposure epoch, hence considering the fact that the shutter reacts delayed in reference to the TTL signal, and, besides, asymmetrically (chapter 4.4.3). A typical measuring process comprises of about 60-80 single solutions. One single solution consists of two images observed in opposite positions. In Fig. 4.2, a section of an inverted star image is depicted. The black dots represent stars, with well recognizable differences in the brightness of the stars.

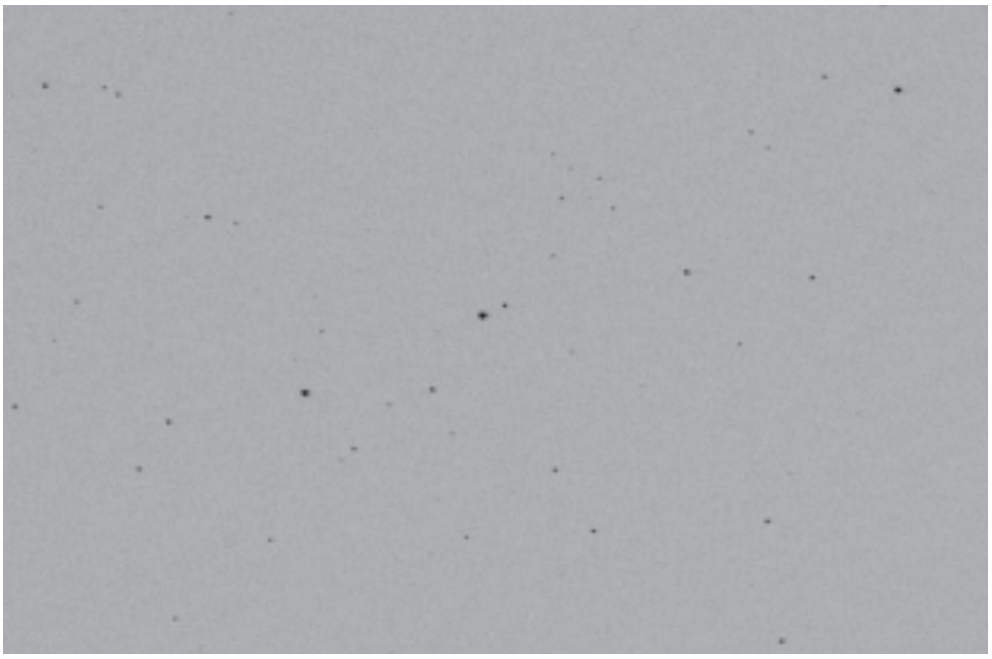

Figure 4.2: Inverted star image observed with DIADEM. The figure represents one fourth of the normal image size corresponding to 13.8 mm by 9.2 mm on the CCD sensor and to 0.75° by 0.5° on the sphere. The brighter a star, the thicker the dot. The visible stars form only a part of those stars, which are finally extracted by dedicated methods of image analysis implemented in AURIGA. In clear and star-opulent nights, up to 200 stars are detected within a single image.

Summary: A typical data acquisition process

Due to new findings, two different measuring configurations for an observation with DIADEM exist: the *azimuth calibration* and the *tripod method*. Both methods are thoroughly described in chapter 4.4.1. The azimuth calibration has been replaced by the newly introduced tripod method (Hirt and Seeber [2007a]), since the latter enables the elimination of the azimuth-dependence of DIADEM observations. In general, the tripod method is favored over the azimuth calibration. However, due to fact that this method still forms a suitable configuration in special measuring situations (as e.g. observations on an island), both procedures shall be described in the following:

Azimuth calibration. The preparation of a measurement starts with the mounting of DIADEM at the observation point and its orientation in an arbitrary azimuth. After that, the fixed substructure of DIADEM is leveled until the termination condition (min. 5 arcsec) is fulfilled. This process is followed by the thorough focussing of the images. Afterwards, the data acquisition process starts. In order to eliminate systematical errors caused by a zero-point offset of the inclination sensors and an eccentric mounting of the CCD camera, the observation is conducted in two opposite positions. Furthermore, to avoid influences caused by a linear drift of the sensor offsets, the observation is always conducted in an I-II-II-I configuration. The opposite positions I/II are realized by turning the superstructure of DIADEM (objective and mounting base of the inclination sensors) for 180° (Fig. 4.10: **A**). Generally, 24 single solutions per azimuthal direction are observed. This number forms a compromise between an efficient observation providing a convenient quantity of images in one position and a finite time span between two

corresponding images. A series of observations comprises the images 1-12 in position I, 1-12 in position II, 13-24 in position II and 13-24 in position I. During the whole image acquisition process, the inclination data are permanently registered with corresponding time informations. Furthermore, the exposure epoch for each image is recorded. After finishing a series of observations in one azimuthal direction, the whole Zenith Camera system is moved into the next direction by turning the tripod platform with the entire system (Fig. 4.10: **B**). There, the whole process is repeated. In general, four different azimuthal directions are observed. The described configuration is necessary to determine azimuthal correction parameters, which have to be considered for the calculation of the direction of the vertical (chapters 4.3 and 4.4.1). The time needed for the whole process is about 30 minutes.

Tripod method. The tripod method allows for the elimination of the azimuth-dependent error described in chapter 4.4.1. The method differs from the azimuth calibration by leveling the tripod platform instead of the fixed substructure of DIADEM (Fig. 4.10: **C**). The leveling process is followed by the focussing of the images. After that, the data acquisition process starts. Again in contrast to the azimuth calibration, the I-II-II-I configuration with 24 single solutions is now realized by turning the tripod platform for 180°. In order to provide a good redundancy, it is reasonable to gather more than 24 single solutions, hence the image acquisition process (I-II-II-I configuration), should be repeated several times. However, it is not necessary to change the azimuthal orientation of DIADEM in between. This forms the main advantage of the tripod method (chapter 4.4.1). Please note: The azimuthal orientation of DIADEM should not be confused with an observation in two opposite positions. Former defines the basic orientation of DIADEM, while the observation in two positions is an always necessary procedure to eliminate systematical instrumental errors. The time needed for four repetitions is about 20 minutes, which is almost half of the time of an azimuth calibration (with the same number of single solutions).

4.1.2 Processing of inclination data

General remarks

The data gathered during an observation have to be prepared for a subsequent and efficient data analysis with AURIGA (chapter 4.2). This mainly concerns the inclination data gathered with Wyler and Lippmann sensors, respectively, which are provided in terms of raw and noisy signals (Fig. 4.3). The signal represents a superposition of sensor noise, microseismic effects and effective inclination fluctuations of the Zenith Camera. Since microseismic effects only influence the pendulars of the inclination sensors but do not cause real inclination changes of DIADEM they have to be eliminated by dedicated filtering techniques. The subject of microseismics is discussed in detail in chapter 5.3.2. The characteristic sampling rate of the Wyler sensors is 2 Hz, while the Lippmann sensor data are provided with a very high temporal resolution of 1000 Hz. The average over 50 values finally yields a sampling frequency of 20 Hz. The filtering technique applied for both types of sensors are described in the following section, with focus on the data gathered by the Lippmann sensors. Finally, the relationship between exposure epochs and filtered inclination values has to be established. In this way, information about the

relation between rotational axis of DIADEM and direction of the vertical in the moment of observation are provided.

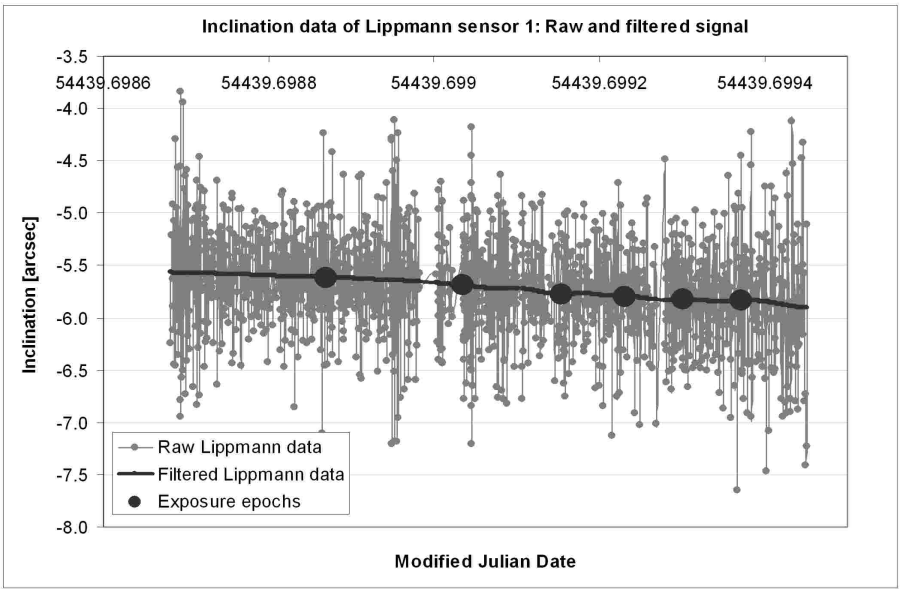

Figure 4.3: Inclination signal registered by Lippmann sensor 1: Raw (gray) and filtered (black) signal. Additionally, the exposure epochs are depicted (black dots). The raw signal is influenced by microseismic effects. They are largely eliminated by a FFT low-pass filtering.

Fast Fourier Transformation (FFT) with low-pass filter

The main source of noise superposing the inclination signal is originated from microseismics effects. In order to separate the interesting inclination information from anomalous accelerations, a Fast Fourier Transformation (FFT) with low-pass filter has been implemented in the data acquisition software (Ganz [2007]). The Fourier transformation represents a fundamental method in signal processing. It enables the conversion of the terms "time-sample value" (time domain) into "frequency-amplitudes" (frequency domain). In this way, operations like filter processes are better feasible. The low-pass filter implemented in the data acquisition software has the function to eliminate frequencies above a dedicated limit frequency. It defines the maximum "acceptable" frequency and equates all higher frequencies to "zero". In order to avoid an unintentional stimulation of the limit frequency when re-transforming the signal into the time domain (Inverse FFT), a Hamming window instead of a simple rectangular window has been implemented. It represents a cosine-function enabling a slow fade in and out. Detailed information about signal processing and filtering can be found in Meyer [2000] and Stearns and Hush [1999].

As already discussed in Hirt [2004], the definition of the limit frequency forms an important issue. The frequency range of the expected inclination signal overlaps those of microseismic effects. According to chapter 5.3.2, microseismic effects might occur in a wide range of ≤ 0.03 Hz up to several Hz. However, long-periodical inclination fluctuations of the Zenith Camera are to be expected within a range up to 0.1 Hz. The critical overlapping range is, therefore, within the 0.1 Hz limit. After Hirt [2004], a limit frequency of 0.1 Hz forms a reasonable compromise for Zenith Camera observations. Frequencies $\geq$

0.1 Hz are eliminated from the signal. However, within the critical overlapping range, a strict separation between inclination signal and anomalous accelerations is not possible. The remaining errors are estimated in chapter 5.3.2. Fig. 4.3 shows Lippmann data (gray), gathered during an observation at the reference station in front of the ETH-HPV building. The signal shows high-frequency noise, possibly induced by anomalous influences (traffic, road works, human activities, etc.) close to the DIADEM station. The filtered signal (black) indicates a significantly smoother behavior, as it is free of anomalous accelerations above the limit frequency ($\geq$ 0.1 Hz).

Resulting inclination data

The final step is the allocation between filtered inclination data and corresponding exposure epochs. Therefore, the filtered inclination values within a defined time span around the respective exposure epoch are averaged and assigned to the epoch. The resulting inclinations in position I (n_1^I, n_2^I) and II (n_1^{II}, n_2^{II}) are computed by:

$$n_1 = \frac{n_1^I - n_1^{II}}{2} \qquad n_2 = \frac{n_2^I - n_2^{II}}{2} \tag{4.1}$$

Eq. (4.1) yields the inclinations (n_1, n_2), which are free from zero-point offsets. They represent directly the absolute inclination of the rotational axis referring to the direction of the vertical. They are defined in the coordinate system of the inclination sensors and have to be transformed into the astronomical coordinate system (see Fig. 4.11) by considering the calibration parameters determined in the frame of a celestial calibration (see chapter 4.4.2). The necessary transformation formulas are given in chapter 4.3. The final inclination corrections (Eq. (4.17)) are applied to the rotational direction $(\Phi, \Lambda)_D$ (Eq. (4.20)), hence yielding the direction of the vertical (Φ, Λ).

4.2 Data analysis

4.2.1 Introduction

Subsequent to the process of data acquisition follows the process of data analysis. The software package AURIGA (Automatic Real-Time Image Processing System for Geodetic Astronomy) realizes a real-time analysis of the data (Hirt [2004]). The process is very complex aiming at the final provision of highly-precise DOV. The procedure comprises the determination of the stars in the image, the extraction of stars from a catalog, the identification of stars imaged as well as the calculation of the rotational direction and the final application of corrections. In order to provide an adequate background knowledge, the individual intermediate steps are outlined within the following subsections. All information refer to (Hirt [2004]), where the whole process of data analysis is described thoroughly.

4.2.2 Image star field

Detection of stars in the image

In order to detect a star imaged, three criteria are decisive: brightness, size and form of the star. A potential star can be regarded as a cohesive pixel region (cluster) with similar gray values. Concerning the size, it is assumed that a star features a diameter of minimum two pixels and, consequently, covers at minimum four pixels. Depending on the exposure time, the form of a star image is either point- (<0.5 s) or line-shaped (≥0.5 s). Based on these conditions, the image segmentation by the method of *region growing* provides good possibilities to detect stars in the image. The main idea is to define each pixel as possible node in a chart and to associate them to neighboring pixel with a defined minimum brightness, hence forming cohesive pixel regions. Based on the above mentioned assumption that a star diameter amounts to a minimum of two pixels, the scanning grid features an increment of two pixels. For each node it is checked, if its gray value g exceeds a defined threshold g_S:

$$g \geq g_S = \mu + n \cdot \sigma \tag{4.2}$$

A pixel whose gray value g differs from the mean value μ for n-times of the image noise σ belongs potentially to a star. Generally, the threshold g_S can be calculated with $n = 3$, hence providing a probability of 99.7 % that a pixel is detected as signal (assuming a normal distribution of the noise). If a pixel indicates a significant gray value, its four neighbouring pixels are also checked. Each pixel that fulfills the threshold condition serves as new starting pixel. Thus, a list of segments (=stars), is generated. The final list contains stars covering minimum four pixels and differing at least for one pixel from the image boundaries.

Determination of image coordinates

The next step is the determination of the image coordinates of the star clusters detected. The two different methods implemented in AURIGA are:

Method of segment center determination. The image coordinates $(x,y)_i$ of each pixel i=1...n of a segment are linearly weighted with the corresponding gray value g $(x,y)_i$. The coordinates of the segment center can be calculated with:

$$x = \frac{1}{\sum g_i} \sum_{i=1}^{n} x_i g_i \qquad y = \frac{1}{\sum g_i} \sum_{i=1}^{n} y_i g_i \tag{4.3}$$

Point Spread Function (PSF). This refined method of image coordinate determination is based on the idea to adapt a model function (e.g. Gauss error distribution model) to a star imaged, until the difference between the respective gray values is minimized. The so called "centering" method is performed by a least-squares-adjustment estimating the form parameters and the center of the function.

In chapter 5.2.1, both methods are compared concerning their accuracy in the determination of image coordinates. According to the results described there, the method of

segment center determination is used for a preliminary astrometric data reduction. It also serves for the provision of approximate values needed for the PSF method. However, due to its higher accuracy, the final data reduction is performed applying the PSF method.

4.2.3 Reference star field

In order to enable the identification of the stars imaged, they have to be compared to stars defined in the celestial reference system. The equatorial coordinates (right ascension α and declination δ) of the so called *reference stars* can be extracted from a star catalog (chapter 2.2). Therefore, information about the *exact exposure epoch* and the *approximate position of the observation point on earth*, respectively, are inevitable:

* The *exposure epoch* is needed to establish the relationship between astronomical coordinates (Φ, Λ) and equatorial coordinates (α, δ) (Eq. (3.2)). Furthermore, it allows for the transformation of mean positions (α_0, δ_0) at a certain catalog epoch T_0 into apparent positions (α_1, δ_1) at the observation epoch T_1 (= exposure epoch) (chapter 2.2.4). In chapter 2.3.2, the necessary time transformations for the analysis of Zenith Camera observations are illustrated (Tab. 2.5) and the most important time scales are shortly described.
* The *approximate position* defines the central point of the selection zone for the reference stars. Furthermore, it serves as touching point for the tangent plane, which is needed to transform spatial into plane star coordinates. The approximate coordinates of the zenithal point (α, δ) are derived by Eq.(4.4), under consideration of the sidereal time $GAST = \Theta$:

$$(\delta_0, \alpha_0) = (\Phi_0, \Lambda_0 + \Theta) \tag{4.4}$$

  The size of the selection zone is calculated in dependence on the focal length of the objective (1000 mm) and on the dimension of the CCD sensor (27.6 mm by 18.4 mm). The resulting field-of-view (FOV) amounts to 1.5° x 1°. In order to reduce the impacts of an unknown azimuthal orientation of the CCD sensor and of inaccuracies of the approximate coordinates, the selection zone is extended for a tolerance zone by about 25 arcmin.

Reduction of equatorial coordinates

As discussed in chapter 2.2.4, the equatorial coordinates listed in the star catalog are *mean star positions*, generally referring to epoch J2000.0. For the analysis of Zenith Camera observations, they have to be corrected for several time-dependent variations:

* Effective variations of equatorial coordinates due to the *proper motions* of stars
* Shifting of reference systems due to effects of *precession* and *nutation*
* Apparent variations due to *refraction*, *daily* and *annual aberration* and *relativistic diversion of light*

The correction formulas implemented in AURIGA allow for the reduction accurate to 0.001 arcsec, hence being negligible in the error budget of the Zenith Camera.

Tangent projection

The equatorial coordinates $(\alpha, \delta)_i$ of the catalog stars are defined on a sphere, while the image coordinates $(x, y)_i$ represent the positions of stars in a plane coordinate system. The link between both systems can be established by the introduction of plane, orthogonal tangent coordinates (ξ, η)[1]. They are derived from the projection of the spherical coordinates into a tangent plane, which is attached to an approximate zenithal point $(\alpha, \delta)_0$. The transformation of $(\alpha, \delta)_i$ into $(\xi, \eta)_i$ is realized by the equations of tangent projection representing an oblique, gnomonic projection after Seeber [1972]):

$$\begin{aligned} \cot q &= \cot\delta \cos(\alpha - \alpha_0) \\ \xi &= \frac{\tan(\alpha - \alpha_0)\cos q}{\cos(q - \delta_0)} \\ \eta &= \tan(q - \delta_0) \end{aligned} \tag{4.5}$$

The backward transformation of $(\xi, \eta)_i$ into $(\alpha, \delta)_i$ is (after Gessler [1975]):

$$\begin{aligned} \alpha &= \alpha_0 + \arctan\frac{\xi}{\cos\delta_0 - \eta\sin\delta_0} \\ \delta &= \arctan\frac{(\eta + \tan\delta_0)\cos(\alpha - \alpha_0)}{1 - \eta\tan\delta_0} \end{aligned} \tag{4.6}$$

4.2.4 Star identification

Principle of similar triangles

The main task of the identification process is to determine, which stars from the catalog and projected into the tangent plane (field I) are imaged in the photo (field II). It has to be considered that both fields are shifted and rotated to each other and that they indicate different scales. This fact demands the determination of four transformation parameters: 2 translations, 1 rotation and 1 scale factor. The identification algorithm implemented in AURIGA is based on the idea that both fields feature similar patterns, as e.g. triangle configurations. This method has been suggested by Groth [1986] and Valdes et al. [1995]. It has the advantage that no a priori information are needed. Three stars existing in both fields form similar triangles and can be characterized by their *aspect ratios*. This fact is invariant to the transformation parameters. In order to reduce the calculation time, only few stars are selected for an identification. Therefore, the stars in both fields are sorted by their magnitudes (image stars: signal-to-noise-ratio, reference stars: apparent brightness) and only the 15 to 30 brightest stars are used. Stars whose spherical distance is $\leq$0.1 arcmin as well as stars in the border area are excluded. The generation of triangles is performed separately for both fields. All possible triangle

[1] Attention: the denotation of the tangent coordinates (ξ, η) is the same as for the DOV (ξ, η).

configurations are constituted, characterized by their sides: $c \geq b \geq a$. Based on the length of each side, the aspect-ratios x_t and y_t are calculated:

$$x_t = \frac{b}{c} \qquad y_t = \frac{a}{c} \tag{4.7}$$

The parameters (x_t, y_t) can be understood as cartesian coordinates in an aspect-ratio-system, where each triangle is represented by one point. For the identification of similar triangles, the parameters $(x_t, y_t)_1$ for the image stars and $(x_t, y_t)_2$ for the reference stars have to fulfill the following condition:

$$|x_{t1} - x_{t2}| < \varepsilon \quad \wedge \quad |y_{t1} - y_{t2}| < \varepsilon \tag{4.8}$$

The limit factor ε can be set to 0.0005 and 0.001, respectively . If Eq. (4.8) is fulfilled, the stars of the according triangle are potentially identical. These stars are indicated in a so called "correspondence matrix" with the dimensions (N1, N2), where N1 denominates the number of image stars and N2 the number of reference stars. Each time a star is identified, the respective entry in the matrix is increased by 1. Since stars belong to different triangle configurations, the number of assignments for identical stars is finally significantly higher than the mean of all matrix entries.

Identification of the whole star field

In order to obtain the parameters for a linear transformation (2D-Helmert transformation) between both fields, two highly-tagged stars are selected forming a linear basis: the image stars $(x, y)_1, (x, y)_2$ and the reference stars $(\xi, \eta)_1, (\xi, \eta)_2$.

The coordinate differences:

$$\begin{aligned} \Delta x &= x_2 - x_1 \qquad \Delta \xi = \xi_2 - \xi_1 \\ \Delta y &= y_2 - y_1 \qquad \Delta \eta = \eta_2 - \eta_1 \end{aligned} \tag{4.9}$$

yield the transformation parameters b_1 and c_1 describing rotation and scale:

$$b_1 = \frac{\Delta\xi\Delta x + \Delta\eta\Delta y}{\Delta x^2 + \Delta y^2} \qquad c_1 = \frac{\Delta\eta\Delta x - \Delta\xi\Delta y}{\Delta x^2 + \Delta y^2} \tag{4.10}$$

and the translations a_1 and a_2:

$$a_1 = \xi_1 - b_1 x_1 + c_1 y_1 \qquad a_2 = \eta_1 - c_1 x_1 - b_1 y_1 \tag{4.11}$$

With the transformation parameters (a_1, a_2, b_1, c_1), all stars imaged $(x, y)_i$ can be transformed into tangent coordinates $(\tilde{\xi}, \tilde{\eta})_i$:

$$\tilde{\xi} = a_1 + b_1 x - c_1 y \qquad \tilde{\eta} = a_2 + c_1 x + b_1 y \tag{4.12}$$

The transformed coordinates $(\tilde{\xi}, \tilde{\eta})_i$ should highly correspond with the tangent coordinates $(\xi, \eta)_i$ of the reference stars and fulfill the following criteria:

$$\sqrt{(\tilde{\xi} - \xi)^2 + (\tilde{\eta} - \eta)^2} < \varepsilon \tag{4.13}$$

A typical value for ε is 10 arcsec. Generally, the bigger part of the stars imaged can be thus identified. This assumes that according reference star positions are listed in the star catalog. For all *identified* stars, a Helmert transformation is calculated yielding an improved set of transformation parameters. They are used to transform a second time all image stars, possibly resulting in an identification of additional stars. In case, the identification of the image stars fails, that means less than four stars have been identified, the whole process is repeated by using a different pair of stars from the correspondence matrix. The identification with a limit of 10 arcsec may provoke a misinterpretation in the case of close stars. Hence, for the final data reduction only stars are selected whose residuals are below 1 arcsec corresponding to 3-times of a typical astrometric uncertainty (0.3 arcsec).

4.2.5 Data reduction

Association of image- and tangent coordinates

The process of data reduction realizes a stable functional relation between the image coordinates and the reference coordinates. Hirt [2004] analyzed different transformation models, like the Helmert transformation (4 parameters), the affine transformation (6 parameters) and the projective transformation (8 parameters) in reference to the respective residuals between transformed and given coordinates. It has been concluded that transformation models of higher order do not contribute to a significant reduction of the residuals, hence, a Helmert transformation (Eq. (4.12)) is completely adequate. After the equalization of the transformation parameters (data reduction), the image scale m and the astronomical azimuth α describing the orientation between CCD sensor system and astronomical coordinate system can be derived:

$$\alpha = \arctan \frac{c_1}{b_1} \qquad m = \sqrt{b_1^2 + c_1^2} \tag{4.14}$$

The next step is the establishment of the relation between the intersection point of "*rotational axis* and *image*" (=pivot) and those of "*rotational axis* and *sphere*" (=rotational direction). This is realized by interpolating the pivot into the zenithal star field.

Calculation of the rotational direction

The overall process of the determination of the rotational direction is depicted in Fig. 4.4.

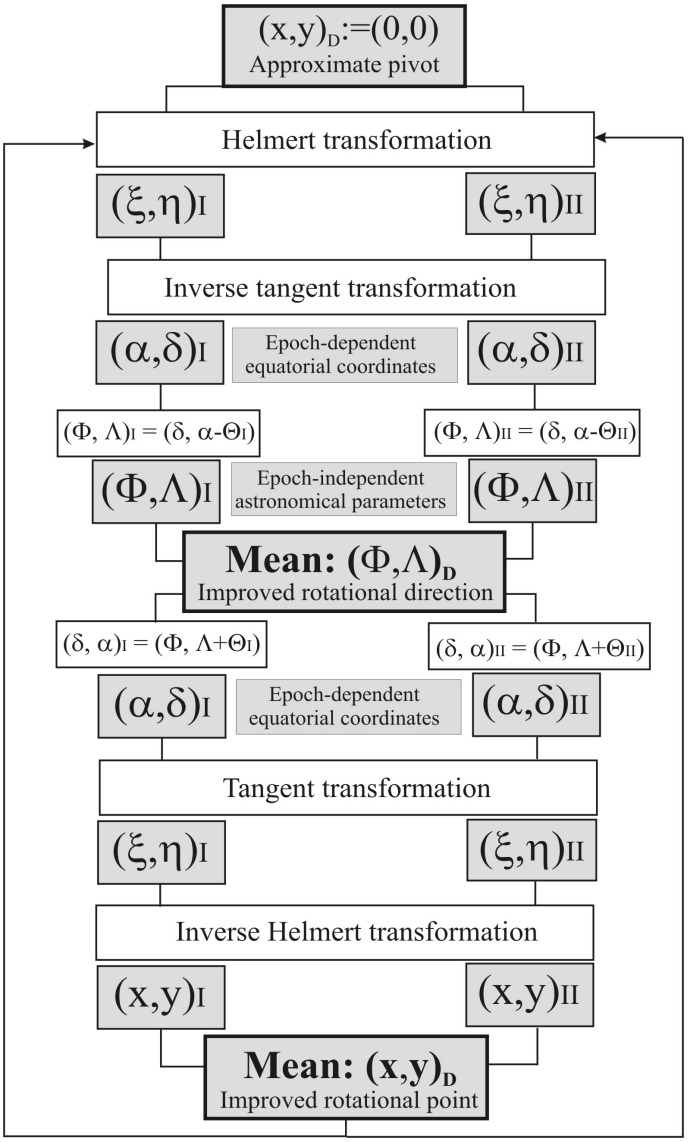

Figure 4.4: Principle of the interpolation of the pivot into the zenith. The scheme is explained in section *Calculation of the rotational direction.*

The interpolation process starts with the assumption that the image-sided intersection point of the rotational axis (=pivot) coincides with the center of the image: $(x, y)_D$=(0,0). This is necessary, since the eccentricity of the CCD sensor is still unknown (in a first-time analysis of Zenith Camera observations). By applying the Helmert transformation (Eq. (4.12)) and the inverse tangent transformation formulas (Eq. (4.6)), the epoch-dependent equatorial coordinates are derived for both images with $(\alpha, \delta)_I$ for position I and $(\alpha, \delta)_{II}$ for position II. In order to obtain epoch-independent astronomical parameters, the respective exposure epochs for both images (Θ_I, Θ_{II}) have to be taken into account (Eq. (4.4)). The results are sphere-sided intersection points of the rotational axis $(\Phi, \Lambda)_I$ and $(\Phi, \Lambda)_{II}$ (=rotational directions). Their spherical average yields the rotational direction

$(\Phi, \Lambda)_D$, which serves as input for a backward transformation. The consideration of the respective exposure epochs as well as the application of the tangent transformation formulas (Eq. (4.5)) and the inverse Helmert transformation (based on Eq. (4.12)) result in image-sided intersection points of the rotational axis $(x, y)_I$ and $(x, y)_{II}$. Their average represents an improved pivot $(x, y)_D$, which can be used for a next iteration. The iterative process terminates when $(\Phi, \Lambda)_D$ fulfills the condition in Eq. (4.15), where i is the number of iterations and ε is the termination condition:

$$\sqrt{(\Lambda_{D(i)} - \Lambda_{D(i-1)})^2 + (\Phi_{D(i)} - \Phi_{D(i-1)})^2} < \varepsilon \tag{4.15}$$

The termination condition ε can be set to 0.001 arcsec. Generally, the process terminates after three iterations. The pivot $(x, y)_D$ found in a first-time analysis of Zenith Camera observations represents the CCD eccentricity and can be used as starting value for further analyses. In order to obtain the final direction of the vertical (Φ, Λ), the rotational direction $(\Phi, \Lambda)_D$ representing the intersection point of the instrumental axis with the sphere has to be corrected for different effects (chapter 4.3).

4.3 Corrections

Inclination correction

Due to a residual vertical misalignment, the rotational axis $(\Phi, \Lambda)_D$ of the Zenith Camera still differs from the direction of the vertical (Φ, Λ). The leveling process prior to an observation aims at the best-possible alignment of the rotational axis into the local direction of the vertical. However, there remains always a residual inclination, since it is impossible to level the system perfectly with a deviation of less than 0.1 arcsec (designated accuracy for the direction of the vertical). Furthermore, the system is subject to several dynamic impacts, e.g. a slow sinking of the tripod into the ground, fluctuations of the inclination due to movements of the observer around the system, temperature influences and wind pressure. Another impact is related to the so called stagger effect of the turning circle that provokes different inclinations of the rotational axis in positions I and II. For these reasons, the inclination of the Zenith Camera has to be registered permanently, hence providing information about the misalignment of the system in the moment of observation. In order to allow for the elimination of systematical effects, as e.g. the zero-point offset of the inclination sensors and the stagger effect, the registration has to be conducted into two opposite positions I and II. Additionally, the observation sequence I-II-II-I largely enables the mitigation of a linear drift of the zero-point offset. Based on the results of the processed inclination data (chapter 4.1.2), the absolute inclinations (n_1, n_2) are available for a transformation into inclination (n_Φ, n_Λ):

$$\begin{aligned} n_\Phi &= \cos(\alpha+\beta) n_1 m_1 - \sin(\alpha+\beta)\left(\frac{n_2 m_2}{\sin\varepsilon} - \frac{n_1 m_1}{\tan\varepsilon}\right) \\ n_\Lambda &= \sin(\alpha+\beta) n_1 m_1 + \cos(\alpha+\beta)\left(\frac{n_2 m_2}{\sin\varepsilon} - \frac{n_1 m_1}{\tan\varepsilon}\right) \end{aligned} \tag{4.16}$$

α...	Astronomical azimuth (orientation CCD sensor to astronomical coordinate system)
β...	Angle between CCD sensor and coordinate system of inclination sensors
m_1, m_2...	Scales of the inclination sensors
ε...	Shearing angle between the inclination sensors

The respective coordinate systems and parameters β and ε are depicted in chapter 4.4.2, Fig. 4.11. The final inclination corrections are:

$$\begin{aligned} \Delta\Phi_n &= n_\Phi \\ \Delta\Lambda_n &= n_\Lambda \sec \Phi_D \end{aligned} \tag{4.17}$$

Azimuth correction

In chapter 4.4.1, it is shown that the result of (Φ, Λ) depends on the azimuthal orientation α of the Zenith Camera. Observations in different azimuths yield results, which describe a circle around the true direction of the vertical. For a determination of the true direction, it is necessary to consider azimuth-dependent corrections. They are represented by the parameters r (radius of the circle around the true direction) and γ (start orientation = angle offset for the astronomical azimuth). The parameters can be converted into azimuthal corrections by:

$$\begin{aligned} \Delta\Phi_a &= r \cos(\alpha + \gamma) \\ \Delta\Lambda_a &= r \sin(\alpha + \gamma) \sec \Phi \end{aligned} \tag{4.18}$$

It has to be noticed that these corrections are redundant if the new tripod method described in chapter 4.4.1 is used.

Polar motion correction

The direction of the vertical (Φ, Λ) corrected for $(\Delta\Phi, \Delta\Lambda)_n$ and $(\Delta\Phi, \Delta\Lambda)_a$ refers to the apparent terrestrial reference system ITRS and, therefore, to the position of the apparent pole of rotation (CEP) (see chapter 2.1.3). In order to link (Φ, Λ) with the conventional ITRS pole of rotation (IRP), the polar motion parameters (x_P, y_P) have to be considered (chapter 2.1.5):

$$\begin{aligned} \Delta\Phi_p &= -(x_P \cos\Lambda - y_P \sin\Lambda) \\ \Delta\Lambda_p &= -(x_P \sin\Lambda + y_P \cos\Lambda) \tan\Phi \end{aligned} \tag{4.19}$$

Final direction and computation of deflections of the vertical

The final direction of the vertical (Φ, Λ) results from an application of all described corrections to the rotational direction $(\Phi, \Lambda)_D$:

$$\begin{aligned} \Phi &= \Phi_D + \Delta\Phi_n + \Delta\Phi_a + \Delta\Phi_p \\ \Lambda &= \Lambda_D + \Delta\Lambda_n + \Delta\Lambda_a + \Delta\Lambda_p \end{aligned} \tag{4.20}$$

Provided that the ellipsoidal coordinates (φ, λ) are known, the DOV (ξ, η) can be derived by Eq. (3.1).

4.4 Calibrations

4.4.1 Azimuth calibration

The dependence of the astronomical parameters (Φ, Λ) on the azimuthal alignment of the Zenith Camera is known since the deployment of the old analog system TZK2 of Hannover in the early eighties (Hirt [2004]). It has been first time described by Wildermann [1988]. In Wirth and Marti [1986], the azimuth-dependent error is discussed in relation with the old analog Zenith Camera TZK3 of ETH Zurich. Also for the new generation of digital Zenith Cameras, this subject requires a special consideration. If the camera is orientated under different astronomical azimuths α, the corresponding solutions (Φ, Λ) describe a circle around the true direction of the vertical $(\Phi, \Lambda)_M$ showing a radial-symmetrical character. In Wildermann [1988], the reason for the error is specified as the difference between optical and rotational axis. However, Hirt [2004] showed that this difference should be negligible due to its point-symmetrical character and an observation in two opposite positions. It is then eliminated in the course of the determination of the rotational axis and the associated calculation of the spherical average (compare Fig. 4.4). In fact, the true reason for the observed azimuthal dependence is not yet fully known. However, there exists a new observation method to avoid the occurrence of this error: the so called *tripod method*. This more precise and efficient method as well as the according analysis procedure have been recently developed at the University of Hannover (Hirt and Seeber [2007a] and Hirt and Seeber [2007b]).

In the following, the classical azimuth calibration is described, as it has been realized with TZK3 and later with DIADEM until the year 2007. Besides, it still forms a dedicated method for special measuring situations (as e.g. by a transportation by boat). Afterwards, the new tripod method is presented.

Basic principle of azimuth calibration

The calibration method aims at the determination of the azimuthal correction parameters r and γ, hence allowing for the *mathematical* elimination of the error. A geometrical explanation of both parameters r and γ is illustrated in Fig. 4.5.

The parameter r represents the radius of the circle, which is described by the solutions resulting from observations in different azimuthal directions. The parameter γ describes the starting orientation depending on the orientation of the CCD sensor in reference to the objective. In order to determine the correction parameters, the Zenith Camera observations have to be conducted in different azimuthal directions. Therefore, the whole system has to be turned with the tripod platform in the designated direction (Fig. 4.10: **B**), where the complete data acquisition process has to be performed as described in chapter 4.1.1. Fig. 4.5 shows the orientation of the Zenith Camera in two azimuthal directions differing for about 120°. The calculation of the correction parameters and its application are implemented in the AURIGA software (chapter 4.3).

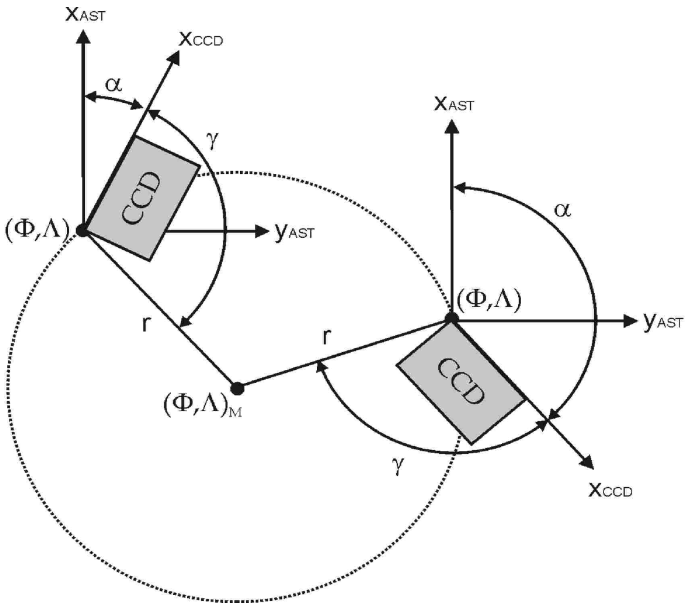

Figure 4.5: Azimuthal correction parameters r and γ at the example of an observation in two different azimuthal directions differing for about 30°. r: Radius of the circle around the true direction of the vertical, γ: Starting orientation of the CCD sensor, α: Azimuthal orientation of the Zenith Camera (Hirt [2004]).

The equalization model of the azimuth calibration is (Hirt [2004]):

$$\begin{aligned} \Phi(X,L) &= \Phi - \Phi_M + r\cos(\alpha+\gamma) = 0 \\ \Lambda(X,L) &= \Lambda - \Lambda_M + r\sin(\alpha+\gamma)\sec\Phi = 0 \end{aligned} \tag{4.21}$$

with

Φ_M, Λ_M...	True direction of the vertical = center of the circle
$\Phi(\alpha), \Lambda(\alpha)$...	Direction of the vertical depending on α
α...	Astronomical azimuth
$X_T = [\Phi_M, \Lambda_M, r, \gamma]$...	Vector of unknowns
$L_T = [(\Phi,\Lambda,\alpha)_1 ... (\Phi,\Lambda,\alpha)_n]$...	Vector of observations

Eq. (4.21) can be theoretically solved with two different azimuthal directions. However, the more azimuthal directions are observed, the more reliable is the solution of the unknowns. Generally, observations in four directions with $\Delta\alpha = 90°$ provide a satisfying configuration.

Analysis of azimuth calibrations with DIADEM

Fig. 4.6 shows the results from an observation in four different azimuthal directions, performed with DIADEM at a station in western Switzerland. Each direction yields a mean direction of the vertical (Φ, Λ) (marked as fat points), which are distributed on a circle around the true direction of the vertical $(\Phi, \Lambda)_M$.

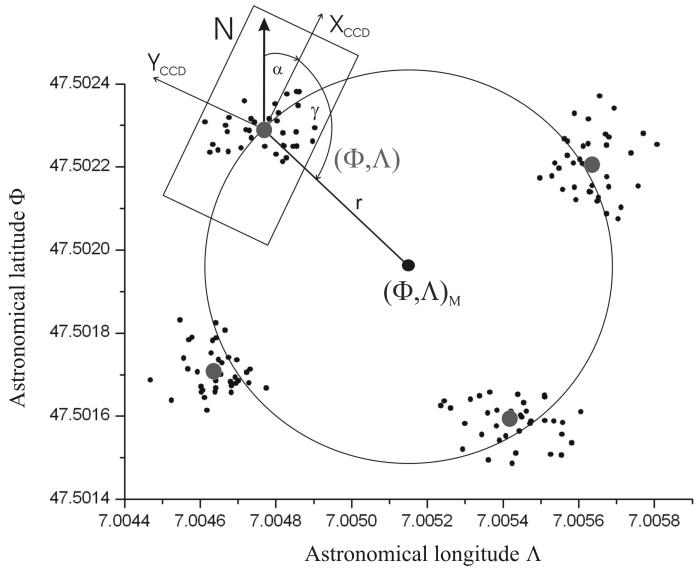

Figure 4.6: Rotational directions $(\Phi, \Lambda)_i$ with $i = 1...4$ for four different azimuthal directions α_i. The distribution of the single results (black points) on a circle is well recognizable. The mean rotational direction of each azimuthal orientation is designated by the fat black points. The true direction of the vertical $(\Phi, \Lambda)_M$ is represented by the center of the circle.

Figs. 4.7 and 4.8 demonstrate the time-dependent behavior of the parameters r and γ at the example of the DIADEM campaign in Greece in 2005 (chapter 7). As recognizable, the parameters show relatively large variations between the stations, hence, they can not be considered as constant. The parameter r (Fig. 4.7) varies between 2.7 and 3.3 arcsec with a standard deviation of about 0.17 arcsec. The mean amounts to 3 arcsec. Possible reasons for these variations are percussions of the system as a result of transportation. Thus, the travel from Zurich (day 0) to the first station in Greece (day 5) might be responsible for the strong variations of r for about 0.6 arcsec. Regarding the parameter γ (Fig. 4.8), large variations of about 27° are observable between days 14 and 19. This might be interpreted as stress impact on the system caused by the transshipping from boat to car. Other possible reasons might be temperature changes, tensions of the system as well as changes of the CCD sensor orientation after an adaption of the focus.

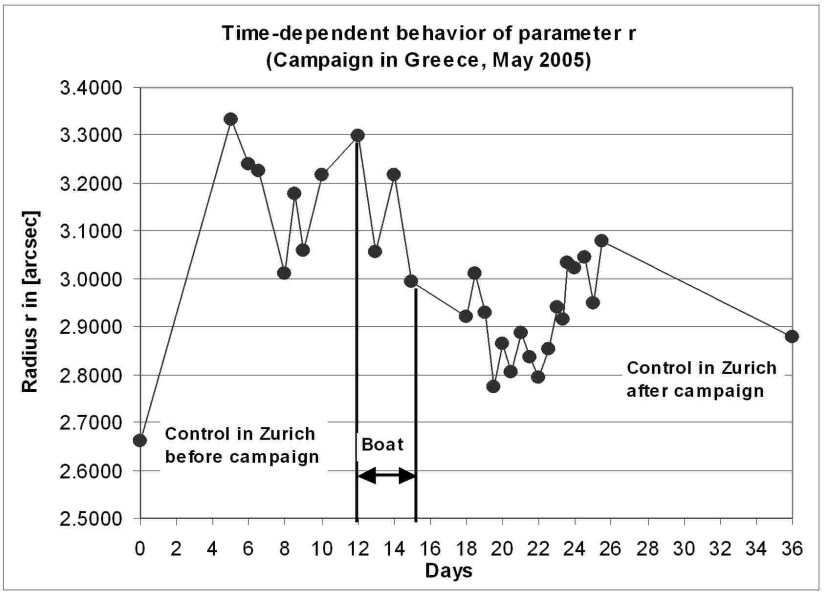

Figure 4.7: Time-dependent behavior of parameter r during the campaign in Greece in 2005. The variations are relatively large with values between 2.7 and 3.3 arcsec and a standard deviation of about 0.17 arcsec. The mean amounts to 3 arcsec.

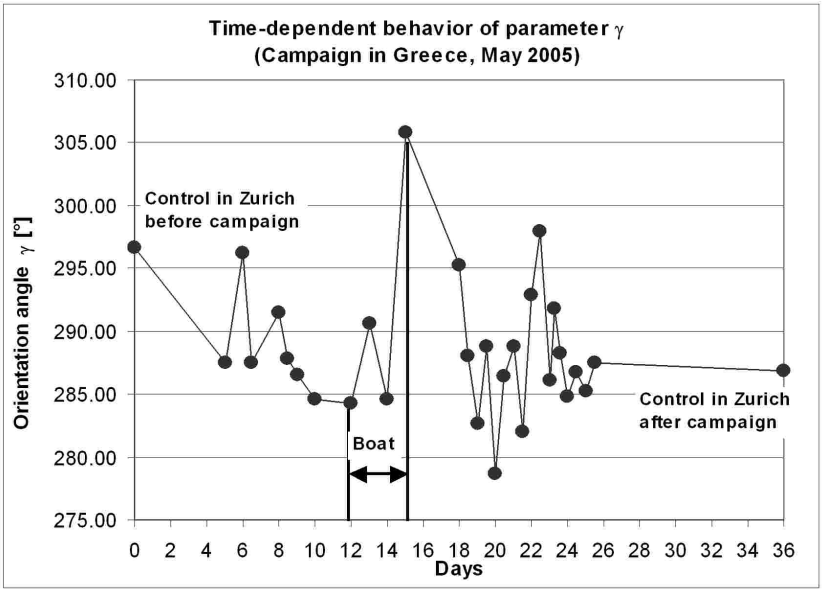

Figure 4.8: Time-dependent behavior of parameter γ during the campaign in Greece in 2005. Also for this parameter, the variations are relatively large with values between 278.6° and 305.8° and a standard deviation of about 5.5°. The mean amounts to 288.7°.

The role of inclination sensors

Interestingly, the inclination sensors seem to play a role within the described problem of azimuth-dependence (Ganz [2007]). Tab. 4.1 shows the results of an azimuth calibration with DIADEM at the reference station in front of the ETH-HPV building, performed in nine different azimuthal orientations. The analysis has been processed twice

using one time the inclination data of the Wyler sensors and another time the data of the Lippmann sensors. As recognizable, the investigation revealed significant differences between the respective azimuthal correction parameters r and γ. This suggests a relation between azimuthal error and the type of inclination sensors or, more reasonable, the position of the sensors on the turning circle.

	Wyler sensors	Lippmann sensors
r [arcsec]	**2.16**	**1.12**
σ_r [arcsec]	0.03	0.03
γ [deg]	**281.84**	**153.87**
σ_γ [deg]	0.78	1.37

Table 4.1: Azimuthal corrections r and γ depending on the inclination sensors.

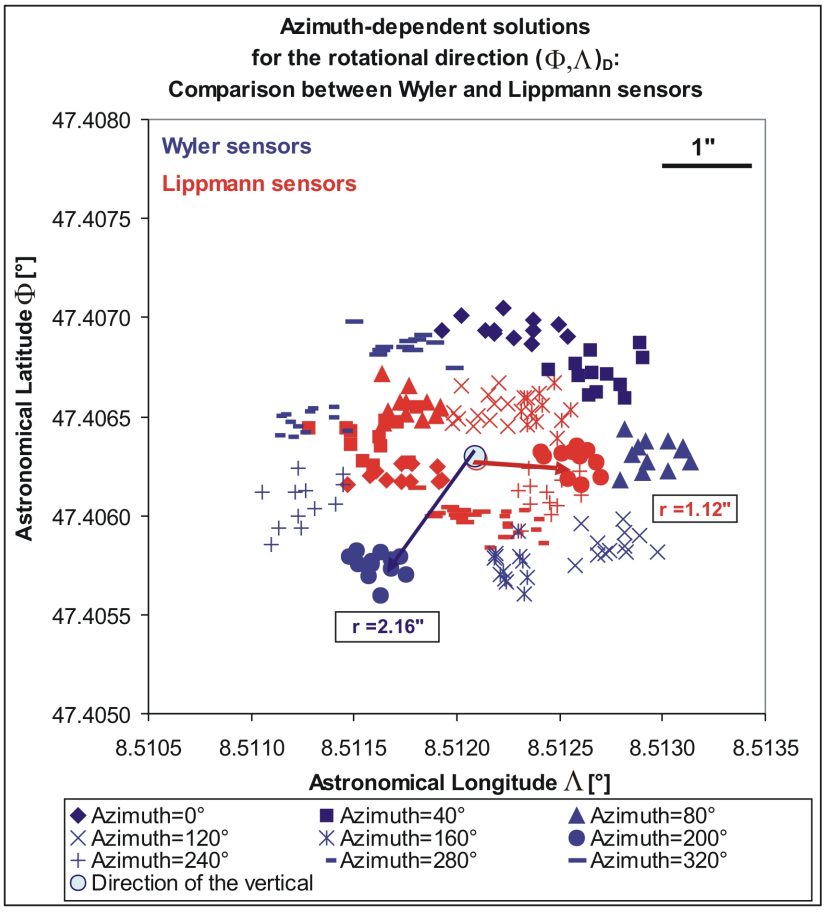

Figure 4.9: Comparison of the azimuth-dependent solutions for the rotational direction as result of an analysis with Wyler (blue) and Lippmann sensors (red), respectively. The symbols represent nine different azimuthal directions. Corresponding symbols label corresponding azimuthal directions. As well recognizable, the azimuth correction parameters r and γ differ significantly (see Tab. 4.1).

The radius r determined with the Wyler sensors is for about 1 arcsec greater than those derived with the Lippmann sensors (Tab. 4.1: 2.16 arcsec vs. 1.12 arcsec). Also the respective orientation angles γ differ significantly for about 130° (281.84° vs. 153.87°). These differences are well recognizable in Fig. 4.9, where an azimuth calibration with

nine different positions is plotted. The blue symbols reflect the Wyler solutions, while the red symbols represent the Lippmann solutions. The azimuthal directions are marked by different symbols, whereas corresponding azimuthal directions between both series are indicated by identical symbols. The circle derived from an analysis with Lippmann sensors is obviously smaller than those from the Wyler series. Furthermore, the respective solutions for same azimuthal directions differ for about 130° according to the difference in γ. The reason for these discrepancies is not yet known. One possible approach might be the fact that Wyler and Lippmann sensors are mounted on different positions on the turnable superstructure of DIADEM. Therefore, they are potentially exposed to different deformations caused by instabilities of the turning platform. An experimental set-up to validate this assumption could be a change of the mounting positions of the sensors. However, as the tripod method described in the next section provides much more precise solutions, a deeper analysis of this problem is not of high priority anymore.

Tripod method

In comparison to the azimuth calibration method, the newly developed tripod method provides a more precise and efficient strategy to determine the direction of the vertical by eliminating the occurrence of an azimuth-dependent error. The old method differs from the new method by the performance of an observation in two opposite positions: While the azimuth calibration requires the turning of the superstructure of the instrument for 180° (Fig. 4.10: **A**), the new method demands the turning of the entire tripod platform into opposite directions (Fig. 4.10: **C**). For a more detailed description of the measuring procedure, please refer to chapter 4.1.1. The resulting direction of the vertical is independent from an azimuthal orientation of the system. It directly represents the true direction of the vertical. Dedicated investigations by Ganz [2007] demonstrated that the tripod method provides a significantly higher external accuracy than the azimuth calibration (chapter 6.5). The new method yields an accuracy of better than 0.1 arcsec, hence representing an improvement of about 50% compared to the method of azimuth calibration. Therewith, the time-consuming and inefficient method of azimuth calibration becomes, theoretically, redundant. However, in case of special measuring situations, the azimuth calibration still represents a dedicated method. Such a dedicated situation was given during the campaign in Greece, where the instrument had to be transported by boat. The modernized tripod was too heavy and bulky for a shipborne transportation, and is, furthermore, not dismountable. Therefore, the old tripod of the analog TZK3 system has been used offering the possibility to buckle the tripod legs. However, it does not provide the conditions for an automatical turning of the platform, which demanded the performance of an azimuth calibration.

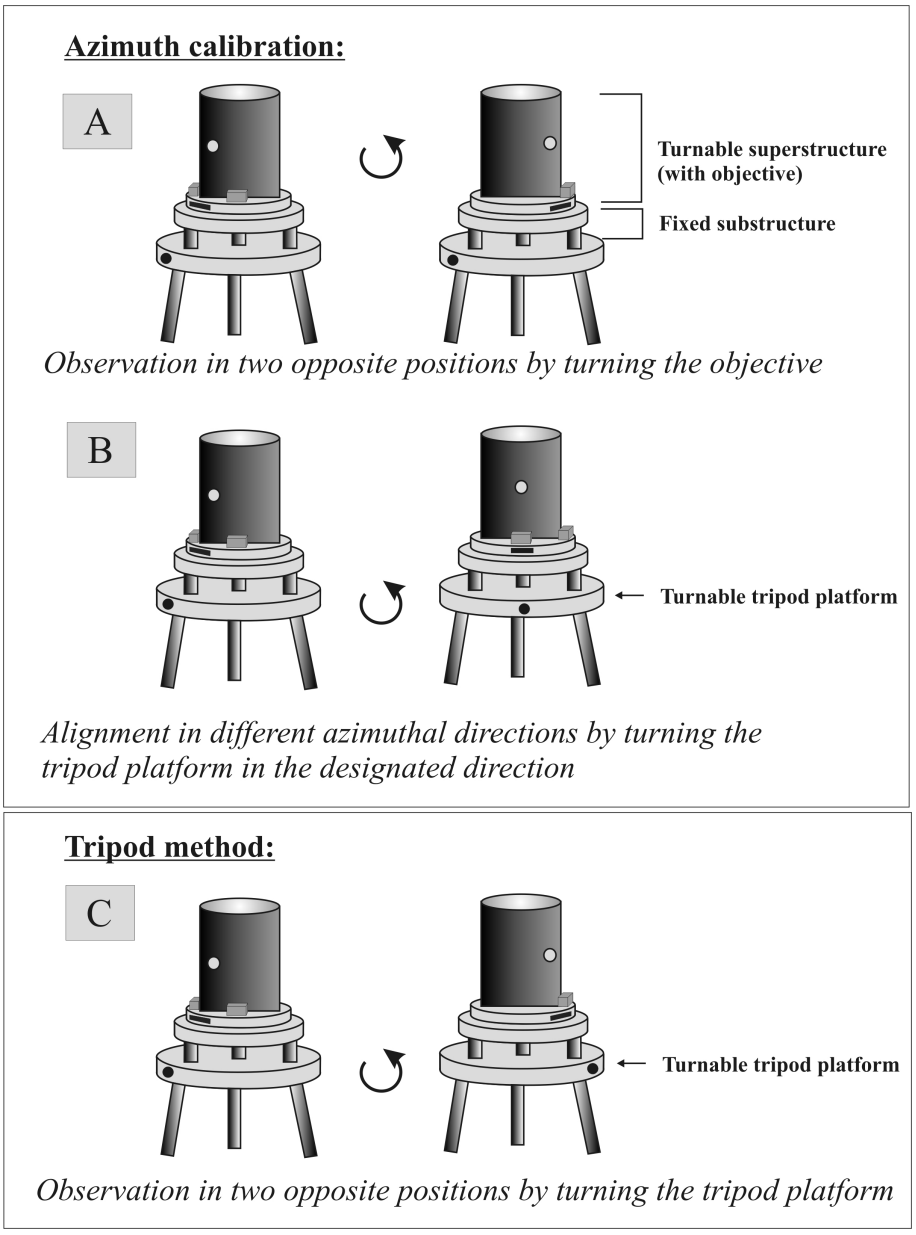

Figure 4.10: Difference between *azimuth calibration* and *tripod method*. If applying the method of azimuth calibration, the observation in two opposite positions is realized by turning the objective (A). In order to eliminate the azimuth-dependent error, it is necessary to turn the whole instrument with the tripod platform in different azimuthal directions (B) and to repeat the complete measuring procedure. In contrast, the tripod method only requires the turning of the whole instrument with the tripod platform for the observation in two opposite positions (C). Then, the azimuth-dependent error does not occur anymore and the alignment in different azimuthal directions is not necessary.

4.4.2 Celestial calibration

With the method of celestial calibration developed by Hirt [2004], it is possible to determine the orientation angle β between CCD coordinate system $(X, Y)_{CCD}$ and coordinate system of the inclination sensors $(X, Y)_{Lev}$. Furthermore, the scales of the inclination sensors (m_1, m_2) and the shearing angle ε between the axes X_{Lev} and Y_{Lev} of the sensor coordinate system can be derived. Fig. 4.11 illustrates the associated coordinate systems. The calibration parameters $\beta, \varepsilon, m_1, m_2$ are needed for the transformation of the inclination data (n_1, n_2) into inclination corrections $(\Delta\Phi, \Delta\Lambda)$ (see Eqs. (4.16) and (4.17)).

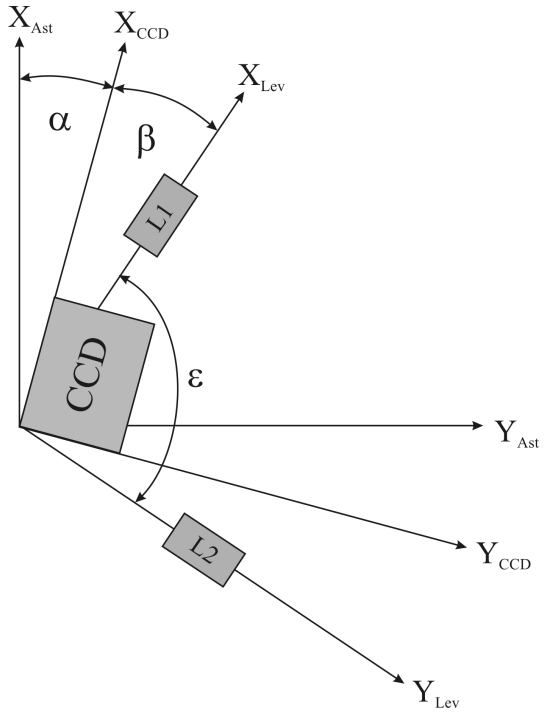

Figure 4.11: Definition of coordinate systems and associated parameters $\alpha, \beta, \varepsilon$. In addition to the inclination scale factors m_1, m_2, the parameters β and ε are a result of the celestial calibration. The astronomical azimuth α is derived from the data analysis and depends on the orientation of DIADEM during an observation.

Basic principle of celestial calibration

The celestial calibration is based on the idea that variations in the inclination of the Zenith Camera are directly reflected both in the *observed rotational direction* $(\Phi, \Lambda)_D$ and the *inclination data* (n_1, n_2). At a station, the sum of rotational direction $(\Phi, \Lambda)_D$ and inclination corrections $(\Delta\Phi, \Delta\Lambda)_n$ is always constant yielding the direction of the vertical $(\Phi, \Lambda)_Z$:

$$\begin{pmatrix} \Phi_Z \\ \Lambda_Z \end{pmatrix} = \begin{pmatrix} \Phi_D \\ \Lambda_D \end{pmatrix} + \begin{pmatrix} \Delta\Phi_n \\ \Delta\Lambda_n \end{pmatrix} \tag{4.22}$$

$$\begin{pmatrix} \Delta\Phi_n \\ \Delta\Lambda_n \end{pmatrix} = \begin{pmatrix} n_\Phi \\ n_\Lambda \sec \Phi_Z \end{pmatrix} \tag{4.23}$$

According to Eq. (4.16), the inclinations (n_Φ, n_Λ) can be calculated by means of the absolute inclinations (n_1, n_2) (Eq. (4.1)), the unknown transformation parameters $\beta, \varepsilon, m_1, m_2$ and the astronomical azimuth α. The equalization model of the celestial calibration is then (Hirt [2004]):

$$\begin{aligned}\Psi(X,L) &= \Phi_D - \Phi_Z + (\cos(\alpha+\beta)n_1 m_1 - \sin(\alpha+\beta)\left(\frac{n_2 m_2}{\sin\varepsilon} - \frac{n_1 m_1}{\tan\varepsilon}\right)) \\ \Psi(X,L) &= \Lambda_D - \Lambda_Z + (\sin(\alpha+\beta)n_1 m_1 - \cos(\alpha+\beta)\left(\frac{n_2 m_2}{\sin\varepsilon} - \frac{n_1 m_1}{\tan\varepsilon}\right))\sec\Phi_Z\end{aligned} \tag{4.24}$$

with

$\Phi_Z, \Lambda_Z ...$	Direction of the vertical
$\Phi_D, \Lambda_D ...$	Rotational direction
$X_T = [\Phi_Z, \Lambda_Z, m_1, m_2, \beta, \varepsilon] ...$	Vector of unknowns
$L_T = [(\Phi_D, \Lambda_D, n_1, n_2, \alpha)_1 ... (\Phi_D, \Lambda_D, n_1, n_2, \alpha)_n] ...$	Vector of observations

The unknown calibration parameters can be derived by comparing the zenithal distance z_D (=difference between $(\Phi, \Lambda)_D$ and $(\Phi, \Lambda)_Z$) and zenithal distance z_n (=inclination of the system):

$$z_n = \sqrt{n_1^2 + n_2^2} \qquad z_D = \sqrt{(\Phi_D - \Phi_Z)^2 + (\Lambda_D - \Lambda_Z)^2 \cos^2\Phi_Z} \tag{4.25}$$

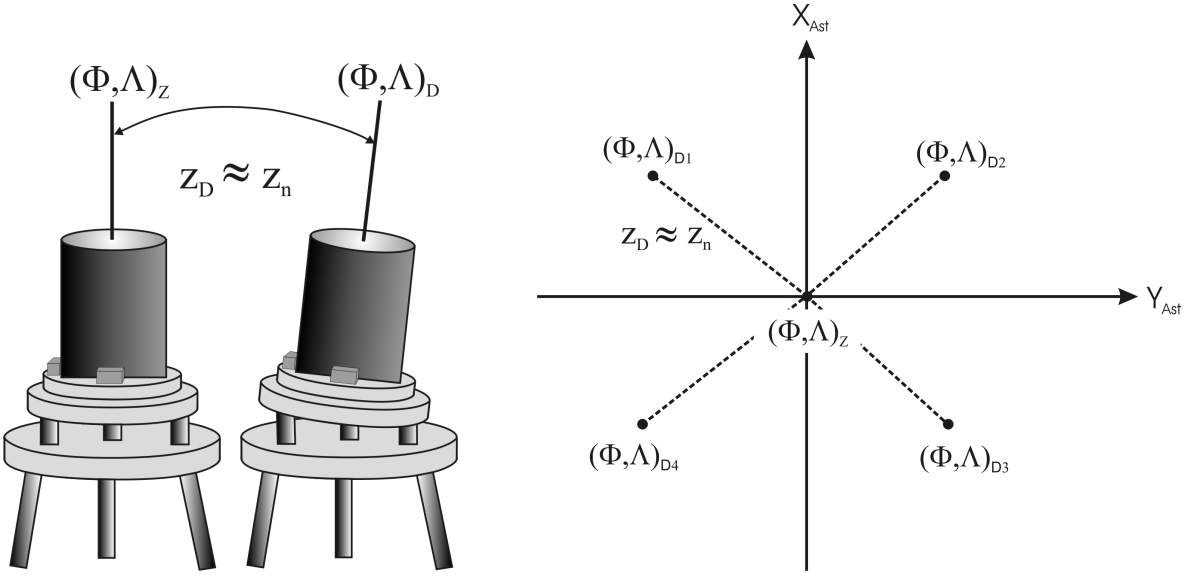

a) Intentional inclination of the Zenith Camera.

b) Inclination of the Zenith Camera in four different directions.

Figure 4.12: Principle of celestial calibration with z_D = Zenithal distance between direction of the vertical $(\Phi, \Lambda)_Z$ and rotational direction $(\Phi, \Lambda)_D$ and z_n = Zenithal distance derived from the inclination data (modified after Hirt [2004]).

Therefore, the Zenith Camera has to be inclined intentionally for about 10 arcsec to 100 arcsec (Fig. 4.12***a)***). The systematical deflection of the rotational axis of the Zenith Camera is performed in different directions (Fig. 4.12***b)***). This allows for a geometrically stable configuration. Provided that the inclination of the Zenith Camera is corrected appropriately, it can be assumed that z_n is approximately equal to z_D (apart from stochastical measurement errors). A systematical difference between both can be attributed to deviant calibration parameters. Hence, e.g. the scales m_1, m_2 of the inclination sensors might differ from 1 or the shearing angle ε between the axes of the inclination sensors might deviate from 90°. In order to allow for the determination of all six unknown parameters X_T (Eq. (4.24)), the observation of the rotational direction under at least three different orientations of the instrument is needed.

Analysis of celestial calibrations with DIADEM

It is recommended to repeat the calibration procedure in regular time intervals, especially after reconstruction works at the system as well as before, during and after a campaign. The long-time observations during the years 2003-2005 (without any reconstruction works in between) show that the parameters remain relatively constant (Tab. 4.2). The orientation angle β amounts to 1.37°, while the shearing angle ε indicates a deviation of 0.14° from an orthogonally mounting of the inclination sensors. Both parameters show a standard deviation of 0.09°. The scale factors of the Wyler inclination sensors differ with a standard deviation of 0.25% for maximum 0.52% from 1.

Nr.	Date	Day index	m_1 [-]	m_2 [-]	β [°]	ε [°]
1	20030917	1	1.0049	1.0021	0.9059	89.7415
2	20040908	358	1.0004	1.0003	1.3187	89.8964
3	20040912	362	1.0038	1.0015	1.4755	89.9871
4	20041003	383	1.0072	1.0014	1.3239	89.9823
5	20041115	426	1.0072	1.0019	1.3858	89.8314
6	20050117	489	1.0070	1.0025	1.4452	89.8208
7	20050516	608	1.0074	1.0045	1.4455	89.7522
8	20050715	668	1.0035	1.0035	1.3858	89.8923
		Mean:	**1.0052**	**1.0022**	**1.3733**	**89.8630**
		Std.dev.:	0.0025	0.0013	0.09	0.09

Table 4.2: Results of celestial calibration between the years 2003-2005. The calibration parameters $(m_1, m_2, \beta, \varepsilon)$ remain relatively constant.

Concluding, it can be stated that the celestial calibration offers a very fast method (about 30 minutes) for the determination of the calibration parameters. Especially, the in-situ determination of the inclination scale factors is very interesting. Indeed, Hirt [2004] recognized that the scale factors determined with this procedure might deviate from those determined by a conventional calibration table in a laboratory (as e.g. used at the Institute of Geodesy and Photogrammetry, ETH Zurich). However, the scale factors resulting from the method of celestial calibration are more relevant for the calculation of *realistic* inclination corrections, as they are adapted to the ICRS scale provided by the star catalogs (Hirt [2004]).

4.4.3 Shutter delay

An error in the determination of the epoch influences directly the astronomical longitude Λ. This component depends linearly on time because of the earth's rotation. Regarding the accuracy of epoch determinations, the characteristic of the electronic blade shutter used in the CCD camera plays an important role. It is well known from other investigations (Käker [2003], Hirt [2004]) that the shutter might react asymmetrically. This means that the times needed to open and to close are different. Besides, the shutter might respond delayed in reference to the TTL signal emitted by the CCD camera in the moment of exposure. These characteristics cause an unknown time delay. In order to assure that the impact of an epoch error on the η-component does not exceed 0.01 arcsec (for the latitude $\varphi_{Zurich} \approx 47.4°$), the epoch has to be determined with an accuracy (Δt) of better than 0.9 ms. This relation is expressed by the following equation:

$$\Delta\eta = (15^{[arcsec/s]} \cdot \cos\varphi) \cdot \Delta t \tag{4.26}$$

Experimental set-up

The analysis of the shutter function is based on the comparison of two different signals:

* TTL signal: The rectangular trigger signal is emitted by the FDL-PCI card of the CCD camera in the moment of exposure and transfered to the shutter. It signalizes the shutter to start the opening process. Additionally, the TTL signal is relayed to a GPS receiver implemented in the PC for the determination of the exact exposure epoch. The user defines if the exposure epoch t_{GPS} either refers to the ascending (start of exposure) or descending edge (end of exposure) of the TTL signal.
* Shutter signal: In order to generate this signal, a laser has been aligned to the edges and the center of the CCD sensor, respectively (Figs. 4.13 and 4.14). As soon as the shutter starts to open, the laser signal is reflected by the sensor surface and detected by a light-sensitive diode. The reflexion terminates, when the shutter is completely closed.

The shutter signal as well as the TTL signal are both monitored by an oscilloscope. The comparison of the signals allows for the analysis of the specific reaction times of the shutter, which can be characterized by the following points in time (compare Fig. 4.15):

* t0: Release of the TTL trigger signal by the CCD camera
* t1: Shutter starts to open
* t2: Shutter is completely open (100% of the CCD sensor are exposed)
* t3: Shutter starts to close
* t4: Shutter is completely closed

For the determination of these points in time, different positions on the sensor have been located (Fig. 4.14). The center of the sensor (p1) corresponds to the points in time t1 and t4: The laser signal is reflected as soon as the shutter starts to open (t1), and the

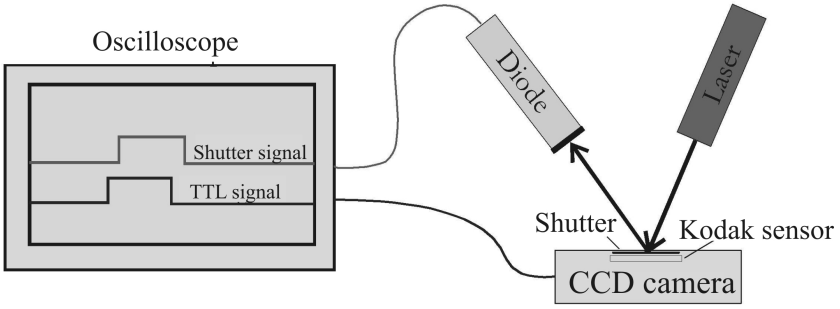

Figure 4.13: Configuration scheme of the experiment for the investigation of the shutter characteristic.

reflexion terminates when the shutter is completely closed (t4). In contrast, the four edges of the sensor (p2-p5) provide redundant information for the time points t2 and t3: these positions do not reflect the signal until the shutter is completely open (t2) and terminate the reflexion as soon as the shutter starts to close (t3).

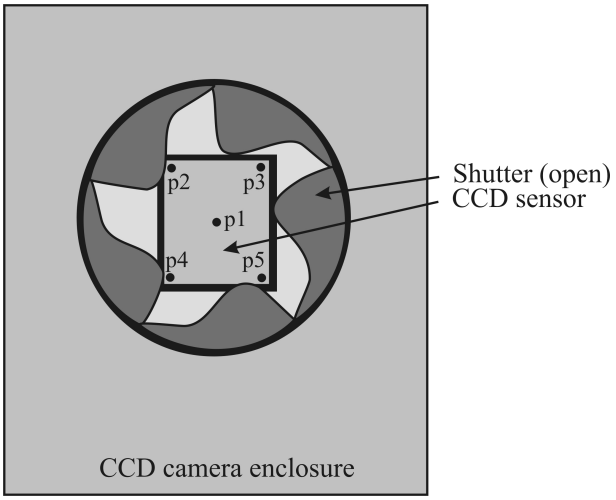

Figure 4.14: CCD sensor with the edge and center points at the moment when 100 % of the shutter are open.

Investigation of exposure time dependence

In order to detect a potential dependence on the exposure time, the investigation has been performed with times varying between 100 ms and 500 ms (Bentz [2006]) (Tab. 4.3).

For each exposure time, points t1-t4 have been determined repeatedly (about 30 times). Points t2 and t3 represent the weighted average of all four sensor edges. With focus on a typical exposure time of 300 ms, the following conclusions can be resumed: The shutter shows a clearly delayed reaction time as it starts to open 5.68 ms (t1) after the TTL signal has been emitted (t0). Other 5.8 ms (t2-t1) elapse until the shutter is open so far that the complete CCD sensor is uncovered. Hence, it needs in total 11.48 ms (t2) until the edges of the sensor are exposed. Another finding is that the shutter acts in fact asymmetrically, as the time needed to open (t2-t1) is 0.35 ms shorter than to close (t4-t3). Finally, the comparison of the target exposure time T with the effective exposure times

revealed that the exposure time for stars in the center of the sensor (t4-t1-T) is 8.47 ms longer than T. However, the exposure time for stars in the edge of the sensor (t3-t2-T) is 3.50 ms shorter than T. These differences have to be considered in the calculation of the effective exposure time delay. The shape of the according shutter function is depicted in Fig. 4.15. Tab. 4.4 shows the means of all analyzed exposure times for each point in time. The question of an exposure time dependence can be abandoned as the mean times show a very good agreement, with a standard deviation of mostly better than 0.15 ms (compare also Fig. 4.16).

T	100 ms		200 ms		300 ms		400 ms		500 ms	
[ms]	t	σ_t	t	σ_t	t	σ_t	t	σ_t	t	σ_t
t1	5.53	0.10	5.65	0.12	**5.68**	0.21	5.49	0.10	5.54	0.05
t2	11.42	0.08	11.50	0.07	**11.48**	0.05	11.45	0.06	11.47	0.06
t3	108.03	0.05	207.96	0.04	**307.98**	0.05	407.93	0.06	508.01	0.06
t4	114.31	0.11	214.23	0.13	**314.14**	0.19	414.29	0.04	514.20	0.06
t2-t1	5.90		5.85		**5.81**		5.97		5.93	
t3-t2	96.61		196.46		**296.50**		396.48		496.54	
t3-t2-T	-3.39		-3.54		**-3.50**		-3.52		-3.46	
t4-t1	108.79		208.58		**308.47**		408.80		508.66	
t4-t1-T	8.79		8.58		**8.47**		8.80		8.66	
t4-t3	6.28		6.27		**6.16**		6.35		6.19	
dt_m	9.82	0.07	9.84	0.07	**9.82**	0.10	9.79	0.06	9.81	0.05

Table 4.3: Shutter reaction times for points in time t1 to t4 depending on the exposure times for a temperature of 22°C. t1: Shutter starts to open, t2: Shutter is 100% open, t3: Shutter starts to close, t4: Shutter is 100% closed, t2-t1: Time needed to open, t3-t2-T: Difference between target (T) and actual exposure time (t3-t2) for stars in the edge of the sensor, t4-t1-T: Difference between target (T) and actual exposure time (t4-t1) for stars in the middle of the sensor, t4-t3: Time needed to close, dt_m: Final correction time after Eq. (4.29) (independent from the exposure time), σ_t: Standard deviations of measured time differences.

[ms]	t_m	σ_{t_m}
t1	5.58	0.08
t2	11.47	0.03
t3		
t4		
t2-t1	5.89	0.06
t3-t2		
t3-t2-T	-3.48	0.06
t4-t1		
t4-t1-T	8.66	0.14
t4-t3	6.25	0.08
dt_m	9.82	0.02

Table 4.4: Mean shutter response times t_m for the exposure times investigated at points in time t1 to t4. σ_{t_m}: Standard deviations of mean time differences.

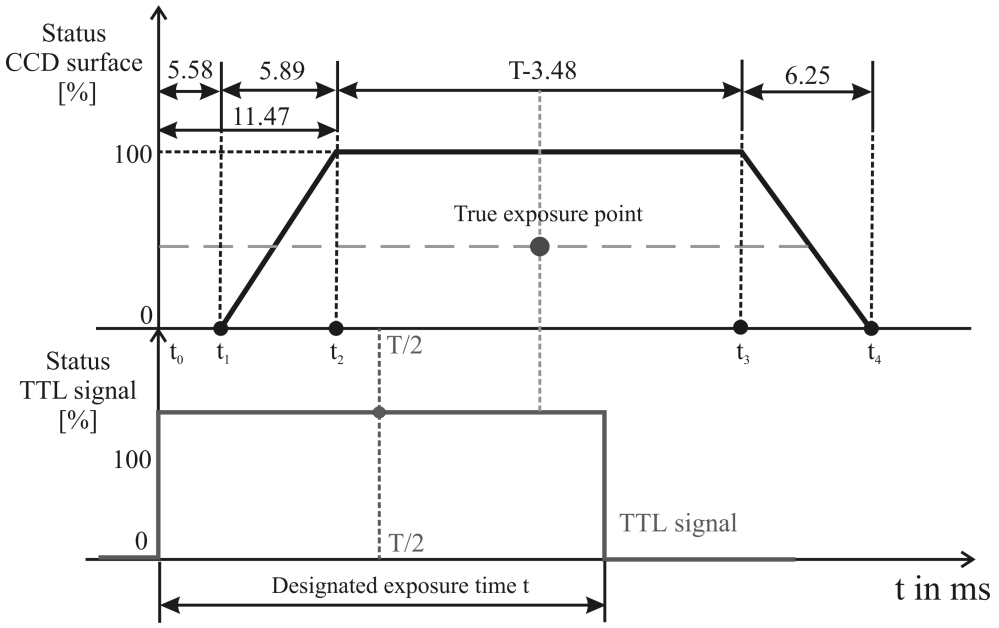

Figure 4.15: Shutter function representing the delays determined for the points in time t1 to t4 (referring to Tab. 4.4).

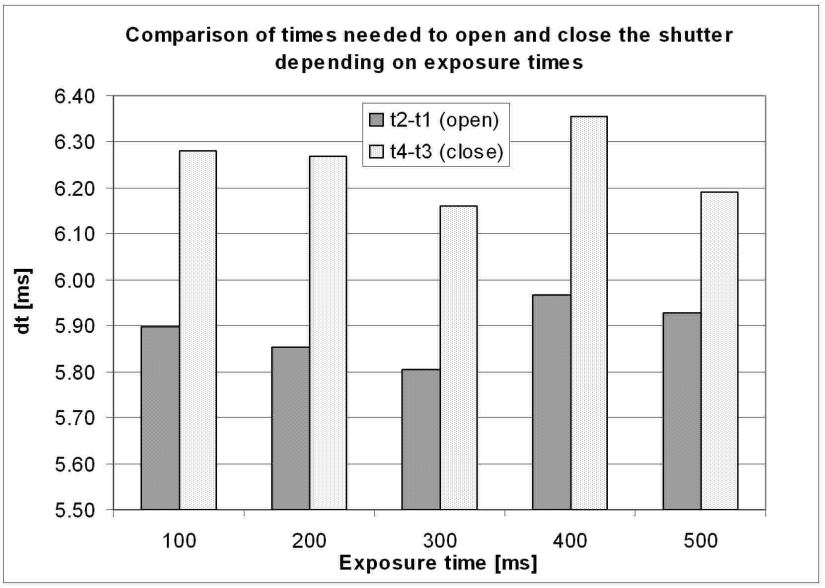

Figure 4.16: Times needed to open (dark gray) and close (light gray) the shutter depending on the exposure time. A correlation with the exposure time is not recognizable. However, it is obvious that the shutter reacts asymmetrically, hence, the time needed to open is shorter than the one to close.

According to the fact that the exposure times vary for stars in the center and in the edge of the sensor, respectively, different equations for the calculation of the effective time delay have to be considered. Eq. (4.27) allows for the computation of the time delay dt_{edge} for stars at the edge of the CCD sensor. They are not exposed unless the complete

CCD sensor is uncovered (t2 to t3).

$$dt_{edge} = t_2 + \frac{t_3 - t_2 - T}{2} \tag{4.27}$$

Eq. (4.28) represents the time delay dt_{center} for stars at the center of the CCD sensor. They are exposed as soon as the shutter starts to open and until it is completely closed (t1 to t4).

$$dt_{center} = t_1 + \frac{t_4 - t_1 - T}{2} \tag{4.28}$$

Eq. (4.29) provides the mean time delay dt_m, based on Eqs. (4.27) and (4.28). It represents a common correction formula for all stars independent from their position on the CCD sensor.

$$dt_m = \frac{dt_{edge} + dt_{center}}{2} = \frac{t_1 + t_2 + t_3 + t_4}{4} - \frac{T}{2} \tag{4.29}$$

Referring to this equation, the time delay dt_m amounts to +9.82 ms (Tab. 4.4). It means that the effective exposure is later than the one represented by the TTL signal and released at t0.

Eq. (4.30) allows for the calculation of the corrected exposure epoch t_{corr}, where t_{GPS} is the epoch provided by GPS referring to the ascending flank, and T is the target exposure time. The corrected epoch than refers to the middle of the shutter function.

$$t_{corr} = t_{GPS} + \frac{T}{2} + dt_m = t_{GPS} + \frac{T}{2} + 9.82 \tag{4.30}$$

Investigation of temperature dependence

In order to analyze also a potential temperature dependence, the reaction times of the shutter have been determined under different temperatures (-10°C, 0°C, 10°C and 22°C) (Bentz [2006]). This has been realized in the climate chamber of the institute, with a repetition of 30 times per point p1 to p5. The exposure time T has been set to 100 ms, as an investigation concerning the correlation between exposure time and temperature did not reveal any significance.

Tab. 4.5 shows the results of the analysis of the points in time t1 to t4 for different temperatures. It is obvious that there exists a strong correlation between temperature and reaction times. Generally, it can be said that the lower the temperature, the longer the reaction times (compare Fig. 4.17).

The time needed to open the shutter at a temperature of -10°C is about 0.5 ms longer than at a temperature of 22°C. The analysis of the closure times reveals a similar result: There, for the same two temperatures, a delay of about 0.4 ms has been observed. The effective mean time delay t_m (Eq. (4.29)) shows a clear increase with decreasing temperature (Fig. 4.18).

Temp	22°C		10°C		0°C		-10°C	
[ms]	t	σ_t	t	σ_t	t	σ_t	t	σ_t
t1	5.58	0.14	5.66	0.06	5.88	0.06	5.77	0.05
t2	11.47	0.10	11.67	0.08	11.81	0.09	12.15	0.08
t3	107.98	0.15	108.95	0.09	109.23	0.09	109.74	0.06
t4	114.23	0.14	115.64	0.09	115.92	0.08	116.36	0.11
t2-t1	5.89		6.01		5.93		6.39	
t3-t2	96.52		97.28		97.43		97.58	
t3-t2-T	-3.48		-2.72		-2.57		-2.42	
t4-t1	108.66		109.98		110.03		110.59	
t4-t1-T	8.66		9.98		10.03		10.59	
t4-t3	6.25		6.69		6.68		6.62	
dt_m	9.82	0.13	10.48	0.08	10.71	0.08	11.00	0.07

Table 4.5: Shutter reaction times t1 to t4 depending on the temperature. The exposure time T has been set to 100 ms. For explanations of the points in time and corresponding differences, please refer to Tab. 4.3.

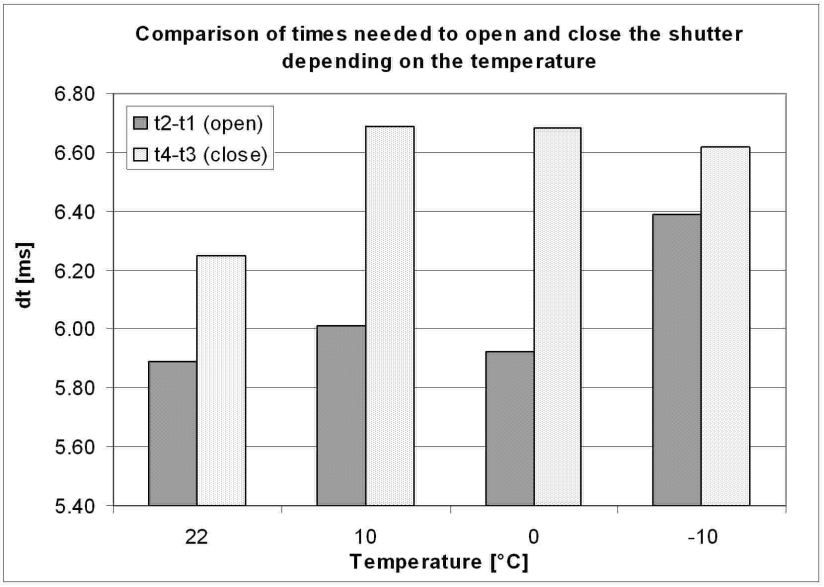

Figure 4.17: Times needed to open (dark gray) and close (light gray) the shutter depending on the temperature. A significant correlation with the temperature is recognizable. The lower the temperature, the longer the respective reaction times. Again it becomes obvious that the time needed to open the shutter is shorter than to close it.

The approximation by a linear regression yields the following function:

$$dt = -0.04 \cdot TT + 10.7 \tag{4.31}$$

with a mean delay of about 0.04 ms per K. The parameter TT indicates the actual ambient temperature [K]. This relation is considered in the computation of the corrected

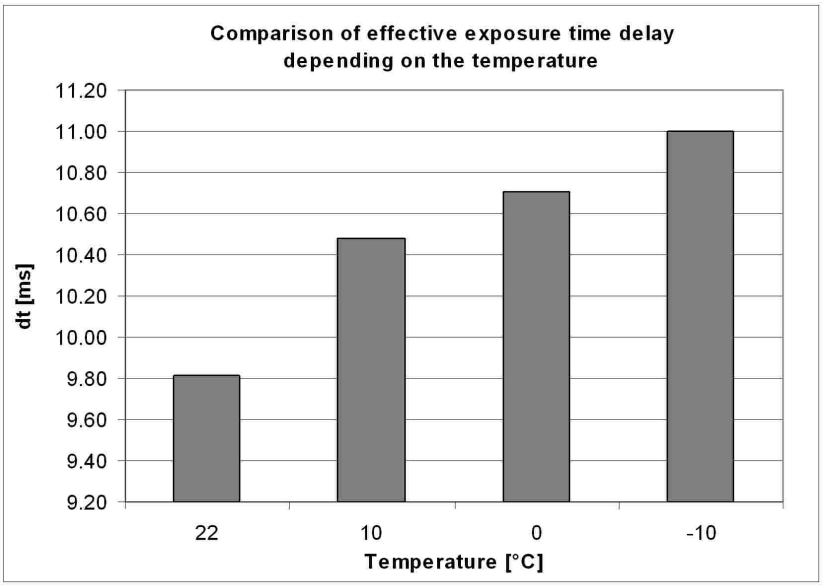

Figure 4.18: Temperature-dependent effective time delays. The difference in delay between a temperature of 22°C and -10°C, respectively, amounts to about 1.2 ms.

exposure epoch t_{corr} referring to a temperature TT of 0K and a corresponding time delay of 10.7 ms:

$$t_{corr} = t_{GPS} + \frac{T}{2} - 0.04 \cdot TT + 10.7 \tag{4.32}$$

It has to be noticed that the investigation has been only performed at four different temperatures and is, therefore, not very significant. However, the results serve as an indicator for a clear correlation between temperature and shutter delay.

Concluding, it can be said that the investigation of the shutter delay revealed very interesting results. The delay between the rectangular TTL signal and the actual shutter function amounts to +9.82 ms. A disregard of the delay would result in a too small astronomical longitude Λ (0.1 arcsec for the latitude of Zurich (compare Eq. (4.26))). In order to keep the time error below a threshold of 0.01 arcsec in longitude, a careful implementation of the shutter properties is mandatory. As regards the problem of temperature dependence, the maximum impact can be derived by the following consideration: For temperatures between -15°C (winter nights) and +30°C (summer nights), the difference in the time delay amounts to 1.8 ms (Eq. (4.31)). This refers to an error of the η-component of 0.02 arcsec and is, therefore, also considerable.

4.4.4 Focus-temperature-function

The quality of a star image photographed with DIADEM decisively depends on the quality of the focus: If the focal adaption is insufficient, the stars will show distortion effects resulting in a decreased accuracy as regards the image coordinate determination. In chapter 5.2.1, a clear correlation between defocussing and astrometric accuracy is demonstrated (Fig. 5.3), as well as between defocussing and maximum magnitude of

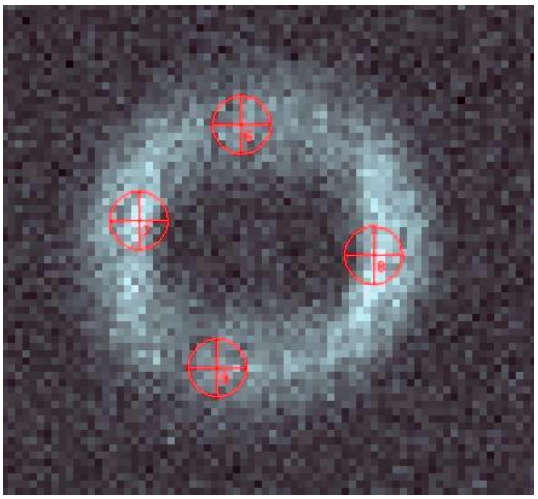

Figure 4.19: Error in the detection of a star (contrast amplified image), caused by a bad focussing. The center of the star is not clearly identifiable, hence the extraction software tags four different stars instead of one (red targets).

stars imaged (Fig. 5.4). A defocussing might also produce errors in the detection of stars imaged, as visible in Fig. 4.19. Due to the ring-shaped form of the star, its center is not clearly identifiable, and the software tags four different stars instead of one. This can be attributed to the fact that AURIGA does not provide a procedure for the recognition of ring centers, but rather for points.

Mechanically, an insufficient focussing exists if the position of the CCD sensor deviates significantly from the position of the focal plane. The focus position of the Zenith Camera is not constant, since the materials of the MIROTAR lens are temperature-dependent. From investigations with the old analog Zenith Camera TZK3, it is known that the correlation between focus position and temperature is nearly linear (Bürki [1989]). Also Käker [2003] and Hirt [2004], respectively, determined an approximately linear function for the TZK-D, which possesses a MIROTAR lens, too. The adaption of the instrument to the ambient temperature might provoke a significant change of the focus during an observation night. This characteristic requires a permanent control of the focus before and during an observation aiming at the provision of high-quality images for the subsequent data analysis.

Experimental set-up

The fact of a functional temperature-focus-correlation can be used for an automatic adaption of the focal position depending on the ambient temperature. In order to investigate this function, extensive observations have been deployed under different temperatures (Rööslı [2006]). Starting from a clearly defocussed position (ring-shaped stars), the focal plane has been moved incrementally by steering a focus motor. At each position, an image has been exposed, and the corresponding focus position has been read in from a digital caliper equipped with a serial interface. Furthermore, the temperature has been registered. For this purpose, two independent measuring systems have been used: the temperature sensors implemented in the Lippmann tiltmeters as well as data from the AGNES GPS station on the roof of the HPV building (GGL offices). The focus position has been changed until the point of best-focussing has been clearly overrun and the

stars showed again a ring-shaped character. In order to determine the optimum focal position for a defined temperature, all images as well as corresponding focus positions and temperatures have been analyzed in a subsequent process. In case of uncertainties in the definitive determination of the best image, the two neighboring pictures have been chosen, and the corresponding position has been averaged.

Determination of temperature-focus-relation

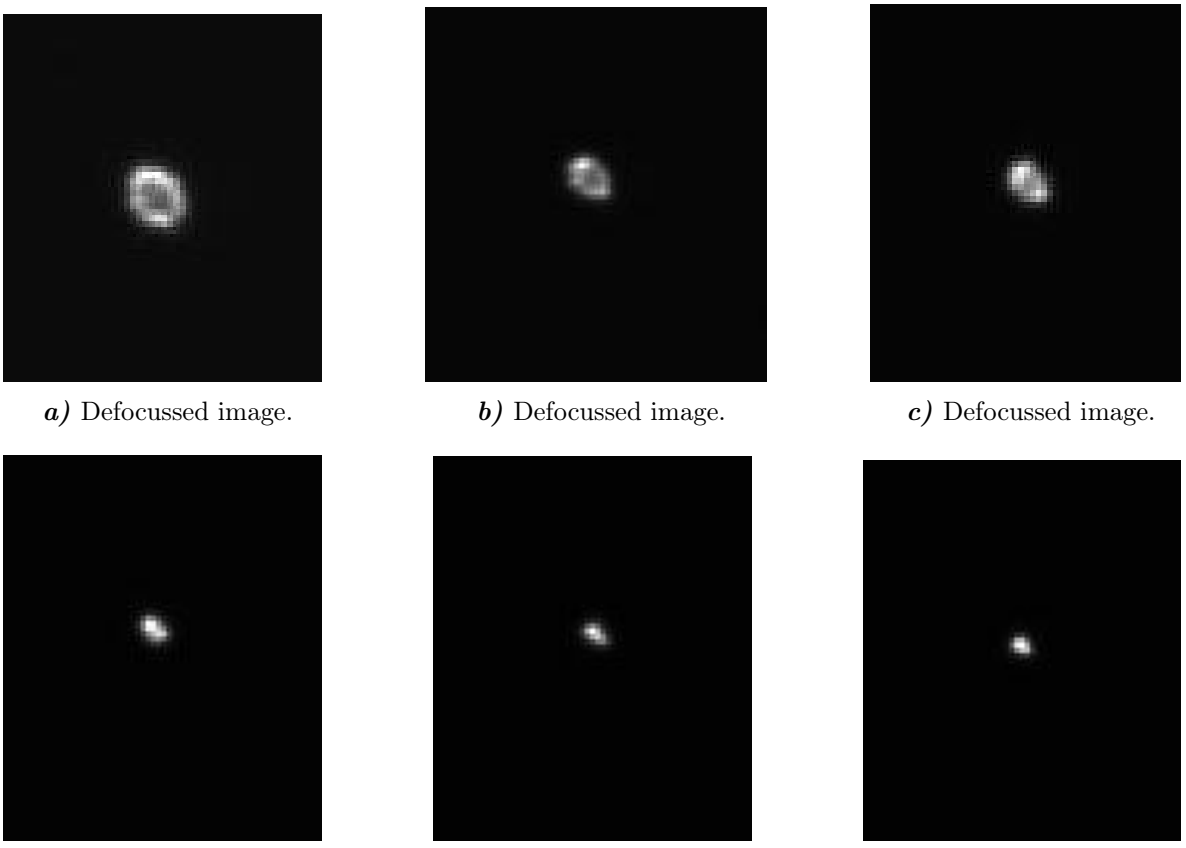

a) Defocussed image.

b) Defocussed image.

c) Defocussed image.

d) Transition from defocussing to focussing.

e) Transition zone from defocussing to focussing.

f) Focussed image.

Figure 4.20: Examples for clearly defocussed images (Imgs. 4.20***a)*** to 4.20***c)***) and a perfectly focussed image (Img. 4.20***f)***). The exposure time is 0.3 s. The ring-shaped form of a star is a typical sign for a defocussing of the images. The better the focal position is adapted, the more point-shaped becomes the star.

The images in Fig. 4.20 represent stars exposed with 0.3 s according to the typical exposure time used for a DIADEM observation. In case of a good focussing, the stars should be sharply point-shaped. Exposure times longer than 0.5 s produce incrementally line-shaped star traces. The examples demonstrate the impact of a bad focussing on a star: Images 4.20***a)*** to 4.20***c)*** are completely defocussed, recognizable from the ring-shaped form of the star. This might provoke misinterpretations during the process of star detection and image coordinate determination concerning the center of the star. The two following images 4.20***d)*** and 4.20***e)*** show a clearly better approach to the focus position: the star trace becomes more and more point-shaped. However, they still show

a slight longish character. Image 4.20***f)*** finally represents a well-focussed image as it can be used for the data analysis. It is interesting to see that the better the focal adaption, the less pixels are covered by the star.

The focus position F and temperature T corresponding to the best-focussed image of a series are plotted in Fig. 4.21. As visible from the diagram, the functional relation between temperature and focus position is nearly linear, with a coefficient of determination of 0.89 (squares = ambient temperature) and 0.70 (points = instrument temperature), respectively. It means that in case of the ambient temperature about 89 % of the function pairs (F,T) are linearly correlated. Referring to the ambient temperature-focus-function, the ascent of the straight line has been determined with **0.04 mm per K**. The absolute value of 3.61 mm refers to the zero-point of the focus, which is arbitrarily defined. In case of reconstruction works and the removal of the CCD camera, this position has to be redetermined.

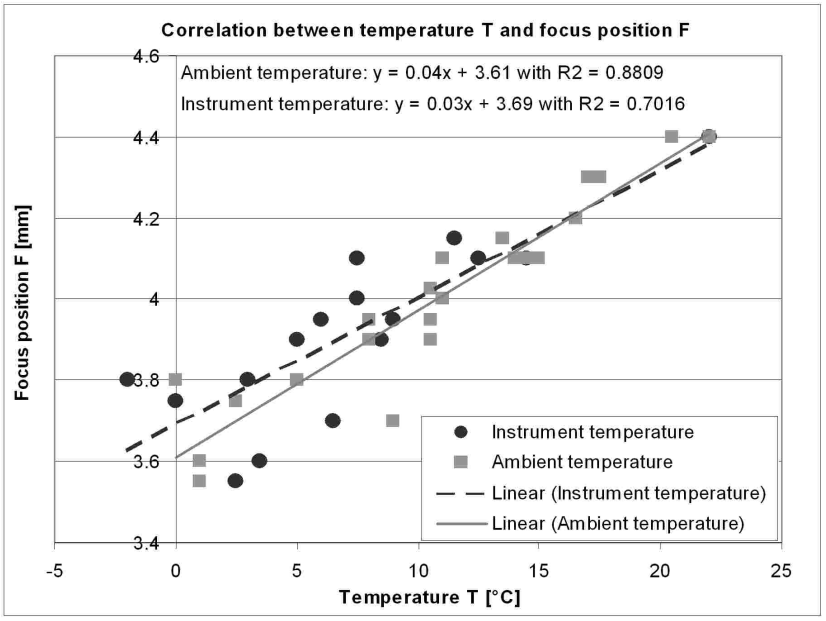

Figure 4.21: Focus-temperature-diagram. The best-focussed image has been determined by a visual evaluation. The corresponding temperature T and focus position F, respectively, have been plotted in the diagram. The squares represent the function corresponding to the ambient temperature, whereas the points refer to the instrument's temperature. As visible, both functions show a relatively good correspondence, especially with regard to the respective ascents of the regression lines.

The factor of 0.04 mm per K has been used in following DIADEM observations and produced convincing results. At the beginning of an observation, the temperature change between last and actual observation night is registered and transformed into a relative value representing the demanded position change. The quality of the focus is visually controlled by exposing an image. Generally, the focus was well-adapted after 1-2 iterations. During an observation, the focus is adapted automatically if the temperature change exceeds a defined limit. As the resolution of the dial counter amounts to 0.01 mm, an adaption of the focus is possible after a temperature change of 0.25K. However, according to the error analysis described in chapter 5.2.1, the astrometric accuracy

remains relatively constant until a defocussing of about 0.1 mm (Fig. 5.3) referring to a temperature change of about 2K. This agrees well with practical experiences, where an adaption of the focus becomes necessary after a temperature change of about 2K to 3K. Therefore, an automatic adaption of the focus is suggested if the temperature change exceeds this value.

5 Error analysis

5.1 Introduction

The thorough error investigation of DIADEM forms an important part of the instrumental evaluation. As regards the digital Zenith Camera, five error groups can be defined (Käker [2003], Hirt [2004]) representing potential "weak points" of the system:

- **Determination of the rotational direction:** Errors in the determination of the rotational direction $(\Phi, \Lambda)_D$ are mainly induced by a) errors in astrometry (stochastical character) and b) external errors (systematical character). Chapter 5.2.1 is concerned with the astrometric quality, which is mainly influenced by scintillation effects, the accuracy of image coordinate determination and the accuracy of the star positions extracted from the star catalog. The information presented there refer to investigations and conclusions in Hirt [2004]. They are largely assumable for the DIADEM system, as the same software package (AURIGA, see chapter 4.2) is used for the analysis of DIADEM and TZK2-D observations, respectively. Chapter 5.2.2 treats the problem of refraction representing an important systematical external error.
- **Inclination measurements:** The quality of inclination measurements plays a fundamental role in the determination of the direction of the vertical with a Zenith Camera. Deviations from a vertical alignment of the instrument have to be permanently registered during an observation. In order to provide redundant inclination information, two pairs of highly-precise inclination sensors are orthogonally mounted on DIADEM (chapter 3.2.4 and 3.2.5). They establish the relationship between the direction of the rotational axis of the instrument $(\Phi, \Lambda)_D$ and the direction of the vertical (Φ, Λ). Errors in the inclination data directly influence the astronomical parameters (Φ, Λ). The issue is that, on the one hand, the inclination sensors are erroneous and limited by their technical features (sensor noise, characteristics of the zero-point offset and hysteresis). These qualities are discussed in chapter 5.3.1. On the other hand, the inclination sensors are subject to external influences. Hence, the pendulars of the sensors are sensitive to anomalous horizontal accelerations, hence producing a signal although the inclination of the Zenith Camera did not change. Such effects are caused by microseismics and described in chapter 5.3.2. At last, uncertainties caused by the measuring process might influence the accuracy of inclination measurements, too. In this context, the azimuthal turning for an observation in two positions is analyzed in chapter 5.3.3.
- The remaining error sources comprise the determination of **observation epoch**, **azimuthal correction parameters** and **geodetic position**. They are discussed in the chapters 5.4, 5.5 and 5.6, respectively.

5.2 Determination of the rotational direction

5.2.1 Astrometry

Astrometric accuracy

In order to estimate the astrometric accuracy, the standard deviation s_{xy} can be determined by means of the residuals (v_x, v_y) resulting from the transformation between image coordinates $(x, y)_i$ and plane reference coordinates $(\xi, \eta)_i$. Furthermore, the number of stars identified (n) as well as the number of transformation parameters (u=4) are necessary:

$$s_{xy} = \sqrt{\frac{\sum v_x^2 + \sum v_y^2}{2n - u}} \tag{5.1}$$

The standard deviations (s_x, s_y) for separate directions (x, y) result from (Berry and Burnell [2000]):

$$s_x = \sqrt{\frac{\sum v_x^2}{\frac{1}{2}(2n-u)}} \qquad s_y = \sqrt{\frac{\sum v_y^2}{\frac{1}{2}(2n-u)}} \tag{5.2}$$

Scintillation

Scintillation can be divided into intensity and directional scintillation depending on origin and source. Intensity scintillation is caused by density variations in air films in several kilometers elevation yielding fluctuations of the star light intensity. However, for astrometric observations, the directional scintillation has more significance. It can be understood as the deflection of a star from its mean position caused by refractivity changes in atmosphere. It is mainly induced close to ground level. The observed "motion" of the star is correlated with neighboring stars in the field-of-view (FOV) of the objective (Winter [1999]). The mean amplitude of directional scintillation σ_0 depends on many conditions, as e.g. the epoch of observation (time of day, season), weather (air convections, temperature), observation point, local features (ground, vegetation) as well as the aperture angle of the telescope. Most papers concerned with this subject (e.g. Zacharias [1996], Winter [1999]) assume that the directional scintillation shows a mainly stochastical character, hence producing a stochastical error σ_{ds} within the astrometric error budget:

$$\sigma_{ds} = \sigma_0 \cdot t^{-0.5} \;\; (if\, t \geq 1\, s) \tag{5.3}$$

It is visible from Eq. (5.3) that the longer the exposure time t, the more the stochastical error σ_{ds} decreases. In literature, the specification of σ_0 varies between 0.05 arcsec and several arcsec. This spread shows the complexity of the phenomenon, mainly attributed to the diversity of involved factors. Hirt [2004] estimated potential amplitudes of the

directional scintillation for the TZK2-D by transforming two photos with nearly identical star fields into each other. As no star catalog is used as reference, the residuals directly indicate errors in the image coordinate determination (see next section) as well as the impact of directional scintillation. Due to similar instrumental features and mostly similar conditions (exposure times between 0.3 and 1 s, observations into zenith, night observations etc.), the results can be approximately assigned to DIADEM observations. After Hirt [2004], the mean amplitude does not exceed a few tenths of 1 arcsec with slight variations due to changing conditions in observation. Generally, between 40 to 80 images are exposed at one station. The average of the direction of the vertical can be largely regarded as scintillation-free.

Determination of image coordinates

Method. As mentioned in the section *Scintillation*, the residuals resulting from a transformation of two pictures into each other contain also a hint on the accuracy of the image coordinate determination. The comparison of the two methods for coordinate determination implemented in AURIGA (*segment center determination* and *PSF method* see chapter 4.2) resulted the following: The method of segment center determination provides an accuracy of 0.3 arcsec to 0.5 arcsec referring to 0.15 Pixel and 0.25 Pixel, respectively. The PSF method is about 1.5-times more precise offering an accuracy of about 0.2 arcsec to 0.3 arcsec.

Apparent brightness. The accuracy of both methods also depends on the signal-to-noise ratio, which is correlated with the apparent brightness of a star. Stars with a very low signal-to-noise ratio, as given for faint stars with a mag of 12 to 14, indicate a significantly reduced accuracy compared to brighter stars (mag 8-12).

Exposure time. Due to the fact that the Zenith Camera is a fixed system without any tracking mechanism, the earth's rotation is affecting the form of the star images: Already an exposure time of ≥ 0.5 s produces a longish instead of a point-shaped form. The analysis of the accuracies in lateral (s_x) and longitudinal (s_y) direction of a star revealed a clear effect on s_y: for exposure times lasting longer than 1 s, the accuracy decreases significantly (Fig. 5.1) indicating a two times worse accuracy for an exposure time of 1.6 s than for exposure times between 0.2 s and 1 s. In contrast, the lateral direction is not significantly affected by the exposure time.

These results are also reproducible in relation with the internal accuracy of the astronomical coordinates (Φ, Λ): the longer the exposure time, the worse the standard deviation of Λ (Fig. 5.2). However, there is no significant debasement in Φ (Müller [2002]).

It can be concluded that the optimum exposure times for an observation with DIADEM ranges between 0.3 s and 0.5 s, hence providing the conditions for a high-quality image coordinate determination.

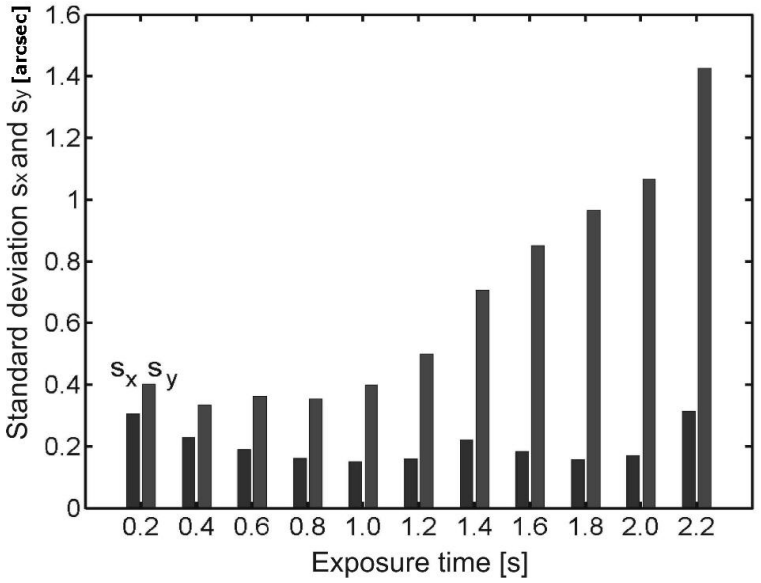

Figure 5.1: Astrometric accuracies (s_x, s_y) depending on exposure time (Hirt [2004]). It is well recognizable that the exposure time only influences the standard deviation s_y, measured in direction of longitude Λ. This is caused by the fact that the star trace becomes increasingly longish due to the earth's rotation.

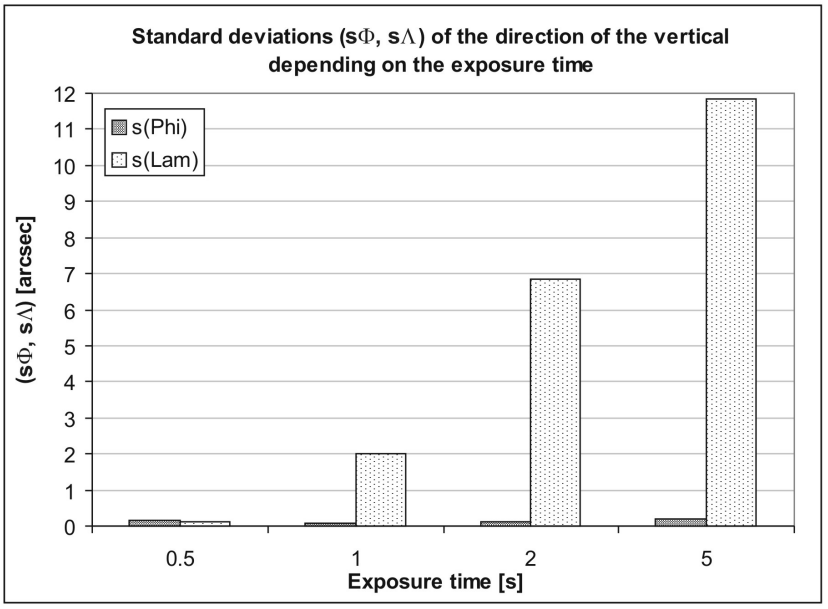

Figure 5.2: Standard deviations (s_Φ, s_Λ) of the astronomical parameters depending on exposure time. The internal accuracy of Λ decreases with increasing exposure time.

Focussing. In chapter 4.4.4, it has been shown that a bad focussing induces problems in the detection of the stars imaged (see Fig. 4.19). Thus, it might happen that AURIGA detects more than one center within a star trace. It is easily to understand that these errors influence significantly the accuracy of the coordinate determination resulting in large residuals after the transformation. Due to the criteria defined in Eq. (4.13), residuals greater than 10 arcsec are interpreted as detection errors and excluded from the process of data reduction. However, remaining detection errors cause a reduced quality

in the coordinate determination.

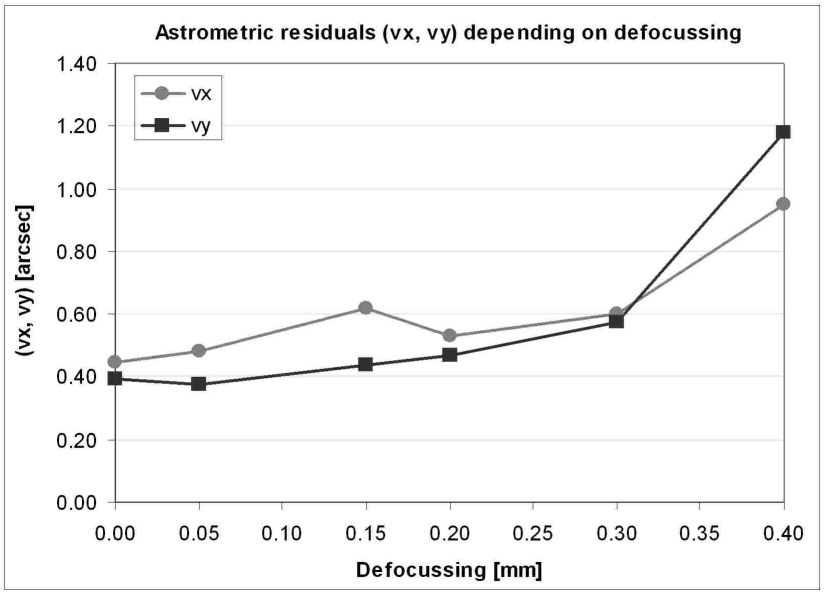

Figure 5.3: Astrometric residuals (v_x, v_y) depending on defocussing. The more the images are defocussed, the larger the residuals.

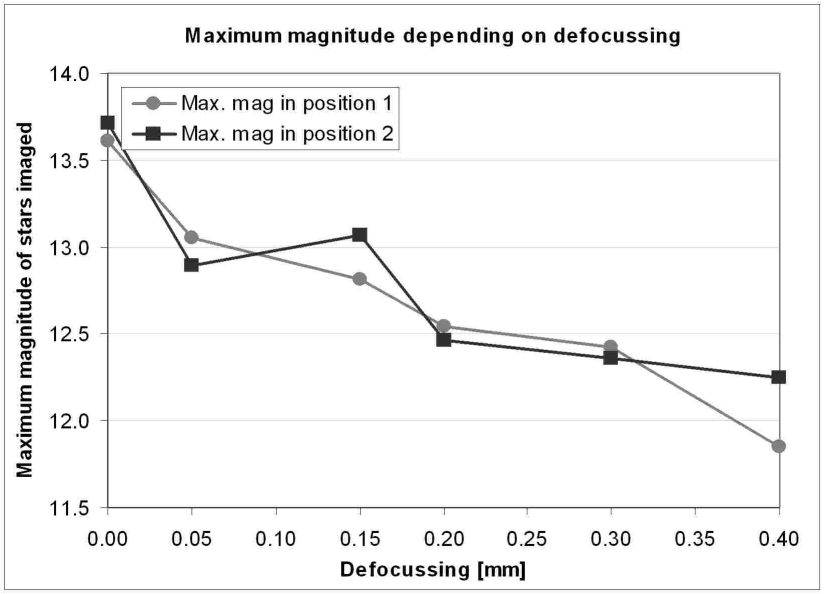

Figure 5.4: Maximum magnitude of stars imaged depending on defocussing. The more the images are defocussed, the smaller the magnitude. Very faint stars with a magnitude of 13 can only be observed, if the focus is nearly perfect adjusted.

A dedicated investigation aimed at estimating the impact of defocussing on the astrometric residuals (v_x, v_y), the maximum magnitude of stars observable and the standard deviations (s_ξ, s_η) of the deflections of the vertical. Therefore, the focussing has been intentionally debased in 0.05 mm steps. At each focus point a series of 30 single solutions has been observed. The analysis revealed the following: Until a defocussing of about 0.1 mm (measured in direction of the optical axis), the astrometric standard deviation remains constantly (Fig. 5.3). After that limit, the defocussing produces increasing astrometric

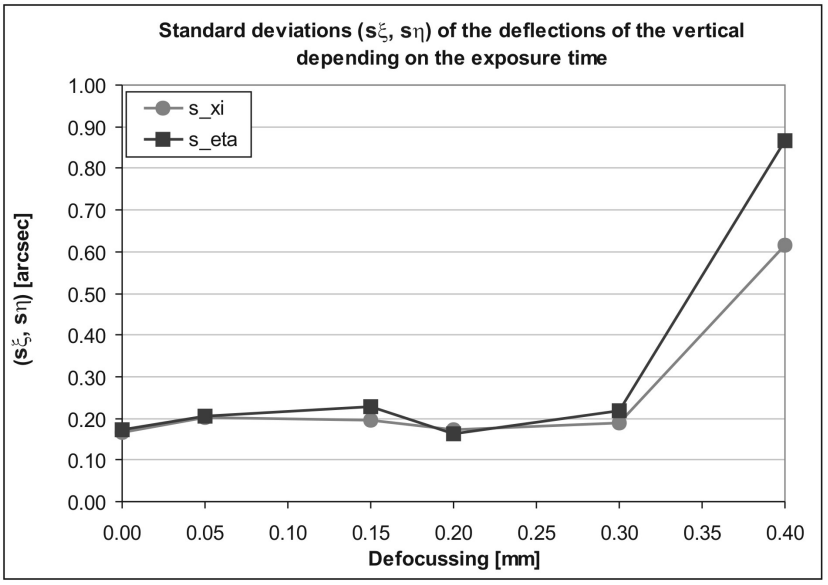

Figure 5.5: Standard deviations (s_ξ, s_η) of the deflections of the vertical depending on defocussing. They remain constantly until a defocussing for about 0.3 mm. After that they increase significantly.

residuals (v_x, v_y) indicating 1.5-times larger residuals for a defocussing of 0.3 mm. Also the maximum magnitude of observable stars decreases significantly with increasing defocussing (Fig. 5.4). Very faint stars with a magnitude of 13 are only observable if the focus is perfectly adjusted. In spite of the demonstrated significance of a proper focussing within a narrow range, a defocussing up to 0.3 mm does not influence the standard deviations (s_ξ, s_η) of the DOV. Up to this range, s_ξ and s_η remain relatively constant at a level of 0.2 arcsec (Fig. 5.5). First a defocussing for more than 0.3 mm is reflected in a clear debasement of the internal accuracy. This can be attributed to the fact that stars with residuals above a defined threshold are excluded from the calculation of the rotational direction $(\Phi, \Lambda)_D$.

Reference stars

Star catalogs. Systematical errors in the coordinates of the reference stars directly affect the result of the direction of the vertical (Φ, Λ). The star catalogs implemented in AURIGA are the Tycho-2 (chapter 2.2.2) and the UCAC (chapter 2.2.3). Zacharias et al. [2000] compared the Tycho-2 with the first generation of the UCAC, the UCAC1. Both catalogs refer to the Hipparcos system and, hence, to the International Celestial Reference System (ICRS). The analysis has been performed on the basis of about 597809 common stars finding only small systematical differences in position (up to 0.015 arcsec), mainly correlated with the magnitude of the stars. These systematics are not significant for the determination of (Φ, Λ). Furthermore, Hirt [2004] verified the accuracies given for Tycho-2, UCAC2 and UCAC3 (provided by USNO prior to publication). The resulting standard deviation of about 0.06 arcsec for the coordinate differences is within the expected range (Zacharias et al. [2000]). The influence of an analysis with Tycho-2 and UCAC2, respectively, on the determination of (Φ, Λ) revealed only small differences within 0.02 arcsec, and is, therefore, negligible.

Calculation of apparent star positions. Errors in the transformation of mean into apparent star positions (chapter 2.2.4) caused by problems in the reduction process can be excluded, since they amount to maximum 0.005 arcsec. This statement is based on the comparison of the AURIGA reduction formulas with different implementations, as e.g. NOVAS-C, Astro-Toolbox (Hirt [2004]).

5.2.2 Refraction

Radial-symmetric refraction

The radial-symmetric refraction describes the directional changing of a light beam crossing different atmospheric layers with individual refraction indices. This causes an apparent lifting of the star in direction to the zenith, hence observing the star under a reduced zenithal distance. The directional changing depends on the zenithal distance and can be described by (Gessler [1975]):

$$R_Z = 58.206“ \cdot \tan z - 0.068“ \cdot \tan^3 z \tag{5.4}$$

The maximum zenithal distance observable with DIADEM is 0.95° according to the FOV of DIADEM of 1° x 1.5° (chapter 3.2.3). The small value allows to neglect the second term in Eq. (5.4) and, furthermore, to equate term $\tan z$ by z. Hence, the impact of refraction on the zenithal distances and, therewith, on the image coordinates of the stars can be regarded as nearly linear. Since a linear effect is supported by the scale factor m (Eq. (4.14)), determined within the process of data reduction (chapter 4.2), there is no need for a further numerical consideration.

Anomalous refraction

In contrast to the radial-symmetric refraction, the anomalous refraction is considered to be a critical factor in the error budget of Zenith Cameras. It describes effects caused by the inclination of atmospheric layers (Ramsayer [1970]), hence generating a directional shifting of the whole star field. The effect of anomalous refraction has been the subject of many recent publications in astronomy (e.g. Stone et al. [1996], Pier et al. [2003] and Hirt [2006]), hence demonstrating the significance of this error source. It is an approved fact that the amplitude of anomalous refraction is very difficult to estimate. Especially, time-dependent variations of the amplitude are still less investigated (Hirt [2006]). The error falsifies the measured direction of the vertical (Φ, Λ) as well as the deflections of the vertical (ξ, η). The origin and impact of anomalous refraction can be divided into two phenomena:

- **Regional phenomenon**: This phenomenon is caused by the inclination of atmospheric layers resulting from horizontal temperature and pressure gradients. Changing weather conditions indicated by the passage of cold or warm weather fronts might have a significant influence on the actual refractivity (Bürki [1989]).
- **Local phenomenon**: This phenomenon occurs close to steep hillsides and mountains, causing the inclination of atmospheric layers close to the ground (Chesi [1984]).

The problem is that the impact of anomalous refraction can not be determined by a single observation at one station. First the comparison of night means determined in different nights might help to estimate the amplitude of refraction. Also simultaneous long-time observations with two Zenith Cameras might be helpful, hence allowing to detect the impact of changing weather conditions and related potential refractivity changes.

Based on results from the campaign in Switzerland in 2005 with two Zenith Cameras, it has been attempted to estimate the influence of anomalous refraction on Zenith Camera observations. The results are described and discussed in chapter 6.3. It can be already anticipated that the data did not allow for convincing statements concerning the amplitude of anomalous refraction. It has been concluded that an influence exists, though, it is very small and superposed by the normal measuring noise. The estimated dimension of maximum 0.1 arcsec is in accordance with the maximum impact of 0.2 arcsec indicated by Hirt [2006].

5.3 Inclination measurements

5.3.1 Sensor qualities

General remarks

Both types of inclination sensors, the Lippmann 1/2 as well as the Wyler sensors 1/2, respectively, have been investigated in the climate chamber of the institute. They were mounted in parallel on a table within the chamber registering permanently the inclination during about four days. While the Wyler sensors sampled with a low rate of 2 Hz, the Lippmann sensors operated within a high-frequency range of 1000 Hz. The goal of the investigation was to validate the manufactory's information concerning the precision of the inclination sensors and, furthermore, to analyze their long-time stability under different temperature conditions. Therefore, the temperature in the climate chamber has been varied between 24°C and -10°C (Fig. 5.6). In the following, the results of the investigation are discussed separately for both types of inclination sensors.

Wyler inclination sensors

Fig. 5.8 represents the long-time behavior of Wyler sensor 1 during 80 hours. The signal varies within a large range of -150 arcsec to 10 arcsec. Since inclination fluctuations of the table can be excluded, the variations are potentially caused by instabilities of the zero-point of the sensor. The comparison with the temperature (Fig. 5.6) reveals a strong correlation, since the sensor signal shows exactly the same course of a stepwise decrease and increase like the temperature. Hence, a temperature change of -10°C induces an according offset drift of about -40 arcsec.

Fig. 5.9 represents the Wyler signal during the first 24 hours of the investigation. A strong decrease of the inclination signal from 8 arcsec to 0 arcsec is clearly recognizable and corresponds well to the temperature adaption during these 24 hours (Fig. 5.7). The amplitude spectrum of the 24h-signal is shown in Fig. 5.10***a)*** with a zoom into the

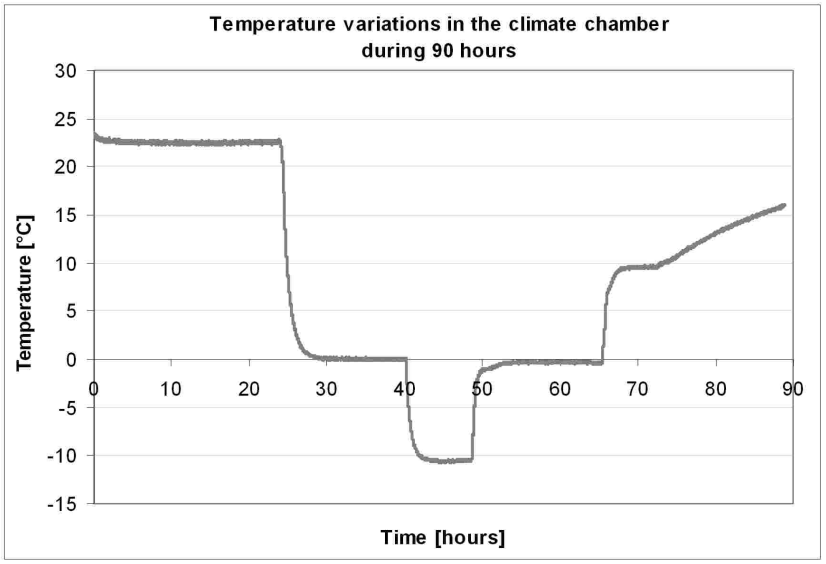

Figure 5.6: Temperature variations between 24°C and -10°C in the climate chamber of the institute. The investigation lasted for about 90 hours.

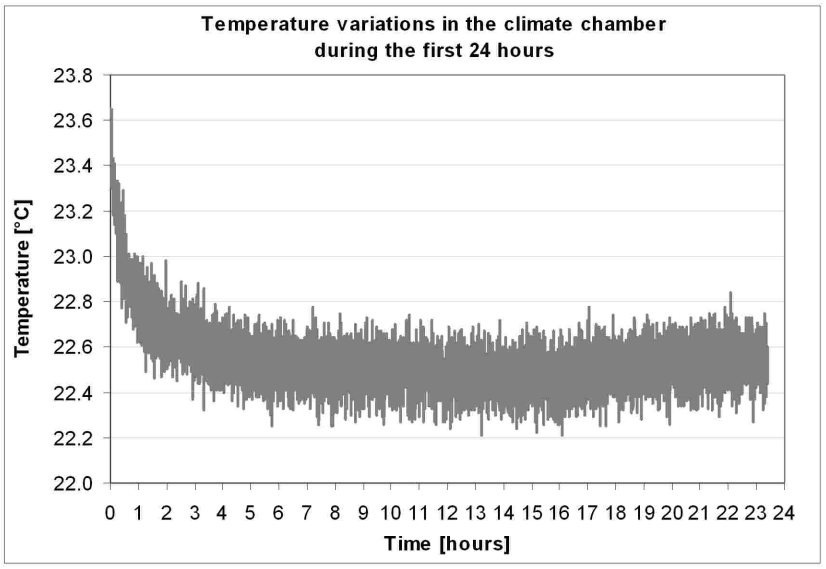

Figure 5.7: Adaption of the temperature within the first 24 hours of the investigation. The temperature adaption in the beginning took about 6 hours.

frequency range 0 Hzz to 0.2 Hz (Fig. 5.10***b)***). The low frequencies up to 0.1 Hz reveal relatively large amplitudes with a maximum of 0.2 arcsec at a frequency of 0.02 Hz, while from 0.1 Hz on the amplitudes are constantly low ($\leq$0.01 arcsec). Most probably, the emphasis in the low-frequency range corresponds to the temperature-dependent offset drift. In order to eliminate these frequencies, a high-pass filtering with a limit frequency of 1 Hz has been performed (Fig. 5.11). Due to the low sampling rate of 2 Hz, anthropogenic microseismics (chapter 5.3.2) can not be detected within the filtered signal. Hence, it has been concluded that the high-pass filtered signal contains a reference to the effective sensor noise expressing the internal accuracy of the Wyler sensors. The standard deviation of these data amounts to 0.15 arcsec, which corresponds to the manufactory's information (Wyler [2007]).

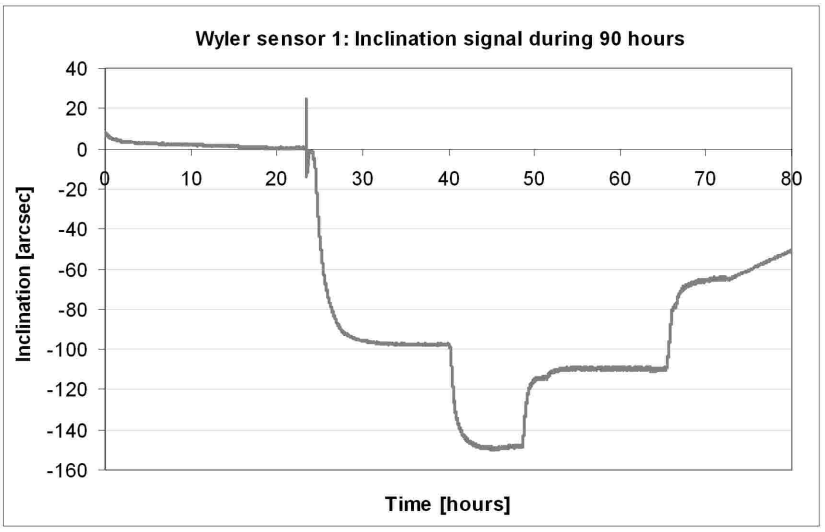

Figure 5.8: Inclination signal of the Wyler sensor 1 during 80 hours. The signal shows strong variations between 10 arcsec and -150 arcsec, mainly caused by instabilities of the zero-point. A correlation with the temperature is obvious (compare Fig. 5.6).

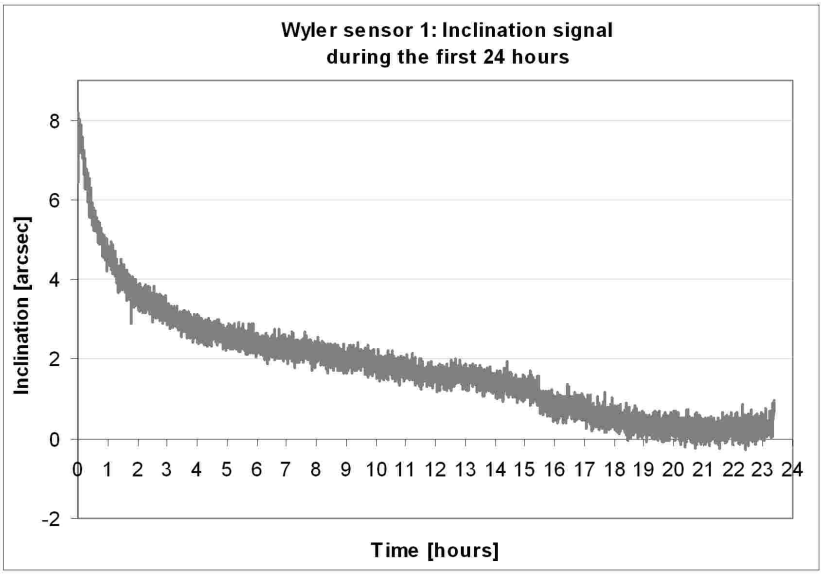

Figure 5.9: Inclination signal of Wyler sensor 1 during 24 hours, with a well recognizable drift from 8 arcsec to 0.5 arcsec.

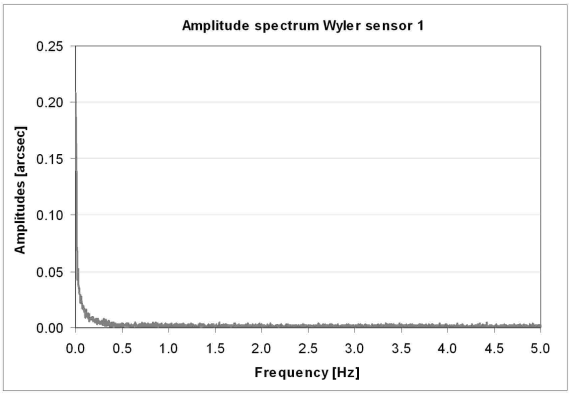

a) Amplitude spectrum within a frequency range of 0 Hz to 5 Hz.

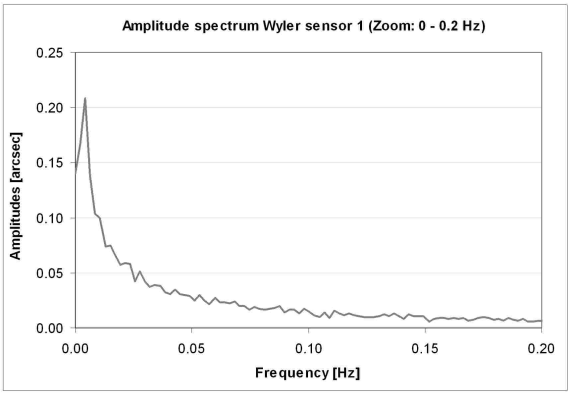

b) Zoomed amplitude spectrum within the range of 0 Hz to 0.2 Hz, with a maximum of 0.2 arcsec at 0.02 Hz.

Figure 5.10: Amplitude spectrum of Wyler sensor 1.

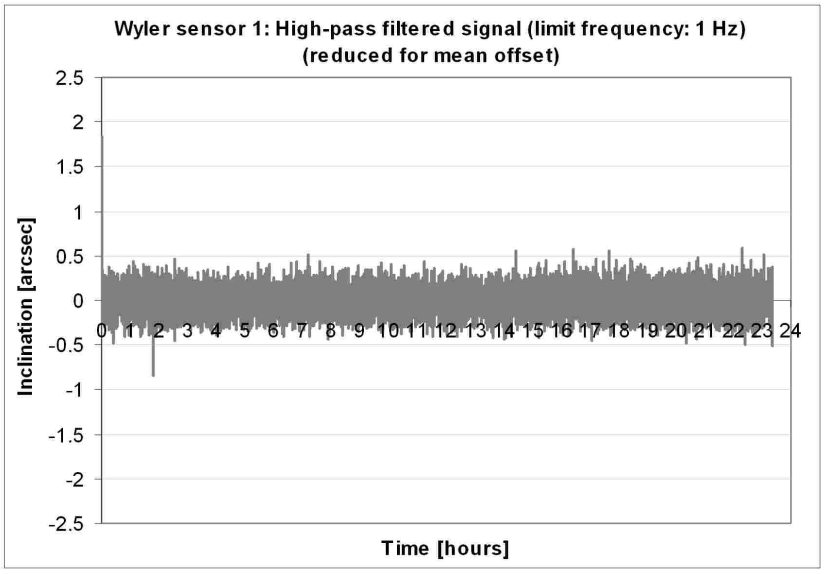

Figure 5.11: High-pass filtered signal of Wyler sensor 1 with a limit frequency of $\geq$1 Hz. Due to the maximum sampling frequency of 2 Hz, the influence of anthropogenic microseismics can not be reconstructed. It is assumed that the filtered signal largely represents the sensor noise.

Lippmann inclination sensors

The long-time inclination signal of Lippmann sensor 1 is represented in Fig. 5.12. The observable variations are significant smaller than those of the Wyler sensor, but even so in a range between 20 arcsec and 35 arcsec. Although the changes between different temperature levels are identifiable by an amplified signal noise, a clear functional relation between signal and temperature can not be derived (Fig. 5.6). However, a focus on the first 24 hours of the investigation might suggests another conclusion. If comparing Fig. 5.13 representing the inclination signal with Fig. 5.7 showing the temperature adaption during 24 hours, a correlation seems to be apparent.

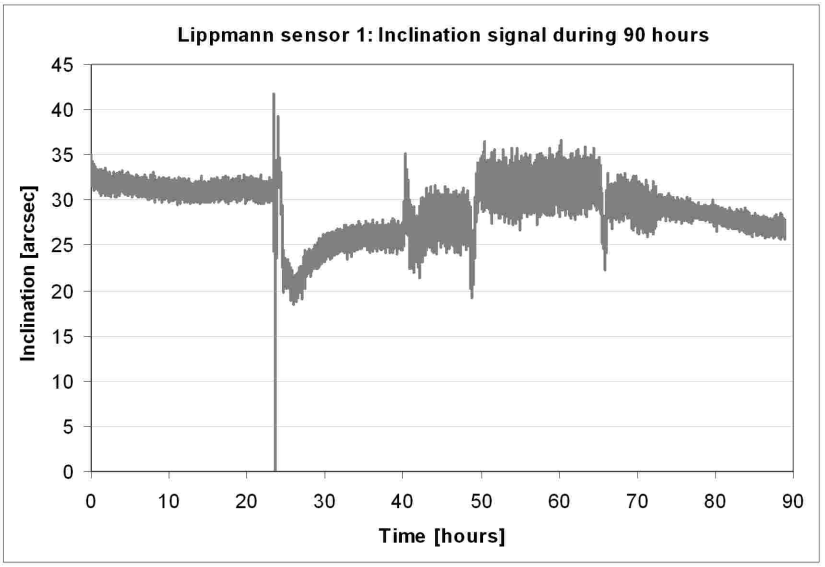

Figure 5.12: Inclination signal of Lippmann sensor 1 during 90 hours. The different temperature levels (compare Fig. 5.6) are identifiable by an amplified signal noise.

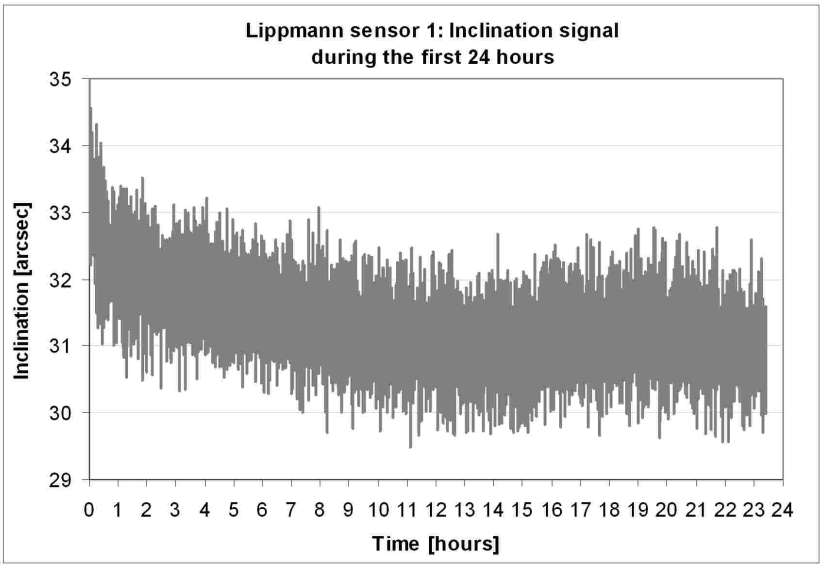

Figure 5.13: Inclination signal of Lippmann sensor 1 during 24 hours, with a drift from about 33 arcsec to 31 arcsec.

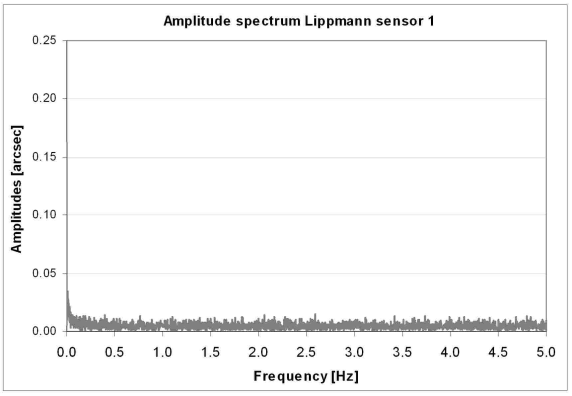

a) Amplitude spectrum within a frequency range of 0 Hz to 5 Hz.

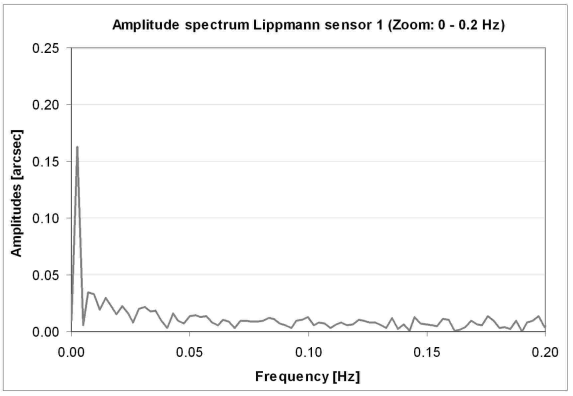

b) Zoomed amplitude spectrum within the range of 0 Hz to 0.2 Hz, with a maximum of 0.16 arcsec at 0.02 Hz.

Figure 5.14: Amplitude spectrum of Lippmann sensor 1.

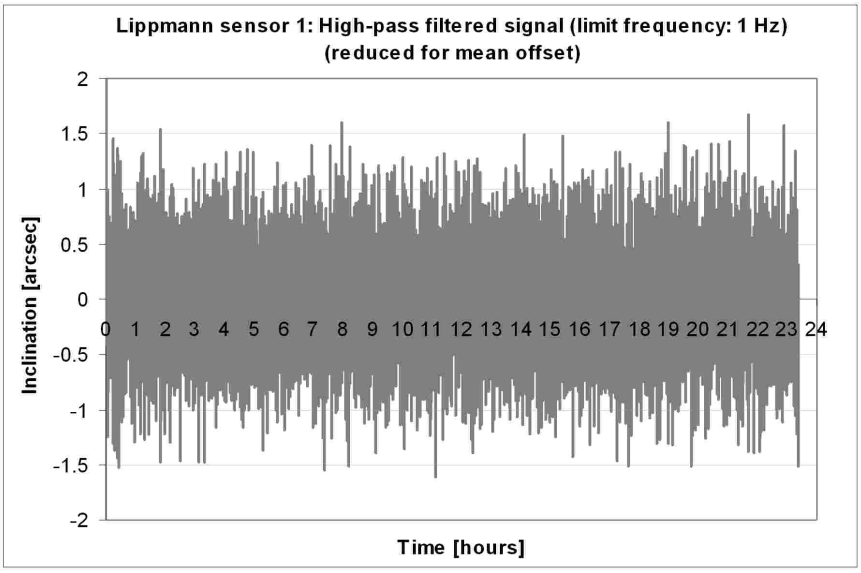

Figure 5.15: High-pass filtered signal of Lippmann sensor 1 with a limit frequency of $\geq$1 Hz. The visible noise is probably a superposition of anthropogenic microseismics ($\geq$1 Hz) and sensor noise.

The analysis of the amplitude spectrum of the 24h-Lippmann signal confirms this assumption (Figs. 5.14***a)*** and 5.14***b)***). Similar to those of the Wyler signal, it reveals a maximum amplitude of 0.16 arcsec at a frequency of 0.02 Hz. The high-pass filtered signal (limit frequency = 1 Hz) still shows strong undulations within a range of -1.5 arcsec and 1.5 arcsec and a standard deviation of 0.5 arcsec (Fig. 5.15). It reflects a superposition of anthropogenic microseismics ($\geq$1 Hz) and sensor noise. This is in contrast to the Wyler signal and can be attributed to the higher sampling rate (1000 Hz) of the Lippmann sensors.

The problem is that the interesting sensor noise can not be easily separated from the superposed microseismics within this frequency range. However, in order to enable a statement about the internal accuracy of the Lippmann sensor, the field investigations described in chapter 6.5 can be consulted. There, it has been demonstrated that an analysis with Lippmann instead of Wyler sensors improves the internal accuracy of the deflections of the vertical (ξ, η) for about 40%. As the accuracy of (ξ, η) is directly influenced by the quality of the inclination measurements, the factor 0.6 is here used to make a statement about the internal accuracy of the Lippmann sensors. According to this, the accuracy amounts to better than 0.1 arcsec.

However, it is assumed that the accuracy of the Lippmann sensors might be far better than derived from the above described experiment. This assumption is based on respective investigations in Hirt [2004], where the Lippmann tiltmeters used for the TZK2-D were analyzed by a dedicated mounting on the turning circle of the Zenith Camera. The sensors have been installed in parallel and not orthogonally, hence reflecting redundant information about the alignment of the instrument in one direction. This experiment allowed for more precise statements concerning the quality of the sensors. Based on the results of this investigation, Hirt [2004] indicated an accuracy of better than 0.05 arcsec.

5.3.2 Microseismics

Due to the fact that the inclination sensors are deployed in a dynamic environment, the inclination signal is potentially superposed by anomalous horizontal accelerations caused by microseismics. The frequencies induced depend on location and environmental conditions as it is well recognizable in Figs. 5.16***a)*** and 5.16***b)*** (Ganz [2007]).

Microseismics can be divided into two parts: *natural* and *anthropogenic* microseismics. Natural microseismics is e.g. induced by oceanic waves indicating typical frequencies between 0.1 Hz and 0.5 Hz with a maximum of 0.2 Hz to 0.3 Hz. Other natural factors are earthquakes, tides (earth and ocean), wind, variations of air pressure as well as variations of the temperature on ground caused by solar radiation. They are distinguished by very low frequencies $\leq$ 0.03 Hz. In contrast, anthropogenic microseismics is caused by human and artificial factors. Especially in urban regions, the anthropogenic part exceeds the natural one. Reasons are large industrial engines and road traffic generating horizontal accelerations with high frequencies $\geq$ 1 Hz (Klinge et al. [2002], Kahlmann [2003]).

Two examples of typical anthropogenic induced accelerations are represented by Figs. 5.16***a)*** and 5.16***b)***. They show the inclination signals registered by Lippmann sensor 1 during DIADEM observations at two different stations in the Swiss alps. The signals at both stations reveal high-frequency microseismic effects as it is also well recognizable in the respective amplitude spectra (Figs. 5.17***a)*** and 5.17***b)***). However, the amplitudes vary significantly. While station Hopflauen (Fig. 5.16***b)***) shows a strongly undulating signal within a range of -6 arcsec to 4 arcsec and a standard deviation of 1.8 arcsec, station Sustenpass (Fig. 5.16***a)***) reveals a relatively smooth signal. It varies between -3 arcsec and 3 arcsec with a standard deviation of 0.6 arcsec. The difference between both stations is attributed to the fact that the DIADEM station at Hopflauen was located near a power station, where an electric generator induced high-frequency noise with

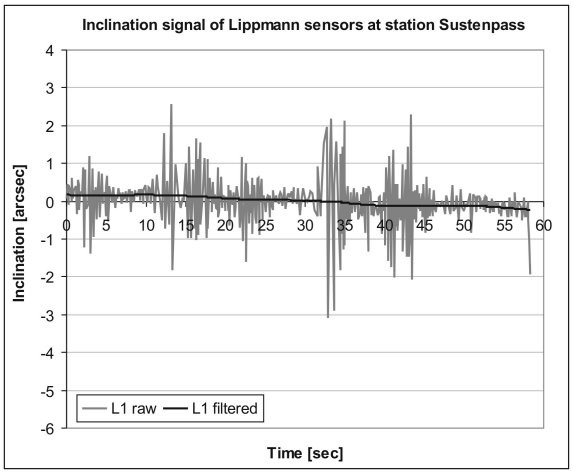

a) Inclination signal at station Sustenpass.

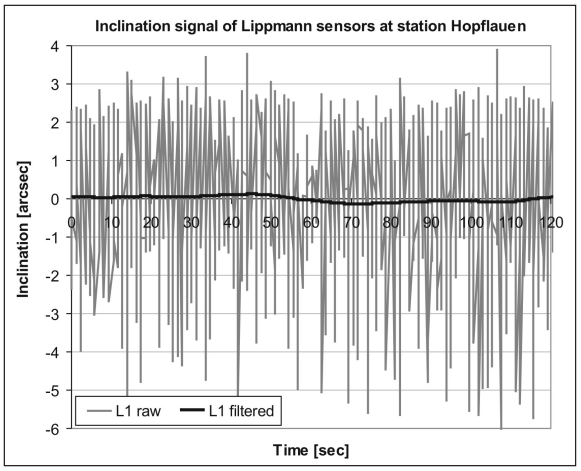

b) Inclination signal at station Hopflauen.

Figure 5.16: Raw (light gray) and filtered (black) inclination signals registered by Lippmann sensor 1 during DIADEM deployments at two different stations in the Swiss Alps: Sustenpass (left) and Hopflauen (right). It is striking that the signal at Hopflauen shows significantly larger amplitudes than the signal at Sustenpass. This is due to the different local feature of both stations. Hence, station Hopflauen was located near a power station generating large amplitudes within the high-frequency range.

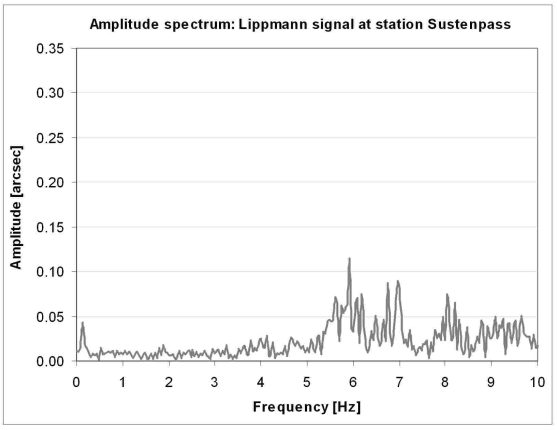

a) Amplitude spectrum at station Sustenpass.

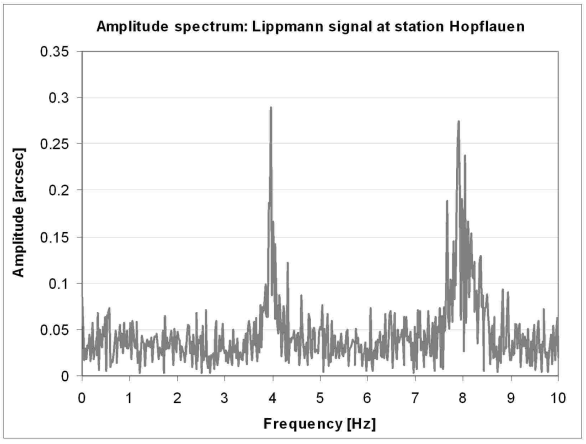

b) Amplitude spectrum at station Hopflauen.

Figure 5.17: Amplitude spectra of Lippmann signals at stations Sustenpass and Hopflauen (see Figs. 5.16***a)*** and 5.16***b)***). The comparison of the maximum amplitudes shows a significant difference amounting to about 0.1 arcsec at Sustenpass and to 0.3 arcsec at Hopflauen.

large amplitudes up to 0.3 arcsec at frequencies around 4 Hz and 8 Hz, respectively (Fig. 5.17***b)***). In contrast, station Sustenpass represents a calm location, which was clearly less influenced by anomalous factors. Hence, the amplitudes in the spectrum only amount to maximum 0.1 arcsec at frequencies between 5 Hz and 8 Hz (Fig. 5.17***a)***). Interestingly, both amplitude spectra show a peak at 8 Hz. This suggests the assumption that the resonance frequency of the inclination sensors might be within this range.

A technical way to reduce anomalous accelerations is the damping of the inclination sensor. The respective implementations of the technical features of the Wyler and Lippmann sensors are described in chapters 3.2.4 and 3.2.5, respectively. Mechanical damping units operate as low pass filter eliminating frequencies above a certain critical frequency (Ingensand [1985]). A mathematical damping can be realized by an integration over time intervals. Another possibility to reduce microseismic effects is the digital filtering of the inclination signals. Therefore, it is decisive, which frequency range is interesting for the signal analysis. For Zenith Camera observations, long-periodical fluctuations, e.g. caused by a slow subsidence of the ground, have to be detected within the signal. Accelerations above a dedicated limit frequency have to be eliminated, since they superpose the interesting information. A suitable filtering technique is provided by a FFT low pass filter. The implementation in the data acquisition software of the Zenith Camera is described in chapter 4.1.2.

A problem is, however, that microseismics also occurs in a low frequency range ($\leq$ 0.03 Hz). As already mentioned in chapter 4.1.2, frequencies smaller than the limit frequency can not be separated from the inclination signal. Consequently, subsequent inclination values can be highly-correlated and systematically affected or even falsified. The dimension of the remaining errors can not be estimated offhand, though, according to Hirt [2004], they should not exceed 0.01 arcsec. It is to be expected that the systematical error behaves stochastically (white noise) in long-time observations of at least 10 min as performed with DIADEM. The determined average of the direction of the vertical is then potentially error-free.

5.3.3 Azimuthal turning

A systematical deviation $\delta\alpha$ from a precise 180° turning takes, on the one hand, influence on the determination of the rotational direction $(\Phi, \Lambda)_D$. The problem has been thoroughly discussed, e.g. in Gessler [1975]. However, due to the algorithm implemented in AURIGA realizing the iterative determination of the rotational direction (chapter 4.2.5), the impact of this error on the accuracy of $(\Phi, \Lambda)_D$ can be disregarded. Hence, even significant deviations from a precise 180° turning do not have to be particularly considered. On the other hand, a systematical deviation $\delta\alpha$ influences significantly the determination of absolute inclination values. After Hirt [2004], the dimension of the impact can be estimated from formulas considering the shearing angle ε between the inclination sensors. The respective coordinate system is depicted in Fig. 4.11. Due to an imprecise turning, sensor 1 in position I measures the inclination value $\tilde{n}_1$, while the same sensor registers a too small inclination value $-\tilde{n}_1$ plus parts of the orthogonal inclination $\tilde{n}_2$ in position II:

$$n_1^I = \tilde{n}_1 \qquad n_1^{II} = \frac{-\tilde{n}_1}{\sin\varepsilon} - \frac{\tilde{n}_2}{\tan\varepsilon} \tag{5.5}$$

Based on Eq. (4.1), it follows than:

$$n_1 = \frac{(n_1^I - n_1^{II})}{2} = \frac{1}{2}\left(\tilde{n}_1 + \frac{\tilde{n}_1}{\sin\varepsilon} + \frac{\tilde{n}_2}{\tan\varepsilon}\right) \tag{5.6}$$

For an assumed inclination of $\tilde{n}_1 = \tilde{n}_2 = 10$ arcsec, and an exemplary deviation $\delta\alpha$ of 10 arcsec, it is $\varepsilon = 90° + (10\ arcsec/3600)$. With Eq. (5.6), n_1 amounts to 10.000315 arcsec instead of 10 arcsec, which is negligible. However, for a deviation of more than 400 arcsec ($= 0.01°$), the inclination value n_1 is significantly falsified for more than 0.01 arcsec. To avoid influences on the accuracy of the inclination corrections, new implementations in AURIGA consider the deviation $\delta\alpha$ within the calculation formulas for the absolute inclinations.

5.4 Epoch determination

The significance of an exact epoch determination has been mentioned several times within this thesis. According to Eq. (4.26), an epoch error of 0.1 s already produces an error in longitude Λ of about 1 arcsec (for the latitude of Zurich, $\varphi = 47.4°$). Aiming at a maximum influence of 0.01 arcsec on the direction of the vertical (Φ, Λ), the epoch should be determined with an accuracy of better than 0.7 ms (equator) and 1 ms (Zurich), respectively. The quality of an epoch determination with DIADEM is influenced by two main system components: a) the GPS receiver providing the absolute epoch in GPS time as response to the TTL signal of the CCD camera and b) the characteristic of the electronic blade shutter used in the CCD camera. According to the manufactory's information (u-blox, Switzerland, u-blox AG [2003]), the time mark accuracy of the GPS receiver is 0.2 ms and forms, therefore, a small part within the error budget. The shutter characteristic plays a more important role within the error budget. In chapter 4.4.3, the corresponding function has been determined. However, errors in modeling the shutter function can not be excluded offhand. The internal accuracy of repeated measurements concerning the determination of dedicated time intervals (e.g. to open and close the shutter) shows an internal accuracy of mostly better than 0.15 ms (see Tab. 4.4). The external accuracy of the shutter depends on several residual systematics, which might occur during the performance of the shutter investigation. Thus, an error caused by a slight misalignment of the laser at the points specified on the CCD sensor (Fig. 4.14) has to be taken into account. Furthermore, an error referring to the approximation of the shutter blades by a radial diaphragm can be estimated from the redundant information of points p2-p5 (edges of the sensor). Also the supposed correction formula has to be considered in the error budget, since it forms an average equation for all stars imaged (Eq. (4.30)). Finally, the temporal resolution of the oscilloscope of 0.1 ms plays a small role, too (Käker [2003] and Hirt [2004]). An estimation of the respective contributions to the error budget yielded a total error of about 1 ms, which corresponds to the defined error limit.

5.5 Azimuthal corrections

The method of azimuth calibration has been described thoroughly in chapter 4.4.1. A non-consideration of the calibration parameters r and γ produces an azimuth-depending radial deviation of the rotational direction from the true direction of the vertical. In case, the once determined calibration parameters are regarded as constant corrections and applied accordingly to all stations, the error of the rotational direction might amount to about 0.2 arcsec. This is attributed to the high variability of both parameters. Therefore, an azimuth calibration has to be conducted at each station. However, also the determined correction parameters r and γ itself can not be considered as free of variances. According to the logging file compiled during the analysis of an azimuth calibration (with AURIGA), the radius r indicates a mean standard deviation σ_r of about 0.05 arcsec, while the orientation angle γ shows a mean standard deviations of σ_{gamma} of 0.8°. According to the error propagation law applied to Eq. (4.18), the standard deviation of $\Delta\Phi_a, \Delta\Lambda_a$ amount to 0.05 arcsec. These estimations show the significance of the newly introduced tripod method, also described in chapter 4.4.1. Hence, a quality reduction of the direction of the vertical (Φ, Λ) caused by errors of the calibration parameters can be excluded. This results in an improvement of accuracy for about 50% (chapter 6.5).

5.6 Geodetic position

According to Eq. (3.1), errors in the geodetic position (φ, λ) directly influence the accuracy of the deflections of the vertical (ξ, η). Hence, they have to be provided with high accuracy. It is aimed to keep the error influence of the geodetic position below 0.01 arcsec, which corresponds to a lateral displacement at the earth's surface of about 30 cm. The single-frequency GPS code-receiver implemented in the Zenith Camera (chapter 3.2.6) is with ±3 m CEP in absolute mode and ±2 m CEP in differential mode, respectively, not suitable for the required level of accuracy. Therefore, additional dual-frequency GPS measurements in differential mode (DGPS) have to be performed. Hence, common error sources of GPS measurements, as e.g. satellite orbit and clock errors as well as impacts due to tropospheric and ionospheric refraction, can be reduced. Different methods exist to consider correction data from reference stations. One possibility is to receive real-time code phase corrections from a close reference station via a GSM module implemented in the receiver. The obtainable accuracy for the geodetic position is indicated with 1 m to 2 m corresponding to about 0.03 arcsec to 0.06 arcsec. Though, for a highly-precise determination of DOV, this range is not sufficient. This can be achieved by using real-time carrier phase corrections. They allow for an accuracy between 1 cm to 5 cm, which corresponds to less than two milli-arcseconds. In Switzerland, the Swiss Positioning Service (SWIPOS) offers the GIS/GEO application via GSM for navigation purposes in cm-range (Wild et al. [2004]). Another possibility is given by the post-processing of GPS measurements. This method has been applied during the campaign in Greece (chapter 7). There, the GPS data have been equalized within a network of four permanent reference stations with given ITRF2000 coordinates. The accuracy of this method amounts to better than 1 cm, hence perfectly satisfying the aspired accuracy of less than 30 cm.

5.7 Total error budget

Based on the considerations in the chapters before, the total error budget can be estimated. As the single errors are largely independent from each other, the standard deviations of the astronomical parameters ($\sigma_\Phi, \sigma_\Lambda$) and of the deflections of the vertical (σ_ξ, σ_η) can be calculated via error propagation law:

$$\begin{aligned} \sigma_\Phi^2 &= \sigma_{\Phi_D}^2 + \sigma_{\Delta\Phi_n}^2 + \sigma_{\Delta\Phi_a}^2 \\ \sigma_\Lambda^2 &= \sigma_{\Lambda_D}^2 + \sigma_{\Delta\Lambda_n}^2 + \sigma_{\Delta\Lambda_a}^2 + \sigma_t^2 \end{aligned} \tag{5.7}$$

$$\begin{aligned} \sigma_\xi^2 &= \sigma_\Phi^2 + \sigma_\varphi^2 \\ \sigma_\eta^2 &= (\sigma_\Lambda^2 + \sigma_\lambda^2) \cdot \cos^2 \Phi \end{aligned} \tag{5.8}$$

Error source	Abbrev.	Error	Azimuth calibration		Tripod method	
	$\sigma...$	[arcsec]	Wyler	Lippmann	Wyler	Lippmann
Rot.dir.	$(\Delta\Phi, \Delta\Lambda)_D$	0.10-0.30	x	x	x	x
Incl.(Lipp.)	$(\Delta\Phi, \Delta\Lambda)_n$	0.05-0.10	[-]	x	[-]	x
Incl.(Wyler)	$(\Delta\Phi, \Delta\Lambda)_n$	0.15-0.20	x	[-]	x	[-]
Epoch	t	0.01-0.02	x	x	x	x
Azi.corr.	$(\Delta\Phi, \Delta\Lambda)_a$	0.05-0.10	x	x	[-]	[-]
Astr.Lat.	Φ		**0.19-0.37**	**0.12-0.33**	**0.18-0.36**	**0.11-0.32**
Astr.Long.	Λ		**0.18-0.37**	**0.12-0.33**	**0.18-0.36**	**0.11-0.32**
Geod.pos.	(φ, λ)	$\leq$0.01	x	x	x	x
DOV (NS)	ξ		**0.19-0.37**	**0.12-0.33**	**0.18-0.36**	**0.11-0.32**
DOV (WE)	η		**0.14-0.29**	**0.09-0.25**	**0.14-0.28**	**0.08-0.24**

Table 5.1: Total estimated error budget of DIADEM in dependence on the method applied. Rot.dir.: Rotational direction, Incl.: Inclination, Azi.corr.: Azimuthal correction parameters, Geod.pos.: Geodetic position, N-S comp. DOV/W-E comp. DOV: components of the deflection of the vertical.

The consideration of correlations is not necessary. The error of η depends also on the astronomical latitude Φ of the observation station, which is for Zurich about 47°.

In Tab. 5.1, the total error budget of a DIADEM observation is listed in dependence on the method applied (AW-Azimuth/Wyler, AL-Azimuth/Lippmann, TW-Tripod/Wyler and TL-Tripod/Lippmann). The largest part is formed by errors in the determination of the rotational direction (0.1 arcsec - 0.3 arcsec) and by errors of the inclination sensors. Especially, the Wyler sensors significantly influence the resulting accuracy. This becomes obvious by comparing their accuracy range (0.15 arcsec-0.2 arcsec) to those of the Lippmann sensors (0.05 arcsec-0.1 arcsec). Also the azimuth calibration parameters represent a considerable error source (0.1 arcsec). In contrast, an error induced by the epoch determination can be almost neglected, provided that the shutter delay is considered in the epoch determination.

Furthermore, an influence of the observation method is recognizable: The total standard deviations of the DOV-components (σ_ξ, σ_η) might improve for about 40% if applying

the TL instead of the AW configuration. The standard deviations of ξ and η are then better than 0.32 arcsec and 0.24 arcsec, respectively. Due to the fact that the resulting DOV at a station always form an average over a certain number of single solutions (min. 40), the mean of the DOV can be determined with an accuracy of about 0.05 arcsec.

These conclusions fit well with the results presented in chapter 6.5. There, the different methods have been analyzed in practice and compared to each other. Based on the DOV determined during different nights, it has been shown that the TL configuration enables an increased internal accuracy (about 33%). The empirically derived standard deviations after an application of the TL method amount to better than 0.29 arcsec, which corresponds well with the above estimated range.

6 Field experiences

6.1 Measurements in Switzerland 2003

In the year 2003, the CHGeo2003 project has been initiated by the Swiss Federal Office of Topography (swisstopo). It aimed at the improvement of the presently used Swiss geoid model CHGeo98 (Marti, 1997). The geoid suffers from long-wavelength errors, hence generating discrepancies between orthometric heights from the new national height system (LHN95) and those derived by the difference between GPS and geoid. The discrepancies are in the order of several centimeters up to decimeters in some regions (Marti [2002]). The project CHGeo2003 included new and improved measurements (GPS/leveling, deflections of the vertical (DOV), gravity values) as well as the use of advanced mass models and calculation methods. The project also contributed to the European Combined Geodetic Network (ECGN) and the European Unified Vertical Network - Densification Action (EUVN-DA) of European Reference Frames (EUREF) (Brockmann et al. [2004]). In the frame of the project, two digital Zenith Cameras - DIADEM (ETH Zurich) and TZK2-D (University Hannover) - have been deployed for the observations of DOV (Fig. 6.1).

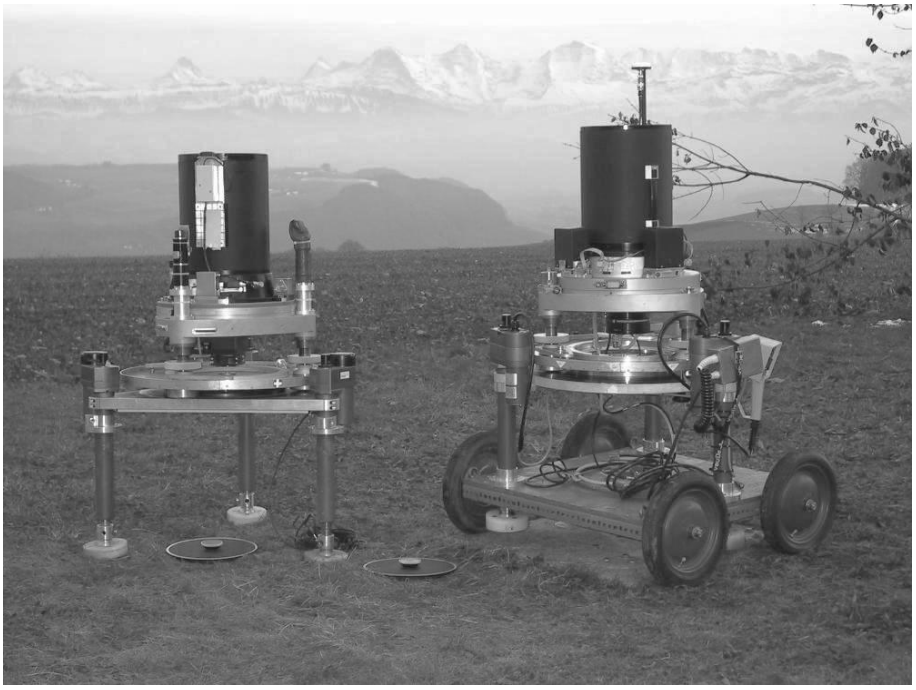

Figure 6.1: Parallel measurements with two digital Zenith Cameras at the reference station Zimmerwald, Switzerland (left: DIADEM (GGL, ETH), right: TZK2-D (IfE, University Hannover).

The goal was to provide additional highly precise DOV. Further goals were the proof of the field capability of the digital Zenith Cameras and the comparison of both systems concerning their accuracy potential. The Astro observations took place during four weeks in October 2003 in Switzerland. In 16 observation nights, a total number of 68 stations has been measured with both Zenith Cameras (Fig. 6.2). This averages to 2-5 stations per night and team depending on weather, location (mountains, valley) and distance between the stations. Four stations have been observed simultaneously, e.g.the geodetic reference station in Zimmerwald (see Fig. 6.4: station 1). This station has been also measured repeatedly during different nights. The data have been used to determine the accuracy of both Zenith Cameras.

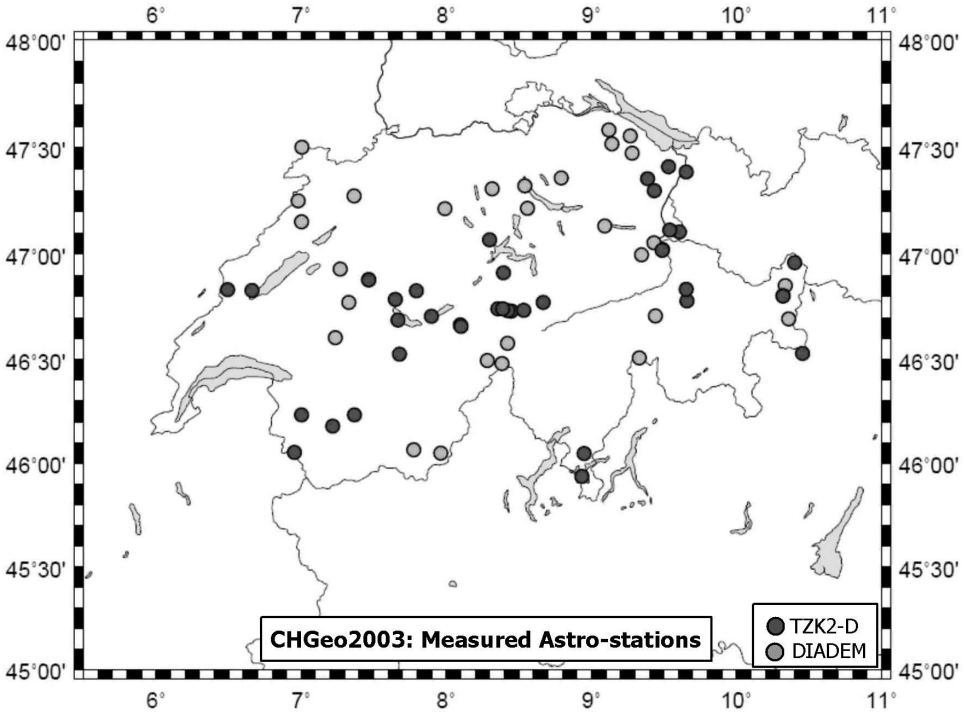

Figure 6.2: Location of 68 Astro stations measured by DIADEM (light gray) and TZK2-D (dark gray) during 16 observation nights.

The CHGeo2003 campaign offered the possibility to deploy two modernized digital Zenith Cameras for the first time (Müller et al. [2004]). It has been concluded that both systems worked reliably and efficiently even under very harsh conditions like in high mountains and with temperatures at -15°C.

The results of the two digital Zenith Cameras show a very good agreement, deducible from the comparison of repeated measurements during different nights at the reference station Zimmerwald. Tab. 6.1 shows the numerical comparison of the results for both instruments. With DIADEM, observations during five different nights have been performed at the reference station (about 80 single solutions per night). With TZK2-D, totally seven different night means have been determined (about 100 single solutions per night). The maximum deviation between DIADEM and TZK2-D derived components amounts to about 0.3 arcsec (compare ξ_{tzk}(Min.) to ξ_{dia}(Max.)). The maximum difference between results observed in the same night is 0.2 arcsec (compare $(d\xi, d\eta)$). The difference between the respective overall-means is on the order of 0.05 arcsec for η and 0.1 arcsec for

ξ ((Fig. 6.3). The standard deviation of repeated measurements is better than 0.1 arcsec for each system. These results demonstrate the excellent repeatability and accuracy of both Zenith Cameras.

	DIADEM			TZK2-D			Difference	
Date	Sol.	ξ_{dia}	η_{dia}	Sol.	ξ_{tzk}	η_{tzk}	$d\xi$	$d\eta$
		[arcsec]			[arcsec]		[arcsec]	
20031009	-	-	-	167	7.66	3.94		
20031011	-	-	-	129	7.83	3.83		
20031013	37	7.96	3.88	108	7.89	4.05	0.07	-0.17
20031022	-	-	-	80	7.87	3.82		
20031025	86	7.89	3.80	89	7.74	3.74	0.15	0.06
20031026	87	7.87	3.96	113	7.76	3.91	0.11	0.05
20031027	58	7.96	4.01	106	7.89	3.81	0.07	0.20
20031028	60	7.86	3.97	-	-	-		
Mean	80	**7.91**	**3.92**	102	**7.81**	**3.87**	0.10	0.05
Std.dev.		0.09	0.10		0.08	0.08		
Min.		7.86	3.80		7.66	3.74	0.20	0.06
Max.		7.96	4.01		7.89	4.05	0.07	-0.04
Range (Min.-Max.)		0.10	0.21		0.23	0.31		

Table 6.1: Parallel measurements with two Zenith Cameras - DIADEM (ETH Zurich) and TZK2-D (University Hannover) - at the reference station Zimmerwald. Sol.: Number of single solutions used for the calculation of the respective night mean, $(d\xi, d\eta)$: Difference between the corresponding night means of both instruments.

Fig. 6.4 shows the DOV observed at 68 stations in Switzerland. The data clearly indicate the influence of the Alpine chain, since the vectors to the north of the Alps indicate an increasing geoid in southward direction. A maximum value of 27 arcsec has been observed at station "Grosse Scheidegg" (station 2), which is located north-east of Grindelwald in the Bernese Oberland. The smallest one has been measured in Pfäffikon (station 3) near Zurich with 2 arcsec. The standard deviation of about 100 single solutions per station is between 0.1 arcsec and 0.3 arcsec. The mean per station has a precision of better than 0.1 arcsec. The results of the Astro campaign have been introduced together with other 690 available DOV for the computation of an improved geoid. Besides these data, also GPS-leveling as well as gravity date have been used for the enhanced computation of the Swiss geoid CHGeo2003 (Marti [2004]).

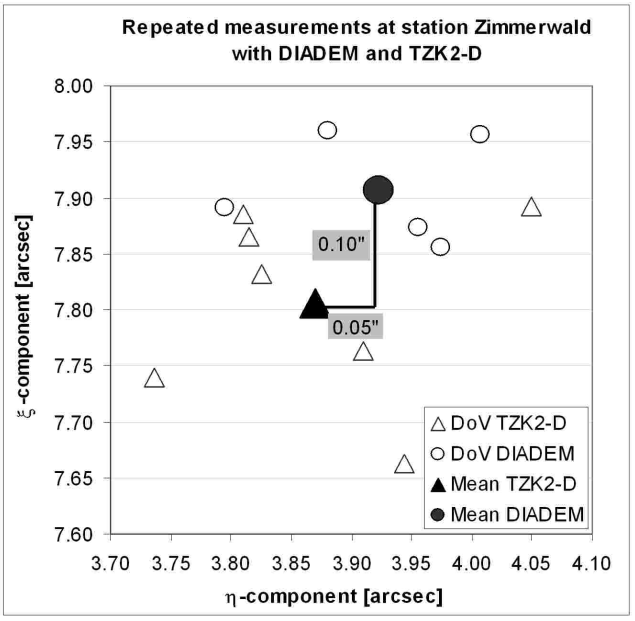

Figure 6.3: Results of repeated measurements with DIADEM (circles) and TZK2-D (triangles) during different nights at the reference station Zimmerwald. The DOV show a very good agreement of better than 0.1 arcsec.

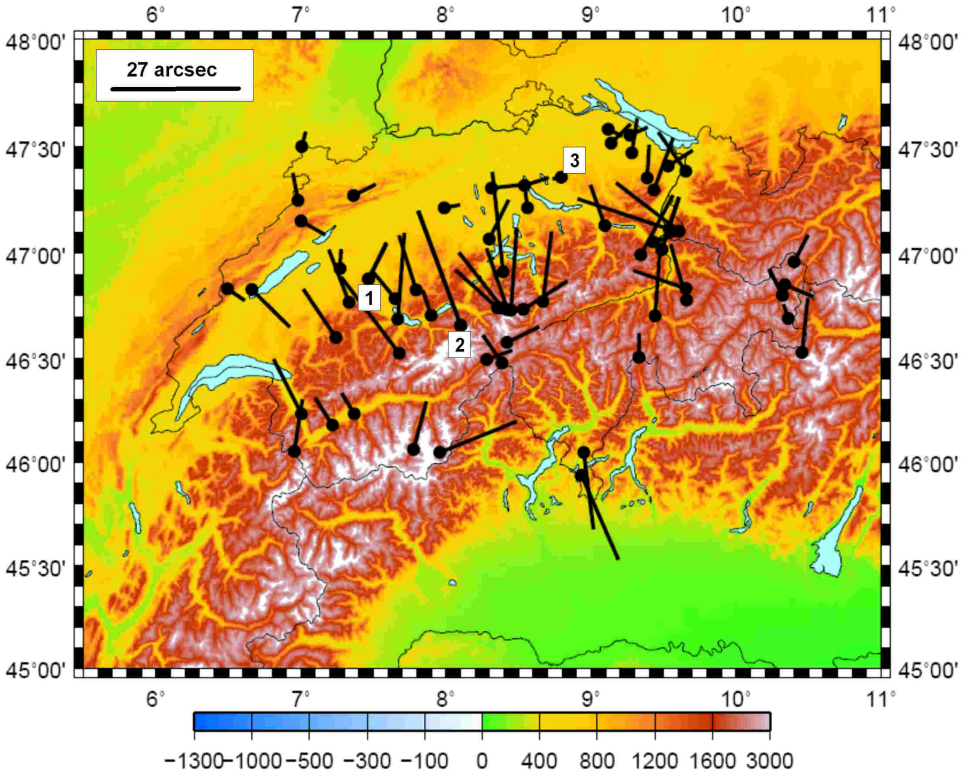

Figure 6.4: DOV observed by DIADEM and TZK2-D during the CHGeo2003 project. Totally, 68 stations in Switzerland have been measured. Station 1 shows the reference station Zimmerwald. The DOV vary between 2 arcsec (station 3: Pfäffikon) and 27 arcsec (station 2: "Grosse Scheidegg").

6.2 Measurements in Portugal 2004

During two campaigns in 1993 and 1997/1998 with the old analog system TZK3, several stations have been measured throughout Portugal. Due to technical problems, four stations in the southern part of Portugal could not be processed. In order to complete the measurements and to provide additional DOV for the Portuguese geoid determination, a third campaign took place in September 2004. The measurements also provided the possibility to demonstrate the field capability of DIADEM. The stations to be observed were suggested by the Instituto Português de Cartografia e Cadastro (IPCC), Lisbon, Portugal. The plan comprised 17 new and repeated observations throughout Portugal on principal and secondary points of the national geodetic network. Fig. 6.5 shows the old (blue) and newly planned (red) stations.

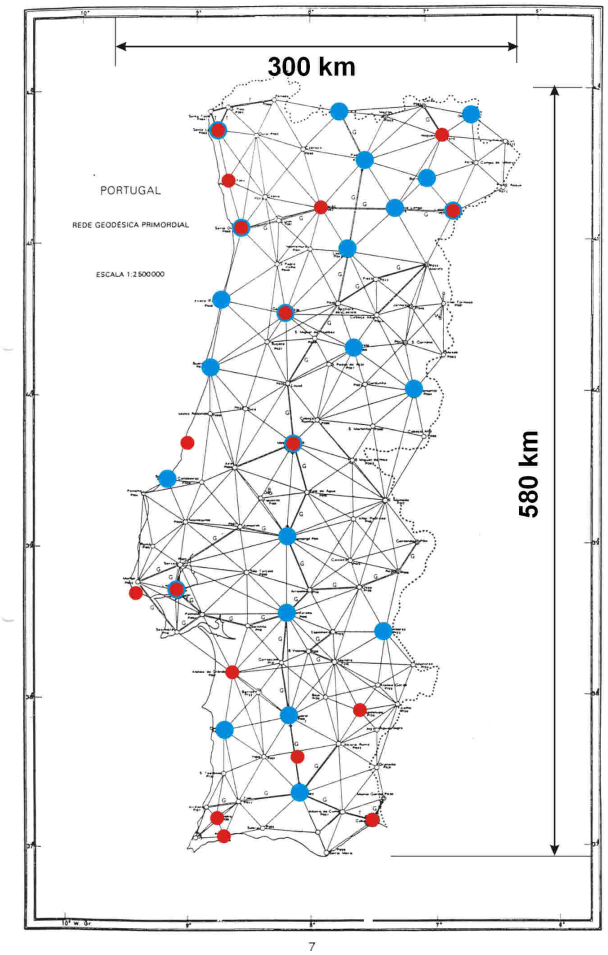

Figure 6.5: Astro stations in Portugal observed in 1993 and 1997/1998, respectively (blue) and in 2004 (red). The stations are primary and secondary points of the national geodetic network.

Within two weeks, all stations have been successfully observed starting at station Lagoaça (Laça) in the north and finishing at station Cabeça (Cabe) in the south. The distances between the stations averaged to about 150 km. Therefore, it was not possible to observe more than two stations per night. In general, the time needed per station was about 45 minutes including assembly and disassembly of the system.

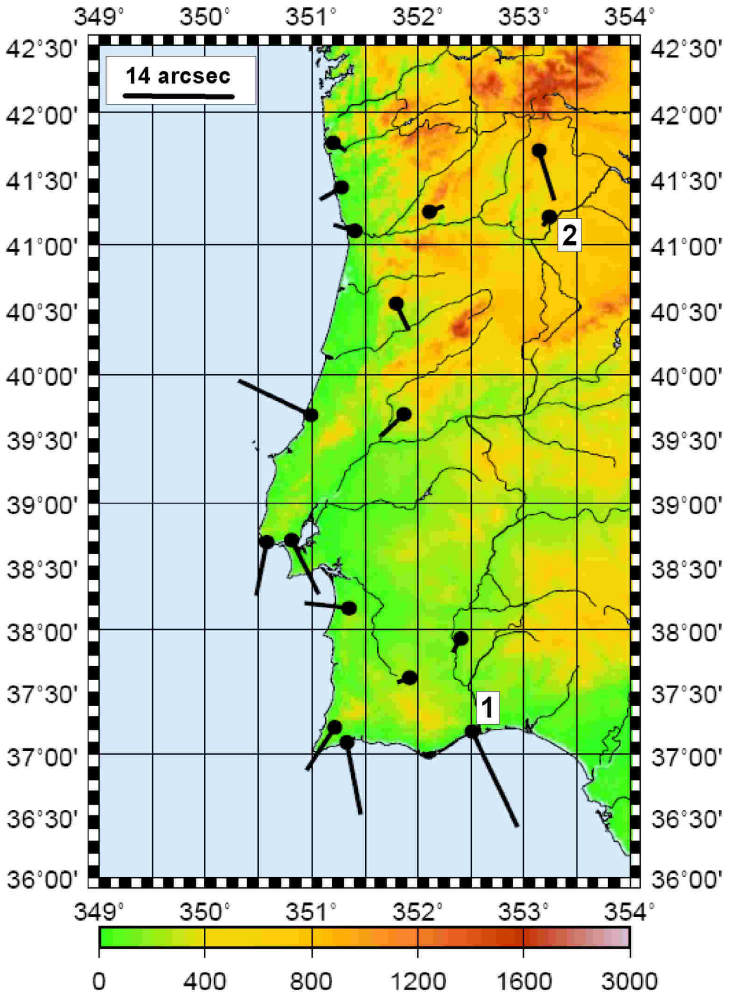

Figure 6.6: DOV observed by DIADEM at 17 stations in Portugal. The DOV vary between 1 arcsec (station 2: Lagoaça) and 27 arcsec (station 1: Cabeça).

Fig. 6.6 shows the DOV observed at 17 stations in Portugal. The maximum value has been observed at Cabeça (station 1), south of Portugal, with 14 arcsec, while the smallest vertical deflection (1 arcsec) has been measured at Lagoaça (station 2), a station in the north near the border to Spain. The standard deviation of about 80 single solutions per station is between 0.1 arcsec to 0.3 arcsec. The mean value per station has a precision of better than 0.1 arcsec. The campaign revealed again the good field capability and high accuracy of DIADEM. The data gathered were used by the IPCC for an improved Portuguese geoid determination.

6.3 Measurements with two digital Zenith cameras in Switzerland 2005

In July 2005, a campaign with two digital Zenith Cameras (DIADEM and TZK2-D) took place in Pradella (lower Engadine), Switzerland, aiming at the error analysis and comparison of both instruments. The main intention was the investigation of the effect of *anomalous refraction*. It forms a potential error source, which influences the determination of the direction of the vertical with a digital Zenith Camera. Anomalous refraction is caused by atmospheric layers, which are inclined with respect to the local plumb line, mainly due to pressure and temperature gradients occurring in horizontal direction (Ramsayer [1970]). The induced systematic misalignment of the zenithal star field results in a falsification of the vertical direction observed. The effect of anomalous refraction can be split into two phenomena: a regional and a local phenomenon (see chapter 5.2.2). The anomalous refraction has been investigated since many years (e.g. Ramsayer [1970]) and is still a subject of ongoing publications, as e.g. demonstrated by Stone et al. [1996] and Pier et al. [2003]. Hirt [2006] analyzed about 70 hours of observations with the digital Zenith Camera TZK2-D comprising 7300 single solutions from six nights. Based on these data as well as in relation with highly-precise reference values, Hirt [2006] estimated the dimension of the effect between 0.05 arcsec and 0.2 arcsec.

The goal of the present campaign was the detection of anomalous refraction by comparing simultaneous long-time observations of two Zenith Cameras. The relative changes of the DOV-components during a night potentially contain a reference to the effect of refraction. A second goal of the campaign was the evaluation of the accuracy potential of the instruments by appraising their internal and external accuracies. The campaign took ten days, however, due to bad weather conditions, comparable long-time observations are only available during two nights: July 3, 2005 and July 12, 2005. In total, about 1500 single solutions per camera were gathered and used for a detailed data analysis.

Comparison of night means

Date	Statistics	ξ_{dia} [arcsec]	η_{dia} [arcsec]	ξ_{tzk} [arcsec]	η_{tzk} [arcsec]	$d\xi$ [arcsec]	$d\eta$ [arcsec]
20050703	Mean	5.73	-3.19	5.72	-3.06	0.01	-0.13
	σ_ξ, σ_η	0.37	0.36	0.23	0.23		
20050712	Mean	5.79	-2.97	5.66	-2.95	0.13	-0.02
	σ_ξ, σ_η	0.29	0.30	0.19	0.20		
	Diff (2 days)	-0.06	-0.22	0.06	-0.11		
	Mean (2 days)	**5.76**	**-3.08**	**5.69**	**-3.00**	0.08	-0.07

Table 6.2: Comparison of night means observed with DIADEM (ξ_{Dia}, η_{Dia}) and TZK2-D (ξ_{Tzk}, η_{Tzk}) at July 3, 2005 (20050703) and July 12, 2005 (20050712), respectively. (σ_ξ, σ_η): Standard deviation of the DOV per system, ($d\xi$,$d\eta$): Difference between the respective DOV-components of DIADEM and TZK2-D.

Table 6.2 shows the mean DOV of two different nights (20050703 and 20050712) measured by DIADEM (ξ_{Dia}, η_{Dia}) and TZK2-D (ξ_{Tzk}, η_{Tzk}). The respective night means of both systems agree very well with a maximum difference of 0.13 arcsec (see *($d\xi, d\eta$)*). The comparison of the night means per system averaged over two nights, show a very good consistency of 0.08 arcsec for ξ and -0.07 arcsec for η. The analysis of single night means measured by DIADEM reveals a very good repeatability for the ξ-component of -0.06 arcsec, while the η-component shows a slight worse repeatability of -0.22 arcsec (see *Diff (2 days)* for DIADEM). The single night means measured by TZK2-D show a very good reproducibility of -0.1 arcsec and better (see *Diff (2 days)* for TZK2-D).

Besides, the analysis of the standard deviations per measuring series allows interesting conclusions regarding the inclination sensors: It is striking that the standard deviation of DIADEM observations (0.33 arcsec[1] for both components) is about 50% worse than those from a TZK2-D observation (0.21 arcsec). This result is attributed to the different types of inclination sensors used on both Zenith Cameras. At this time, DIADEM solely worked with the Wyler sensors (chapter 3.2.5), while the TZK2-D already used the more precise Lippmann sensors (chapter 3.2.4). After the campaign, two Lippmann inclination sensors have been implemented into the process of data acquisiton and analysis with DIADEM (Münch [2006] and Ganz [2007]). The results of afterwards performed investigations concerning the impact of Wyler and Lippmann sensors, respectively, on the internal accuracy are presented in chapter 6.5.

Comparison of the long-time characteristics

Figs. 6.7 and 6.8 represent the course of the ξ- and η-component, respectively, for both Zenith Cameras (triangles: DIADEM, points: TZK2-D). The data were gathered during five hours in the night of July 12, 2005. Concerning the ξ-component (Fig. 6.7), the mean difference of 0.13 arcsec between DIADEM and TZK2-D is well recognizable (see Table 6.2), as the DIADEM data show constantly greater values. In contrast, the η-components (Fig. 6.8) show a very good agreement. If the data are fitted by a four-degree polynomial function, it becomes obvious that the DIADEM observations (straight light gray line) undulate stronger than those of TZK2-D (straight black line), with amplitudes of about 0.2 arcsec. In contrast, the TZK2-D data show maximum amplitudes of 0.1 arcsec. Comparing the trends of the ξ- and η-components, respectively, they do not show an obvious consistency. At least it might be claimed that the η-components indicate a slight increase of about 0.1 arcsec over the whole observation time. However, these variations are within the range of the above discussed standard deviations of each Zenith Camera system (see section *Comparison of night means*) and are, therefore, not significant. Hence, they can not be interpreted offhand as a reference to anomalous refraction.

[1]The value is an average over the four standard deviations given in Tab. 6.2

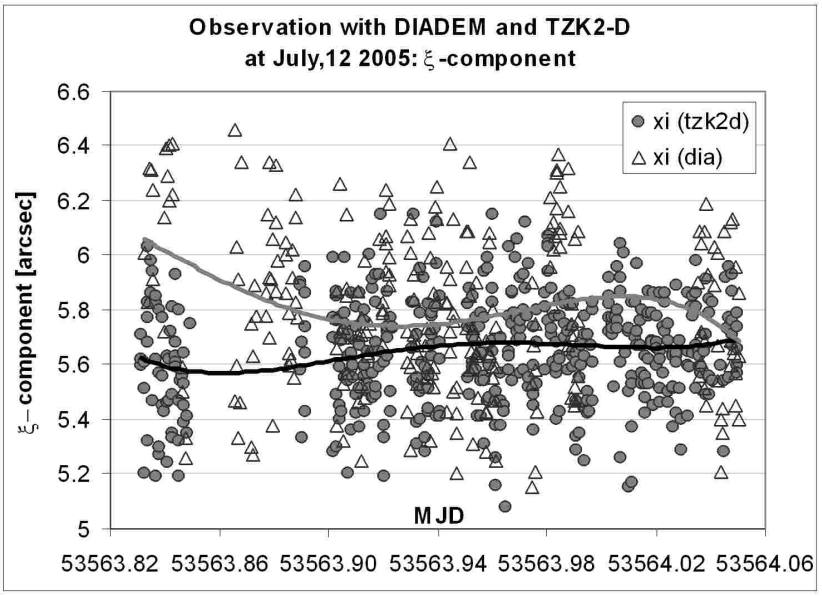

Figure 6.7: Comparison of the ξ-components measured by DIADEM (triangles) and TZK2-D (points) at July 12, 2005 in Pradella. The straight lines represent a four-degree polynomial function (DIADEM: light gray, TZK2-D: black). The mean difference of 0.13 arcsec between DIADEM and TZK2-D is clearly recognizable.

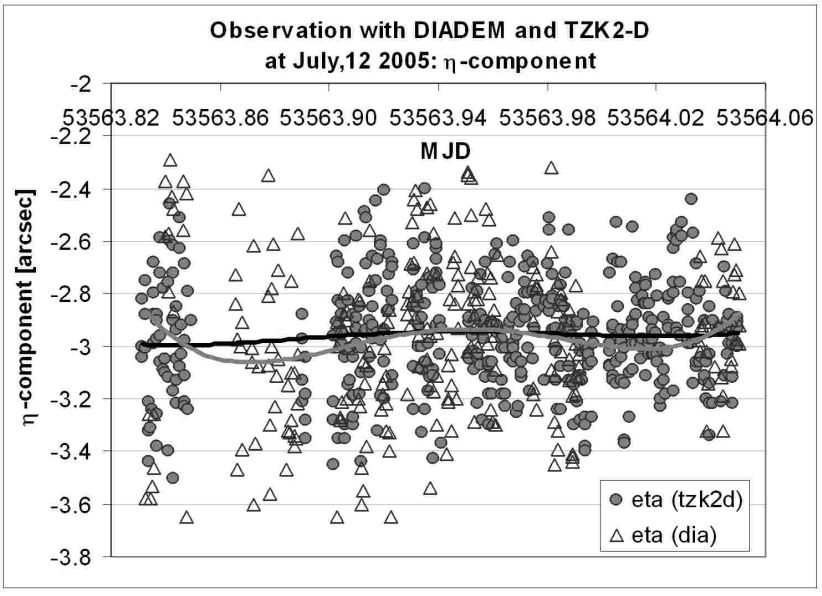

Figure 6.8: Comparison of the η-component measured by DIADEM (triangles) and TZK2-D (points) at July 12, 2005 in Pradella. The data show a very good agreement.

Figs. 6.9***a)*** and 6.9***b)*** allow for a visual appraisal of correlations between corresponding components measured by DIADEM and TZK2-D is provided by (for July 12th, 2005). It becomes clear that the respective components are not highly correlated, as they show a relatively broad distribution.

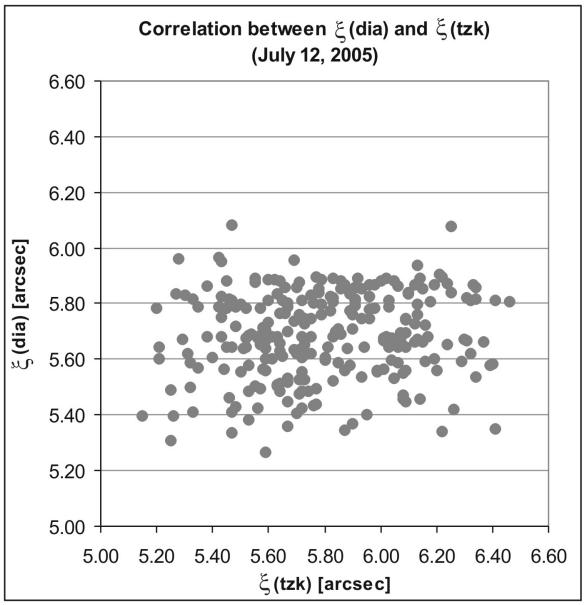

a) Correlation between ξ_{dia} and ξ_{tzk}.

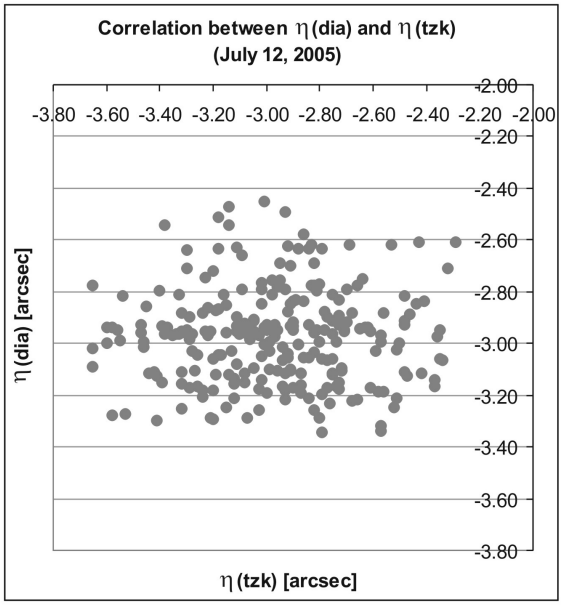

b) Correlation between η_{dia} and η_{tzk}.

Figure 6.9: Correlation between ξ-components and η-components, respectively, measured by TZK2-D (abscissa) and DIADEM (ordinate) at July 12, 2005 in Pradella. The correlation between the respective components is very low amounting to 0.12 for ξ and 0.01 for η.

The correlation coefficient between ξ_{dia} (Diadem) and ξ_{tzk} (TZK2-D) for n measurements can be calculated by:

$$r_{\xi_{dia}\xi_{tzk}} = \frac{\sum_{i=1}^{n} ((\xi_i - \bar{\xi})_{dia} \cdot (\xi_i - \bar{\xi})_{tzk})}{\sqrt{\sum_{i=1}^{n} (\xi_i - \bar{\xi})^2_{dia}} \cdot \sqrt{\sum_{i=1}^{n} (\xi_i - \bar{\xi})^2_{tzk}}} \tag{6.1}$$

The correlation coefficient for the η-components can be calculated, if ξ in Eq. (6.1) is replaced by η. The coefficients $r_{\xi_{dia}\xi_{tzk}}$ and $r_{\eta_{dia}\eta_{tzk}}$ amount to 0.07 and -0.01, respectively, for the observations at July 3rd, 2005, and to 0.12 and 0.01 at July 12th, 2005 (Tab. 6.3). These coefficients indicate a very low correlation.

Date	$r_{\xi_{dia}\xi_{tzk}}$	$r_{\eta_{dia}\eta_{tzk}}$
20050703	0.07	-0.01
20050712	0.12	0.01

Table 6.3: Correlation coefficients $r_{\xi_{dia}\xi_{tzk}}$ between ξ_D (Diadem) and ξ_T (TZK2-D) as well as $r_{\eta_{dia}\eta_{tzk}}$ between η_D and η_T for both observation nights.

Concluding, it can be stated that the analysis of the night means as well as the comparison of the long-time characteristics measured with both Zenith Cameras did not allow for convincing conclusions concerning the impact of anomalous refraction. Due to the absence of highly-precise reference values, the experiment was not qualified to predicate absolute refraction magnitudes, but only refraction changes. It is concluded that an influence exists, however, potentially occurring changes in refraction are superposed by the normal measuring noise of the instrument. They were, therefore, not significantly reproducible. The maximum impact has been estimated at about 0.1 arcsec. This assumption agrees well with Hirt [2006], who indicated a range of 0.05 arcsec to 0.2 arcsec. In order to deepen the knowledge in this subject, further observations would be necessary using additionally local weather information. Hence, it would be interesting to conduct long-time observations during some days/weeks with changing weather conditions, again with two Zenith Cameras.

6.4 Alptransit measurements in Switzerland 2005

On the behalf of the Swiss Alptransit project and related construction works at the Gotthard Base Tunnel in Switzerland, highly-precise DOV have been measured in July 2005. The observations were carried out at five Alptransit portal stations, which are used as gyro-calibration reference points: Amsteg, Erstfeld, Sedrun, Faido and Bodio (Fig. 6.10). In addition to the DOV, also astronomical azimuths have been measured at these stations (Bürki et al. [2005]).

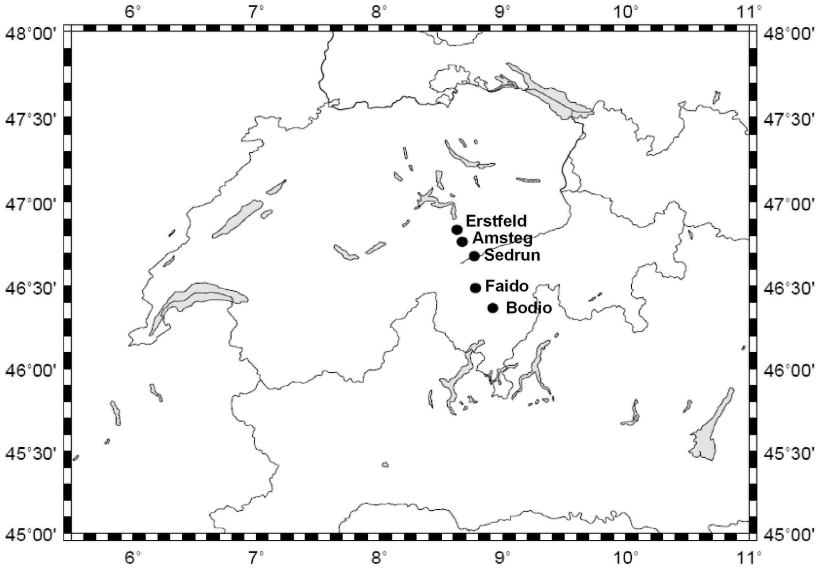

Figure 6.10: Location of the Alptransit portal stations Erstfeld, Sedrun, Amsteg, Faido and Bodio, Switzerland.

Due to the fact that the campaign with two digital Zenith Cameras had just taken place (see chapter 6.3), it was possible to perform the Alptransit measurements with two instruments. Hence, the observations are also interesting for a further comparison

of both systems at four different stations (Sedrun has been measured by DIADEM only).

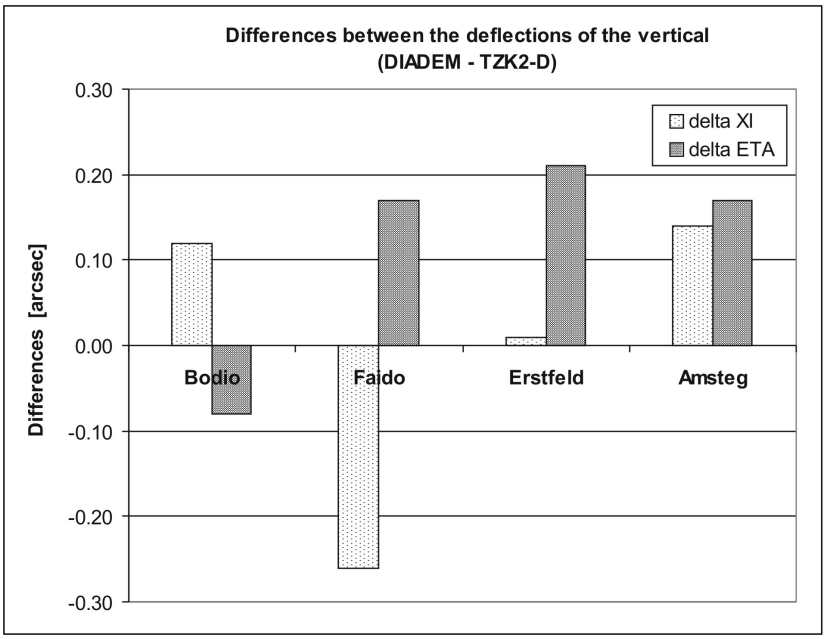

Figure 6.11: Differences (DIADEM - TZK2-D) between the DOV ($d\xi$: light gray, $d\eta$: dark gray) measured by DIADEM and TZK2-D.

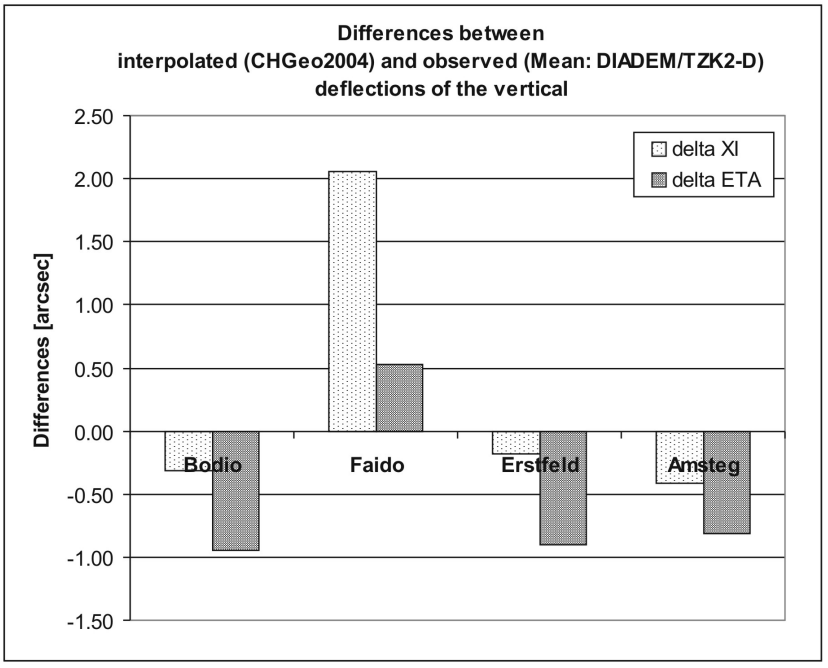

Figure 6.12: Differences between interpolated (CHGeo2004) and observed (Mean: DIADEM/TZK2-D) DOV ($d\xi$: light gray, $d\eta$: dark gray).

The measurements have been performed during one night at four stations (DIADEM and TZK2-D) finishing in a second night at station Sedrun (DIADEM only). The points are located along a profile with a maximum distance between Erstfeld and Bodio of about 60 km (Fig. 6.10). The differences between the DOV measured by DIADEM and TZK2-D are shown in Fig. 6.11. They range between 0.01 arcsec and 0.26 arcsec. The mean difference amounts to 0.15 arcsec for both components with a standard deviation of 0.05 arcsec. These results demonstrate the high-precision potential of both instruments.

A further analysis has been concerned with the comparison of computed and observed DOV. Therefore, Urs Marti (swisstopo) interpolated DOV for the five Alptransit stations from the new Swiss geoid model CHGeo2003 (chapter 6.1). The differences between interpolated and observed DOV range between -0.9 arcsec and 2.1 arcsec (Fig. 6.12). Allowing for the accuracy of the geoid model and the limits of the interpolation method, maximum differences of about 0.5 arcsec have been expected. Due to the above demonstrated good agreement between the two Zenith Camera systems, significant errors caused by instrumental insufficiencies can be excluded. More likely, these results contain a reference to still existing problems in the present geoid solution.

6.5 Control measurements at Zurich

In order to allow for statements concerning the long-term stability and accuracy of DIADEM, repeated observations took place from 2004 to 2007 at two different reference points. The control measurements have to be divided into two groups *Session A* and *B* showing differences in reference station, measuring method and inclination sensors:

- Session A: From August 2004 to June 2005, repeated observations took place at the roof of the HPV-ETHZ building. The station already served as reference station for the old analog system TZK3 since the early eighties. Hence, long-time reference values ($\xi_r^A = -2.08$ arcsec, $\eta_r^A = 3.62$ arcsec) are available showing an accuracy of better than 0.1 arcsec. The measuring configuration applied during session A is the so called *azimuth calibration* (chapter 4.4.1). The inclination measurements have been performed by using the *Wyler inclination sensors* (chapter 3.2.5).
- Session B: After elaborate enhancements of DIADEM, a new series of observations took place from April to December 2007 at the reference station on the southern front of the HPV-ETHZ building. The reference values ($\xi_r^B = -2.04$ arcsec, $\eta_r^B = 3.61$ arcsec) of this station have been determined by the TZK2-D in July 2005. The have an accuracy of better than 0.1 arcsec. Due to new findings, the time-consuming azimuth calibration has been replaced by the newly introduced *tripod method* (chapter 4.4.1). Furthermore, additional to the Wyler inclination sensors, the more precise *Lippmann inclination sensors* (chapter 3.2.4) have been used. In order to investigate and compare the field capability, efficiency and accuracy potential of the two measuring methods (*azimuth calibration* and *tripod method*) as well as of the inclination sensors (*Wyler* and *Lippmann sensors*), the observations of session B have been performed in different constellations (Ganz [2007]).

In the following sections, the results of the two sessions are treated and discussed separately.

Session A

Tab. 6.4 represents the comparison of the DOV observed during eight nights in 2004/2005 with about 40 to 60 single solutions per night. They show a very good agreement, with a standard deviation of about 0.08 arcsec for ξ and 0.16 arcsec for η (see *Std.dev.*(ξ, η) in Tab. 6.4). The differences with respect to the reference DOV (ξ_r^A, η_r^A) amount in average to 0 arcsec and -0.04 arcsec, respectively (see $(d\xi, d\eta)$). The mean standard deviation of a single component per night reaches to about 0.32 arcsec for both components (see $(\sigma_\xi, \sigma_\eta)$). The accuracy of the night mean can be indicated with better than 0.05 arcsec.

Date	Meth/Sensors	ξ [arcsec]	η [arcsec]	σ_ξ [arcsec]	σ_η [arcsec]	d_ξ [arcsec]	d_η [arcsec]
20040822	AW	-2.03	3.72	0.31	0.27	-0.05	-0.10
20041023	AW	-2.04	3.70	0.28	0.28	-0.04	-0.08
20041115	AW	-1.99	3.56	0.32	0.26	-0.09	0.06
20050117	AW	-2.08	3.78	0.37	0.38	0.00	-0.16
20050404	AW	-2.02	3.75	0.35	0.36	-0.06	-0.13
20050415	AW	-2.06	3.79	0.31	0.29	-0.02	-0.17
20050511	AW	-2.21	3.31	0.28	0.38	0.13	0.31
20050616	AW	-2.20	3.65	0.32	0.27	0.12	-0.03
	Mean:	**-2.08**	**3.66**	**0.32**	**0.31**	**0.00**	**-0.04**
	Std.dev.:	0.08	0.16	0.03	0.05		

Table 6.4: Results of session A. The measurements took place on the roof of the HPV-ETHZ building. AW: Azimuth calibration/Wyler sensors. $(\sigma\xi, \sigma\eta)$: Standard deviations of a single component per night. (d_ξ, d_η): Differences between respective night mean and reference DOV (ξ_r^A, η_r^A).

Session B

The DOV observed during five nights in 2007 are shown in Tab. 6.5. As mentioned above, the measurements have been deployed using different measuring configurations concerning method (azimuth calibration/tripod method) and inclination sensors (Wyler/Lippmann). Hence, in some nights both measuring methods have been conducted and the analysis of the data has been performed using the inclination data of *Wyler* and *Lippmann sensors*, respectively. All data sets comprise of about 40 to 60 single solutions. In order to evaluate the quality of the respective measuring configuration, the data have been analyzed considering the standard deviations of a series per night (internal accuracy) as well as the differences with respect to the reference DOV (ξ_r^B, η_r^B) (external accuracy).

Fig. 6.13 shows the comparison of the internal accuracies of the four different measuring configurations: Azimuth/Wyler (AW), Azimuth/Lippmann (AL), Tripod/Wyler (TW) and Tripod/Lippmann (TL). The values represent the respective mean standard deviations of series with same configurations (see $(\sigma_\xi, \sigma_\eta)$ in Tab. 6.5). It is clearly visible that the use of inclination sensors plays an important role concerning the internal accuracy

Date	Meth/Sensors	ξ [arcsec]	η [arcsec]	σ_ξ [arcsec]	σ_η [arcsec]	d_ξ [arcsec]	d_η [arcsec]
20070512	AW	-2.08	3.80	0.36	0.41	0.04	-0.19
20071128	AW	-2.34	3.86	0.38	0.32	0.30	-0.25
	Mean:	**-2.21**	**3.83**	**0.37**	**0.36**	**0.17**	**-0.22**
	Std.dev.:	0.18	0.04	0.01	0.06		
20070506	AL	-2.23	3.93	0.22	0.30	0.19	-0.32
20070512	AL	-2.04	3.78	0.29	0.30	0.00	-0.17
20070525	AL	-2.09	3.66	0.29	0.28	0.05	-0.05
20071128	AL	-2.29	3.92	0.32	0.24	0.25	-0.31
	Mean:	**-2.16**	**3.82**	**0.28**	**0.28**	**0.12**	**-0.21**
	Std.dev.:	0.12	0.13	0.04	0.03		
20070512	TW	-2.07	3.60	0.41	0.50	0.03	0.01
20071128	TW	-2.17	3.62	0.29	0.35	0.13	-0.01
20071205	TW	-2.15	3.83	0.31	0.58	0.11	-0.22
	Mean:	**-2.13**	**3.68**	**0.34**	**0.48**	**0.09**	**-0.07**
	Std.dev.:	0.06	0.13	0.06	0.12		
20070512	TL	-2.14	3.68	0.21	0.18	0.10	-0.07
20071128	TL	-2.10	3.64	0.21	0.18	0.06	-0.03
20071205	TL	-2.14	3.71	0.22	0.29	0.10	-0.10
	Mean:	**-2.13**	**3.67**	**0.21**	**0.25**	**0.09**	**-0.06**
	Std.dev.:	0.02	0.04	0.01	0.08		
	Mean all:	**-2.15**	**3.75**	**0.29**	**0.33**	**0.11**	**-0.14**
	Std.dev. all:	0.08	0.16	0.07	0.11		

Table 6.5: Results of session B. The measurements took place on the southern front of the HPV-ETHZ building. AW: Azimuth calibration/Wyler sensors, AL: Azimuth calibration/Lippmann sensors, TW: Tripod method/Wyler sensors, TL: Tripod method/Lippmann sensors. $(\sigma_\xi, \sigma_\eta)$: Standard deviations of a single component per night, (d_ξ, d_η): Differences between respective night mean and reference DOV (ξ_r, η_r).

of a series. Hence, the use of the Wyler sensors results a mean standard deviation of worse than 0.34 arcsec for both measuring methods (azimuth calibration/tripod). In contrast, the use of the Lippmann sensors yields a standard deviation of better than 0.28 arcsec, which further declines to 0.25 arcsec and better if the tripod method is applied. The accuracy gain amounts to 24% (between AW and AL)) and to 43% (between TW and TL), respectively. Besides the inclination sensors, also the measuring method seems to have an influence. This is derivable from the fact that the application of the TL instead of the AW configuration induces an improvement in precision of about 33 %.

Fig. 6.14 shows the comparison of the external accuracies of the four different measuring configurations. The values represent the respective mean differences between reference DOV and observed DOV of series with same configurations (see $(d\xi, d\eta)$ in Tab. 6.5). If the tripod method instead of the azimuth calibration is applied, the accuracy gain is significant. It amounts to 48% (between AL and TL) and 57% (between AW and TW), respectively. If instead of the AW configuration the TL configuration is used, the

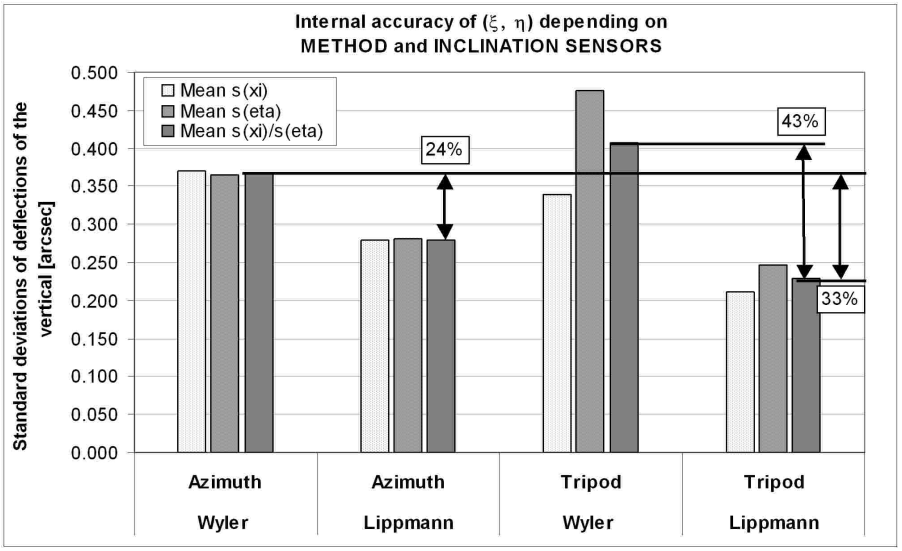

Figure 6.13: Comparison of the internal accuracies (see $(\sigma_\xi, \sigma_\eta)$ in Tab. 6.5) of the four different measuring configurations: Azimuth/Wyler, Azimuth/Lippmann, Tripod/Wyler, Tripod/Lippmann. The values given represent mean standard deviations of series with same configurations.

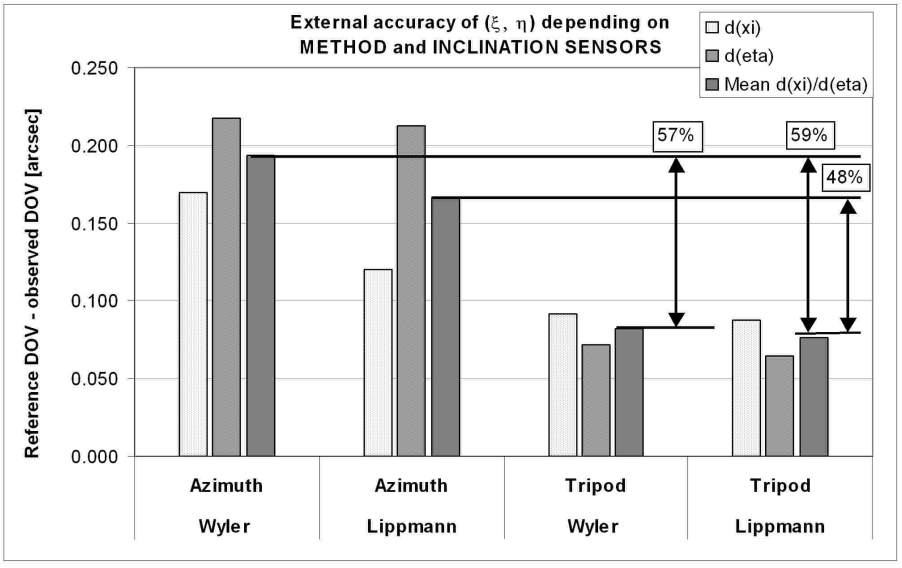

Figure 6.14: Comparison of the differences between reference DOV and observed DOV (see $(d\xi, d\eta)$ in Tab. 6.5) of the four different measuring configurations. The values given represent the respective mean of different nights with same measuring configurations.

accuracy gain almost reaches the level of 60%! It is interesting that the type of inclination sensors does not play a significant role for the external accuracy.

Concluding, two findings can be emphasized:
a) Referring to the longer statistical series using the AW configuration, the accuracy potential of DIADEM can be indicated as follows[2]:

[2]Calculation based on all observations in session A and two observations in session B

Internal accuracy:

* Standard deviation of a single observation: about **0.3 arcsec**
* Standard deviation of the mean (with 40 single observations): $\leq$**0.05 arcsec**

External accuracy:

* Comparison between reference and observed value: $\leq$**0.15 arcsec**
* Standard deviation of different night means (repeatability): $\leq$**0.15 arcsec**

b) The application of the tripod method as well as the use of the Lippmann inclination sensors denotes a great leap forward concerning internal and external accuracy. It has been demonstrated that the change from Wyler to Lippmann inclination sensors produces a significant increase concerning the internal accuracy of the observations. The measuring method (azimuth calibration or tripod method) does also have an impact on the internal accuracy, however, it contributes more to the external accuracy. The accuracy gain between the usually applied AW configuration and the TL configuration is considerable and amounts to about 30% for the internal accuracy and to about 60 % for the external accuracy!

It has to be noted that the analysis of series B only refers to four observation nights, hence, the statements can not be considered as statistically significant. However, the results give a clear advice on the potential of the TL method. This conclusion is in a good agreement with according results obtained with the TZK2-D of Hannover (Hirt and Seeber [2007a], (Hirt and Seeber [2007b]). There, the replacement of the azimuth calibration by the tripod method allowed likewise for an increased accuracy in the determination of DOV .

7 Research area *North Aegean Sea*

7.1 Introduction

From the early seventies on, systematic attempts for precise geoid determinations have been carried out in the Hellenic area (Tziavos and Andritsanos [1999]). The first Hellenic geoid has been presented by Balodimos [1972] using astrogeodetic deflections of the vertical (DOV). Arabelos [1980] calculated a gravimetric solution. A first combined geoid from astrogeodetic and gravimetric data has been computed by Tziavos [1984]. Another geoid determination has been presented by Doufexopoulou-Patsada [1985] with emphasis on geophysical parameters related to the gravity field. Fotiou et al. [1986] published the first comparison between the various geoid solutions in the Hellenic area. A more detailed gravimetric geoid solution has been presented by Arabelos and Tziavos [1989]. In Arabelos and Tziavos [1990], a comparison between the gravimetric geoid for the southern Hellenic area and Geosat altimetry data has been performed.

The recent gravimetric geoid solution HGFFT98 for the Hellenic area has been presented by Tziavos and Andritsanos [1999] and is outlined in chapter 7.3.3. Due to a lack of gravity data in the marine area, the solution suffers for long-wavelength errors (Müller et al. [2006]). Aiming at the provision of additional and independent data sets for an improved local geoid solution, a dedicated campaign was carried out in May 2005. It was realized in the frame of a joint project between the Geodesy and Geodynamics Laboratory (GGL) of ETH Zurich, and the Department of Geodesy and Surveying (DGS) of the Aristotle University of Thessaloniki (AUTH). The research area is situated within $38° < \varphi < 42°$ northern latitude and $22° < \lambda < 27°$ eastern longitude and covers the North Aegean Sea. The region is dominated by the North Aegean Trough (NAT), which is considered to be a continuation of the seismically active North Anatolian Fault Zone (Karakaisis and Papazachos [2002]). Different methods for geoid determination have been applied including astrogeodetic observations with the digital Zenith Camera DIADEM aiming at the determination of highly-precise DOV. Furthermore, GPS boat and buoy measurements have been performed determining Sea Surface Heights (SSH). These data have been used to compute an Astro geoid (based on DOV) and a combined geoid solution (based on DOV and SSH corrected for marine effects), respectively. Chapter 7.2 gives a survey of the topographic/bathymetric, geological and geophysical features of the research area. In chapter 7.3, available geoid models in the research area are introduced, whereas in chapter 7.4, the gathered data are presented and discussed.

7.2 Domain characteristics

7.2.1 Topography, bathymetry and geology

Fig. 7.1 shows the topography and bathymetry of the research area in the North Aegean Sea in Greece based on the SRTM30 data presented in chapter 8.3.

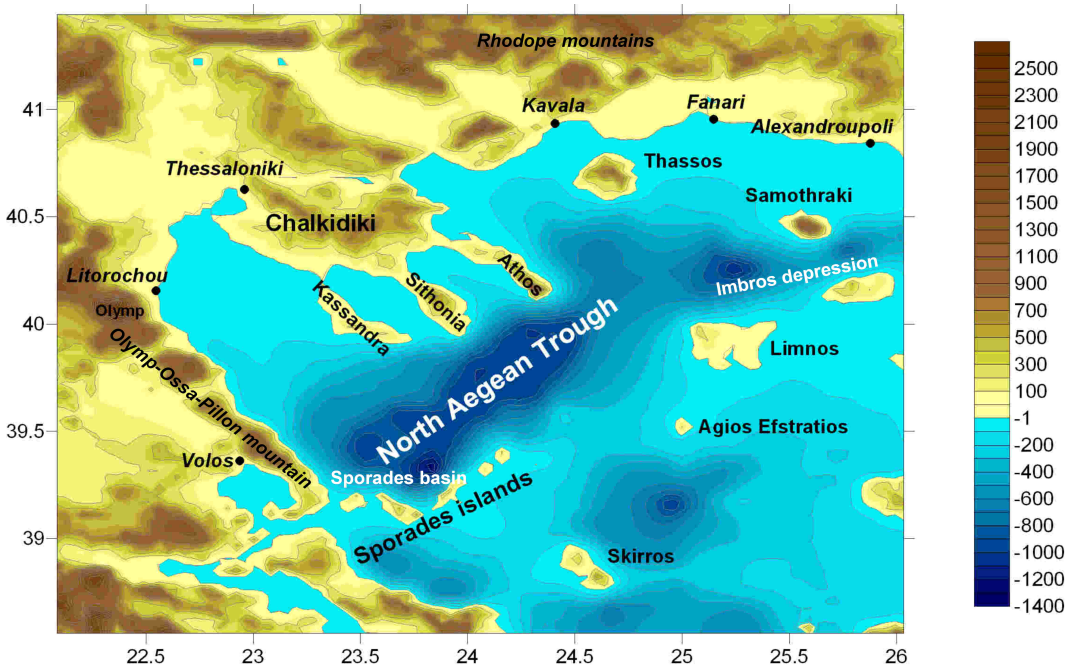

Figure 7.1: Research area in Greece. The North Aegean Trough is characterized by two main depressions: the Sporades basin and the Imbros depression.

The marine area is dominated by the NAT forming an elongate zone of deep water. It is a result of the tectonic activities in the research area, which are explained in detail in chapter 7.2.2. The NAT extends in SW-NE-direction between the Sporades islands, the islands of Limnos, Samothraki and Thassos as well as the peninsula of Chalkidiki. It is characterized by two main depressions: The eastern depression between the islands of Samothraki to the north and Limnos and Imbros to the south is called Imbros depression and features a system of narrow V-shaped valleys with a maximum depth of -1000 m. Furthermore, a wide flat-bottom basin called Sporades basin is located north of the Sporades islands, with a maximum depth of -1500 m (Mascle and Martin [1990]).

The topography in the research area varies strongly showing mountainous regions alternating with very flat regions. The Olympus-Ossa-Pilion mountain range extends along the western coastline with the highest elevation of Greece: mount Olympus (2900 m). The region west of Thessaloniki is characterized by a flat plane, whereas the peninsula of Chalkidiki is again mountainous with a prominent elevation of about 2000 m at the southern point of Athos (mount Athos). Northern Greece is dominated by the foothills of the Rhodope mountains, which extend until Kavala with elevations of about 1700 m. The northern coastline between Kavala and Alexandroupoli is again flat. The island of Samothraki features an interesting topography with the Fengari mountain featuring an

elevation of 1600 m. Also the bathymetry south of the island shows strong variations with depths amounting to -1000 m. The characteristics described play an important role in the course of the interpretation of the observed DOV, which mainly reflect topographic and bathymetric features (chapter 7.4.1). The topographic and bathymetric data are used for the reduction of the DOV (chapter 8.6).

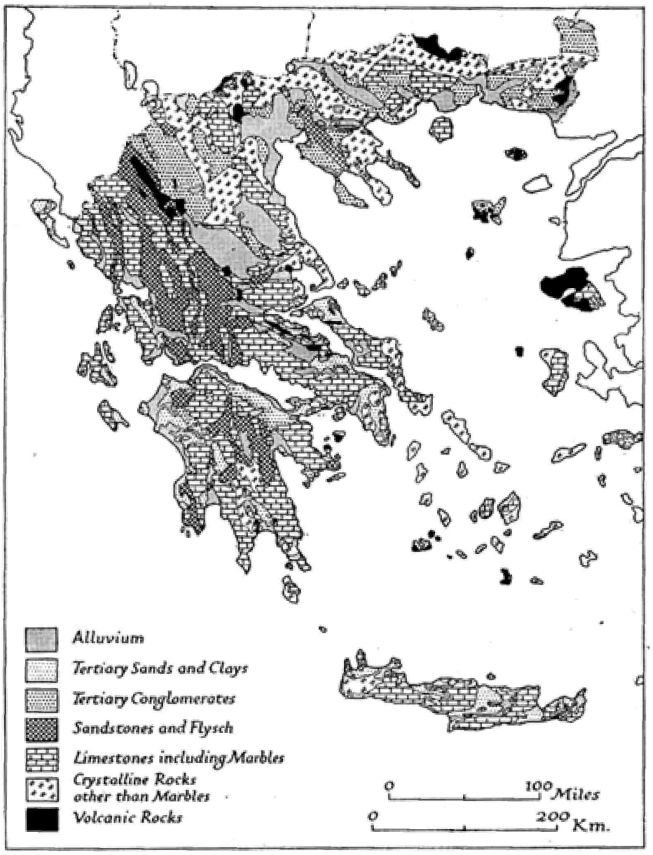

Figure 7.2: Generalized map of density variations in Greece (Naval Intelligence Division [1944]).

Fig. 7.2 shows the density variations in Greece. The map indicates the appearance of alluvium, limestones, crystalline rocks, sandstones, flysch, tertiary sands and clays as well as tertiary conglomerates. The densities of these rocks are generally specified with 1.6 g/cm^3 (clay) to 3 g/cm^3 (volcanic rocks), hence showing a relatively wide range. In addition, Fig. 7.3 indicates the occurrence of large plio-quaternary sedimentary basins in the North Aegean Sea. The sediment layers are relatively thick and mainly terrigenous[1]. According to Mascle and Martin [1990], they give evidence of important vertical displacements in the form of uplift and subsidence, often accompanied by gravity-induced processes (slumps and mass sliding).

Unfortunately, a digital density model for Greece is not available, therefore, it was not possible to consider suitable density distributions. Instead, a mean density of 2.67 g/cm^3 has been used for the topography. For the marine area, a density contrast of 1.67 g/cm^3 has been assumed resulting from the difference between the densities of oceanic crust (2.67 g/cm^3) and water (1 g/cm^3). In order to estimate the effect of different densities

[1] terrigenous = material derived from the erosion of rock on land

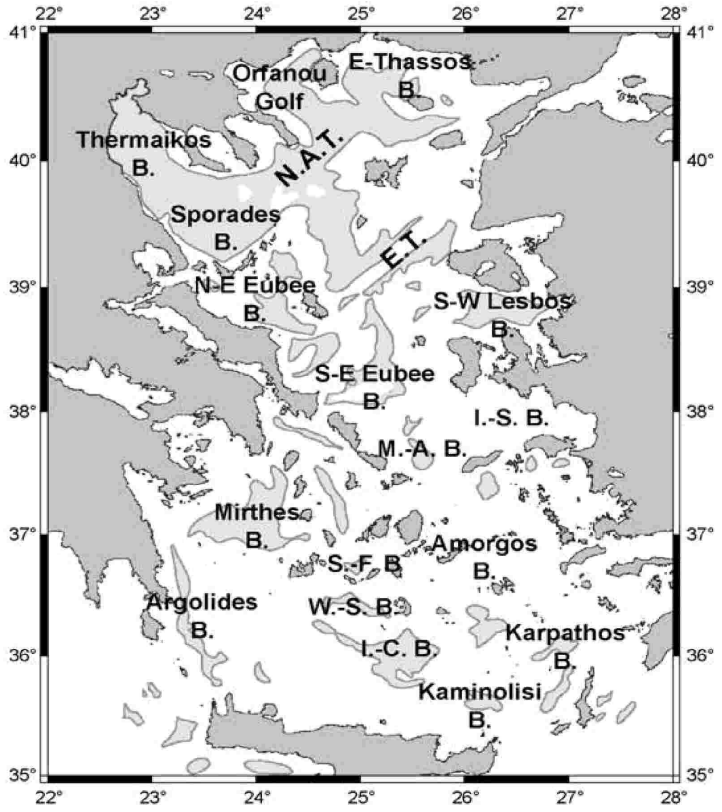

Figure 7.3: Appearance of plio-quaternary sedimentary basins in the Aegean Sea.

on the DOV, a dedicated analysis has been performed at the example of the island of Samothraki (chapter 8.7.3).

7.2.2 Deformation field and active tectonics in the Aegean region

A high level of seismicity and numerous evidences of active tectonic deformations provoked elaborate studies of the Aegean region, e.g. by McKenzie [1972], Le Pichon and Angelier [1979] and McClusky et al. [2000]). In order to understand the implications of tectonics for deformation, seismological data, active fault distributions as well as sea floor bathymetry data have been used to define the major tectonic boundaries of the Aegean (Nyst and Thatcher [2004]).

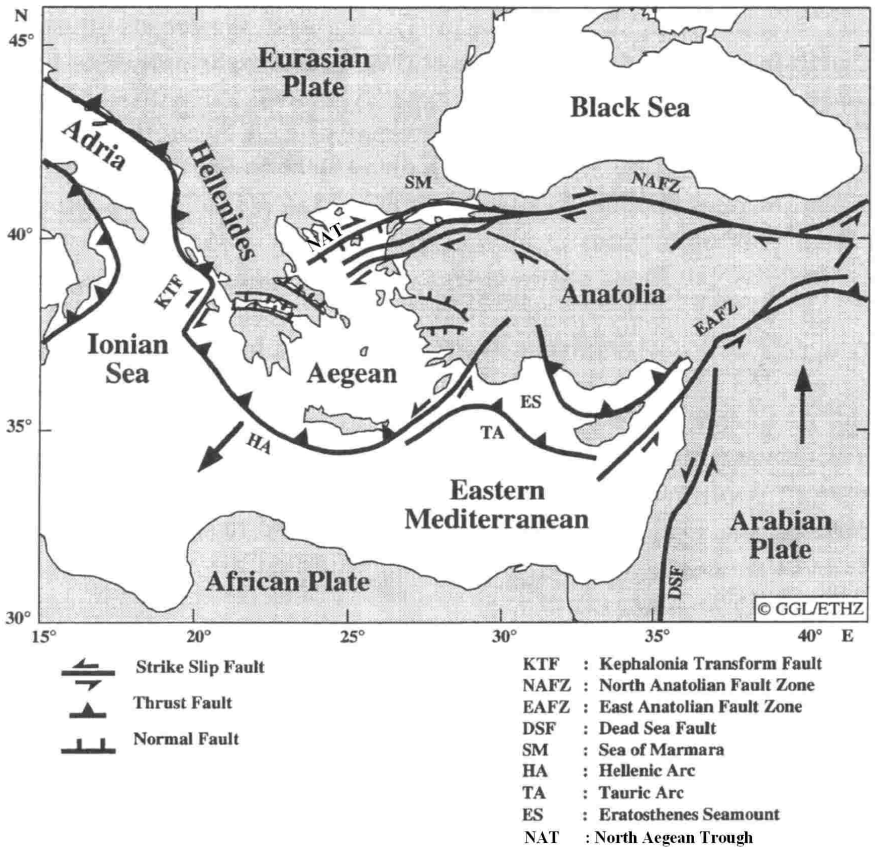

Figure 7.4: Simplified tectonic settings of the Eastern Mediterranean (Kahle and Müller [1998]).

The main tectonic element of the Aegean domain is the Hellenic Arc induced by the subduction of the African plate beneath Eurasia (Fig. 7.4). It forms a "semicircle" from the Ionian islands to south-west Anatolia (Kahle et al. [1999]). The Hellenic Arc is an example for a retreating subduction boundary, where the rate of convergence (10 mm/yr) is less than the rate of subduction. The second tectonic attribute of the Aegean domain is formed by the west-southwestward motion of the Anatolian-Aegean microplate. It can be described as a superposition of a westward motion of Anatolia and a fast southwestward movement of the Aegean. The westward motion of Anatolia can be interpreted as an extrusion caused by the northward push of the Arabian plate. Though the extrusion of Anatolia contributes to the southwestward motion of the northern Aegean, the main reason for the movement of the southern Aegean is back-arc extension in response to the retreat of the Hellenic subduction system (Hollenstein [2006]).

In Hollenstein [2006], velocities of the described motions in the Aegean region, inferred from GPS networks and campaigns, are published. The velocities in Fig. 7.5 are given relative to Eurasia. The rates increase from about 20-26 mm/yr in the northeastern part of the Aegean up to 30-36 mm/yr in the southwest. A prominent feature in the Aegean is formed by the North Aegean Trough (NAT), which is thought to be the continuation of the North Anatolian Fault Zone. Regarding the velocity field in the northern Aegean, the NAT separates the slow south-southwestward motion of northeastern Greece from the fast west-southwest directed motion of the Anatolian-Aegean microplate. Furthermore, the analysis of seismic data (e.g. Hatzfeld et al. [1999]) showed that the borders of the

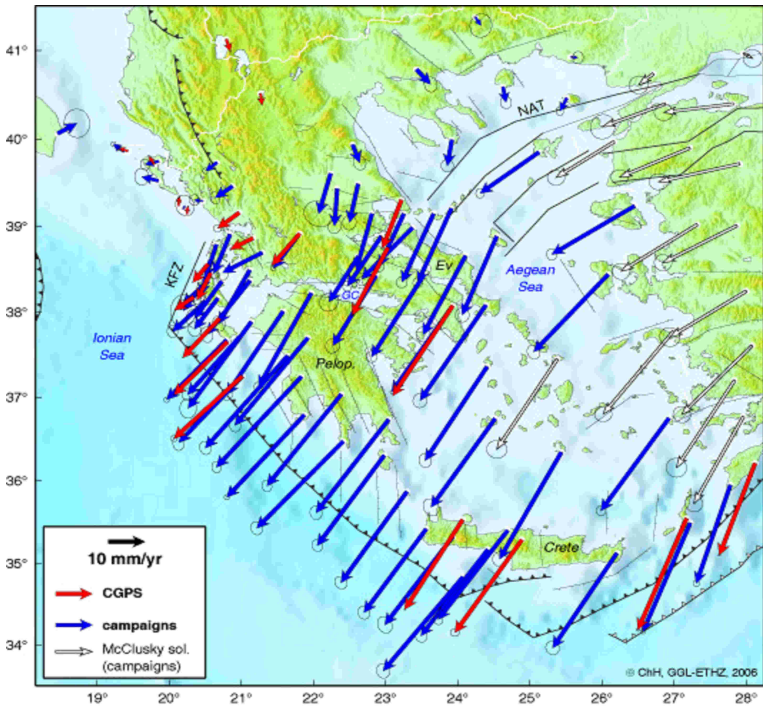

Figure 7.5: GPS velocities for the region of Greece, relative to Eurasia, for the period 1993-2003. The McClusky solutions are published in McClusky et al. [2000]. The error ellipses define the 1-sigma confidence region (Hollenstein [2006]).

Anatolian-Aegean microplate feature the highest concentration of large earthquakes in the Mediterranean region.

7.3 Available data

7.3.1 Earth Geopotential Model *EGM96*

EGM96 stands for Earth Geopotential Model 1996 and consists of spherical harmonic coefficients complete to degree and order 360. It represents the long-wavelength characteristic of the earth's gravity field. The model is the result of a collaboration between the National Imagery and Mapping Agency (NIMA), the NASA Goddard Space Flight Center and the Ohio State University. It includes improved surface gravity data, altimeter-derived anomalies from ERS-1 and GEOSAT Geodetic Mission, satellite tracking data as well as direct altimeter ranges from TOPEX/POSEIDON, ERS-1 and GEOSAT (Lemoine et al. [1998]).

Fig. 7.6 shows a detail of the EGM96 for the research area in the North Aegean Sea. The geoid heights are given with respect to the WGS84. Due to the long-wavelength character of the geoid, the influence of the NAT is not included. The mean geoid height in the plotted area amounts to 40.4 m, with variations between 32.2 m and 45 m.

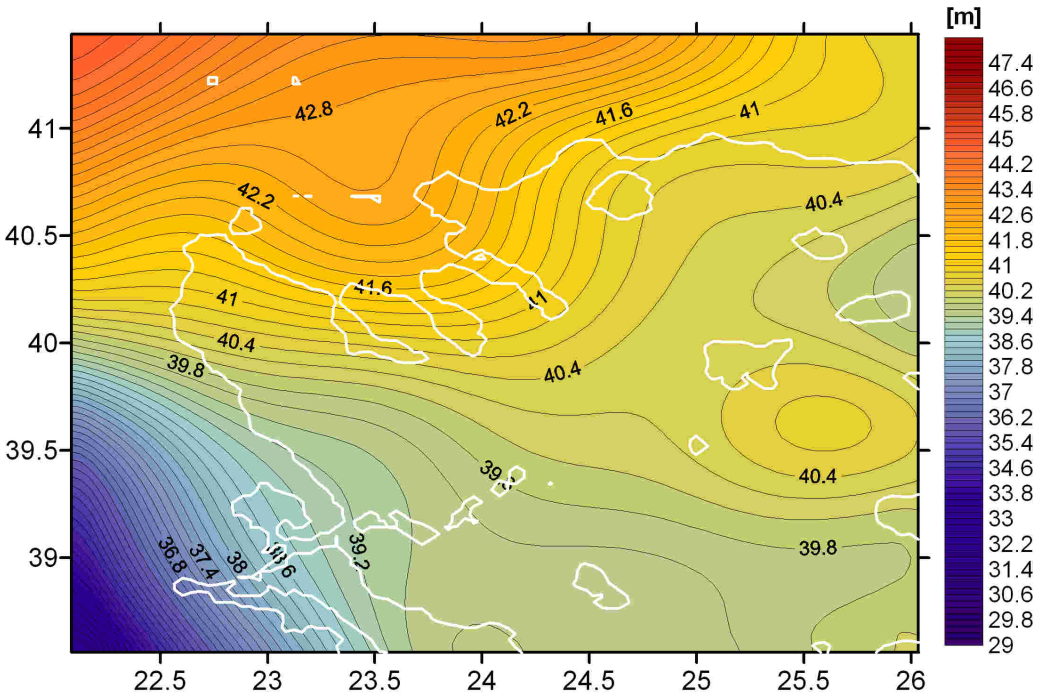

Figure 7.6: Detail of the European Gravity Model EGM96 representing the research area in the North Aegean Sea. The geoid heights in the plotted area vary between 32.2 m and 45 m showing the long-wavelength characteristic of the earth's gravity field.

7.3.2 GRACE Gravity Model *GGM02*

The Gravity Recovery And Climate Experiment (GRACE) is a joint mission between the National Aeronautics and Space Administration and the German Aerospace Center (NASA/DLR) aiming on the mapping of the time-variable and mean gravity field of the earth. In March 2002, the GRACE twin satellites have been launched measuring continuously the varying distance between the satellites. This allows for the detection of changes in the earth's gravity field. Based on approximately 14 months of data gathered in 2002 and 2003, a new generation of gravity field models called GGM02 was derived (Tapley et al. [2005]).

There exist two versions of the GGM02:

* GGM02S: The model was estimated to degree and order 160, with no constraints or regularizations included. It is a combination of 14 monthly gravity field solutions used for the computation of a mean gravity field model.
* GGM02C: In order to create a complete mean earth geopotential model up to higher degrees, the GGM02S model information were combined together with terrestrial gravity information (surface gravity and mean sea surface). The terrestrial data were introduced in terms of spherical harmonic coefficients of the EGM96. To constrain the higher degrees to the harmonic coefficients of the EGM96, the TEG4 (Texas Earth Gravity model 4) error covariances were used, which are complete to degree and order 200. The GGM02C model is computed to degree and order 200 and can be smoothly extended to degree and order 360 by using the EGM96 coefficients.

Fig. 7.7 shows a detail of the GGM02C for the research area in the North Aegean Sea. The mean geoid height in the plotted area amounts to 40.7 m and vary between 32.7 m and 45.7 m.

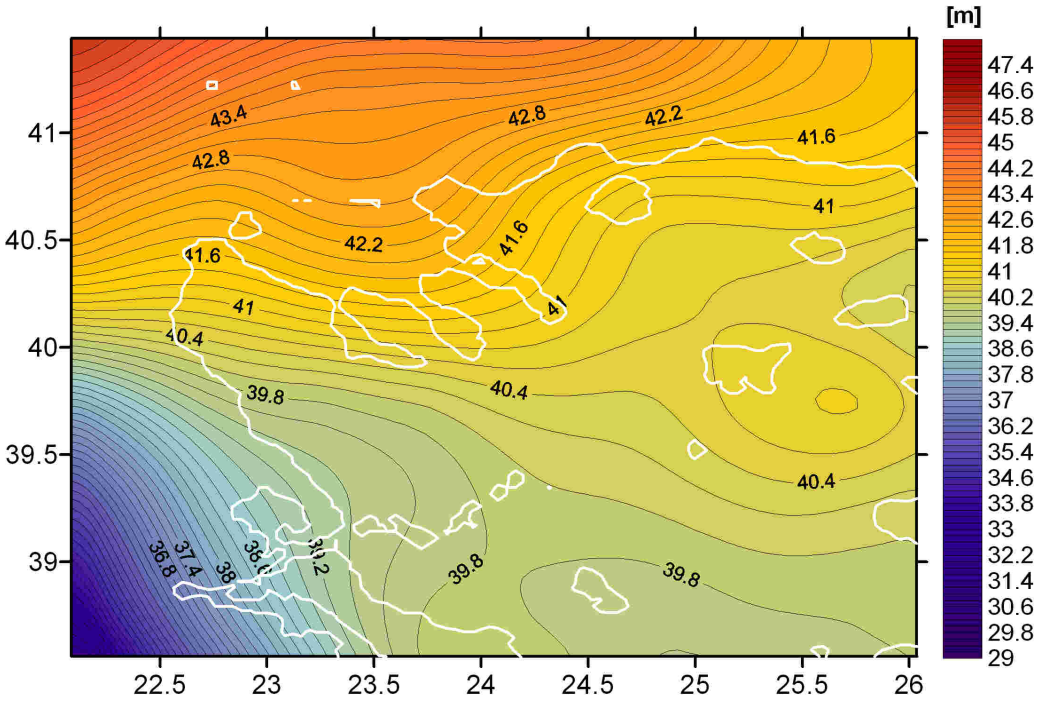

Figure 7.7: Detail of the GRACE Gravity Model GGM02C for the research area in the North Aegean Sea. The geoid heights in the plotted area vary between 32.7 m and 45.7 m.

7.3.3 Gravimetric geoid *HGFFT98*

In Tziavos and Andritsanos [1999], the gravimetric geoid solution for the Hellenic area, called HGFFT98, has been presented. The computation area is within $34° < \varphi < 42°$ northern latitude and $18° < \lambda < 29°$ eastern longitude. The development of the model was based on an optimal combination of different data sets. Hence, free-air gravity anomalies from old and new data bases have been selected for the land area (19700 values). Also GPS/leveling heights were introduced. The marine gravity data were derived from an inversion of satellite altimetry data from GEOSAT and ERS-1 geodetic missions (5900 values) and a digitization of Morelli's sea gravity maps (51000 values). Totally, 77000 point free-air gravity anomalies have been selected for the computation of the gravimetric geoid. Furthermore, a 1 km x 1 km digital terrain model, the GTOPO30 from the U.S. Geological Survey, has been introduced. The EGM96 geopotential model (chapter 7.3.1) served as reference field, hence providing the long-wavelength signal of the global gravity field. The combined solution was determined using the FFT-based MIMOS Theory (=Fast Fourier Transformation-based Multiple Input-Multiple Output System Theory) presented by Andritsanos [2000] and Andritsanos et al. [2001], respectively (Müller et al. [2006]).

The final HGFFT98 model has been validated by other available geoid models for the test area. A first comparison with the current European Gravimetric Geoid 1997 (EGG97)

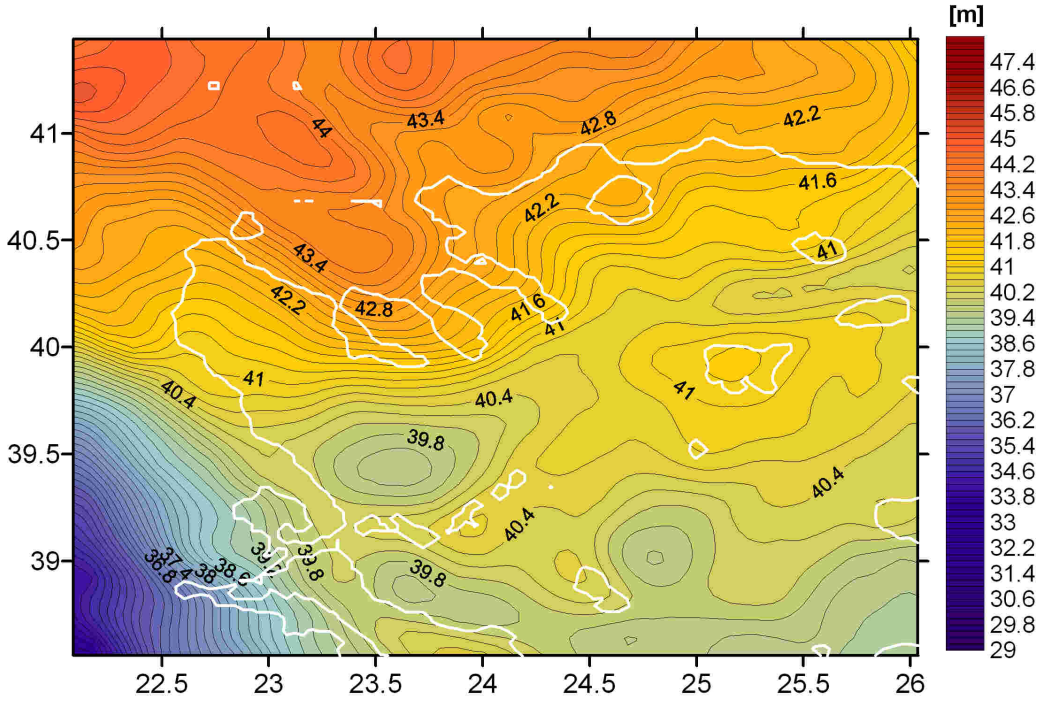

Figure 7.8: Detail of the gravimetric geoid (Tziavos and Andritsanos [1999]) representing the research area in the North Aegean Sea. The geoid heights in the plotted area vary between 33.5 m and 45.1 m.

showed an agreement of about 75 cm standard deviation. A second comparison in the continental area with 29 GPS/leveling stations in northern Greece and 10 stations in the central-western part of Greece revealed an accuracy of 8.7 cm and 2.9 cm, respectively. A third comparison was made in the marine area between the HGFFT98 heights and a number of TOPEX/Poseidon derived SSH. The differences showed significantly larger values than the continental area, with standard deviations of 31.2 cm in the North Aegean Sea and of 16.4 cm in the South Aegean Sea and the central Mediterranean. These results demonstrate the strong need for an improvement of the geoid model, especially in the marine area. This can be mainly achieved by filling the data gaps there. Fig. 7.8 represents a detail of the HGFFT98 for the research area in the North Aegean Sea. The mean geoid height amounts to 41.1 m ranging between 33.5 m and 45.1 m. The gravimetric geoid clearly indicates the influence of the NAT by varying geoid heights of about 2.6 m when crossing the marine area between the Chalkidiki peninsula to the north and the Sporades islands to the south.

7.3.4 Altimetric geoid

The altimetric geoid model used as validation data set was computed by the DGS (AUTH) using altimetric data from the Exact Repeat mission of ERS-1/2 and TOPEX/Poseidon. The ERS-1 data (95576 point values) are taken from the 35-day ERM mission 1992/1993 and 1995, respectively. From ERS-2, six years of data have been used (368617 point values) covering the period between 1995 and 2001. Finally, nine years of the Topex/Poseidon derived SSH were employed (488634 point values) covering the period between 1992 and 2001.

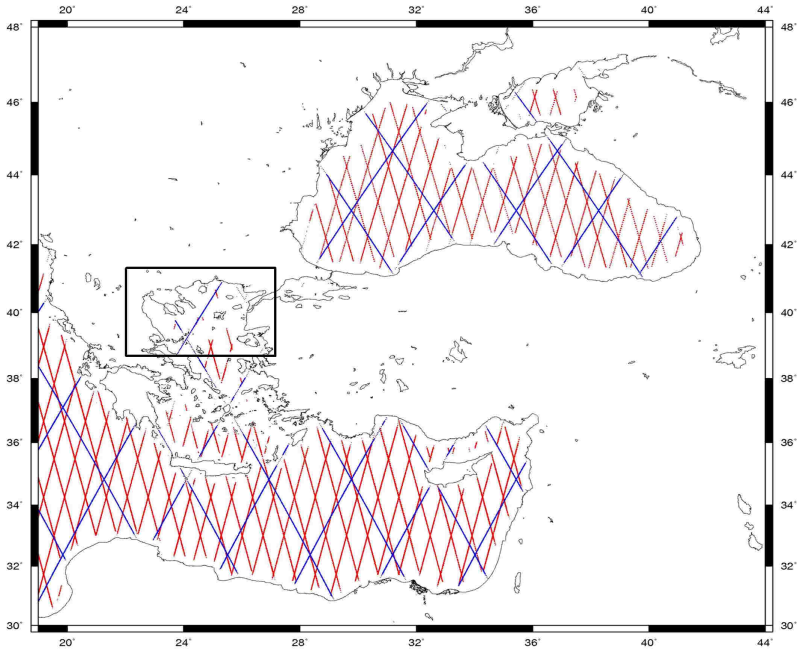

Figure 7.9: Area for the development of the altimetric geoid and course of ERS-1, ERS-2 (red) and T/P (blue) tracks. The research area of the North Aegean Sea is signalized by the black frame.

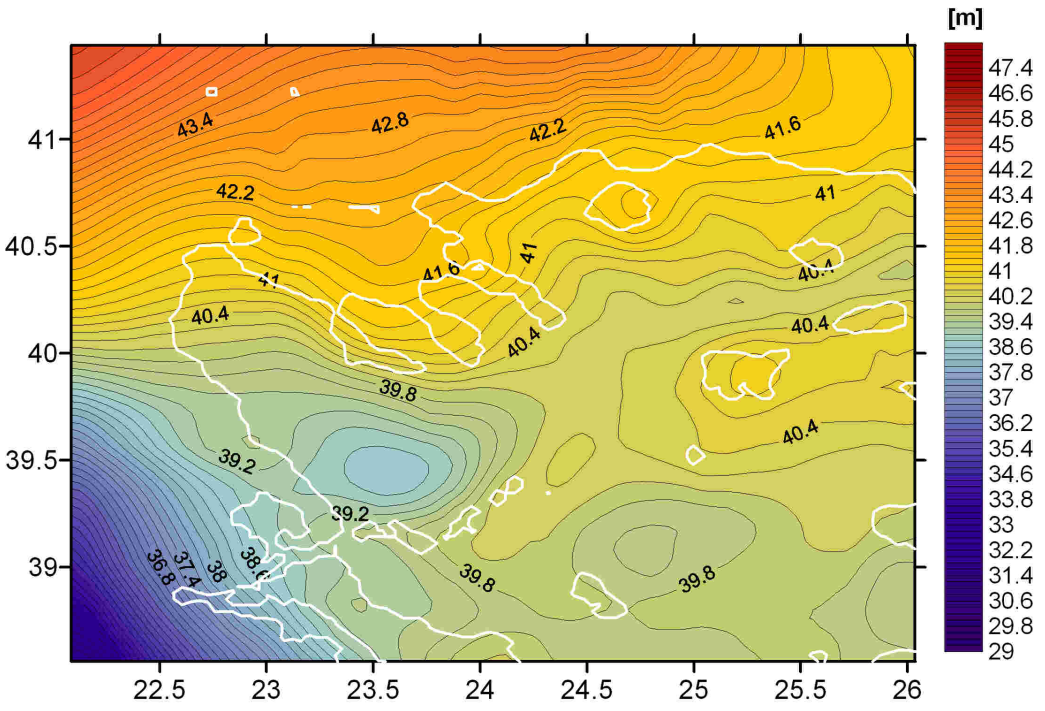

Figure 7.10: Detail of the altimetric geoid representing the research area in the North Aegean Sea. The geoid heights in the plotted area vary between 32.4 m and 45.5 m.

The final altimetric model forms a combination of all data sets employing least-squares-collocation and using the Remove-Restore method (Tziavos et al. [2005]). Hereby, the global geopotential solution EGM96 and the effects of the bathymetry have been taken into account. In addition, the altimetric SSH have been crossover adjusted and stacked. Hence, data over a much wider region than the area under study were used (Fig. 7.9). Moreover, the altimetric data have been reduced from the sea surface to the geoid using a local sea surface topography model developed by Rio [2004]. A detailed review of methods for the computation of altimetric geoid models either by stochastic or spectral techniques is given by Vergos et al. [2005].

Regarding the traces of the ERS-1/2 and T/P satellites within the project area in the North Aegean Sea (black frame in Fig. 7.9), it becomes obvious that only very few data are available there. This can be mainly attributed to the fact that altimeter satellites do not receive radar signals over land and in marine areas with low depths of water, as e.g. close to coastlines. The resulting lack of data in the North Aegean Sea might cause a weak geoid solution in the marine area. A detail of the final altimetric geoid model for the research area in the North Aegean Sea is depicted in Fig. 7.10. The mean geoid height amounts to 40.5 m ranging between 32.4 m and 45.5 m. Similar to the gravimetric geoid, the altimetric geoid clearly indicates the influence of the NAT by varying geoid heights of about 2.4 m, when crossing the sea between the peninsula of Chalkidiki to the north and the Sporades islands to the south.

7.4 Data acquisition

7.4.1 Determination of deflections of the vertical

The distribution of Astro stations was mainly motivated by the intention to cover the area around the NAT. The trough forms an important geological feature of the test area (see chapter 7.2.2). The observations with DIADEM were carried out along the shoreline of the North Aegean Sea including the Sporades islands (Skiathos, Skopelos, Alonissos, Kira Panagia, Psathoura) and the islands of Thassos, Samothraki, Limnos and Agios Efstratios (Fig. 7.12). Fig. 7.11 shows the preparation of an observation on the island of Kira Panagia. Details concerning the instrument and the measuring principle can be found in chapter 3.

In total, 27 stations have been observed in 20 nights yielding an average of one to two stations per night. At each station, about 80 to 120 single solutions have been observed and used for the determination of the direction of the vertical (Φ, Λ). During the whole campaign, the method of azimuth calibration has been applied (chapter 4.4.1). The time needed per station was about one to two hours including GPS measurements. At each observation point, differential GPS measurements during about 30 minutes have been performed applying a two-frequency Trimble receiver (see Fig. 7.11). The final geodetic coordinates (φ, λ) have been determined in post-processing by a network equalization using recent ITRF2000 coordinates from four different reference stations (Alonissos, Limnos, Agios Efstratios, Nisi). The accuracy of the geodetic position is better than 0.01 arcsec corresponding to a lateral displacement at the earth's surface of

Figure 7.11: Preparation of an observation with DIADEM on the island of Kira Panagia. The ton served as shipping container for DIADEM. For the transportation by boat, the ton has been mounted at the stern (Fig. 7.13***b)***). In order to perform differential GPS measurements, a GPS antenna is temporarily fixed on top of DIADEM. The antenna is removed when starting the DIADEM observations.

0.3 m. The standard deviation of the final deflections of the vertical is better than 0.2 arcsec.

The DOV (ξ, η) are shown in Fig. 7.12. The absolute values vary between 0.8 arcsec (Sporades islands) and 23.7 arcsec (island of Samothraki, eastern station). The vectors indicate the impact of surrounding masses. Hence, the DOV on the three peninsulas of Chalkidiki, on the Sporades islands and on the islands of Thassos, Samothraki and Limnos denote a decreasing geoid in direction to the NAT. The trough forms a distinct mass deficit with respect to the surrounding area. An interesting station is Kipos, the eastern station on the island of Samothraki. It is striking that the DOV there is about five times larger than on the western station (Kamariotissa) and nearly points to an opposite direction. This is mainly due to topographic and bathymetric features encountered there. The bathymetry at Kipos side shows a very steep gradient caused by the trough between Limnos and Samothraki (Imbros depression), while at Kamariotissa the relief is much less inclined. The topography of the island is characterized by the Fengari mountain with an elevation of about to 1600 m. This topographic mass excess causes larger gravity effects in the SE than in the NW of the island.

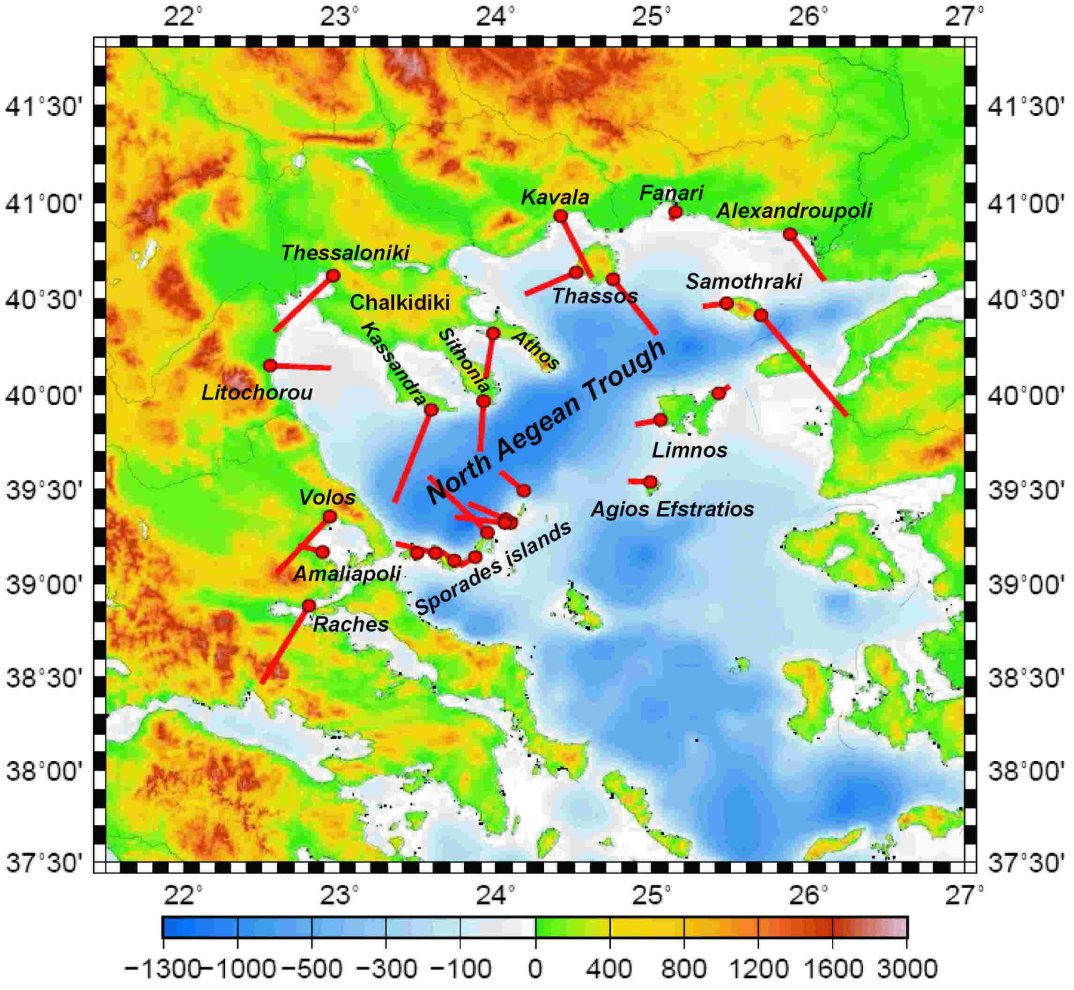

Figure 7.12: DOV observed at 27 stations in the North Aegean Sea. The vectors reflect the DOV projected into a horizontal plane (components are equal to ξ and η). The DOV vary between 0.8 arcsec (Sporades islands) and 23.7 arcsec (Island of Samothraki, eastern station).

7.4.2 Determination of Sea Surface Heights

In addition to the determination of DOV, shipborne multi-antenna GPS as well as GPS buoy measurements took place (Limpach et al. [2006] and Müller et al. [2006]) aiming at the precise determination of SSH (Fig. 7.13).

a) Waterproofed buoy equipped with GPS receiver, antenna and battery.

b) Boat equipped with four GPS antennas, indicated by the arrows. The Zenith Camera was mounted within the ton at the stern of the boat.

Figure 7.13: Mobile marine research platforms: buoy and sailing boat.

The SSH data provide local-scale information on the short-wavelength structure of the gravity field and can be applied to improve local marine geoid solutions. They also contain information on the local dynamic ocean topography (DOT) and can be used for the validation and calibration of radar altimeter satellites. Last but not least, the SSH data provide a link between offshore radar altimeter data and tide-gauge records.

In order to achieve a highly-precise GPS positioning of the buoys and the boat, the buoy receivers, the receivers aboard the boat and several permanent terrestrial GPS reference stations have been operated simultaneously at a sampling rate of 1 Hz. The coordinates of the reference stations were first determined with respect to the ITRF reference frame. The kinematic positions of the buoys and the boat were then determined through differential GPS carrier phase processing with respect to the reference stations. In order to derive the Sea Surface Topography (SST) from the instantaneous SSH, several corrections have to be applied, especially for tides and atmospheric effects (inverse barometric effect). The tide corrections have been provided by E.C.Pavlis from the Joint Center for Earth Systems Technology (JCET) using the GOT00.2 tidal model (Arabelos et al. [2007]). The local tidal effects have been determined using own tide gauges installed in the survey area. The inverse barometer corrections have been computed over the entire Mediterranean Sea using atmospheric pressure data from the European Center for Medium-Range Weather Forecasts (ECMWF).

Fig. 7.14 shows the Astro stations (chapter 7.4.1) as well as the SSH tracks from two different GPS surveys in 2004 and 2005. The SSH data cover more than 1000 nautical miles of ship tracks. For the calibration and validation of radar altimeter missions, the survey area has been defined in the vicinity of Jason-1 ground-tracks. Dedicated buoy measurements have been performed along these tracks including deployments with direct Jason-1 cross-overs, which provide precise ground-truth SSH information during the overflight.

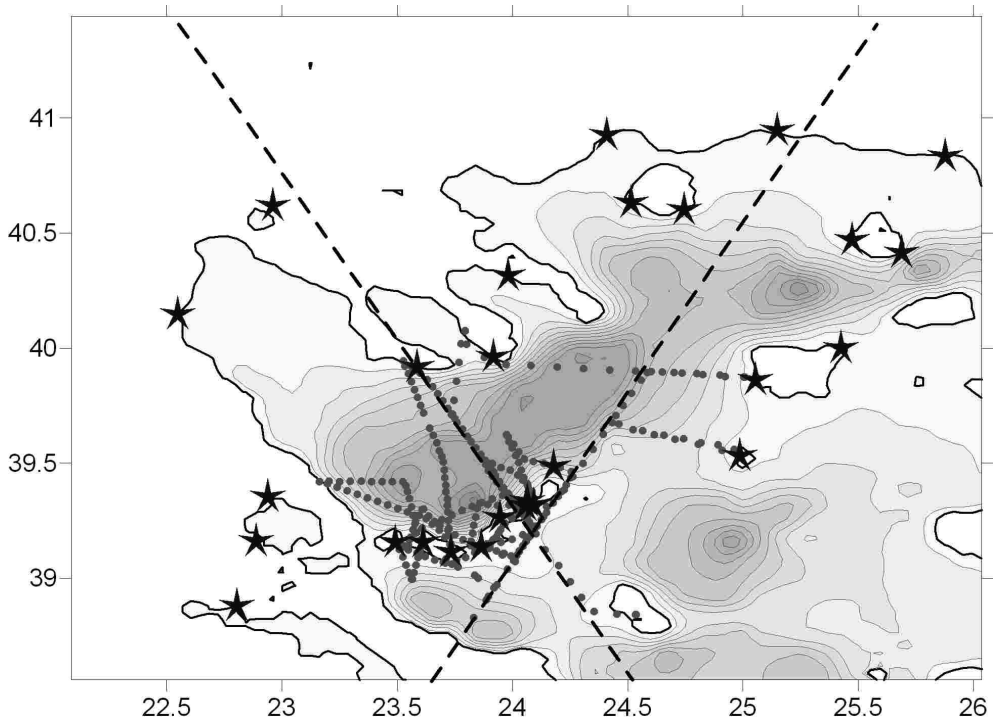

Figure 7.14: DOV (stars) and SSH (points) used for combined geoid determination. The altimetric data provided by the JASON altimeter satellite (dashed lines) have been used for calibration purposes.

Fig. 7.15 presents the color-coded SSH. A minimum of 37.5 m (above WGS84 ellipsoid) is associated with a distinct bathymetric low caused by the NAT. The SSH increase to about 40.5 m towards the northern and eastern part of the survey area.

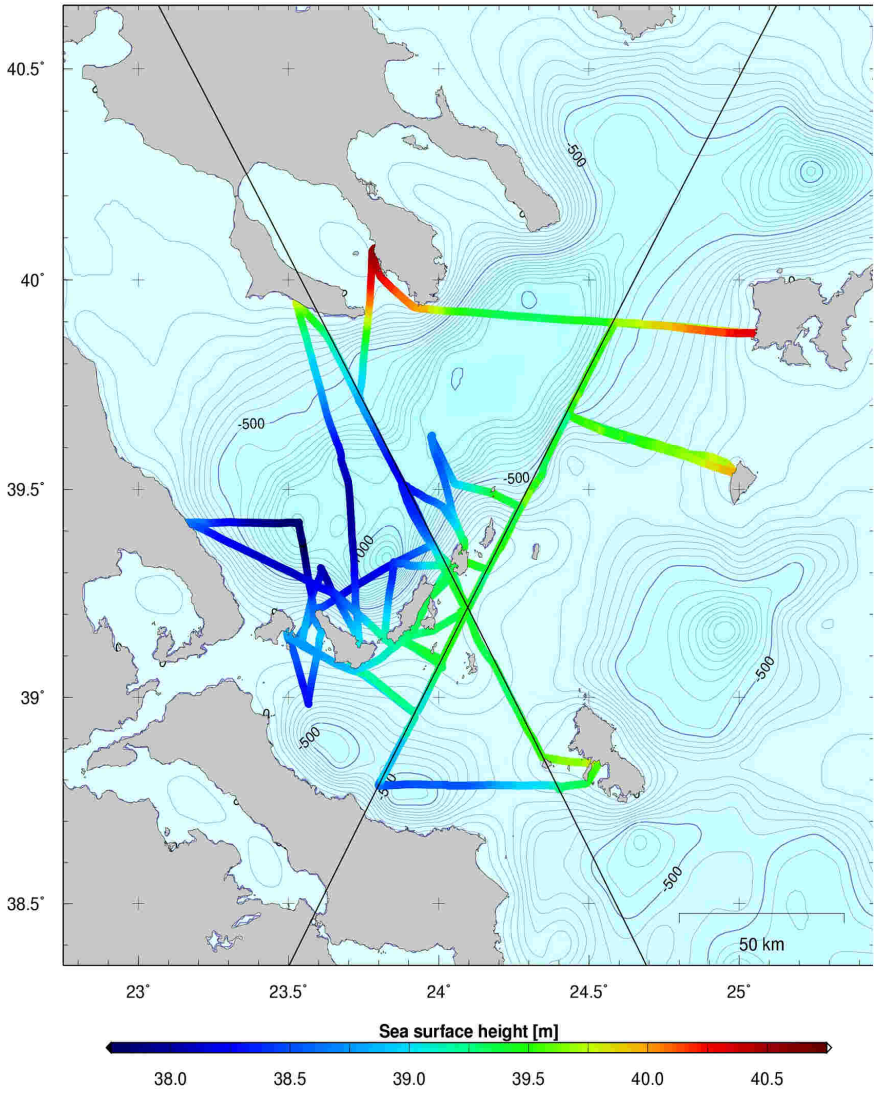

Figure 7.15: Color-coded SSH from combined shipborne/buoy GPS observations. The minimum of 37.5 m coincides with the distinct bathymetric low of the NAT. Towards north and east, the SSH increase to about 40.5 m. Black lines: Jason-1 ground-tracks, background: Bathymetry (Limpach et al. [2006]).

The SSH contain impacts of the above mentioned local DOT, mainly caused by ocean currents, wind, salinity and different temperatures. The Mean Dynamic Ocean Topography (MDOT) for the research area provided by the Aristotle University of Thessaloniki allows for the correction of these effects. Fig. 7.16 reflects the variations of the MDOT within the research area of the North Aegean Sea. The variations range between 2 cm and 5 cm along the boat tracks. They show a mainly constant level of about 5 cm in the area between the peninsula of Chalkidiki and the Sporades islands.

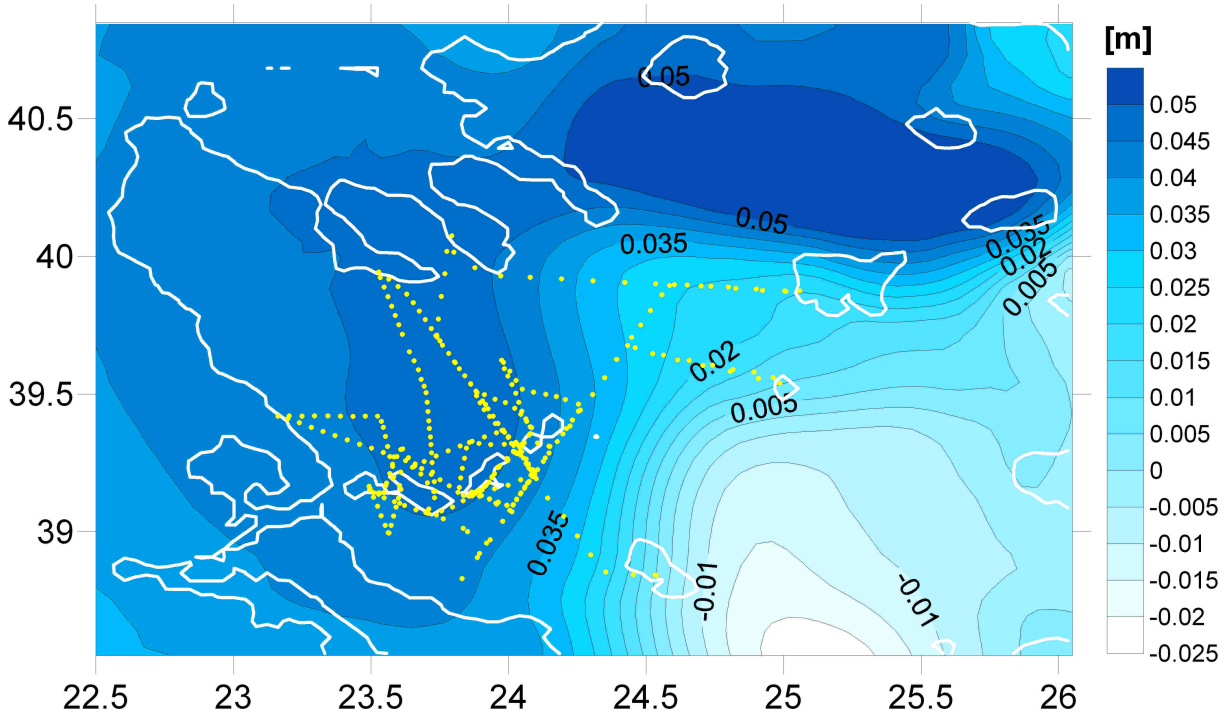

Figure 7.16: Mean Dynamic Ocean Topography (MDOT), provided by the DGS/AUTH. The yellow points indicate the shipborne GPS measurements.

The DOV and the corrected SSH have been used for a combined geoid determination. The resulting geoid is presented in chapter 9.3.4.

8 Mass reductions

8.1 Introduction

Deflections of the vertical (DOV) reflect the mass distributions of the station vicinity (Torge [2001]). Especially in areas with changing topography and complex geological structures, they might show a very unsettled behavior and are, therefore, not suitable for a precise interpolation of the gravity field. The smoothing of the data can be achieved by considering mass effects, which produce high- and low-frequency perturbations of the gravity field. By using information from topography, density and isostatic models, the influence on the DOV-components ξ and η can be computed and subtracted from the raw observations. The residual data show then a significantly smoother behavior. This enables the interpolation of the gravity field with an adequate accuracy, also for mountainous regions (Marti [2004]).

In case all known masses have been removed, the residual DOV mainly reflect unmodeled masses, density anomalies and, on a small scale, errors of the astrogeodetic measuring method. The reduced data form a valuable data set for the interpretation of geological, geodynamic and geophysical features of the region. Hence, deep-rooted anomalous bodies might be detected, as it has been demonstrated by Bürki [1989] at the example of the Ivrea body in Switzerland.

The mathematical background for the computation of gravitational potential and attraction from masses refers to Mader [1951] and is described in chapter 8.2. The different mass models used, like the Digital Terrain Model (DTM) from the Shuttle Radar Topography Mission, isostatic models as well as a Moho model, are presented in chapters 8.3, 8.4 and 8.5. The reduced DOV are discussed in chapter 8.6.

For the interpolation of the residual data, the least-squares-collocation (LSC) has been found to be an adequate method. Besides, this procedure allows for the common introduction of different data sets for a combined interpolation of the gravity field (Wirth [1990]). The method is described in chapter 9.2. The resulting cogeoid solutions representing a "geoid subtracted for dedicated masses" are presented and interpreted in chapters 9.3.1 and 9.3.2.

In the course of the final geoid computation, the subtracted masses have to be restored. The final geoid solutions are anaylsed in chapters 9.3.3 and 9.3.4. The whole process of **removing** and **restoring** masses is called **Remove-Restore method** and is commonly used for geoid determinations (Gurtner [1978], Forsberg and Tscherning [1981], Marti [1997]).

8.2 Computation of mass effects

Due to the complex structure of topography, it is difficult to describe the surface by closed analytical forms. Therefore, the DTM is mostly represented by discrete points with horizontal coordinates and corresponding heights. The type of horizontal coordinates (e.g. orthogonal-cartesian (x,y) or geographical coordinates (φ, λ)) specifies a possible segmentation of the model producing simple geometrical figures. They form the basis for the application of the *law of gravitation after Newton* aiming at the computation of gravitational attractions. Orthogonal-cartesian coordinates suggest a segmentation into *cuboids*, while geographical coordinates define so called *tesseroids*. If in spite of given geographical coordinates the "cuboid method" is preferred, the tesseroids have to be replaced by cuboids which approach best possible the volume and height of the tesseroid (see Fig. 8.1).

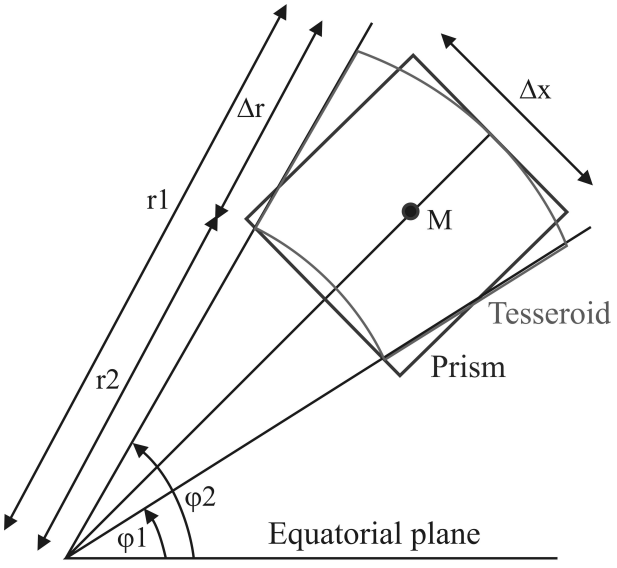

Figure 8.1: Principle of replacing a tesseroid by a cuboid (after Grüninger [1990])

In Grüninger [1990], complete derivations for an approximation of a tesseroid by a cuboid can be found. The final relations between the edge lengths of a tesseroid $(\Delta\varphi, \Delta\lambda)$ and those of a cuboid $(\Delta x, \Delta y)$ are:

$$\begin{aligned} \Delta x &\approx r_M \cdot \Delta\varphi \qquad \Delta y \approx r_M \cdot \cos\varphi_M \cdot \Delta\lambda \\ r_M &= (r_1 + r_2)/2 \qquad \varphi_M = (\varphi_1 + \varphi_2)/2 \end{aligned} \tag{8.1}$$

r_1,r_2... Radial distances from the earth's center to the edges of the tesseroid

Detailed formulas to compute the gravitational attraction of a tesseroid based on the Newton integral can be found in Grüninger [1990]. In the present work, the calculation of the gravitational potential and attraction has been performed using mass cuboids. As the DTM data used for the mass computation are given in geographical coordinates (chapter 8.3), the thus predefined tesseroids have been approximated by cuboids of the

same volume (Eq. (8.1)). In each computation point P, a local coordinate system has been defined, which refers to the coordinate system of the DTM (Fig. 8.2). The defined cuboids stand orthogonally on the x-y-plane of the coordinate system coinciding with the tangent plane in P.

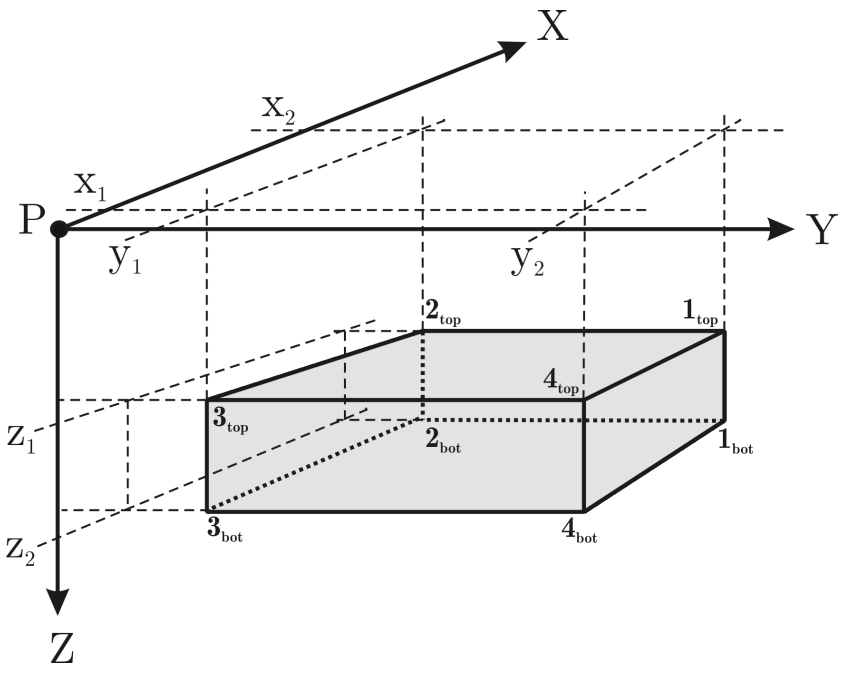

Figure 8.2: Definition of a coordinate system of a cuboid (after Bürki [1989]).

The edges of the cuboids run in parallel to the axes of the local coordinate system. The horizontal size of the mass cuboids has been defined with regard to the resolution of the DTM (chapter 8.3). In order to reduce the computation time, the vicinity up to a distance of 50 km around P has been considered by cuboids with a size of 90 m x 90 m (SRTM3 resolution), while greater distances have been approximated by cuboids with a size of 180 m x 180 m. The maximum distance for the consideration of masses around P (="area of influence") has been set to 150 km resulting from dedicated investigations (chapter 8.7.1). The principle of so called "block construction" has been already used by Elmiger [1969] and can be also found in more recent works as Marti [1997] and Flury [2002]. The mean density of the topographic mass cuboids has been defined with 2.67 g/cm^3, which is a commonly used value in this context (Marti [1997]). The bathymetric area has been considered with a density contrast of 1.67 g/cm^3 resulting from the difference between rock (2.67 g/cm^3) and water (1.0 g/cm^3).

Gravitational potential

In Mader [1951], the complete formulas for the potential of a finite and an infinite cuboid and the derivations of the potential to the third degree can be found.

The potential V is given in $[m^2/s^2]$ by:

$$V = G \cdot \rho \cdot \int_{x1}^{x2} \int_{y1}^{y2} \int_{z1}^{z2} \frac{1}{r} \cdot dx \cdot dy \cdot dz \tag{8.2}$$

with $r = \sqrt{x^2 + y^2 + z^2}$

ρ... Mass density in $\left[\frac{kg}{m^3}\right]$
G... Gravitational constant: $(6.6742 \pm 0.0010) \cdot 10^{-11} \frac{m^3}{kg \cdot s^2}$
dx,dy,dz... Dimensions of a mass element in [m]

The solving of the integral yields (after intermediate computations outlined in Appendix A.2, Eqs. (A.7) to (A.11)):

$$\begin{aligned}\frac{1}{G \cdot \rho} V &= y_2 \cdot z_2 \cdot \log(x_2 + r_2) + x_2 \cdot y_2 \cdot \log(z_2 + r) - \frac{y_2^2}{2} \cdot \arctan\left(\frac{x_2 \cdot z_2}{y_2 \cdot r}\right) \\ &+ x_2 \cdot z_2 \cdot \log(y_2 + r) - \frac{x_2^2}{2} \cdot \arctan\left(\frac{y_2 \cdot z_2}{x_2 \cdot r}\right) - \frac{z_2^2}{2} \cdot \arctan\left(\frac{x_2 \cdot y_2}{z_2 \cdot r}\right) \\ &- \{x_2 y_2 z_1\} - \{x_2 y_1 z_2\} + \{x_2 y_1 z_1\} - \{x_1 y_2 z_2\} + \{x_1 y_2 z_1\} + \{x_1 y_1 z_2\} - \{x_1 y_1 z_1\}\end{aligned} \tag{8.3}$$

Please note: The expressions in curly brackets indicate that the preceding explicit expression has to be applied accordingly to the denoted coordinates of the cuboid.

Gravitational attraction

By knowing the gravitational potential, the attractions V_x, V_y and V_z can be calculated by the first derivatives in direction of the three coordinate axes x, y, z.

At the example of the gravitational attraction V_x (in x-direction), it is:

$$V_x = -G \cdot \rho \cdot \int_{x1}^{x2} dx \int_{y1}^{y2} dy \int_{z1}^{z2} dz \cdot \frac{x}{r^3} \tag{8.4}$$

The solving of the integral yields (after intermediate computations outlined in Appendix A.2, Eqs. (A.12) to (A.15):

$$\begin{aligned}\frac{1}{G \cdot \rho} \cdot V_x &= z_2 \cdot \log(y_2 + r) + y_2 \cdot \log(z_2 + r) - x_2 \cdot \arctan\left(\frac{y_2 \cdot z_2}{x_2 \cdot r}\right) \\ &- \{x_2 y_2 z_1\} - \{x_2 y_1 z_2\} + \{x_2 y_1 z_1\} - \{x_1 y_2 z_2\} + \{x_1 y_2 z_1\} + \{x_1 y_1 z_2\} - \{x_1 y_1 z_1\} \\ &= 1_{bottom} - 1_{top} - 2_{bottom} + 2_{top} - 4_{bottom} + 4_{top} + 3_{bottom} - 3_{top}\end{aligned} \tag{8.5}$$

Please note: The expressions in curly brackets indicate that the preceding explicit expression has to be applied accordingly to the denoted coordinates of the cuboid. The gravitational effect V_y and V_z can be derived by a cyclical permutation of the coordinates in Eq. (8.5). The numeration refers to Fig. 8.2.

Residual deflections of the vertical

Based on the relation between the horizontal components V_x and V_y, respectively, and the normal gravity vector $\overrightarrow{\gamma}$, the topographic DOV (ξ_t, η_t) in [arcsec] can be derived for a single cuboid by (Bürki [1989]):

$$\xi_t = -c \cdot \frac{V_x}{\gamma} \qquad \eta_t = -c \cdot \frac{V_y}{\gamma} \tag{8.6}$$

c... Conversion factor from Radian to Arcsecond with $\rho = \frac{180 \cdot 3600}{\pi} = \frac{648000}{\pi}$
γ... Normal gravity in the station $[m/s^2]$

The sum of all cuboids around the computation point yields the final topographic DOV at P. As the DOV have been observed at a certain height H above the geoid, the effect of the *curvature of the plumb line (=orthometric correction E)* between H (surface) and H = 0 (geoid) has to be taken into account. In the following, it is demonstrated that this effect is already considered within the process of mass reduction (Gurtner [1978]):

The absolute DOV observed at geoid level ($\varepsilon_{obs}^{geoid}$) (with ε after Eq. (9.1)) result from the DOV observed at surface level (ε_{obs}^{surf}) and reduced for the orthometric correction E and the so called free-air correction ΔFA:

$$\varepsilon_{obs}^{geoid} = \varepsilon_{obs}^{surf} + E + \Delta FA \tag{8.7}$$

After Eq. (9.3), the computation of the orthometric correction E requires the knowledge of gravity values at the observation point. However, in the present work, these information are not available. Following Elmiger [1969], the orthometric correction E can be also considered as difference between DOV calculated from masses at geoid level ($\varepsilon_{calc}^{geoid}$) and those at surface level ($\varepsilon_{calc}^{surf}$):

$$E = \varepsilon_{calc}^{geoid} - \varepsilon_{calc}^{surf} \tag{8.8}$$

Furthermore, the residual DOV ($\varepsilon_{red}^{cogeoid}$) represent the difference between the DOV observed at the geoid ($\varepsilon_{obs}^{geoid}$) and those calculated from masses at geoid level ($\varepsilon_{calc}^{geoid}$):

$$\varepsilon_{red}^{cogeoid} = \varepsilon_{obs}^{geoid} - \varepsilon_{calc}^{geoid} \tag{8.9}$$

With Eqs. (8.7) to (8.9), it follows:

$$\begin{aligned} \varepsilon_{red}^{cogeoid} &= \varepsilon_{obs}^{surf} + (\varepsilon_{calc}^{geoid} - \varepsilon_{calc}^{surf}) + \Delta FA - \varepsilon_{calc}^{geoid} \\ \varepsilon_{red}^{cogeoid} &= \varepsilon_{obs}^{surf} - \varepsilon_{calc}^{surf} + \Delta FA \end{aligned} \tag{8.10}$$

with:

$\varepsilon_{red}^{cogeoid} = F(\xi_{tr}, \eta_{tr})...$ Residual DOV at cogeoid level

$\varepsilon_{obs}^{surf} = F(\xi, \eta)...$ Observed DOV at surface level

$\varepsilon_{calc}^{surf} = F(\xi_t, \eta_t)...$ Calculated DOV at surface level

The free-air correction ΔFA considers the fact that the plumb line runs also curved in free air. The according correction between surface and geoid yields only for the ξ-component and depends on latitude φ and height H of the station (Elmiger [1969]):

$$\Delta FA = \Delta\varphi = -0.00017^{[arcsec]/[m]} \cdot \mathrm{H} \cdot \sin(2\varphi) \tag{8.11}$$

Concerning the DIADEM observations in Greece, the correction $\Delta\varphi$ is very small: Due to the fact that the observations in Greece ($\varphi \approx 40°$) took mostly place close to sea level, the maximum elevation of an observation point amounts to 100 m. This yields a $\Delta\varphi$ of about 0.02 arcsec.

The formulas above show that the **residual DOV** can be computed by reducing the **DOV observed** for the **DOV calculated from masses at surface level** and for the **free-air correction**. However, according to Gurtner [1978], this method only apparently eludes the problem of the orthometric correction, since the potentials of the same mass model have to be calculated at geoid level. Elmiger [1969] estimated the mean error of the computation of E from masses to 0.5 arcsec.

The final correction formulas amount to (Elmiger [1969]):

$$\xi_{tr} = \xi - \xi_t + \Delta\varphi \qquad \eta_{tr} = \eta - \eta_t \tag{8.12}$$

Please note: Effects caused by the difference between cogeoid and geoid can be neglected (Elmiger [1969]).

Earth's curvature

The definition of a cuboid standing orthogonally on the tangent plane holds true for topography close to point P. However, due to the earth's curvature, the deviation of the tangent plane from the underlying ellipsoidal reference model becomes more and more significant with increasing distance to P (Grüninger [1990], Flury [2002]). According to Grüninger [1990], the height offset E of a point P' ($x', y', z' = H$) in reference to the computation point P ($x = 0, y = 0, z = H$) (zero-point of coordinate system) can be estimated by:

$$\begin{aligned} E &\approx \frac{s'^2}{2R} \qquad s' = \sqrt{x'^2 + y'^2} \approx \overline{PP'} \\ R &= \sqrt{MN} = \frac{a\sqrt{1-e^2}}{1 - e^2 \sin^2 \phi} \end{aligned} \tag{8.13}$$

with:

s'...	Distance between P' and P
R...	Earth's radius
M...	Radius of earth's curvature in the meridian
N...	Normal radius of earth's curvature
a...	Semi-major axis of reference ellipsoid
e^2...	Numerical eccentricity
φ...	Geographical latitude of P

The effect of earth's curvature on the height offset is demonstrated in Fig. 8.3. In a distance of 10 km, the offset amounts to about 8 m, while in 50 m, it is already about 200 m.

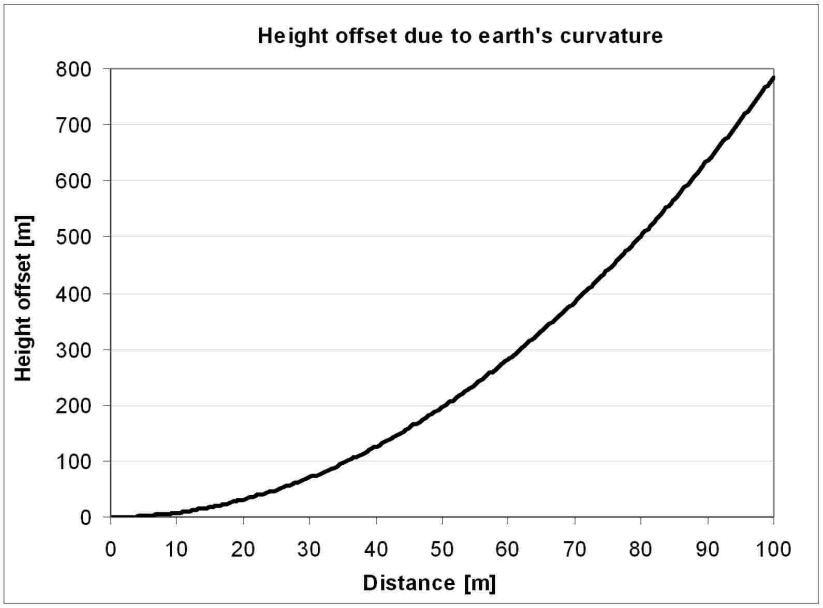

Figure 8.3: Height offset due to earth's curvature depending on the distance to the computation point. In a distance of 100 m, it amounts to 800 m.

The impact of disregarding the effect of earth's curvature within the process of mass reduction has been estimated at the example of a cuboid with the dimensions 1000 m x 1000 m x 1000 m. The maximum impact amounts to 0.0003 arcsec (for a single cuboid!) and remains constantly from a distance of about 10 km on. Although this is very low, it has to be regarded that the effect in P forms a sum of all cuboids around the station. Hence, it is recommended to consider the height offset within the process of data reduction.

8.3 Topography from the NASA Shuttle Radar Topography Mission

The topography and bathymetry information used in this work have been extracted from the *SRTM3* and *SRTM30 plus* models published by the United States Geological Survey (USGS) (see http://www2.jpl.nasa.gov/srtm/cbanddataproducts.html). The data result from a collaborative Shuttle Radar Topography Mission (SRTM) by the National Aeronautics and Space Administration (NASA), the National Imagery and Mapping Agency (NIMA/NGA)[1], the German Space Agency (DLR) and the Italian Space Agency (ASI). The goal of the SRT mission was to generate a near-global elevation model of the earth using dual radar antennas, which aquire interferometric radar data (Rodriguez et al. [2005], Farr et al. [2007]).

SRTM30 and SRTM30 plus

The *SRTM30* is a digital elevation model that spans the globe from 60° northern latitude to 56° southern latitude with a resolution of 30 arcsec (about 900 m at equator). Despite the fact that the SRTM30 has the same resolution as the older GTOPO30 model, it can be considered as a more accurate global digital data set. Due to the fact that it was created over a short period of time from a single source, it shows a more seamless and uniform representation. However, GTOPO30 data were used to complete the SRTM model, where SRTM data were not available. The *SRTM30 plus* model additionally contains information about the bathymetry. The ocean data are based on the Smith and Sandwell global 2-minute grid between latitudes ±72 degrees. The arctic bathymetry is taken from the International Bathymetric Chart of the Oceans (IBCAO).

SRTM3

Furthermore, for a more detailed approximation of the topographic masses, the SRTM3 model has been used. This model is also published by the USGS but has a higher resolution of 3 arcsec (about 90 m at equator). A disadvantage of this model is that bathymetric information are not included, so they have to be extracted from the SRTM30 data set.

A detailed analysis concerning the quality of the SRTM3 data can be found in Rodriguez et al. [2005]. As part of the SRT mission, an extensive global ground campaign has been conducted by NIMA/NGA and NASA. The goal was to collect ground-truth which would allow for the global validation of the SRTM data set. Based on the results from this campaign, the absolute height error for Eurasia is given with 6.2 m, the relative height error with 8.7 m and the absolute geolocation error with 8.8 m.

[1] NIMA changed the name in November 2003 to National Geospatial-Intelligence Agency (NGA)

8.4 Isostasy

8.4.1 Theory

Isostasy is the condition of a gravitational equilibrium between the earth's lithosphere and asthenosphere (Torge [2001], Rummel [2005]). In the simplest example, isostasy is the principle of Buoyancy observed by Archimedes in his bath, where he realized that the immersion of an object into water causes the displacement of an amount of water with the same volume as the object. Referring to the earth's crust, an isostatic equilibrium is reached if below a certain depth (=compensation depth) the weight and, hence, the pressure of masses above is the same everywhere. The immersion depth of the lithosphere depends on its thickness and density. In Fig. 8.4, the principle is explained at the example of oceanic and continental crust, respectively: Due to its higher thickness, the continental crust sinks deeper into the mantle than the oceanic crust. The transition zone between crust and mantle is called Mohorovičić discontinuity, abbreviated "Moho" discontinuity (chapter 8.5).

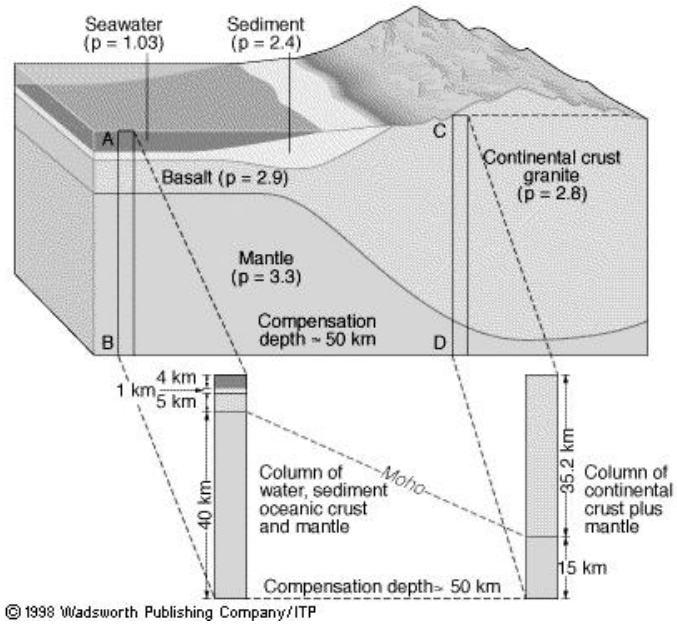

Figure 8.4: Mass compensation at the example of ocean and continent, published by the Department of Earth and Planetary Science, Northwestern University, Evanston (http://www.earth.northwestern.edu/people/seth/107/Gravity/Image66.gif).

Since the earth is a dynamic system, the establishment of a hydrostatic equilibrium can be observed wherever mass loads have changed. Hence e.g., the deposit of large amounts of sediments on a particular region might cause the crust below to sink. In contrast, the erosion of large amounts of material might provoke a rising of the land for compensation. Other examples are the glaciation/deglaciation at the poles or the effect of continental drift. An interesting example are the Swiss Alps, where the isostatic equilibrium has not yet been reached. As a consequence, some parts of the Swiss Alps are uplifted at a rate of up to 1.5 mm/year (Schlatter [2007]).

The condition of hydrostatic equilibrium is based on the principle of Buoyancy as described by Archimedes (Gerthsen [1966]):

$$F_W = F_L \tag{8.14}$$

$$\underbrace{\rho_B \cdot V_B}_{m_B} \cdot g = \underbrace{\rho_{Fl} \cdot V_{Fl}}_{m_{Fl}} \cdot g \tag{8.15}$$

$$m_B = m_{Fl} \tag{8.16}$$

with:

F_L...	Lifting force $[(kg \cdot m)/s^2 = N]$
F_W...	Weighting force $[N]$
ρ_B, V_B, m_B...	Density $[kg/m^3]$, volum $[m^3]$ and mass of body [kg]
$\rho_{Fl}, V_{Fl}, m_{Fl}$...	Density, volum and mass of fluid
g...	Gravity $[m/s^2]$

The so called *condition of mass equilibrium* (Eq. 8.16) forms the background for two well-known theories of isostasy: the Airy-Heiskanen and the Pratt-Hayford model. Since the Pratt-Hayford theory is outdated, only the Airy-Heiskanen model is treated in detail. Within this work, it has been used for the reduction of the DOV for isostatic compensation masses (chapter 8.6). Another famous theory is established by the Vening-Meinesz model, where the crust acts as an elastic plate and its inherent rigidity spreads deflections of topographic loads over a broader region. This theory is not discussed in this work. For more information concerning this theory, please refer to Moritz [1990] or Ebbing [2002].

8.4.2 Airy-Heiskanen model

The Airy-Heiskanen model is based on the theory that the lighter earth crust ($\rho_c = 2.67\ g/cm^3$) floats on the denser mantle ($\rho_M = 3.3\ g/cm^3$) like icebergs on water. A normal column without topography (H=0) is assumed with an average density of the crust ρ_C and a compensation depth D = 30 km. A continental column with H>0 has to be compensated by a so called "root" with the depth t dipping into the mantle (Fig. 8.5). Hence, a mass deficit due to the density contrast $\Delta\rho = \rho_M - \rho_C$ unlike a normal column is produced. In contrast, an oceanic column with a bathymetric depth H_W is compensated by a so called "anti-root" t_W. The boundary layer between crust and mantle is called Moho discontinuity. An equilibrium is produced by the uplift of the lighter crust compared to the denser mantle. The condition of balance can be expressed by (Rummel [2005]):

Continental columns:

$$H \cdot \rho_C = t \cdot \Delta\rho \tag{8.17}$$

$$t = \frac{\rho_C}{\Delta\rho} \cdot H \tag{8.18}$$

Oceanic columns:

$$H_W(\rho_C - \rho_W) = t_W \cdot \Delta\rho \tag{8.19}$$

$$t_W = \frac{(\rho_C - \rho_W)}{\Delta\rho} \cdot H_W \tag{8.20}$$

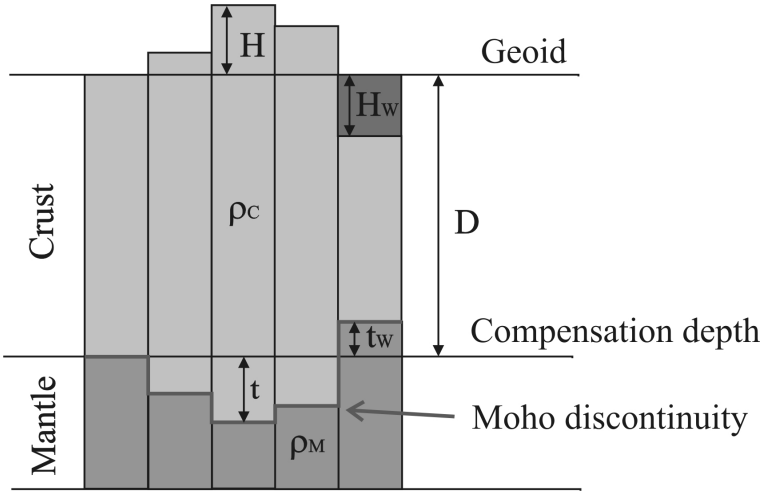

Figure 8.5: Airy-Heiskanen isostatic model. The theory is based on the idea of a local mass compensation in columns, with varying compensation depths depending on the height of the column above the geoid.

The formulas above do not consider the column convergence in direction to the center of the earth. The consideration of the convergence yields the following equations:

Continental column:

$$t = \frac{\rho_C}{\Delta\rho}\left(\frac{R}{R-D}\right)^2 H \tag{8.21}$$

Oceanic column:

$$t_W = \frac{\rho_C - \rho_W}{\Delta\rho}\left(\frac{R}{R-D}\right)^2 H_W \tag{8.22}$$

8.5 Mohorovičić discontinuity

8.5.1 Moho in Greece: a state of research

The topography of the crust-mantle boundary (Moho discontinuity) in the Aegean domain is the result of a complex tectonic history (see chapter 7.2.2). The determination of the significant density contrast at this boundary has been the focus of numerous studies:

* Papazachos et al. [1995] studied the compressional velocity structure of the crust and upper mantle by inverting residuals of the first P arrivals from earthquakes in south-eastern Europe (16°-31°E, 34°-43°N). The resulting map of Moho discontinuities yields depths from 25 km in the cyclades to 40 km beneath continental Greece. For the North Aegean Sea, a mean depth of 30 km is indicated.
* Tsokas and Hansen [1997] and Tirel et al. [2004], respectively, estimated the crust-mantle-boundary in the Aegean Sea by the inversion of gravity data. Tirel et al. [2004] (here: Tirel model) used Fourier transforms to invert filtered Bouguer anomalies reduced for the effect of the subducting African slab. The Moho depths are only available for the marine area. They average to 25 km with a minimum depth of 22 km in the Cretan Sea and a maximum depth of 30 km around Crete and the Peloponnessos (along the African-Eurasian subduction zone, see chapter 7.2.2). The depths in the North Aegean Sea range between 23 km and 27 km (Fig. 8.6***a)***). The Moho topography estimated by Tsokas and Hansen [1997] (here: Tsokas model) are used in the present work for the data reduction and will be described in detail in chapter 8.5.2.
* Sodoudi et al. [2006] (here: Sodoudi model) determined common P and S receiver functions from tele-seismic events at 65 temporary and permanent seismic stations of different networks (GEOFON, National Observatory Athens, Cyclades Network and Seisfaultgreece Experiment). Their analysis allowed for the determination of seismic discontinuities to a depth of several hundreds of kilometers. The Moho topography varies between 20 km in the Cretan Sea and 40 km below continental Greece. The North Aegean Sea features Moho depths between 26 km and 30 km (Fig. 8.6***b)***). Furthermore, the analysis of the S receiver function enabled the tracing of the subducting African lithosphere towards northern Greece. The *African Moho* (Fig. 8.7) shows a depth of 40 km along the Hellenic arc (Fig. 7.4 for the location of the Hellenic arc). Below the volcanic arc (dashed line near the stations MILO and SANT in Fig. 8.7), the depths increase to 100 km and to about 220 km below northern Greece.
* Casten and Snopek [2006] estimated the 3D-density structure of the Hellenic subduction zone around Crete by means of gravity modeling (computed Bouguer anomalies). Active and passive seismic studies on and around Crete served as input for first structural and density suppositions for the gravity modeling. The final interpretation was based on a newly compiled Bouguer map from land, marine and satellite data (observed Bouguer anomalies). The observed and computed Bouguer anomalies were consistent within the low-frequency range, which is mainly controlled by Moho depth variations and very thick sedimentary coverage. The *Eurasian continental Moho* in the Hellenic zone shows an arc-shaped structure south off Crete with depths between 25 km and 30 km along the Hellenic arc. The Moho depths below Crete reach a value of about 35 km and indicate an uplift to less than 20 km in the Cretan Sea. Furthermore, the structure of the *subducted oceanic Moho* has been estimated. The clearly arc-shaped character of the African Moho indicates a depth of 40 km along the Hellenic arc and decreases to 50 km north of Crete. In Snopek et al. [2007], a detailed comparison between seismic constraints and the 3D-density model can be found.

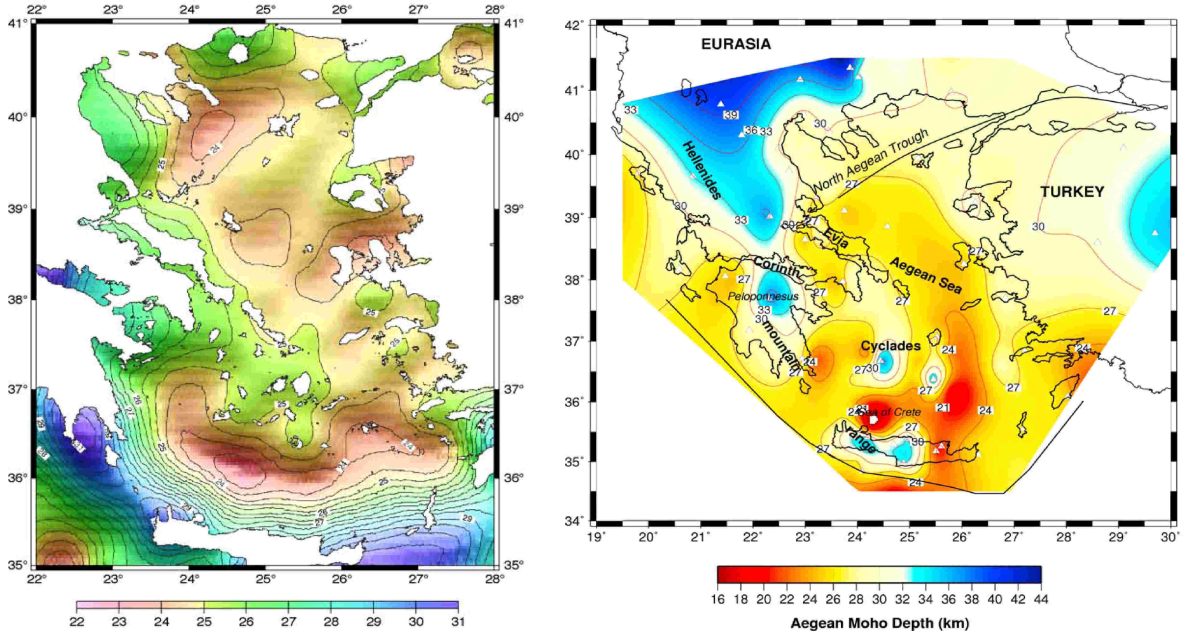

a) Moho topography based on the inversion of filtered Bouguer anomalies reduced for the effect of the subducting African slab (Tirel et al. [2004]). The Moho depths in the North Aegean Sea range between 23 km and 27 km.

b) Moho topography based on the analysis of common P and S receiver functions (Sodoudi et al. [2006]). The Moho depths in the North Aegean Sea range between 26 km and 30 km.

Figure 8.6: Two different models of Moho topography in the Aegean Sea, Greece.

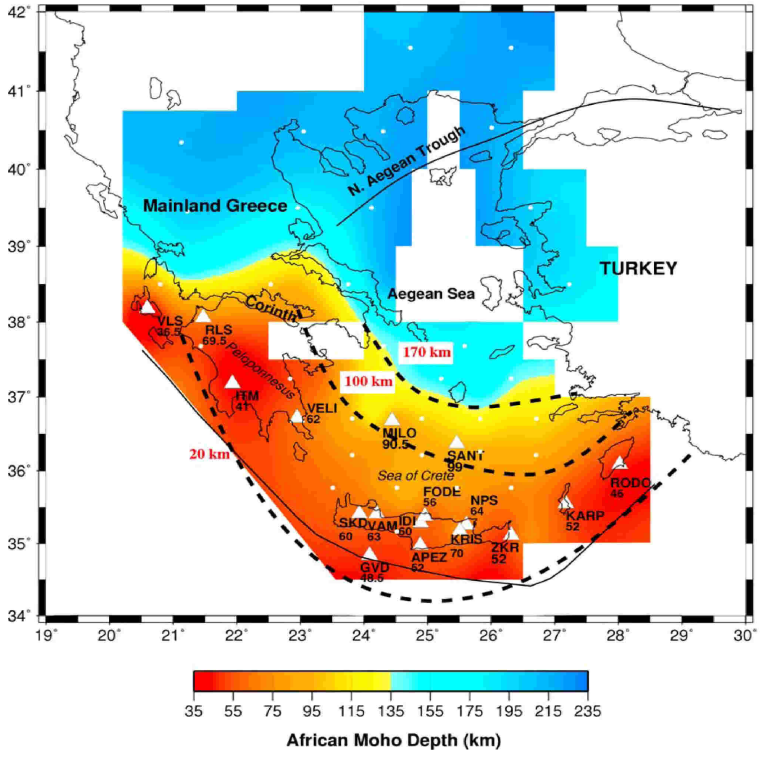

Figure 8.7: Moho topography of the subducting African lithosphere (Sodoudi et al. [2006]). The African Moho has been traced towards northern Greece by analyzing the S receiver function. The depths amount to 40 km along the Hellenic arc, increase to 100 km below the Hellenic arc and reach about 200 km below northern Greece.

8.5.2 Moho model applied for data reduction

Tsokas and Hansen [1997] determined crustal thicknesses in Greece by applying the Multiple-Source Werner Deconvolution method (MSWD) along profiles extracted from the Bouguer anomaly map of Greece. The MSWD method is an inverse technique for the interpretation of magnetic and gravity anomalies, respectively. The resulting estimates have been used to generate the Moho topography (Fig. 8.8). The depth averages to 32 km, with a minimum in the Aegean Sea and a maximum beneath the western part of the Greek Peninsula. Within the North Aegean Sea, the Moho depths vary between 23 km (peninsula of Athos (=A)) and 39 km (western Greece).

A detailed comparison of the Tsokas model with other Moho models revealed significant differences. It has to be noted that the following comparison only refers to models that also indicate Moho depths for the North Aegean domain as the main research area of this project:

* Concerning the relative variations of the Moho depths in the Aegean Sea, the differences are significant: While the Tsokas model indicates variations in the Aegean domain of about 15 km, the Tirel model identifies 9 km in agreement with the Sodoudi model. In the North Aegean Sea, the differences are also considerably high with variations of about 10 km in the Tsokas model and about 4 km in the Tirel model.
* Regarding the location of minima and maxima of Moho depths, the following discrepancies are detected: In the North Aegean domain, the Tsokas model shows a significant shallower depth beneath the peninsula of Athos, while the Tirel model reveals an elongated zone of shallower Moho along the North Aegean Trough (NAT). The Tirel model here proves a clear negative correlation between bathymetry and Moho depths, hence indicating a low Moho depth for a distinctive bathymetry. This negative correlation is not recognizable in the Tsokas model. Furthermore, the Tsokas model reveals a significant shallower Moho south of Evia (=E), northeast of the cyclades. This result is in contrast to the other models, since both the Tirel and the Sodoudi model rather predicate the opposite. Another region of discrepancy is the Cretan Sea, where the Tirel model proposes an elongate zone of shallower Moho. However, in the Tsokas model, the Moho depth variations show a rather different characteristic as no elongate minimum of crustal thickness is indicated (Tirel et al. [2004]).

One reason for the discrepancies mentioned - at least between Tsokas and Tirel model - might be due to the fact that Tirel et al. [2004] used Bouguer anomalies reduced for the gravitational effect of the African slab, while Tsokas and Hansen [1997] did not consider this effect in the inversion. Furthermore, both models did not take the influence of sedimentary basins into account (chapter 7.2.1). The disregard of low density sediments as they can be found in the North Aegean Sea might result in an overestimation of Moho depths. After Tirel et al. [2004], the sedimentary thickness in the North Aegean Sea, and especially in the Sporades basin, might reach values up to 6 km, hence producing a shallower Moho than proposed by the Tirel and Tsokas model, respectively.

Despite the revealed discrepancies between the Tsokas model and other studies, this model has been used in the present study for data reduction. If the problems discussed above apply to the Tsokas model, the residual DOV should indicate corresponding characteristics. This subject is analyzed in chapter 9.3.2.

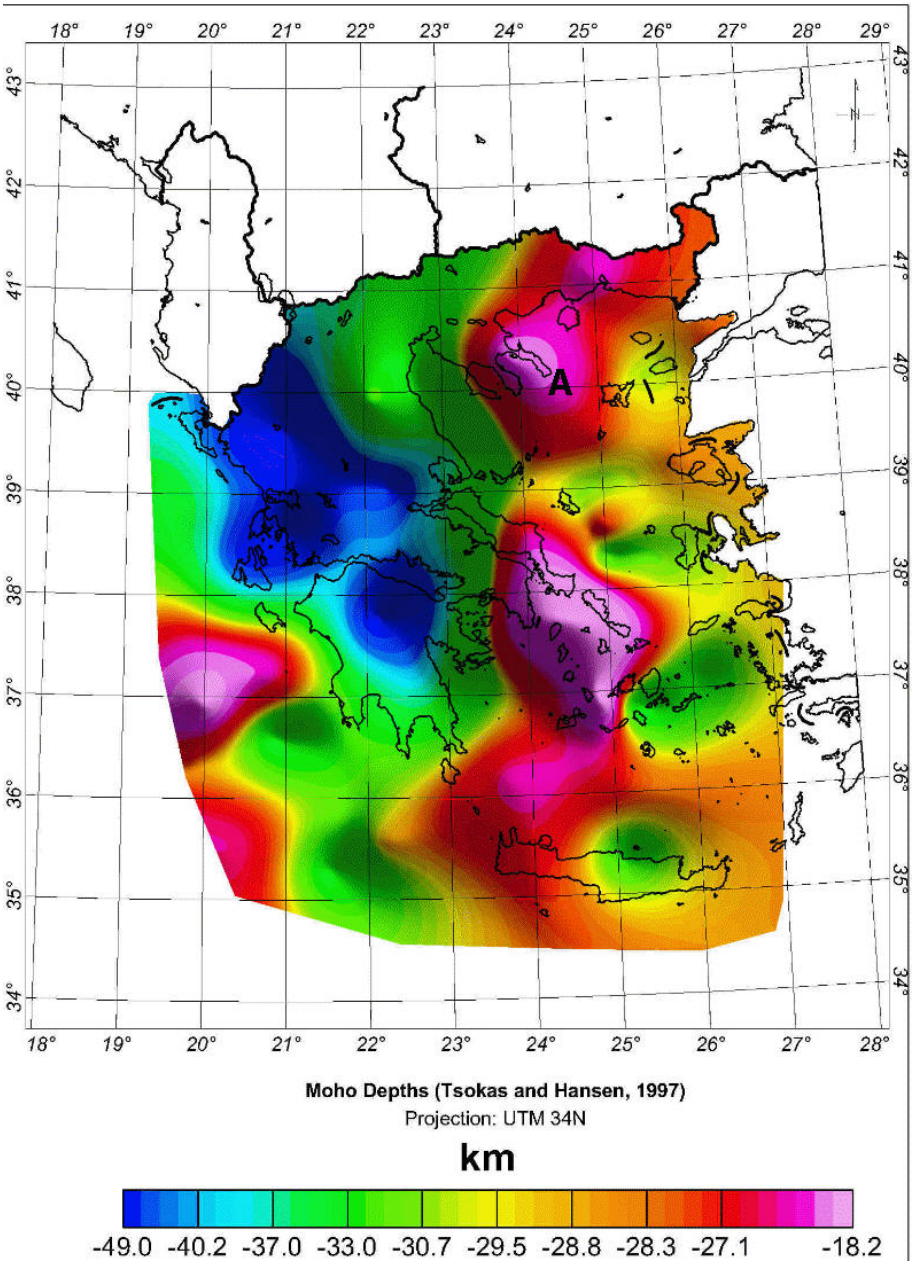

Figure 8.8: Estimated variations in Moho depths in the area of Greece (Tsokas and Hansen [1997]). In the North Aegean Sea, the Moho depths show a minimum of 23 km beneath Athos (Chalkidiki) (=A) and a maximum of 42 km beneath western Greece.

8.6 Reduced observations

The DOV observed have been presented and discussed in detail in chapter 7.4.1. In order to produce smoothed data for a geoid determination as well as residual data for a geophysical interpretation, the DOV observed have been reduced for dedicated mass effects (chapter 8.2). The residuals form the basis for the computation of appropriate cogeoids (chapters 9.3.1 and 9.3.2) as an intermediate result on the way to the final geoid solution (chapters 9.3.3 and 9.3.4). Based on thorough investigations concerning the area of influence[2] (chapter 8.7.1), masses in a distance of 150 km around the station have been considered. Until a distance of 50 km around the computation point (=Astro station), the basic resolution of the SRTM3 model of 90 m x 90 m has been used to define the size of the mass cuboids. For distances between 50 km and 150 km, the size of the cuboids has been increased to 180 m x 180 m. This helped to reduce the computation time. The density of the continental masses has been assumed with 2.67 g/cm^3, while the bathymetric region has been considered with a density contrast of 1.67 g/cm^3 resulting from the difference between rock and water.

Fig. 8.9 represents the residuals after a reduction for topographic and bathymetric masses (TB). The DOV reduced show a clearly smoother behavior than the DOV observed (Fig. 7.12). However, the residuals are still quite large with values between 1.4 arcsec (island of Agios Efstratios = AE) and 23.3 arcsec (Raches = R) and a standard deviation of 4.9 arcsec. The directions of the vectors indicate a mass concentration along the NAT. This is most likely due to the fact that isostatic compensation masses have not yet been considered within the reduction process.

Consequently, the residuals are remarkable smaller after an additional consideration of isostatic masses, based on the theory of Airy-Heiskanen (TBAH) (chapter 8.4.2). The parameters assumed are a compensation depth of 30 km and a density contrast between crust and mantle of 0.63 g/cm^3 (mantle: 3.3 g/cm^3, crust: 2.67 g/cm^3). The vectors indicate values between 0.9 arcsec (island of Agios Efstratios = AE) and 16.9 arcsec (Raches = R) and a standard deviation of 3.7 arcsec (Fig. 8.10). It is striking that the residuals at the western mainland and at Kassandra (=K) are still quite large within a range of 10 arcsec to 16 arcsec. They reflect a mass overload within the marine area, especially north of the Sporades islands (=SI). Also station Kipos (=KI) at the island of Samothraki still shows a significant residual vector of about 9 arcsec. All these effects can be attributed to different reasons, as e.g. an incomplete isostatic compensation of the region, insufficiencies of the isostatic theory or, on a small scale, errors of the astrogeodetic method and in the data reduction process. Hence, also unconsidered density variations in the crust might produce residual components of a few tenth of 1 arcsec. In chapter 8.7.3, this problem is discussed at the example of the island of Samothraki.

[2] Area of influence = Area around the computation point, in which the masses have to be considered within the process of data reduction

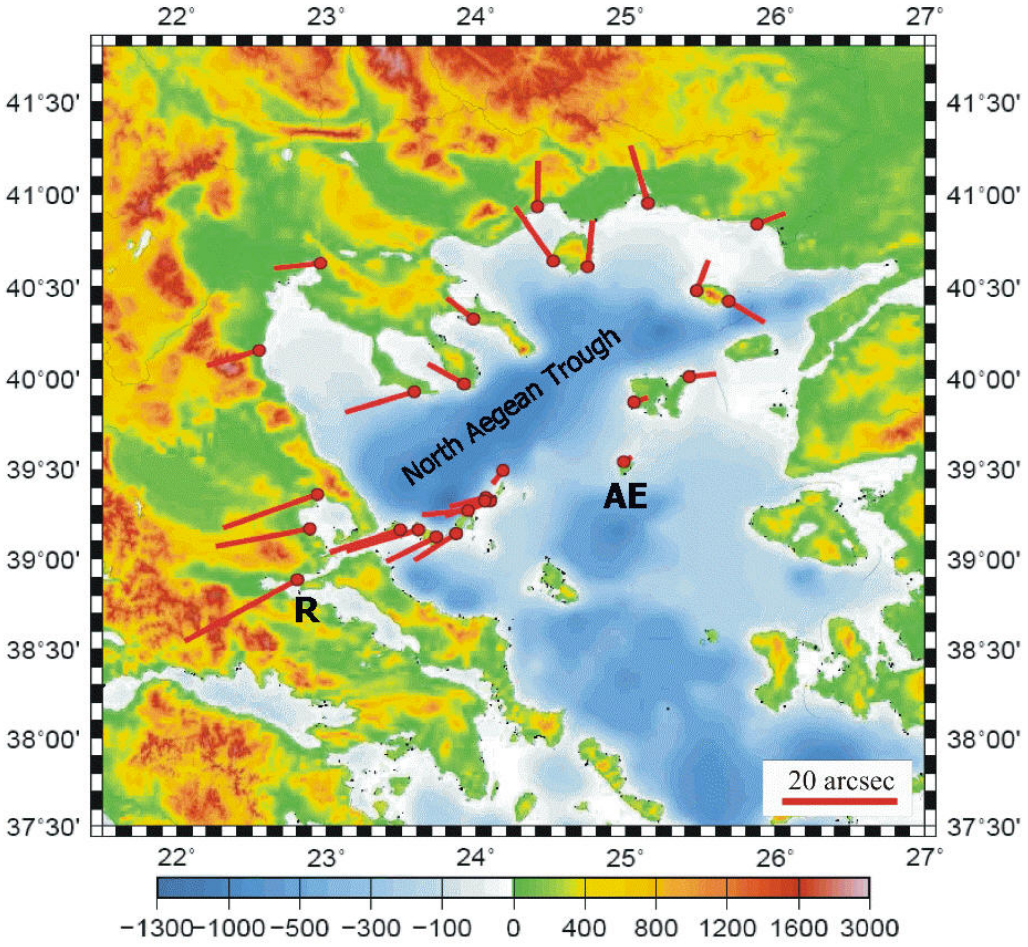

Figure 8.9: DOV reduced for topography and bathymetry. Background: topography and bathymetry from the SRTM30 plus model (chapter 8.3). The DOV reduced show values between 1.4 arcsec (island of Agios Efstratios = AE) and 23.3 arcsec (Raches = R). The residuals largely indicate a mass excess along the NAT, mainly attributed to unconsidered isostatic compensation masses.

Finally, based on the information from the Moho model of Tsokas and Hansen [1997] (chapter 8.5.2), the DOV have been reduced for topography, bathymetry and Moho (TBMoho) (Fig. 8.11). The density contrast between crust and mantle has been set to 0.35 g/cm^3 in accordance with the contrast used by Tsokas and Hansen [1997]. Compared to the DOV reduced for topography and bathymetry, the residuals are clearly smaller, with values between 0.9 arcsec (island of Limnos = L) to 13.6 arcsec (Raches = R) and a standard deviation of 2.6 arcsec. It is striking that the reduced data generally denote a mass concentration along the NAT. Especially, the vectors at the western mainland, the Sporades islands (=SI) and at the peninsula of Chalkidiki (=C) indicate an upwarp of the Moho discontinuity in the region north of the Sporades islands. Similar to the TBAH reduced DOV, the reasons for the remaining residuals are various, as e.g. insufficiencies of the Moho model applied and characteristics of the isostatic settings of the region, respectively. A detailed discussion of the appropriate cogeoids can be found in chapter 9.3.2.

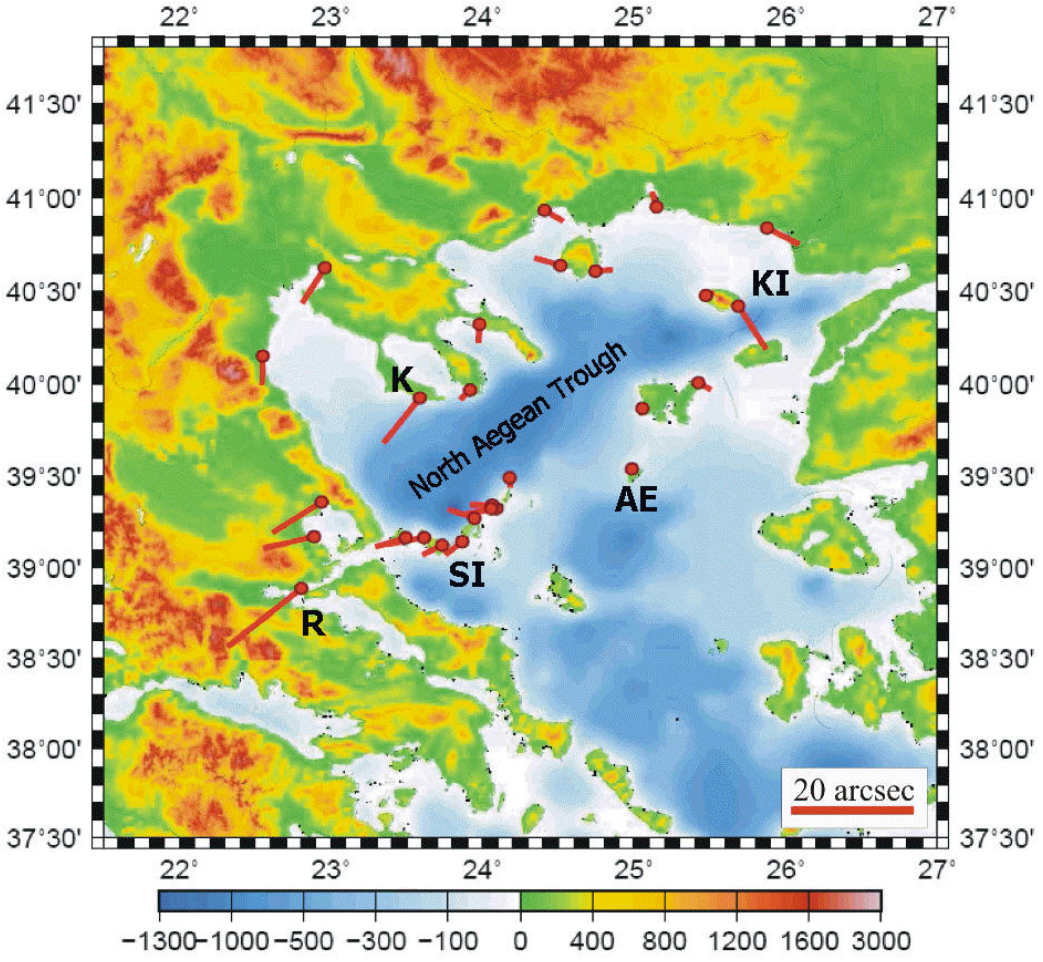

Figure 8.10: DOV reduced for topography, bathymetry and isostasy (Airy-Heiskanen). The residuals vary between 0.9 arcsec (island of Agios Efstratios = AE) and 16.9 arcsec (Raches = R). The residuals reflect a mass excess within the marine area, especially north of the Sporades islands (=SI), hence most probably reflecting an isostatic overcompensation of the region. KI = Kipos (island of Samothraki); K = Kassandra (Chalkidiki peninsula).

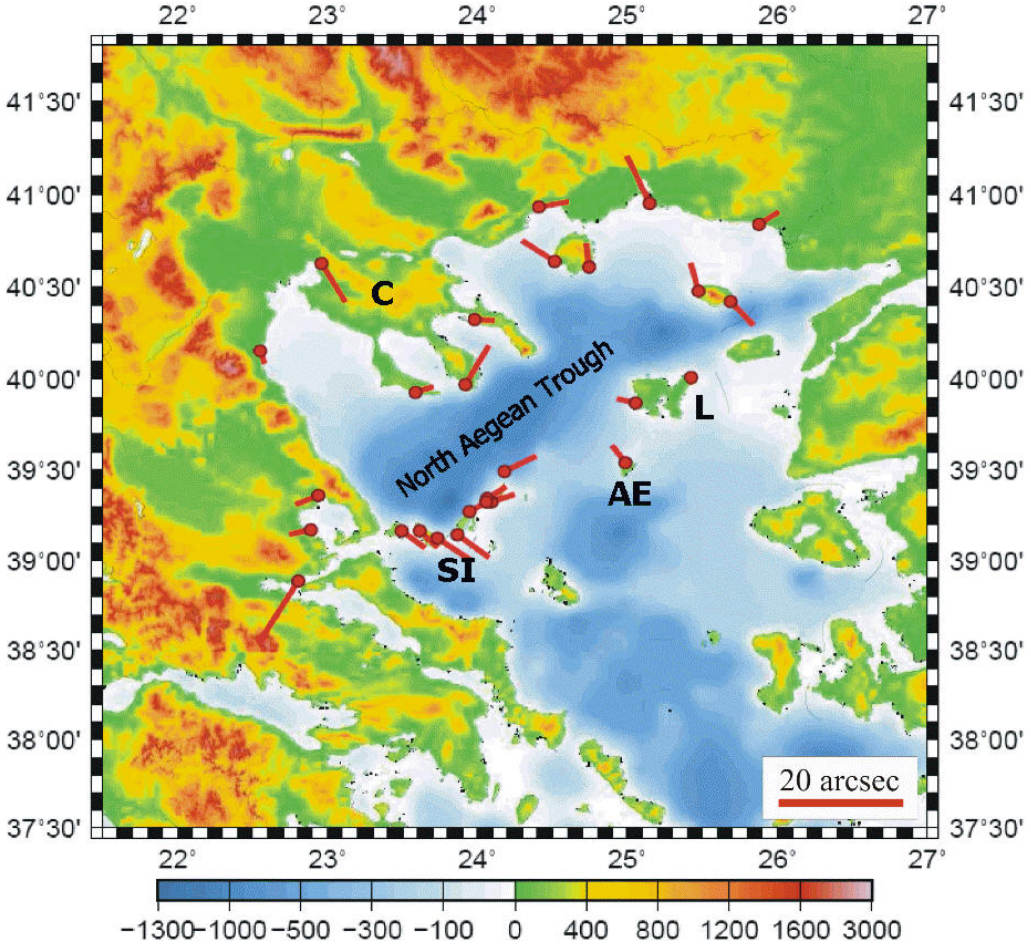

Figure 8.11: DOV reduced for topography, bathymetry and Moho. The residuals vary between 0.9 arcsec (island of Limnos = L) and 13.6 arcsec (Raches = R). The residuals reflect a mass concentration along the North Aegean Trough, hence suggesting the application of too large Moho depths for the data reduction. C = Chalkidiki.

8.7 Additional investigations

8.7.1 Dimension of the area of influence

As explained in chapter 8.1, the DOV observed show a relatively coarse behavior due to their sensitivity on surrounding masses. In order to enable a high filtering and prediction quality in the least-squares-collocation (LSC) (chapter 9.2), the Remove-Restore-technique is applied. In a first step, this method comprises the removal of mass effects within a defined area (=area of influence, short AoI). The AoI forms a rectangular region around a station. The goal of the following investigation is to determine the optimal AoI for a) the geoid determination and b) the interpretation of residual data. Both intentions demand different "terminating conditions", which will be qualified in the following.

Geoid determination

For a precise geoid determination, the optimal dimension of the AoI corresponds to an adequate smoothing of the observations, by eliminating high-frequency mass impacts. In order to determine the optimum AoI for a best-possible smoothing of the DOV, they have been reduced for topography, bathymetry and isostasy after Airy-Heiskanen (TBAH) within differently sized AoIs. Therefore, the dimension of the AoI has been stepwise increased for 10 km starting at 10 km. In Figs. 8.12 (ξ-component) and 8.13 (η-component), the results of the investigation for different AoIs between 10 km and 70 km (*CA10* to *CA70*) are depicted. It is well recognizable that the raw observations (*xi obs.* and *eta obs.* in the respective diagram) show relatively strong variations. However, already a reduction comprising masses in a 10 km distance (*CA10*) yields a significant smoother behavior of both components. Up to a AoI of 30 km (*AoI30*), the data become clearly smoother. After that, the courses of the DOV-components remain rather unmodified (*AoI50* to *AoI70*). It means that a AoI of **30 km** allows for a sufficient elimination of high-frequency mass impacts. This also corresponds to the results presented in chapter 9.4.4, where the prediction quality has been investigated using the cross-validation method. As a result of this analysis, the optimal AoI has been determined to 30 km. The conclusion also holds true for data which are reduced for topography and bathymetry only (no isostatic masses considered), since the topographic masses are mainly responsible for high-frequency perturbations.

Interpretation of residual data

The residual data mainly reflect unconsidered masses and density anomalies, respectively. Hence, for an extensive interpretation of the data, the reduction should comprise all known masses taking influence on the DOV. To determine the maximum AoI necessary, the following investigation has been performed: The AoI has been increased step-wise for 5 km starting at 10 km. For each AoI, an average over the residual ξ- and η-components, respectively, at all 27 Astro stations has been computed. The mean difference between two consecutive residuals is interpreted as impact of "additional" masses on the DOV-components. The analysis has been performed for data reduced for topography and bathymetry (TB) (Fig. 8.14) as well as for additionally isostatic reduced data (TBAH) (Fig. 8.15).

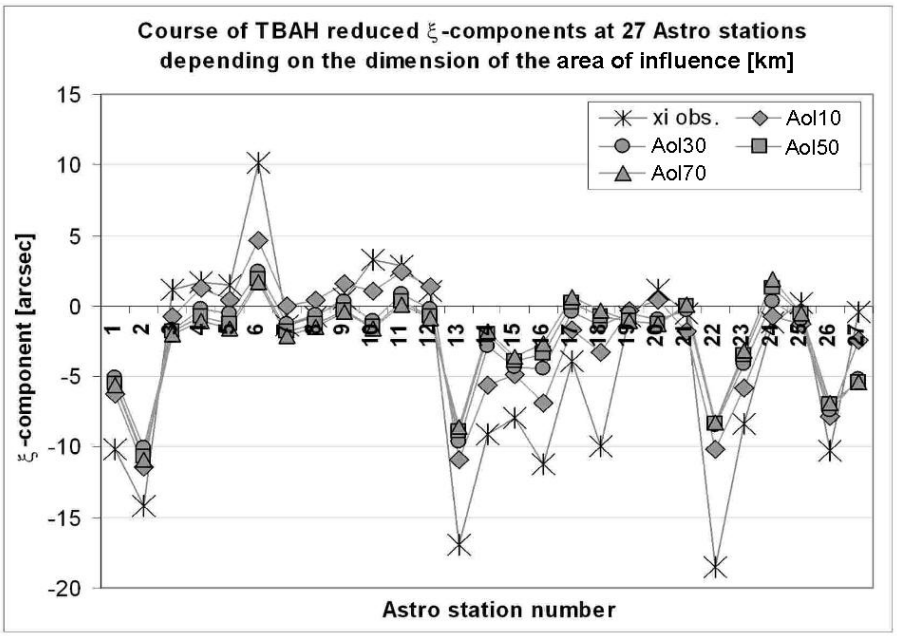

Figure 8.12: Course of TBAH-reduced ξ-components at 27 Astro stations depending on the dimension of the area of influence (AoI) [km]. The AoI has been extended by steps of 10 km. The plot shows selected examples for an AoI of 10 km, 30 km, 50 km and 70 km. *xi obs.*: observed ξ-components.

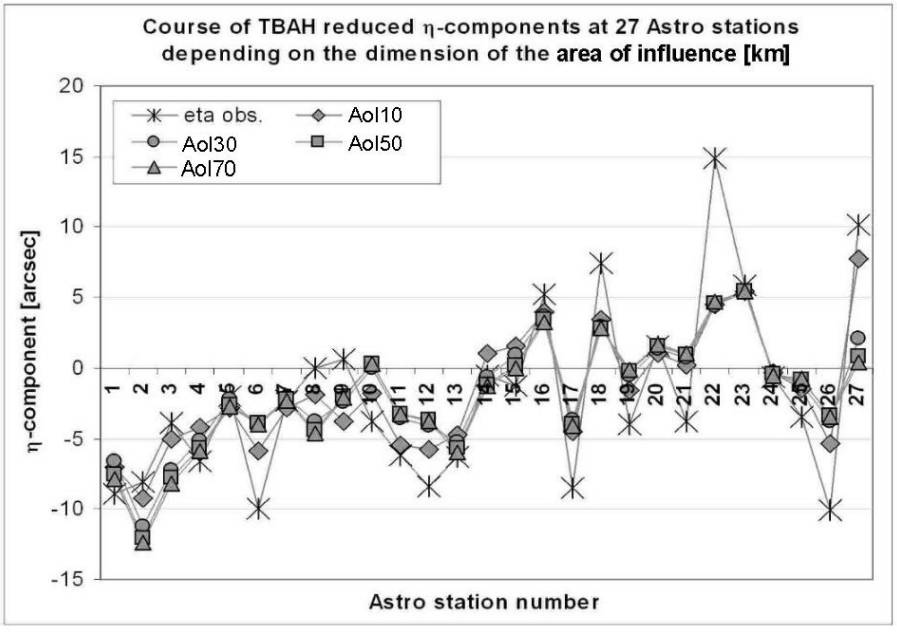

Figure 8.13: Course of TBAH-reduced η-components at 27 Astro stations depending on the dimension of the area of influence (AoI) [km] according to Fig. 8.12. *eta obs.*: observed η-components.

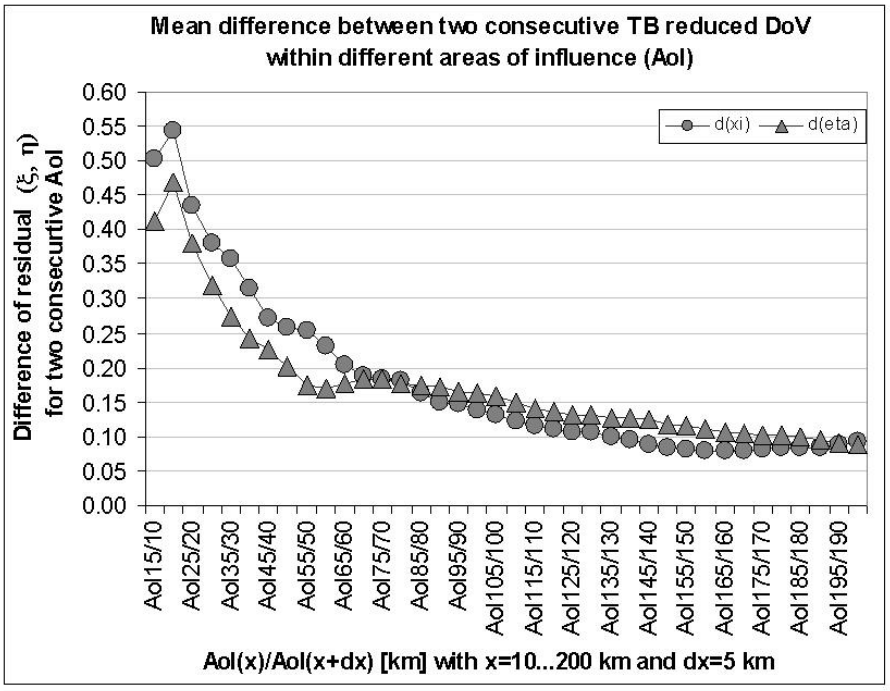

Figure 8.14: Difference of consecutive ξ- (points) and η-components (triangles) reduced for topography and bathymetry (TB). The size of the AoI [km] has been increased by steps of 5 km starting at 10 km. The label "AoI15/10" considers additional mass impacts computed between a AoI of 10 km and 15 km, respectively.

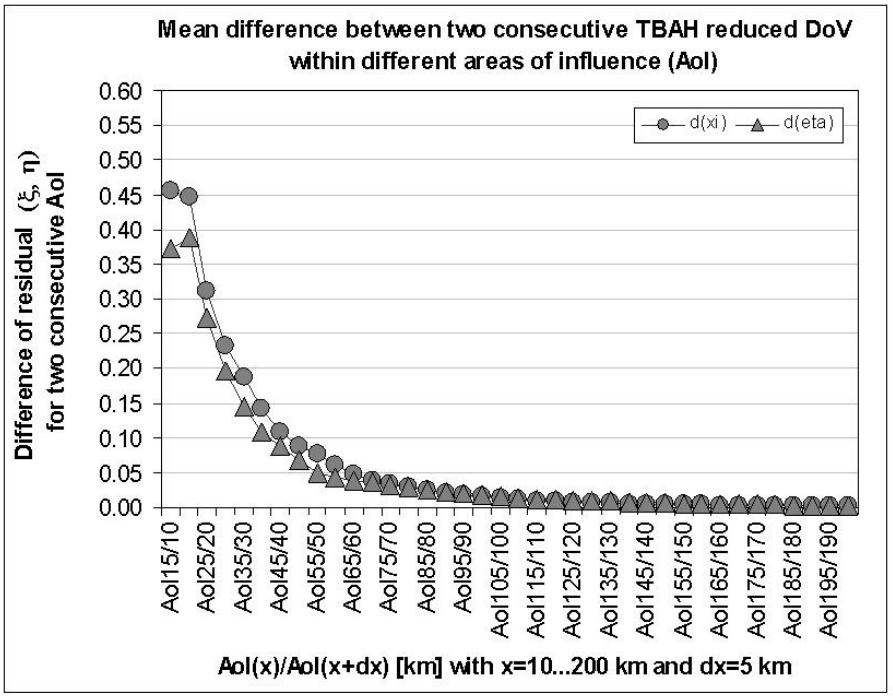

Figure 8.15: Difference of consecutive ξ- (points) and η-components (triangles) reduced for topography, bathymetry and isostasy (TBAH) according to Fig. 8.14.

As visible in Fig. 8.14, the mean difference between two consecutive TB reduced observations is relatively large regarding masses in the station vicinity. Thus, if the data are reduced for masses in 20 km and 25 km distance, respectively, the additional mass impact amounts to 0.43 arcsec for ξ and 0.38 arcsec for η. These high values might be attributed to the fact that close masses have a very high impact on the observations. For a AoI of 70 km, the impact is below 0.2 arcsec for both components, and for a AoI of 115 km it is below 0.15 arcsec. It is obvious that the mean differences remain relatively high ($\geq$0.1 arcsec), also for distant masses. Though, it has to be noticed that the impact of masses between two consecutive AoIs represents only a part of all unconsidered masses off the analyzed AoI! Interestingly, the mean differences of the components additionally reduced for isostatic masses (Fig. 8.15) show a rapid decrease for the station vicinity. For a AoI of 30 km, the impact is below 0.2 arcsec, and for a AoI of 45 km below 0.1 arcsec. For a AoI of 90 km, the impact is below 0.02 arcsec and, therefore, within a negligible range. The difference between the TB and TBAH reduced data show the relevance of an isostatic compensation. Hence, if the isostatic masses are considered, topographic masses are compensated by according masses inside the earth (chapter 8.4). The missing isostatic compensation seems to be the reason for the relatively high remaining impacts in Fig. 8.14. The final data reduction has been performed with a AoI of **150 km** forming an adequate compromise for both geoid determination and interpretation of the residual data.

8.7.2 Comparison of different data reductions

An interesting investigation is the comparison of different masses and their impact on the DOV-components. Hence, the data have been reduced within an AoI of 200 km for:
1) Topography and bathymetry (TB)
2) Topography, bathymetry and isostasy after Airy-Heiskanen (TBAH)
3) Topography, bathymetry and Moho (TBMoho)

Fig. 8.16 shows the ξ-component reduced for TB, TBAH and TBMoho, respectively, while Fig. 8.17 represents the corresponding information for the η-component. It becomes obvious that the TB residuals are relatively large within a range of 22.5 arcsec for ξ and 26.3 arcsec for η. They reflect unconsidered isostatic mass impacts. Consequently, the corresponding TBAH and TBMoho residuals, respectively, show a clearly smoother behavior. The reduction for TBAH mass impacts produces the smallest residuals within a range of 13.3 arcsec for ξ and 18.3 arcsec for η. The meaning of an isostatic compensation becomes again clear if comparing the topographic/bathymetric with the isostatic mass impact (Airy-Heiskanen) (ξ: Fig. 8.18 and η: Fig. 8.19). They largely show a negative correlation. The average over all Astro stations for the TB residuals yields values of -3.6 arcsec for ξ and 3.6 arcsec for η. The corresponding average for the TBAH residuals results in 2.1 arcsec for ξ and -3.3 arcsec for η. This comparison shows that an additionally isostatic mass reduction will produce a relatively good mass compensation in the η-component (3.6 arcsec vs. -3.3 arcsec). In contrast, the ξ-component will still show larger residuals (-3.6 arcsec vs. 2.1 arcsec). In chapter 8.6, maps with the respective residual DOV can be found (Figs. 8.9 to 8.11). A thorough interpretation of the corresponding cogeoids is presented in chapter 9.3.2.

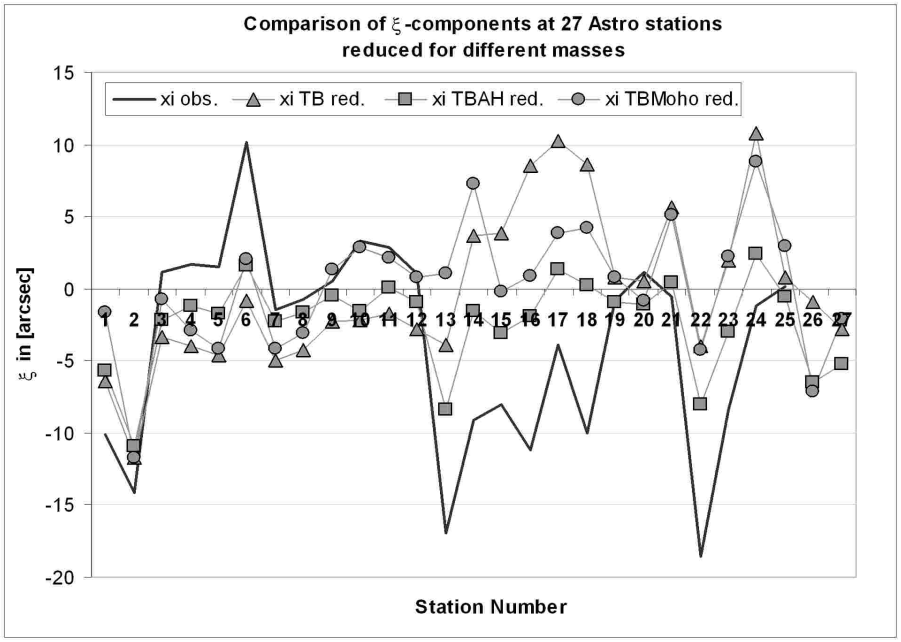

Figure 8.16: ξ-component reduced for 1) topography and bathymetry (TB), 2) topography, bathymetry and isostasy (TBAH) and 3) topography, bathymetry and Moho (TBMoho). The TBAH reduction produces the smallest ξ-residuals.

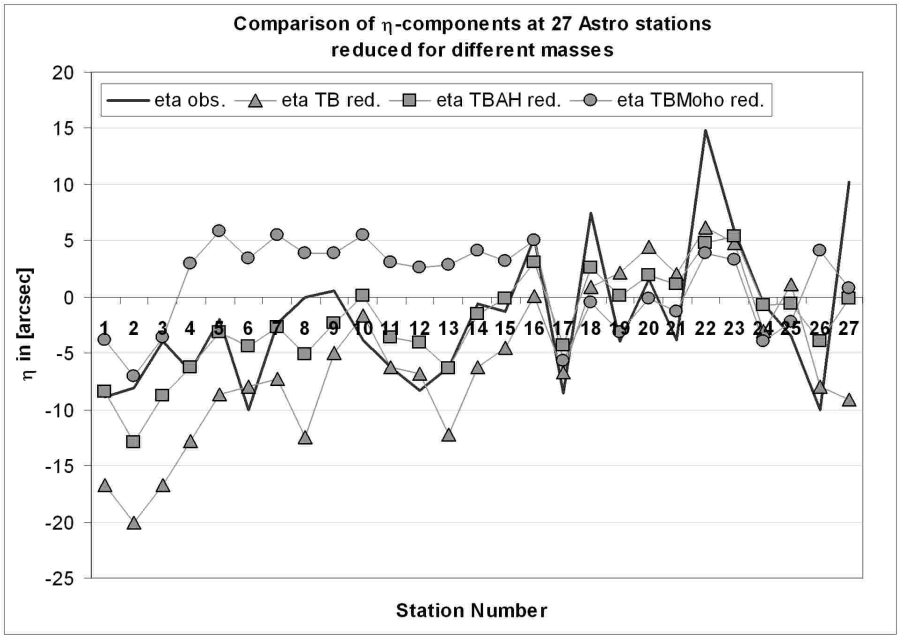

Figure 8.17: η-component reduced for 1) topography and bathymetry (TB), 2) topography, bathymetry and isostasy (TBAH) and 3) topography, bathymetry and Moho (TBMoho). Similarly as for the ξ-component, the TBAH reduction produces the smallest η-residuals.

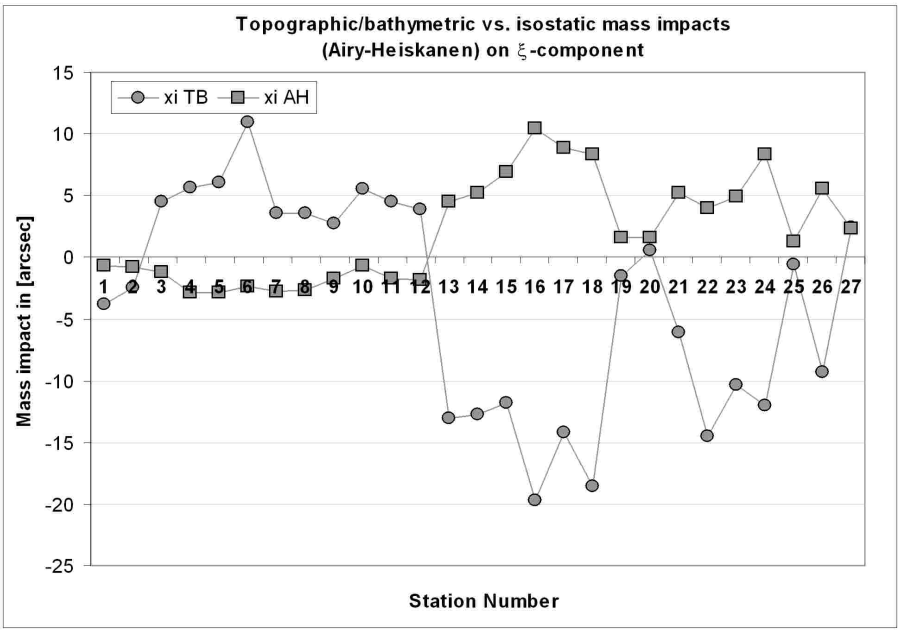

Figure 8.18: Comparison of the impacts of topographic/bathymetric (TB) and isostatic (AH) masses on the ξ-components in 27 Astro stations. They clearly show a negative correlation.

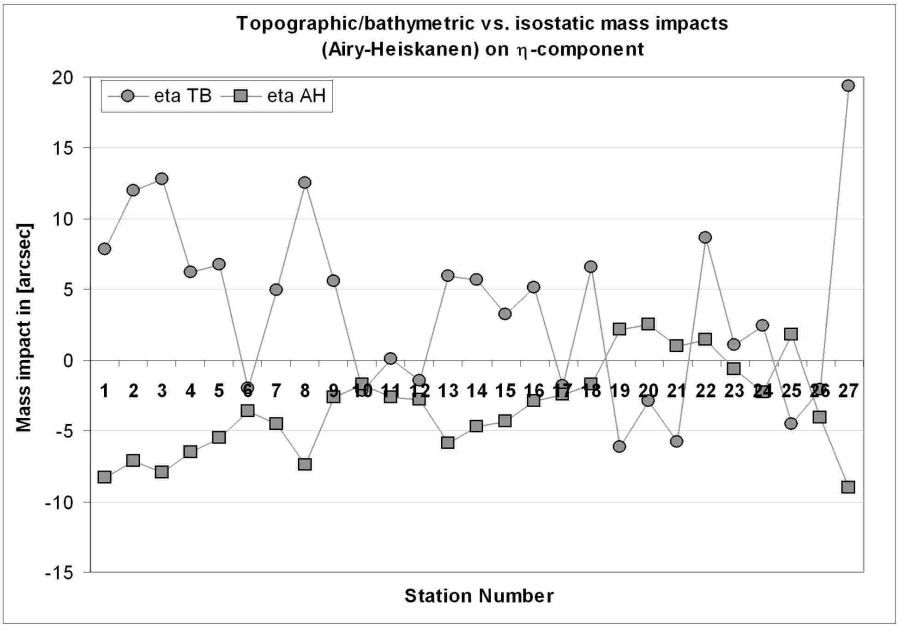

Figure 8.19: Comparison of the impacts of topographic/bathymetric (TB) and isostatic (AH) masses on the η-components in 27 Astro stations. Similar to the ξ-component, they clearly show a negative correlation.

8.7.3 Impact of density variations

Due to a lack of digital and processable data concerning the density variations in the research area, a mean density of 2.67 g/cm^3 has been assumed for all topographic masses considered within the process of data reduction. However, based on information from geological maps (e.g. Fig. 7.2), it is known that this simplification ignores the diversity of geological formations occurring in the research area. The densities for the rocks indicated in Fig. 7.2 range between 1.3 g/cm^3 (clay) and 3.2 g/cm^3 (volcanic rocks). More detailed information can be found in chapter 7.2.1.

In order to estimate the impact of assuming a mean density instead of using "true" densities, a dedicated investigation has been performed at the example of the island of Samothraki. The western station Kipos shows a large residual after the reduction for topography, bathymetry and isostasy (see *KI* in Fig. 8.10). The island largely consists of basaltic rocks, whose densities are indicated with a mean value of 3 g/cm^3. It extends for about 26.7 km in W-E direction and 13.6 km in N-S direction. The topography is dominated by mountain Fengari, with an elevation of about 1600 m. The mean height amounts to 460 m. For the analysis, the island has been approximated by a cuboid with the dimensions 19300 m x 11800 m x 460 m (light gray box in Fig. 8.20). The computation has been performed with a density of 0.33 g/cm^3 according to the difference between test (3.0 g/cm^3) and usual density (2.67 g/cm^3). The station under consideration is located vertically at height "0" and horizontally in the center of the cuboid (red point in Fig. 8.20). In the experiment, this station has been shifted continuously in western direction (green point). This allows for the computation of the gravitational and potential effect in W-E direction according to the definition of the η-component. Furthermore, it enables the investigation of the distance dependence.

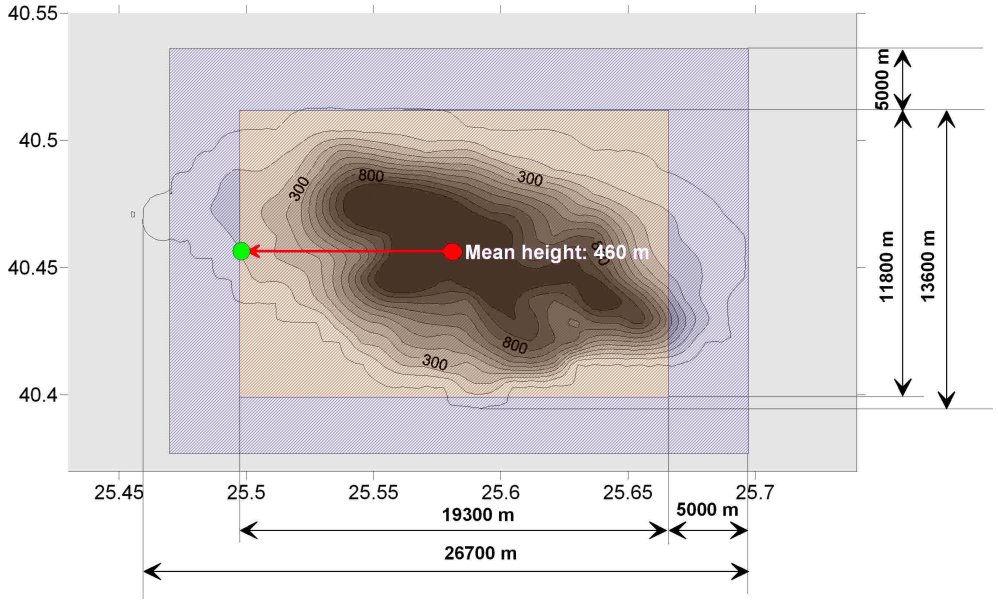

Figure 8.20: Island of Samothraki. For the investigation of the impact of different densities, the topography of the island has been approximated by a cuboid (brown beige box). Furthermore, in order to consider also the effect caused by the bathymetry around the island, a peripheral zone of 5 km has been defined (blue box).

In Fig. 8.21, the result for the η-component (light gray line) is plotted. It is clearly

recognizable that the effect on the component is "0" in the center (red point in Fig. 8.20) and reaches a maximum of about 1.5 arcsec, if the station is located at the border of the cuboid (green point). Afterwards, the effect decreases rapidly against zero. For a station 20 km away from the center of the cuboid, the effect is already below 0.2 arcsec.

A further test considered the fact that basaltic rock also occurs at the oceanic bottom around the island. In order to estimate this effect, a 5 km - zone of water around the island has been defined, with a mean depth of -500 m (blue box in Fig. 8.20). The assumption of a higher density for the bottom (3 g/cm^3 than 2.67 g/cm^3) involves also a higher density contrast between water and rock (2 g/cm^3 than 1.67 g/cm^3). Hence, a density of 0.33 g/cm^3 is used for the peripheral zone. The result of this investigation is plotted in Fig. 8.21 for the η-component (dark line). As recognizable, the maximum impact (about 1.8 arcsec) was shifted by 5 km corresponding to the zone of water, which has been additionally considered. An interesting distance is at 9650 m, where the station is located at the edge of the cuboid (green point in Fig. 8.20). This point shows a reduction of the before discussed maximum effect from 1.5 arcsec to 0.36 arcsec.

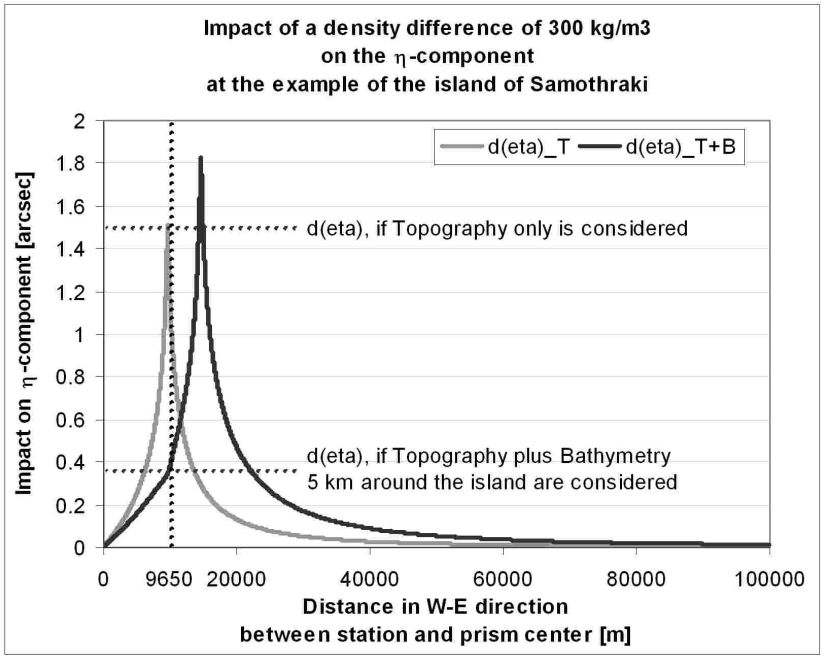

Figure 8.21: Impact of an incorrect density assumption at the example of the island of Samothraki. The light gray line shows the impact of a density contrast of 0.33 g/cm^3 on the η-component if topography only is considered. The dark line shows the impact of the same density contrast on η if also bathymetry is considered.

Although the described investigation only represents an estimation, the results contain a reference to the impact of disregarded density variations. This might be considered in the interpretation of the residual DOV presented in chapter 8.6. Referring to Fig. 8.10 showing the data reduced for topography, bathymetry and isostasy, it might be concluded that the residuals still contain a component of about some tenth of 1 arcsec caused by a higher rock density than assumed. These results are particularly interesting with regard to the interpretation of corresponding cogeoids (chapter 9.3.2). An adequate consideration

of the density variations in the research area could help to avoid misinterpretations of cogeoid anomalies.

9 Geoid determination

9.1 Measuring methods

9.1.1 Astrogeodetic method

The astrogeodetic geoid determination is based on the theory of astronomical leveling, described e.g. by Heiskanen and Moritz [1967] and Torge [2001]. The input data are surface deflections of the vertical (DOV), also called Helmert deflections, which are represented by a North-South component ξ and an East-West component η. The absolute value ε observed at the surface can be calculated by:

$$\varepsilon = \sqrt{\xi^2 + \eta^2} \tag{9.1}$$

The value ε in a defined azimuth α is given by (Torge [2001]):

$$\varepsilon(\alpha) = \xi \cos\alpha + \eta \sin\alpha \tag{9.2}$$

For the calculation of the geoid, the surface deflection ε has to be reduced to the geoid (ε_0) (compare Fig. 3.2). The difference $E = \varepsilon - \varepsilon_0$ is called orthometric correction and caused by the curvature of the plumb line. The orthometric correction E_{AB} between two stations A and B can be calculated by introducing the surface gravity g along the profile, the mean gravities $\bar{g}_A$ and $\bar{g}_B$ between A and B, respectively, and the geoid, the height difference dn between height H_A in station A and height H_B in station B as well as the normal gravity $\gamma_0^{45^\circ}$ at latitude $\varphi = 45^\circ$ (Torge [2001]):

$$E_{AB} = \int_A^B \frac{g - \gamma_0^{45^\circ}}{\gamma_0^{45^\circ}} \cdot dn + \frac{\bar{g}_A - \gamma_0^{45^\circ}}{\gamma_0^{45^\circ}} \cdot H_A - \frac{\bar{g}_B - \gamma_0^{45^\circ}}{\gamma_0^{45^\circ}} \cdot H_B \tag{9.3}$$

While the surface gravity g can be derived from gravity data bases (Hirt and Flury [2007]), the mean gravities $\bar{g}_A$ and $\bar{g}_B$ require hypotheses about the mass and density distributions between surface (H>0) and geoid (H=0). This is in contrast to the quasigeoid determination, where the orthometric correction E_{AB} is substituted by the normal correction E^n_{AB}. For the computation of E^n_{AB}, the mean gravities $\bar{g}_A$ and $\bar{g}_B$ are replaced by the normal gravities $\bar{\gamma}_A$ and $\bar{\gamma}_B$, respectively, hence, no hypotheses are necessary (Torge [2001]).

Finally, the geoid height difference ΔN_{AB} between two points A and B at a distance ds results from the integration of:

$$\Delta N_{AB} = -\int_{A}^{B} \varepsilon \cdot ds - E_{AB} \tag{9.4}$$

An important advantage of the astrogeodetic method is the fact that a local geoid can be determined from relatively few data within the computation area. This is in contrast to the gravimetric method (chapter 9.1.2), where the application of the Stokes formula (Eq. (9.7)) theoretically requires a coverage over the whole earth. A disadvantage of the astrogeodetic method might be the fact that the DOV should be provided with an adequate spatial resolution along a profile or within a network. This is necessary for a precise representation of the gravity field and a reliable interpolation between the data (Hirt and Flury [2007]). However, due to the enhancement of the astrogeodetic technique within the last years, this fact does not form a big challenge anymore, since the method is now significantly less time-consuming and expensive than before. Indeed, it has to be considered that the method only provides relative geoid undulations. In order to get absolute information, the geoid height has to be known at one station in minimum. That implicates an error cumulation with increasing distance to the reference station.

The accuracy of the geoid heights in dependence on the distance ds can be derived from a simple error propagation. Based on Eq. (9.4) (by neglecting the orthometric correction), a fictive uncertainty for ε of 1 arcsec over a distance ds of 1000 m yields about 4.9 mm for the geoid height difference dN. For an arbitrary error σ_ε and a distance ds, it is then (Hirt [2004]):

$$\sigma_{dN} = 4.9\ mm \cdot \frac{ds\,[m]}{1000\,[m]} \cdot \frac{\sigma_\varepsilon\,[arcsec]}{1\,[arcsec]} \tag{9.5}$$

The sum over n geoid height differences dN along a profile yields then an error $\sigma_{\Delta N}$ of the resulting geoid undulation by:

$$\sigma_{\Delta N} = \sqrt{n} \cdot \sigma_{dN} \tag{9.6}$$

9.1.2 Gravimetric method

The classical method is based on Stokes (1849) and provides absolute geoid undulations in a geocentric system (Heiskanen and Moritz [1967]):

$$N = \frac{R}{4\pi\gamma} \iint \Delta g \cdot S(\Psi) \cdot d\sigma \tag{9.7}$$

R... Mean earth radius
γ... Normal gravity in computation point P (φ,λ)
Δg... Gravity anomaly in surface element $d\sigma$
S(ψ)... Stokes function at a spherical distance ψ between P and $d\sigma$

The weighting of the observations Δg is provided by the Stokes function:

$$S(\psi) = \frac{1}{\sin\frac{\psi}{2}} - 6 \cdot \sin\frac{\psi}{2} + 1 - 5 \cdot \cos\psi - 3 \cdot \cos\psi \cdot \ln(\sin\frac{\psi}{2} + \sin^2\frac{\psi}{2}) \tag{9.8}$$

with a spherical distance ψ:

$$\cos\psi = \sin\varphi_P \cdot \sin\varphi_Q + \cos\varphi_P \cdot \cos\varphi_Q \cdot \cos(\lambda_Q - \lambda_P) \tag{9.9}$$

P... Model point
Q... Integration point

The integration area covers the whole earth. The fact that gravity data are not obtainable everywhere forms an essential limitation of the method (Wirth [1990]). A lack of data produces long-wavelength errors in the geoid solution. However, the influence of data in a spherical distance Ψ greater than 30° is relatively low, hence, the integration can be terminated at a defined radius Ψ_0. Outside this radius, the observations are normally combined with data from a global spherical harmonic model, e.g. the EGM96 (Earth Gravitational Model 1996). Another problem is given by the fact that the integral has to be replaced by a summation of finite surface elements. Therefore, the measured gravity anomalies have to be expressed by representative mean values per surface element.

Generally, the gravity anomalies Δg are introduced in terms of free-air anomalies. They are easy to calculate and do not require assumptions about the density distribution inside the earth. However, they show a coarse behavior depending on the topography, and the calculation of a mean value per surface element might be difficult. Furthermore, the Stokes formula is based on the assumption that no masses exist outside the geoid which is not true for free-air anomalies. Despite of these limitations, they are more suitable for a geoid determination than Bouguer anomalies, because of the smaller indirect effect.

9.1.3 Satellite missions

The satellite-based indirect determination of the gravity potential uses satellites as sensors in the earth's gravity field. The analysis of the variations of satellite orbits, e.g. of CHAMP and GOCE satellites, allows for the estimation of the earth's gravity field structure. Other missions process information about the distance variations between two satellites, as e.g. provided by the GRACE twin satellite system. Hence, the coefficients C_{nm} and S_{nm} of the spherical harmonic series expansion can be derived and used for the calculation of the geoid undulation N (Heiskanen and Moritz [1967]):

$$N = \frac{G \cdot \mathrm{M}_E}{r \cdot \gamma} \sum_{n=2}^{n^*} \left(\frac{a_e}{r}\right)^n \sum_{m=0}^{n} P_{nm}(\sin\varphi)(C_{nm}\cos m\lambda + S_{nm}\sin m\lambda) \tag{9.10}$$

$G \cdot M_E$...	Product of gravitational constant G and earth's mass M_E
r...	Geocentric radius of the geodetic position (φ, λ)
a_e...	Mean earth radius
n*...	Limiting degree (e.g.: $n^* = 180$ yields about 32760 coefficients)
γ...	Normal gravity
P_{nm}...	Corresponding Legendre polynomials of degree n and order m
C_{nm}, S_{nm}...	Dimension-less coefficients

The method provides only long-wavelength structures of the earth's gravity field. An example for a resulting gravity field model is provided by the GGM02 (GRACE Gravity Model), which is presented in chapter 7.3.2. Within the last years, the spatial resolution could be improved from several thousands to several hundred kilometers by means of dedicated gravity field missions. The implementation of terrestrial gravity data, satellite altimetry data, topographic information as well as models of the sea surface topography in the modeling process enabled the enhancement of the resolution in the determination of the gravity field.

9.1.4 Direct observation of geoid undulations

The geoid determination by GPS based methods refers to the simple relation between two height systems (chapter 2.4):

$$N = h - H \tag{9.11}$$

N...	Geoid undulation
h...	Ellipsoidal height (GPS)
H...	Orthometric height

The geoid undulation N can be determined if the ellipsoidal height h from GPS as well as the orthometric height H are known at a station. For the definition of the respective height systems, see chapter 2.4. Orthometric heights can be determined by combining precise leveling and gravity measurements. A particular case is formed by marine areas. The sea surface describes approximately an equipotential surface representing the geoid. The scanning of the sea surface, e.g. by marine *GPS* or via *satellite altimetry*, provides direct information about the geoid (H=0). Detailed information related to marine GPS measurements can be found in chapter 7.4.2. Satellite altimetry uses a satellite (e.g. Topex/Poseidon, JASON) sending radar pulses to the sea surface. The distance between satellite and sea surface is calculated from the runtime of the radar impulse, reflected from the water surface. The scanned sea surface deviates from a true equipotential surface for the so called Dynamic Ocean Topography (DOT), which is caused by ocean currents, waves, wind, temperature and salinity of the water (see also chapter 7.4.2). These effects can be modeled and serve as corrections for marine observations.

The advantage of this method is that the gravity field can be determined with high resolution along a profile. However, because of the profile-like distribution of the observations, the spatial interpolation of geoid undulations is difficult.

9.2 Collocation

9.2.1 Theoretical background

Least-squares-collocation (LSC) forms a common interpolation and prediction method in geodesy and is thoroughly described e.g. in Moritz [1980], Wirth [1990] and Torge [2001]. The theoretical and mathematical background of LSC presented in the following subsections refer to Wirth [1990].

Collocation represents an extension of the least-squares-adjustment and is usually applied in problems, where not only the parameters of a functional model but also a stochastically-correlated part has to be estimated. The improvements of the observations are not considered to be uncorrelated, but split into two parts: the signal s and the noise n. The signal s is a stochastically-correlated part, while the noise n is regarded as a stochastically-uncorrelated information.

Generally, three problems are treated within the LSC approach (Moritz [1980]):

1) Parameter estimation: Determination of unknown function parameters
2) Filtering: Simultaneous determination of unknown function parameters and signal s in reference points
3) Prediction: Determination of signal s' in defined interpolation points

For the collocation method, correlations between the observations have to be assumed. They are represented by the variances and covariances between signal s and noise n, respectively, in observation points. Signal s and noise n are supposed to be normally distributed with an expectation value of "0". The covariances of the signal are specified by matrix C_{ss} (see Appendix A.3, Eq. (A.16)), while those of the noise are described

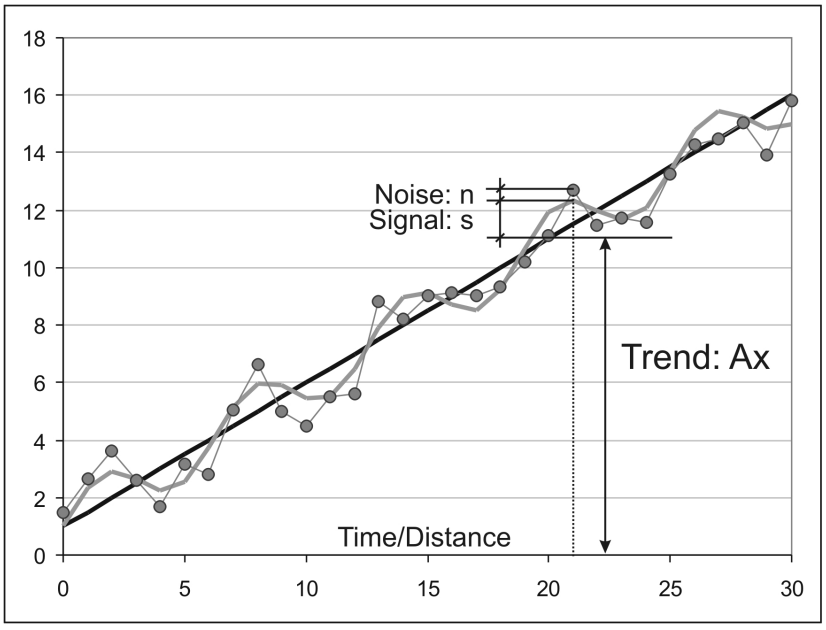

Figure 9.1: Trend, signal and noise.

by matrix C_{nn} (Eq. (A.17)), respectively. It is assumed that signal and noise are uncorrelated ($C_{sn} = 0$).

The basic equation of LSC is provided by the linearized observation equation:

$$l = Ax + s + n \tag{9.12}$$

with

$$l = f - F(x_0) \tag{9.13}$$

f... Observations
$F(x_0)$... Function F depending on approximate values x_0 for the unknown parameters
l... Vector of reduced observations
A... Design matrix = Derivatives of F with respect to the unknown parameters x
s... Signal: Stochastically-correlated part
n... Noise: Stochastically-uncorrelated part
x... Vector of unknowns

Provided that the matrices C_{ss} and C_{nn} are known (chapter 9.2.2), the further equations are:

$$D = C_{ss} + C_{nn} \tag{9.14}$$

$$x = (A^T D^{-1} A)^{-1} A^T D^{-1} l \tag{9.15}$$

$$n = C_{nn}D^{-1}(l - Ax) \tag{9.16}$$

$$s = C_{ss}D^{-1}(l - Ax) \tag{9.17}$$

$$s' = C_{ss'}D^{-1}(l - Ax) \tag{9.18}$$

$$t = A_1x + s' \tag{9.19}$$

with:

s'...	Predicted signal in interpolation points
t...	Interpolated data
$C_{ss'}$...	Covariances between signal s (in reference points) and s' (in interpolation points)
A_1...	Design matrix in dependence on the position of interpolation points

Special cases are:

$C_{nn} = 0 \rightarrow C_{ll} = C_{ss}$:	No filtering, observations are free of noise (n=0)
$C_{ss} = 0 \rightarrow C_{ll} = C_{nn}$:	Simple parameter estimation without signal = classical adjustment theory: $-n = v = -(l - Ax) = Ax - l$
$A = 0$:	Prediction without parameter estimation

The error matrices can be calculated a priori without any observations l. They are defined by the covariance matrices of signal and noise and the geometrical information about the location of the reference stations.

Variance-covariance matrix E_{xx} of the unknown parameters x:

$$E_{xx} = (A^TD^{-1}A)^{-1} \tag{9.20}$$

Variance-covariance matrix E_{ss} of signal s (with $\sigma_0 = 1$):

$$E_{ss} = C_{s's'} - C_{s's}D^{-1}C_{s's}^T + C_{s's}D^{-1}AE_{xx}A^TD^{-1}C_{s's}^T \tag{9.21}$$

Variance-covariance matrix E_{tt} of the complete signal t (signal s and trend Ax):

$$E_{tt} = C_{s's'} - C_{s's}D^{-1}C_{s's}^T + (HA - A_1)E_{xx}(A^TH^T - A_1^T) \tag{9.22}$$

with:

$$H = C_{s's}D^{-1} \tag{9.23}$$

9.2.2 Correlations between gravity field parameters

The gravity field parameters N, ξ, η and Δg are strongly correlated, since they are all induced by the same anomalous potential T. Based on the Stokes formula in planar approximation (compare Eq. (9.7)) (Shaw et al. [1969],Wirth [1990], Schwarz et al. [1990]):

$$N(x,y) = \frac{1}{2\pi\gamma} \int_{-\infty}^{\infty} \int_{-\infty}^{\infty} \frac{\Delta g(u,v)}{\sqrt{(x-u)^2 + (y-v)^2}}\, du\, dv \tag{9.24}$$

with:

N(x,y)...	Geoid undulation in point P(x,y)
$\Delta g(u,v)$...	Gravity anomaly in surface element (du,dv)
γ...	Normal gravity

the DOV-components (ξ, η) and the gravity anomaly Δg can be derived in the following way:

$$\xi(x,y) = -\frac{1}{\gamma}\frac{\partial T}{\partial x} = -\frac{\partial N}{\partial x} \qquad \eta(x,y) = -\frac{1}{\gamma}\frac{\partial T}{\partial y} = -\frac{\partial N}{\partial y} \tag{9.25}$$

$$\Delta g = -\frac{\partial T}{\partial r} - \frac{2}{r}T \approx -\frac{1}{\gamma}\left(\frac{\partial N}{\partial r} + 2\frac{N}{r}\right) \qquad \lim_{r\to\infty} \Delta g = -\frac{\partial T}{\partial z} \tag{9.26}$$

The relations above can be applied to the auto-covariance function Φ_{NN} of the geoid undulation N (chapter 9.2.3). Based on this function, all variances and covariances can be derived (Wirth [1990]):

$$\Phi_{\xi\xi} = -\frac{\partial^2}{\partial x^2}\Phi_{NN} \tag{9.27}$$

$$\Phi_{\eta\eta} = -\frac{\partial^2}{\partial y^2}\Phi_{NN} \tag{9.28}$$

$$\Phi_{gg} = g_0^2(\Phi_{\xi\xi} + \Phi_{\eta\eta}) = -g_0^2\left(\frac{\partial^2}{\partial x^2} + \frac{\partial^2}{\partial y^2}\right)\Phi_{NN} \tag{9.29}$$

$$\Phi_{\xi\eta} = -\Phi_{\eta\xi} = -\frac{\partial^2}{\partial x \cdot \partial y}\Phi_{NN} \tag{9.30}$$

$$\Phi_{N\xi} = -\Phi_{\xi N} = -\frac{\partial}{\partial x}\Phi_{NN} \tag{9.31}$$

$$\Phi_{N\eta} = -\Phi_{\eta N} = -\frac{\partial}{\partial y}\Phi_{NN} \tag{9.32}$$

$$\Phi_{Ng} = -g_0\frac{\partial}{\partial z}\Phi_{NN} \tag{9.33}$$

9.2.3 Covariance function

The covariance function Φ_{NN} (chapter 9.2.2) is generally defined by two parameters: the amplitude σ_0^2, which represents the variance of the signal and the characteristic length d, also called correlation length.

There exist different covariance functions that often produce similar results (Wirth [1990]):

$$\Phi(r) = \sigma_0^2 \cdot e^{-\frac{r}{d}} \qquad \text{First order Markov model} \tag{9.34}$$

$$\Phi(r) = \sigma_0^2 \cdot \frac{d}{\sqrt{r^2+d^2}} \qquad 1/\mathrm{r} - \text{model used by Wirth} \tag{9.35}$$

$$\Phi(r) = \sigma_0^2(1 + \frac{r}{d} + \frac{r^2}{3d^2}) \cdot e^{-\frac{r}{d}} \qquad \text{Third order Markov model} \tag{9.36}$$

All the functions depend on the distance r between the points (homogeneity), but are independent from the azimuth (isotropy). In Wirth [1990] and Marti [1997], the third-order Markov model (Eq. 9.36) is used forming a self-consistent model for gravity field determination. The model fulfills the requirements that:

a) the covariance function for DOV should have a finite value for r = 0:

$$-\infty < \lim_{r\to 0} \frac{\partial \Phi_{NN}(r)}{\partial r}\frac{1}{r} < 0$$

b) the covariance function for gravity anomalies should have a horizontal tangent for r = 0:

$$\left.\frac{\partial \Phi_{gg}(r)}{\partial r}\right|_{r=0} = 0$$

Referring to Eqs. 9.27 to 9.33, all variance and covariance functions between the parameters ξ, η, g, N can be found by applying the covariance function Φ_{NN} (compare Eq. 9.36) (Wirth [1990]):

$$\Phi_{NN} = \sigma_N^2(1 + \frac{r}{d} + \frac{r^2}{3d^2}) \cdot e^{-\frac{r}{d}} \tag{9.37}$$

$$\Phi_{N\xi} = -\sigma_\varepsilon^2(1 + \frac{r}{d}) \cdot \Delta x \cdot e^{-\frac{r}{d}} \tag{9.38}$$

$$\Phi_{N\eta} = -\sigma_\varepsilon^2(1 + \frac{r}{d}) \cdot \Delta y \cdot e^{-\frac{r}{d}} \tag{9.39}$$

$$\Phi_{\xi\xi} = \sigma_\varepsilon^2(1 + \frac{r}{d} - \frac{\Delta x^2}{d^2}) \cdot e^{-\frac{r}{d}} \tag{9.40}$$

$$\Phi_{\eta\eta} = \sigma_\varepsilon^2(1 + \frac{r}{d} - \frac{\Delta y^2}{d^2}) \cdot e^{-\frac{r}{d}} \tag{9.41}$$

$$\Phi_{gg} = \sigma_g^2(1 + \frac{r}{d} - \frac{r^2}{2d^2}) \cdot e^{-\frac{r}{d}} \tag{9.42}$$

9.2.4 Covariance parameters

As mentioned in the beginning of chapter 9.2.3, the two main parameters of a covariance function are:

Characteristic distance (correlation length) d

The parameter d has a significant impact on the interpolation of the gravity field. It determines the smoothing quantity of the resulting function: If d is too small, the signal compared to the mean distance between the stations is overestimated. In contrast, a too large correlation length causes a too strong filtering at the stations, hence loosing signal information. The impact of d on the course of the interpolated gravity field is demonstrated in chapter 9.4.1.

Sigma of signal σ_0

The parameter σ_0 does not directly affect the interpolation of the gravity field. However, in combination with the sigma of noise (σ_n), it defines the weighting between signal and noise.

Both parameters can be empirically determined from observations. For centered observations it is:

$$E[l_i \cdot l_k] = \Phi_{l_i l_k} \tag{9.43}$$

The expectation value E of the product of two observations l_i and l_k with a distance r is an estimation for the covariance function $\Phi(r) = \Phi_{l_i l_k}$. Hence, for homogeneous approaches, the empirical covariances can be estimated by calculating the product of observations, which are allocated to dedicated distance classes. The parameter d and σ_0 of the covariance function can then be determined by a least-squares-adjustment.

Applied to the DOV (ξ,η), the averaged products $[\xi_i \cdot \xi_k]$, $[\eta_i \cdot \eta_k]$ and $[\xi_i \cdot \eta_k]$ have been calculated for defined distance classes. Fig. 9.2 represents the classified mean empirical covariances of $[\xi_i \cdot \xi_k]$ (blue dots) and $[\eta_i \cdot \eta_k]$ (red dots), respectively. Before, the

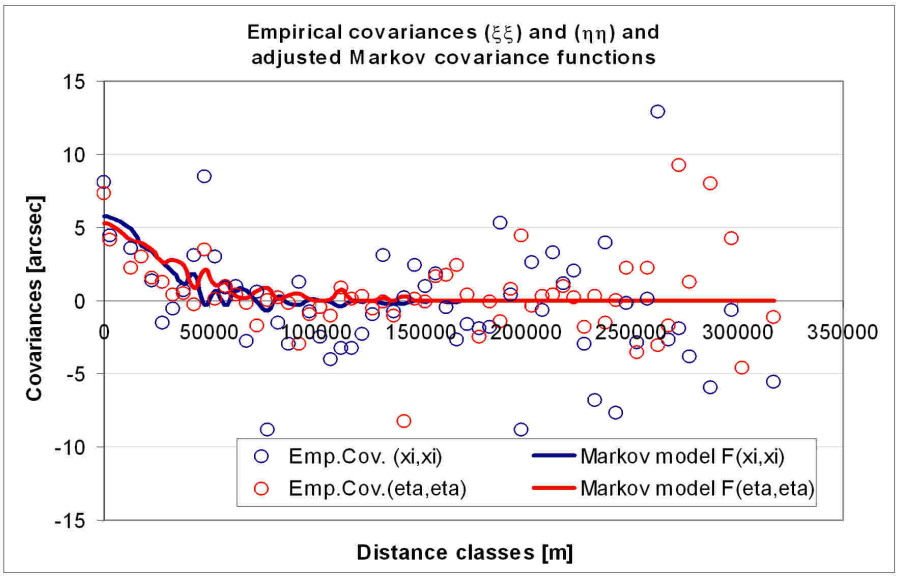

Figure 9.2: Empirical covariances $[\xi_i \cdot \xi_k]$ (blue) and $[\eta_i \cdot \eta_k]$ (red) assigned to different distance groups. The correlation length d amounts to 23 km, and the sigma of signal σ_ε to 2.5 arcsec.

DOV have been reduced for topography, bathymetry and isostasy (after Airy-Heiskanen) and a second-order trend. It is well recognizable that the empirical covariances show a maximum for distance "0" and decrease with increasing distance. The undulating amplitudes for groups of large distances are caused by a smaller number of stations belonging to these groups.

The empirical covariances served as input for a least-squares-adjustment. The functional models used are the respective covariance functions derived from the third-order Markov model (Eqs. 9.27 and 9.28) with the unknown parameters d and σ_ε. In Fig. 9.2 the adjusted functions are depicted as blue line ($[\xi_i \cdot \xi_k]$) and red line ($[\eta_i \cdot \eta_k]$). The unknown parameters have been determined to 23 km (d) and 2.5 arcsec (σ_ε), respectively. However, as the mean distance between all Astro stations is about 130 km, "d" should not be smaller than 65 km, otherwise the interpolation of the gravity field might be inadequate (see chapter 9.4.1). Hence, for the final collocation, the parameters d=65 km and σ_ε=2.5 arcsec have been used.

9.3 Cogeoid and Geoid

9.3.1 Theoretical background

As explained in chapter 8.1, the so called Remove-Restore technique has been applied in the frame of geoid determination. The computation of mass effects within a defined area (chapter 8.2) and the reduction of the observations for these effects provide smoothed residual DOV (chapter 8.6). The interpolation between the Astro stations has been realized by means of the LSC method (chapter 9.2) using the third-order Markov covariance model (chapter 9.2.3). The covariance parameters *correlation length d* and *sigma of signal* σ_0 have been defined to 65 km and 2.5 arcsec, respectively (chapters 9.2.4 and 9.4.1). The prediction has been performed in a 5 km x 5 km grid. The resulting surface, called *cogeoid*, represents a regularized geoid, which is free of dedicated masses (Elmiger [1969]). The term "cogeoid" has been introduced in 1948 by the International Union for Geodesy and Geophysics (IUGG). The following considerations might help to understand the concept of a cogeoid (Gurtner [1978]):

The difference between the true potential W and the normal potential U is called anomalous potential T (see also chapter 2.4):

$$T = W - U \tag{9.44}$$

The anomalous potential T can be split into two parts: the anomalous potential T_M, which is induced by masses considered within a model (e.g. DTM, isostasy models, Moho model) and the anomalous potential T_S, which is generated by unknown masses that have not been considered within a mass model:

$$T = T_M + T_S \tag{9.45}$$

According to Eqs. (9.44) and (9.45), the potential of the cogeoid $(W - T_M)$ forms a sum of normal potential U and anomalous potential T_S. The potential T_S is responsible for the remaining residuals after the mass reduction (Eq. (8.12)). In case all masses would have been suitably modeled ($T_S = 0$), the residual DOV should amount to "0" representing then the normal vectors to the ellipsoid (normal potential U). Depending on the masses considered in the reduction, different cogeoid models can be calculated. The respective surfaces reveal the impact of unaccounted masses and form, therefore, an interesting surface for dedicated interpretations (chapter 9.3.2).

The missing difference dN between geoid undulation N_{Geoid} and cogeoid undulation $N_{Cogeoid}$ (Fig. 9.3) can be derived from the application of Bruns law to the anomalous potential T_M (Gurtner [1978]):

$$\begin{aligned} N_{Geoid} &= N_{Cogeoid} + dN \\ dN &= \frac{T_M}{\gamma} \\ N_{Geoid} &= N_{Cogeoid} + \frac{T_M}{\gamma} \end{aligned} \tag{9.46}$$

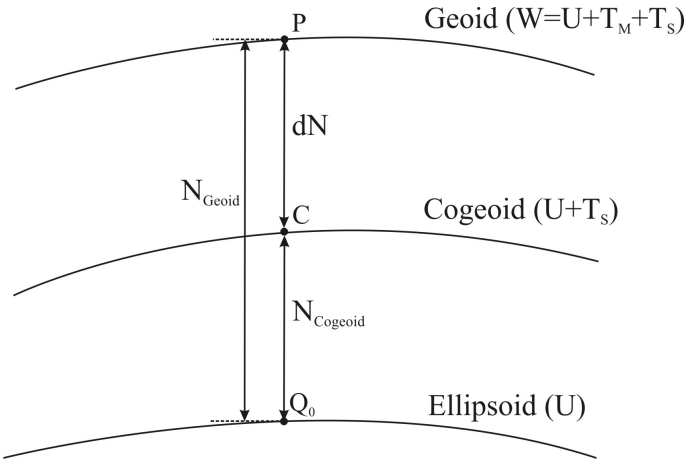

Figure 9.3: Depiction of geoid, cogeoid and ellipsoid (modified after Gurtner [1978]).

The anomalous potential T_M is determined within the computation of mass effects (chapter 8.2), while γ represents the normal gravity at the ellipsoid.

9.3.2 Interpretation of cogeoids

Topographic-bathymetric cogeoid (TB cogeoid)

The TB cogeoid represents the geoid as it would be without topography and bathymetry. The variations of the TB cogeoid (Fig. 9.4) amount to about 13 m in the research area showing continuously increasing cogeoid undulations in SW-NE direction. The maximum is located between Athos[1], the island of Limnos (=L) and the Sporades islands (=SI). This trend might result from a non-consideration of a global spherical harmonic model (e.g. EGM96, chapter 7.3.1) within the process of mass reduction. Hence, long-wavelength information of the gravity field are still included in the TB cogeoid.

After subtracting a first-order trend, the variations are smaller and range between -1.8 m and 1.5 m (Fig. 9.5). The TB cogeoid now clearly indicates a negative correlation with the mass distribution in the region, most likely reflecting unconsidered isostatic masses (Moho discontinuity). This is reinforced by the recognizable upwarp of the cogeoid along the North Aegean Trough (NAT), which indicates a thinner oceanic crust. By contrast, the minima beneath the western and northern mainland denotes a thicker continental crust. Both corresponds to the isostatic theory described in chapter 8.4.

Please note: Due to the fact that the DOV and SSH data do not cover the whole prediction area, the border zones of the cogeoid and geoid solutions presented in Figs. 9.4, 9.5 and following figures indicate a decreasing significance. Regions with an accuracy of the geoid undulations worse than 0.6 m have been designated by white points. The accuracy appraisal refers to the investigation of the error matrix E_{tt} (chapters 9.4.2 and 9.4.3). For the Astro Geoid, Fig. 9.17 and for the DOVSSH07 geoid, Fig. 9.25 were decisive.

[1]For geographic references see Figs. 7.1 and 7.12, respectively

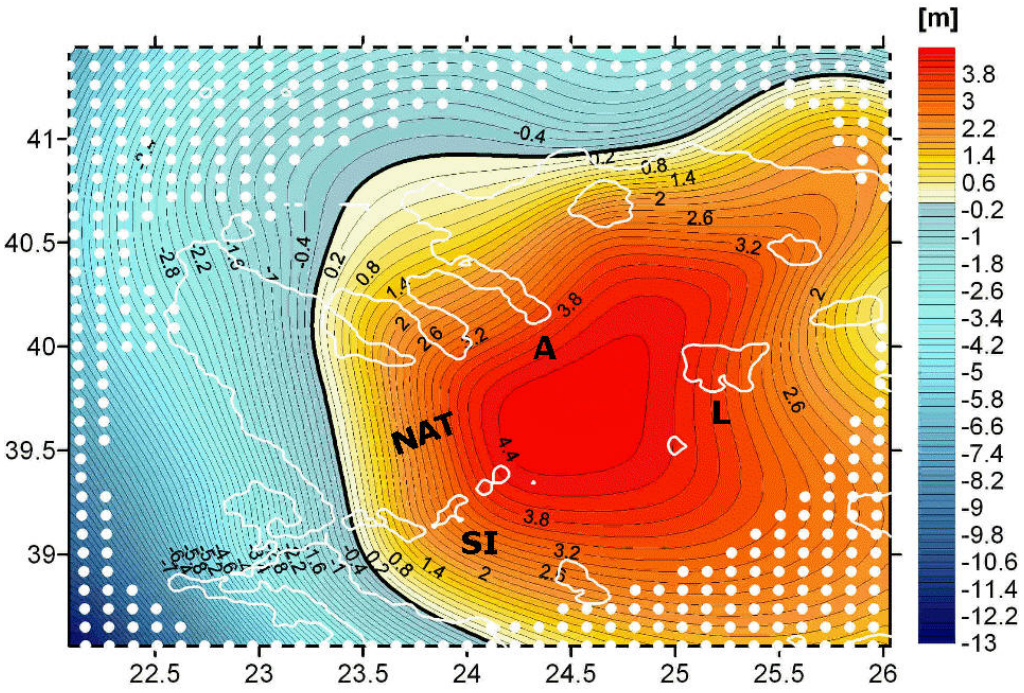

Figure 9.4: Topographic-bathymetric cogeoid (TB cogeoid). A mean offset has been removed. The white points signalize an accuracy of the geoid undulation worse than 0.6 m according to Fig. 9.17. A trend in SW-NE direction is clearly recognizable showing variations of about 13 m. NAT = North Aegean Trough; SI = Sporades islands; A = Athos; L = Limnos.

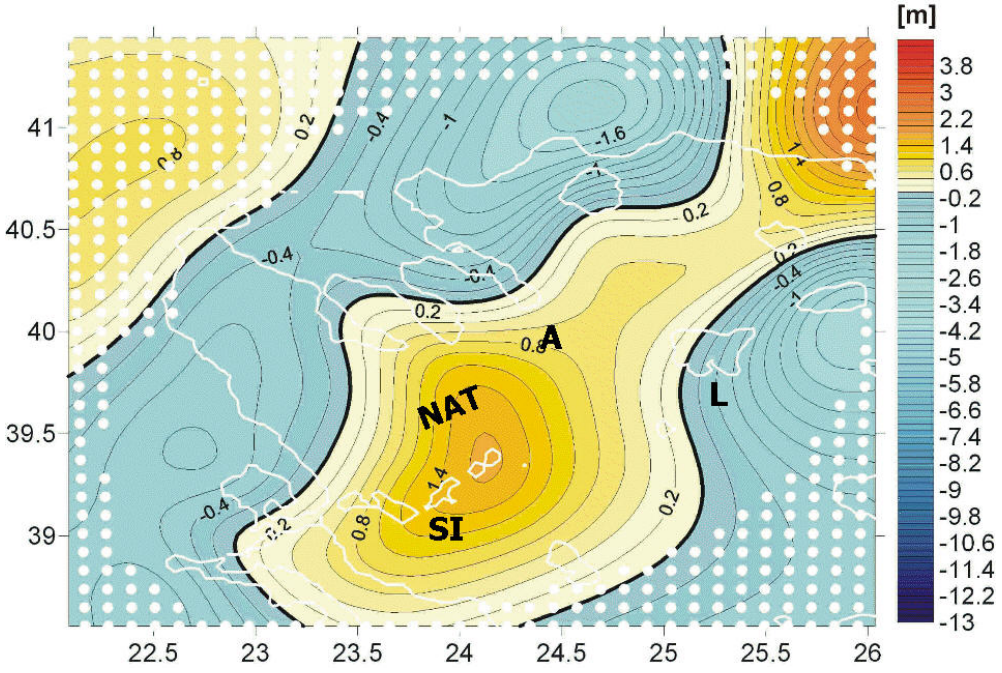

Figure 9.5: Topographic-bathymetric cogeoid (TB cogeoid) after subtracting a first-order trend. It is assumed that the remaining variations between -1.8 m and 1.5 m are largely induced by unconsidered isostatic masses. NAT = North Aegean Trough; SI = Sporades islands; A = Athos; L = Limnos.

Topographic-bathymetric-isostatic cogeoid (TBAH cogeoid)

If the assumption applies that the TB cogeoid reflects mainly unconsidered isostatic compensation masses, an additional removal of these masses should yield a relatively flat cogeoid. This would suggest that the region is in a state of isostatic equilibrium. The isostatic model used for the data reduction is the Airy-Heiskanen model (chapter 8.4.2). As regards the resulting TBAH cogeoid, a SW-NE trend becomes obviously, with variations of about 9 m (Fig. 9.6). Similar to the TB cogeoid (Fig. 9.4), this trend might be ascribed to the fact that no long-wavelength gravity field model has been used within the process of mass reduction. Deep-rooted structures like the effect of the African slab (chapter 8.5.1) have not been considered.

After subtracting a first-order trend, short-wavelength variations of the TBAH cogeoid become apparent (Fig. 9.7). As derivable from the remaining variations between -3.2 m and 1.6 m, the isostatic compensation in the region seems to be incomplete. Hence, an upcoming Moho is indicated within the marine area, with a maximum beneath the Sporades islands (=SI). By contrast, a decreasing Moho is denoted in direction to the western and northern mainland, respectively. Most likely, these variations can be attributed to the particularly tectonic settings of the region. As described in chapter 7.2.2, the region is characterized by a west-southwestward motion of the Anatolian-Aegean microplate, with extension rates of up to 36 mm/yr (Fig. 7.5). This produces a stretching of the oceanic crust and, hence, an upcoming Moho.

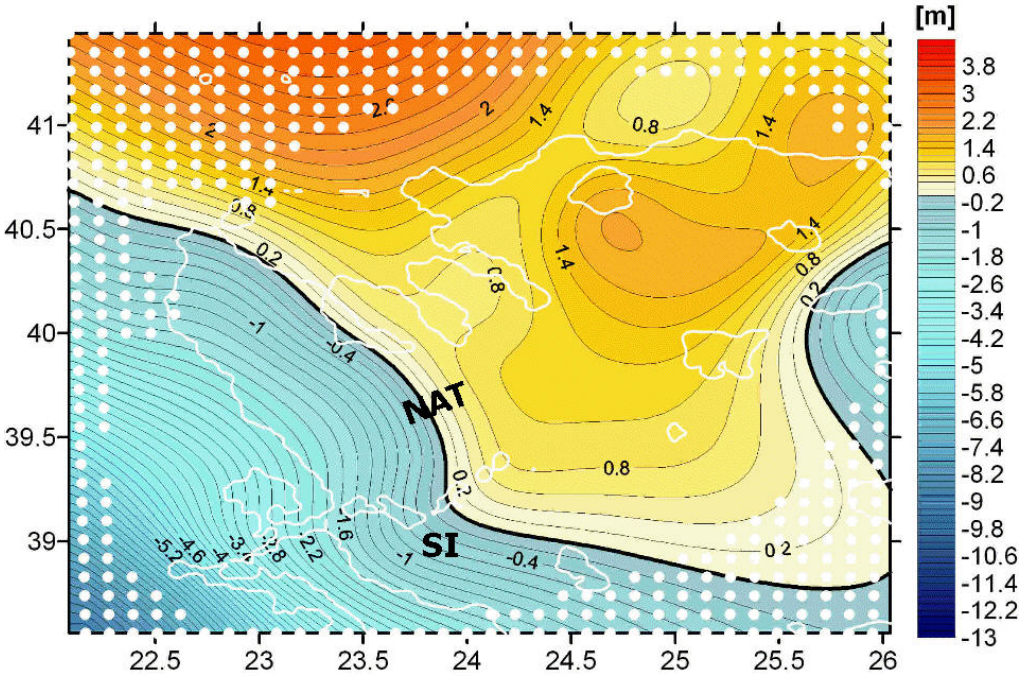

Figure 9.6: Topographic-bathymetric-isostatic cogeoid (TBAH cogeoid). The isostasy model applied is based on the theory of Airy-Heiskanen. A mean offset has been removed. The variations show a clear SW-NE trend with a range of about 9 m. NAT = North Aegean Trough; SI = Sporades islands.

A part of the cogeoid variations might be also caused by other reasons, as e.g. insufficiencies of the isostatic theory applied, measuring errors of the astrogeodetic method as well

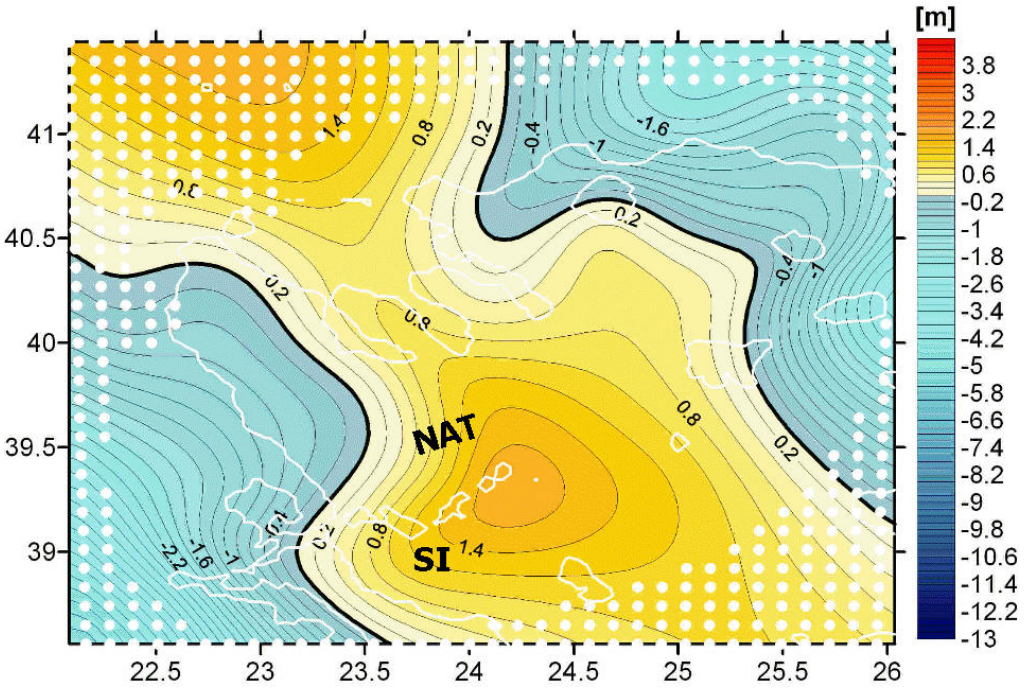

Figure 9.7: Topographic-bathymetric-isostatic cogeoid (TBAH cogeoid) after the subtraction of a first-order trend. The remaining variations between -3.2 m and 1.9 m suggest an incomplete isostatic equilibrium of the region. This might be caused by the particularly tectonic setting of the region. NAT = North Aegean Trough; SI = Sporades islands.

as errors in the process of data reduction and collocation. However, due to the rather large amplitudes of variations, these reasons can be widely excluded.

Topographic-bathymetric-Moho cogeoid (TBMoho cogeoid)

Since the Airy-Heiskanen isostasy model only reflects a theoretical correlation between masses above the earth and compensations masses inside the earth, it is more appropriate to use a Moho model predicted by real measurements. Hence, for the computation of the TBMoho cogeoid, Moho depths based on the model of Tsokas and Hansen [1997] (Tsokas model) have been used (chapter 8.5.2). The TBMoho cogeoid (Fig. 9.8) represents the geoid after the removal of all masses down to the crust-mantle-boundary. The recognizable signal in the TBMoho cogeoid has a short-wavelength character of about 100 km with variations between -2.5 m and 1 m. They reflect most likely insufficiencies of the Moho model.

Hence, the two significant bulges along the NAT, one north of the Sporades islands (=SI) and one between the islands of Thassos (=T), Samothraki (=S) and Limnos (=L), represent an upwarp of the Moho discontinuity. This implies that the Tsokas model is rather to deep in this region. Furthermore, the depression beneath the peninsulas of Athos and the northern mainland reveals the assumption of a rather too shallow Moho. These results agree well with the conclusions in chapter 8.5.2, where the Tsokas model has been compared to other models available in the Aegean Sea domain:

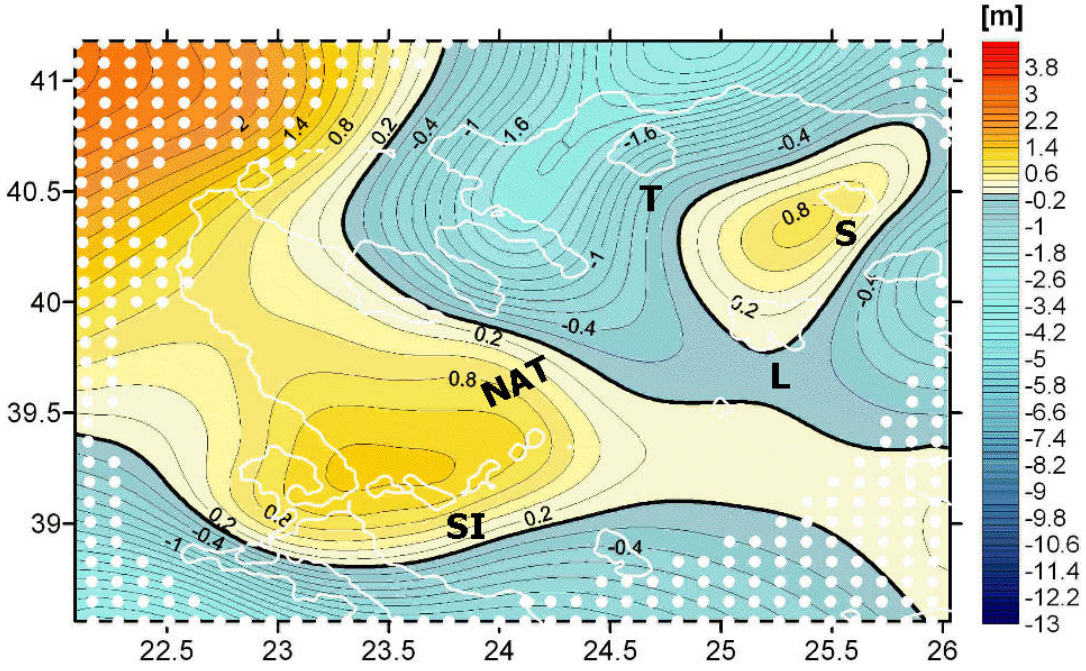

Figure 9.8: Topographic-bathymetric-Moho cogeoid. The Moho depths used for the data reduction are based on the Moho model of Tsokas and Hansen [1997]. The mean offset has been removed. The variations between -2.5 m and 1 m are potentially caused by insufficiencies of the Moho model. NAT = North Aegean Trough; SI = Sporades islands; T = Thassos; S = Samothraki; L = Limnos.

- A significant deficit of the Tsokas model (Fig. 8.8) is the absence of a negative correlation between topographic/bathymetric features and Moho depths, as it is assumed by the isostatic theory and indicated by other Moho models (e.g. by Tirel et al. [2004], Fig. 8.6***a)***). Hence, the Tirel model suggests an elongate zone of shallower depths along the NAT (chapter 8.5.1). This characteristic is not recognizable in the Tsokas model (compare Figs. 8.6***a)*** and 8.8). It rather suggests a minimum depth beneath Athos (Chalkidiki). The TBMoho cogeoid variations confirm these discrepancies by a corresponding increase along the NAT and decrease beneath Athos.
- Another point of discrepancy is induced by the large Moho depth variations in the northern Aegean of about 10 km in the Tsokas model compared to about 4 km in the Tirel model. Hence, the detection of overestimated Moho depths north of the Sporades islands (cogeoid bulge) and underestimated depths beneath Chalkidiki (cogeoid decline), respectively, well correspond to the smaller variations suggested by the Tirel model.

The following points might provide explanations for the revealed discrepancies of the Tsokas model: First of all, the model has been computed by an inversion of Bouguer anomalies extracted from the Bouguer anomaly map of Greece along four profiles (Tsokas and Hansen [1997]). A potential error source might result from the fact that they have not been reduced for the effect of the African slab. Hence, the Bouguer anomalies used for the estimation of Moho depths are still superposed by a long-wavelength signal of the subducting African lithosphere. A further error source might be ascribed to the disregard of lighter sediments, as they occur in the whole North Aegean Sea (Fig. 7.3). Tirel et al. [2004] indicated a layer thickness of 5 to 6 km there. The resulting density

variations have been considered neither in the computation of Moho depths by Tsokas and Hansen [1997] nor in the reduction of the DOV presented in chapter 8.6. This fact might produce overestimated Moho depths causing a part of the two indicated bulges in the TBMoho cogeoid (Fig. 9.8). Besides, their neglect in the process of data reduction rather yields a too steep bulge. In both cases, a consideration of the sediment layer would potentially result in flatter bulges.

It is interesting that the discovered variations of the TBMoho cogeoid fit well with the particularly tectonic settings of the region. As already explained in association with the TBAH cogeoid, the extension of the Aegean Sea (chapter 7.2.2) results in a streching of the oceanic crust. This characteristic is supported by the two Moho bulges occuring along the NAT. Of course, also other reasons for the revealed TBMoho cogeoid variations have to be considered. Hence, similar to the reasons discussed in relation with the TBAH cogeoid, errors of the astrogeodetic method as well as errors within the process of data reduction and collocation have to be kept in mind. However, the rather large scale variations more likely argue against these reasons.

It has to be noticed that the Moho model is given within $34.5° < \varphi < 41.5°$ northern latitude and $19° < \lambda < 27°$ western longitude. Hence, in the northern and eastern part, the significance of the presented TBMoho cogeoid is limited due to the inadequate coverage of the research area by Moho data.

9.3.3 Astro geoid

The TB cogeoid presented in chapter 9.3.2 forms the basis for the final computation of the Astro geoid. Therefore, the removed topographic and bathymetric masses have to be restored at height "zero" (Marti [1997]). Since the astrogeodetic geoid determination only allows for the calculation of relative undulations, the geoid has been added to a mean geoid height of 40.7 m. This value refers to the mean height computed from the SSH data (chapter 7.4.2).

Fig. 9.9 represents the final Astro geoid based on the collocation of 27 ξ- and 27 η-components. The geoid undulations vary between 34.6 m and 46.3 m. By comparing the geoid with local topographic and bathymetric features in this region (chapter 7.2.1, Fig. 7.1), the correlation between both is well recognizable. Hence, the effect of the NAT and, especially, the distinctive low north of the Sporades islands (Sporades basin = SB) are well identifiable in the geoid. Between the peninsula of Kassandra (=K) to the north and the Sporades islands (=SI) to the south, the bathymetry varies strongly with a maximum depth of about -1100 m. This characteristic is reflected by geoid variations reaching about 2.6 m. Another remarkable fact is that the geoid reproduces the influences of the islands of Thassos (=T), Samothraki (=S) and Limnos (=L), located in the northeastern part of the North Aegean Sea, by indicating respective local maxima there. Furthermore, the impact of distant masses is well recognizable in terms of long-wavelength signals. Hence, the northern land masses are indicated by a significant increase of the geoid heights in this direction. Moreover, it is assumed that the decrease of the geoid in the southwestern part of the region is caused by the characteristics of the Moho model denoting large depths beneath the western mainland (compare Figs. 8.6***b)*** and 8.8 and see chapter 9.3.2).

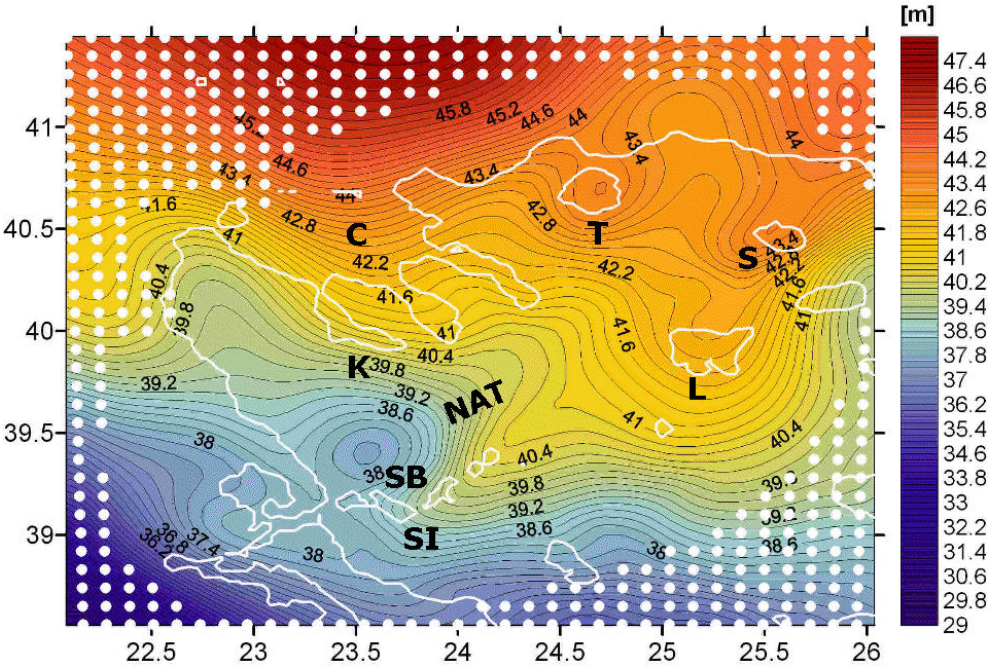

Figure 9.9: Astro geoid based on the calculation of 27 ξ- and 27 η-components. The white points denote an accuracy of the geoid undulation worse than 0.6 m according to Fig. 9.17. The most prominent feature of the Astro geoid is the well recognizable impact of the NAT between the Sporades islands (=SI) to the south and Chalkidiki (=C) to the north. NAT = North Aegean Trough; SB = Sporades basin; K= Kassandra; T = Thassos; S = Samothraki; L = Limnos.

9.3.4 DOVSSH07 geoid

In order to close the lack of Astro stations in the marine area, 240 SSH corrected for tidal effects and the Mean Dynamic Sea Surface Topography, have been additionally introduced into the collocation process. Before the interpolation, they have been reduced for topography and bathymetry, hence representing the same reference surface as the residual DOV used for the computation of the Astro geoid (chapter 9.3.3). The distribution of DOV and SSH, respectively, within the prediction area is shown in Fig. 7.14. In the following, the combined geoid is called *DOVSSH07 geoid* (Fig. 9.10).

At a first glance, the use of additional data does not involve a big change. The geoid undulations vary between 34.6 m and 45.3 m, hence showing a similar range like the Astro geoid. However, making a more elaborate analysis, the benefit of additional information is significant. Based on a visual comparison of both geoids, the main differences appear in the region of the NAT. Compared to the bathymetric isolines in Fig. 7.1, the DOVSSH07 geoid reproduces better the location and SW-NE extension of the NAT. Concerning the relative changes of geoid heights crossing the NAT in N-S direction between Kassandra (=K) and the Sporades islands (=SI), there are also significant differences. While the Astro geoid indicates variations of 2.6 m, the DOVSSH07 geoid heights only change for about 1.6 m. Another interesting region of discrepancy can be found between the Sporades islands (=SI), the islands of Agios Efstratios (=AE) and Skiros (=SK). As visible in Fig. 7.1, the bathymetry shows a distinctive low with a depth of -900 m there. This local minimum is clearly indicated in the DOVSSH07 geoid, while it is not

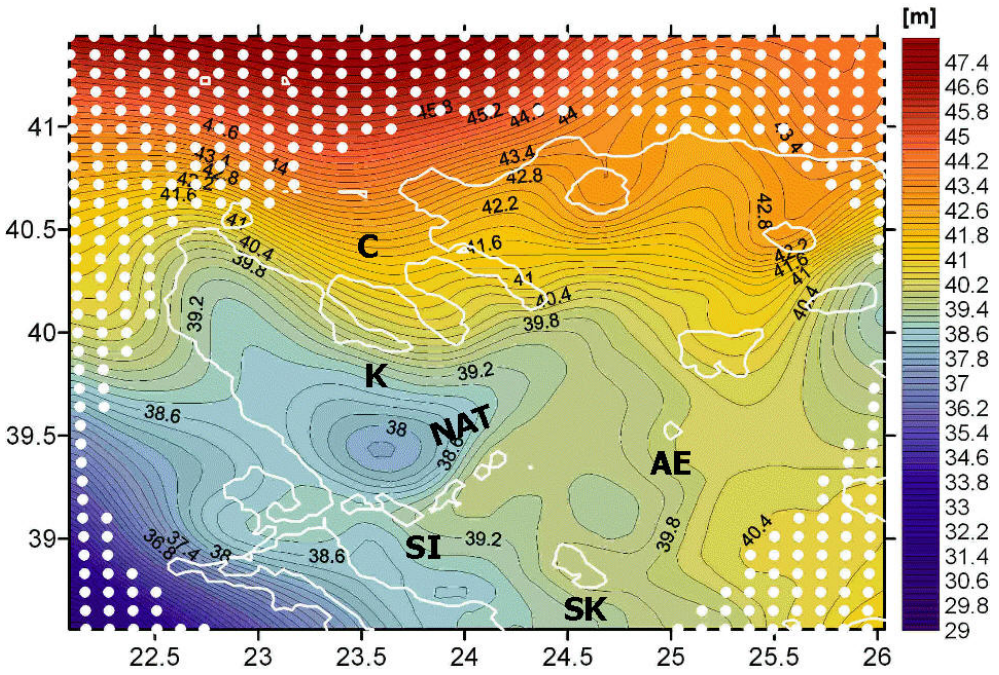

Figure 9.10: DOVSSH07 geoid based on the calculation of 27 ξ- and 27 η-components and 240 "corrected" SSH. The white points denote an accuracy of the geoid undulation worse than 0.6 m according to Fig. 9.25. In comparison to the Astro geoid (Fig. 9.9), the combined solution clearly reflects the SW-NE extension of the NAT. NAT = North Aegean Trough; SI = Sporades islands; AE= Agios Efstratios; SK = Skiros; K = Kassandra; C = Chalkidiki.

recognizable in the Astro solution.

A more descriptive representation of the differences between Astro and DOVSSH07 geoid is represented by the plot "*DOVSSH07 geoid* minus *Astro geoid*" (Fig. 9.11). The mean difference amounts to -0.35 m. After subtracting the offset, the differences range between -1.44 m and 2.61 m. The visual analysis of the difference plot reveals the following features: A maximum difference of +0.7 m is detected at the western mainland. The differences decrease continuously in northern and northwestern direction, respectively. They reach a minimum of -0.8 m beneath the peninsula of Kassandra (=K) and and another one of -1.7 m beneath the island of Limnos (L). The described discrepancies might be attributed to the lack of Astro stations in the marine area, which has been bridged by the SSH. The northern minimum might result from the fact that the SSH have been only measured to a maximum northern latitude of about 40°, while the information in the Astro geoid are supported by three observations located more northerly (Kassandra, Thessaloniki (=T) and Litochorou (=LI), compare also Fig. 7.12).

9.3.5 Validation of the DOVSSH07 geoid

In order to validate the final DOVSSH07 geoid presented in chapter 9.3.4, it is compared to existing geoid models within the research area of the North Aegean Sea. These models have been presented in chapter 7.3. A statistical comparison of the validation results can be found in Tab. 9.1.

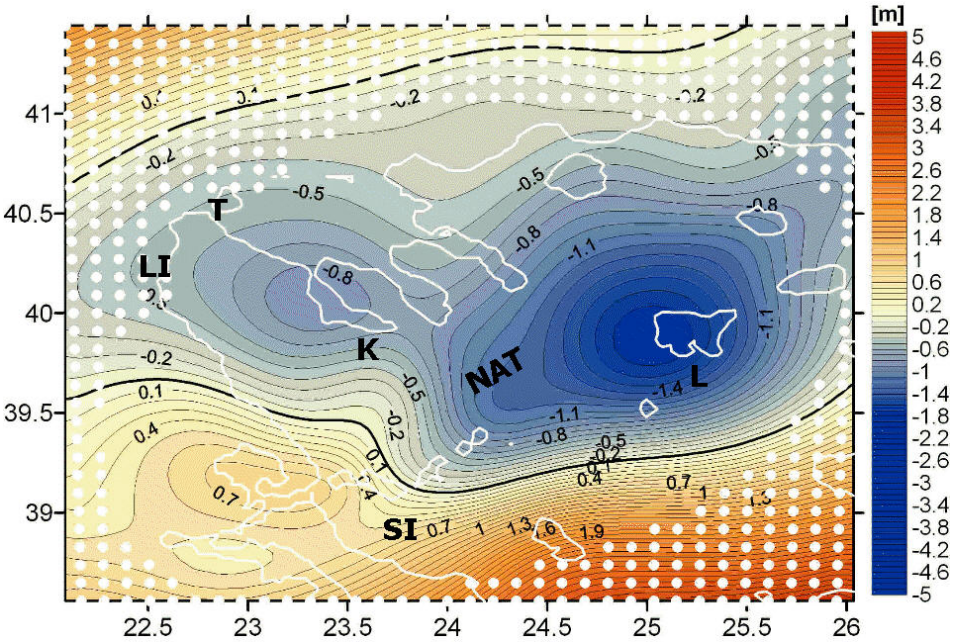

Figure 9.11: "*DOVSSH07 geoid* minus *Astro geoid*". After subtracting the mean offset of -0.35 m, the differences vary between -1.44 m and 2.61 m. They are mainly caused by the different data sets used for the computation of the respective geoid. NAT = North Aegean Trough; SI = Sporades islands; K = Kassandra; LI = Litorochou; T = Thessaloniki; L = Limnos.

DOVSSH07 - [...]	min [m]	max [m]	mean [m]	sigma [m]	$min_0[m]$	$max_0[m]$
Astro geoid	-1.79	2.25	-0.35	0.76	-1.44	2.61
GGM02 geoid	-1.96	2.42	-0.23	0.96	-1.74	2.64
Altimetric geoid	-1.56	2.80	-0.01	0.92	-1.55	2.81
Gravimetric geoid	-2.67	2.31	-0.73	1.01	-1.95	3.03

Table 9.1: Validation results of the comparison between DOVSSH07 geoid and different geoid models. min/max/mean: minimum/maximum/mean difference, sigma: standard deviation, min_0/max_0: minimum/maximum difference after offset subtraction.

Comparison between DOVSSH07 geoid and GGM02

Fig. 9.12 shows the difference "*DOVSSH07 geoid* minus *GGM02*". The mean difference between both models is -0.23 m. After subtracting the offset, the differences range between -1.74 m and 2.64 m. The differences are mainly induced by the fact that in contrast to the DOVSSH07 geoid, the GGM02 does not reflect short-wavelength information. Regions with significant local topographic and bathymetric features are not reproduced by the GGM02. Hence, the SW-NE extension of the NAT is clearly recognizable in Fig. 9.12. In the region north of the Sporades islands (=SI), the differences amount to -1.6 m. Similar values are reached in the bay of Thessaloniki (=BT). In the northeastern part of the North Aegean Sea, the differences take positive values of up to 2.2 m.

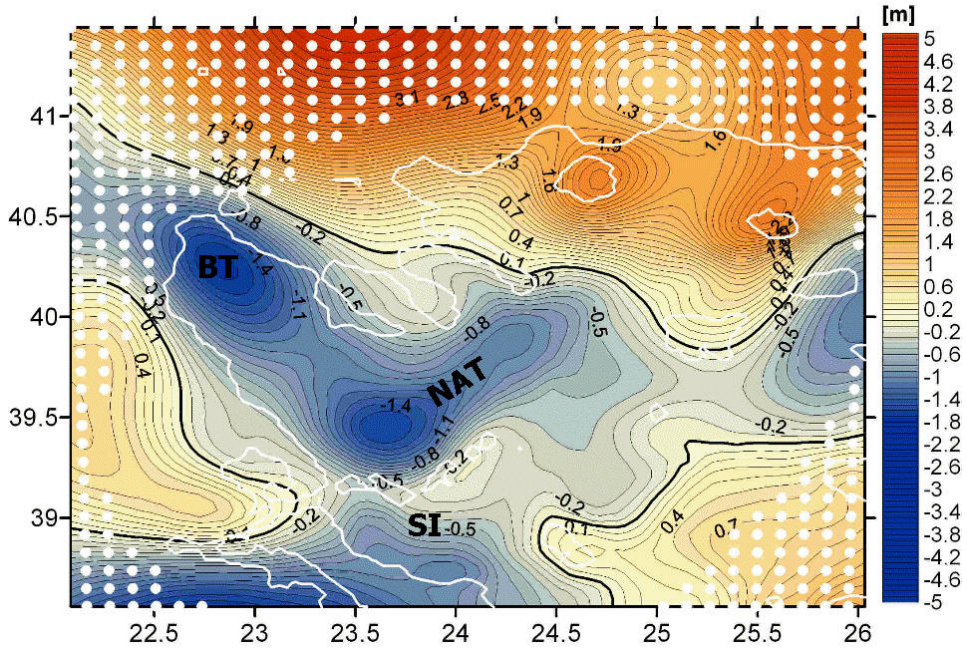

Figure 9.12: "*DOVSSH07 geoid* minus *GGM02*". After subtracting the mean offset of -0.23 m, the differences vary between -1.74 m and 2.64 m. These differences are mainly due to the long-wavelength character of the GGM02, while the DOVSSH07 geoid reflects local topographic and bathymetric features (e.g. the NAT). NAT = North Aegean Trough; SI = Sporades islands; BT = Bay of Thessaloniki.

Comparison between DOVSSH07 geoid and altimetric geoid

Fig. 9.13 shows the difference "*DOVSSH07 geoid* minus *altimetric geoid*". In terms of the mean geoid heights, both models agree very well revealing a difference of -0.01 m. However, the variations are relatively large ranging between -1.55 m and 2.81 m. It is obvious that the appearance of positive and negative deviations is very similar to the difference plot "*DOVSSH07 geoid* minus *GGM02*" (Fig. 9.12). This is due to the fact that both geoid solutions, the GGM02 as well as the altimetric geoid, use the same EGM96 coefficients to model the long-wavelength signal of the gravity field. The distinctive bathymetric low of the NAT is clearly identifiable in Fig. 9.13. A maximum difference of -0.8 m indicates an underestimation of the bathymetric impact by the altimetric geoid. Also the bay of Thessaloniki (=BT) features large deviations of about -1.5 m. Positive values can be observed in the northeastern part of the marine area. The discrepancies can be attributed to the fact that altimetry observational data in the North Aegean Sea are very rare. Radar altimeter measurements can be only performed over sea and until a distance of 20-30 km to the coastline. As the North Aegean Sea is bordered by land masses to the west, north and south, the region does not provide optimum conditions for altimetric observations. Therefore, the resolution of altimetric data forming a combination of ERS-1/2 and TOPEX/Poseidon mission data is relatively low (compare Fig. 7.9) and short-wavelength signals of the gravity field can not be reliably reproduced.

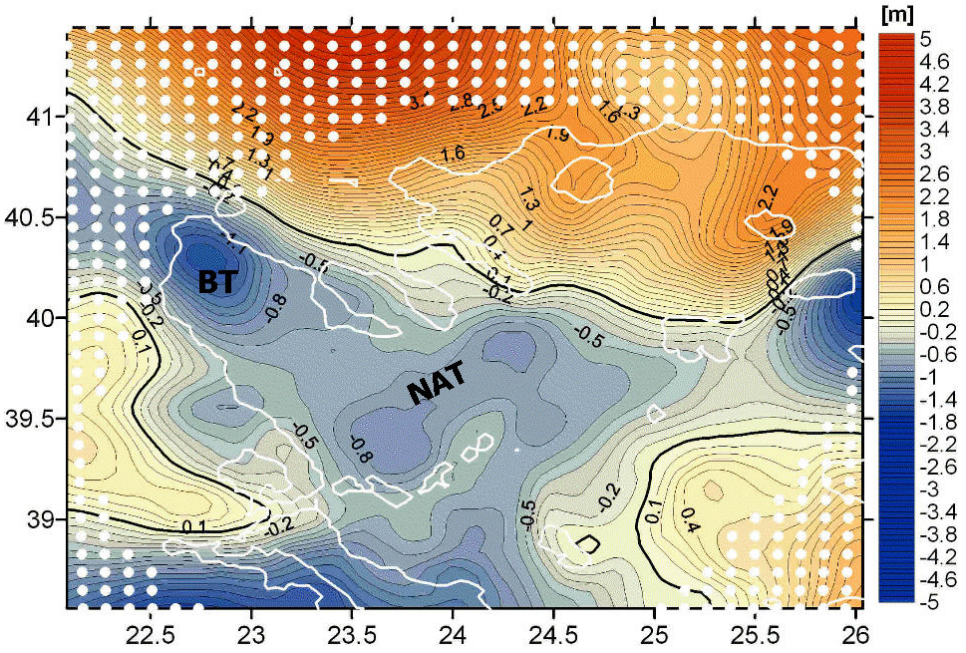

Figure 9.13: "*DOVSSH07 geoid* minus *altimetric geoid*". The variations range between -1.55 m and 2.81 m. They can be mainly attributed to a lack of altimetric data used for the computation of the altimetric geoid (compare also Fig. 7.9). NAT = North Aegean Trough; BT = Bay of Thessaloniki.

Comparison between DOVSSH07 geoid and gravimetric geoid HGFFT98

Fig. 9.14 represents the difference "*DOVSSH07 geoid* minus *gravimetric geoid*". It shows very similar characteristics like the difference "*DOVSSH07 geoid* minus *altimetric geoid*" (Fig. 9.13). This can be attributed to the fact that both models, the altimetric and gravimetric geoid, respectively, refer to the long-wavelength information of the EGM96. Besides, the gravimetric data in the marine area have been obtained from an inversion of satellite altimetry data from GEOSAT and ERS-1 geodetic missions. Hence, the marine geoid information of both models are partly based on the same data source. The gravimetric geoid uses additionally marine gravity data obtained by a digitization of sea gravity maps (chapter 7.3.3). As regards the differences between DOVSSH07 geoid and HGFFT98, the values vary strongly within a range of -1.95 m and 3.03 m, after reducing for a mean offset of -0.73 m. The large offset is not yet completely explainable, since possible reasons (permanent tides, reference systems, mean dynamic sea surface topography) can be ruled out. Similar as the differences between DOVSSH07 and altimetric geoid, the bathymetric low north of the Sporades islands (=SI) is underestimated by the gravimetric geoid. This is reflected by differences of up to -0.9 m. The bay of Thessaloniki (=BT) denotes even stronger differences with values up to -1.9 m. In the northeastern part, positive differences are indicated amounting to about 2.4 m. The discrepancies between DOVSSH07 geoid and HGFFT98 can be mainly attributed to deficiencies of marine gravity and altimetric data used for the computation of the HGFFT98 (compare section *Comparison between DOVSSH07 geoid and altimetric geoid*).

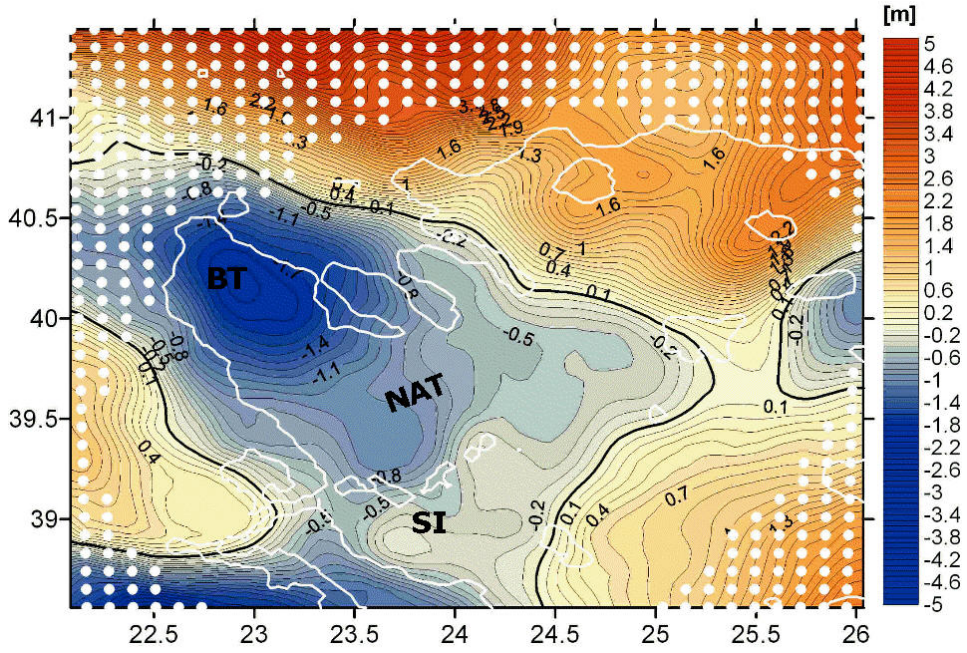

Figure 9.14: "*DOVSSH07 geoid* minus *gravimetric geoid*". The variations range between -1.95 m and 3.03 m. They can be mainly attributed to the deficiency of marine data used for the computation of the gravimetric geoid. NAT = North Aegean Trough; SI = Sporades islands; BT = Bay of Thessaloniki.

9.4 Additional investigations

9.4.1 Impact of covariance parameters

As explained in chapter 9.2.4, the correlation length d has a significant impact on the interpolation of the gravity field, since it represents a smoothing factor of the signal. If d is to small, the interpolation in areas with a low station density is not adequate. In contrast, a too large d results in a too strong filtering of the data. This characteristic becomes obvious in Figs. 9.15***a)*** to 9.15***f)***. In order to demonstrate the impact of d, the collocation has been processed using different correlation lengths varying from 10 km to 110 km. It is clearly recognizable that a length d=10 km (Fig. 9.15***a)***) produces a strongly undulating gravity field with peaks referring to the location of the Astro stations. It means that the signal in the stations is overestimated. The course of the gravity field becomes smoother with increasing d (Figs. 9.15***b)*** to 9.15***e)***). It seems that a length d=110 km results in an inadequate interpolation, because the smoothing effect is too strong causing a loss of information (Fig. 9.15***f)***). The optimum length d ranges somewhere between 30 km and 90 km. For these length, the signal is neither overestimated nor neglected. Based on these visual considerations, a correlation length of d=65 km was found to be appropriate for the final interpolation.

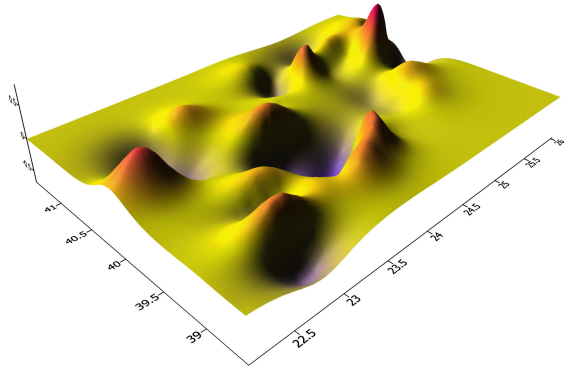

a) Correlation length d = 10 km.

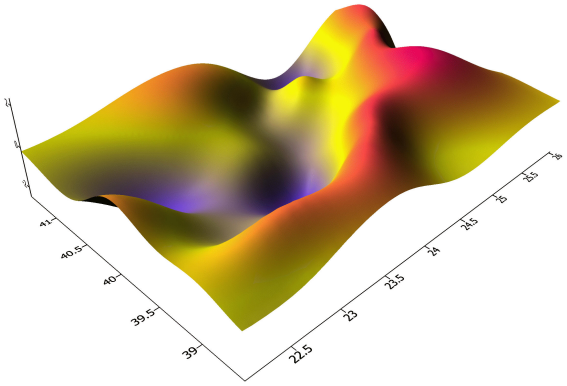

b) Correlation length d = 30 km.

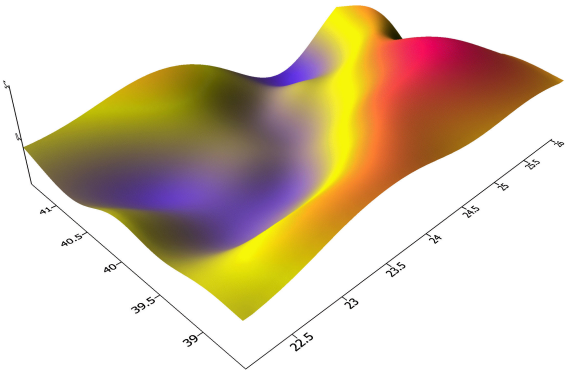

c) Correlation length d = 50 km.

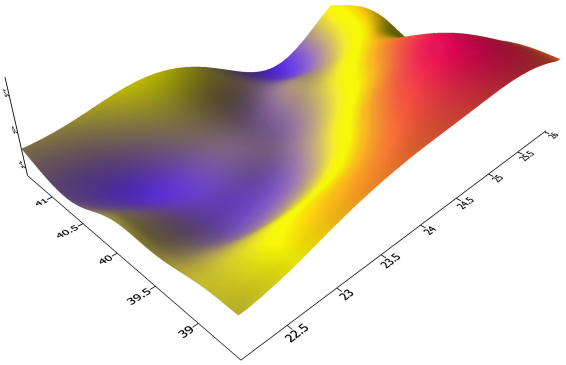

d) Correlation length d = 70 km.

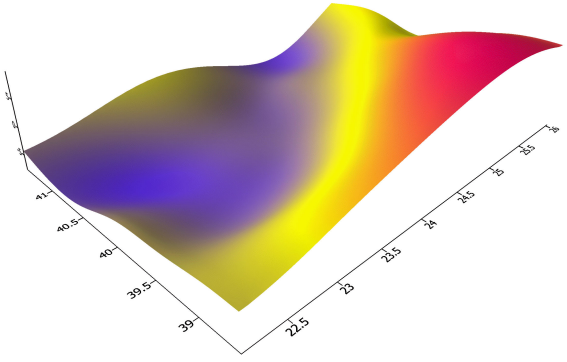

e) Correlation length d = 90 km.

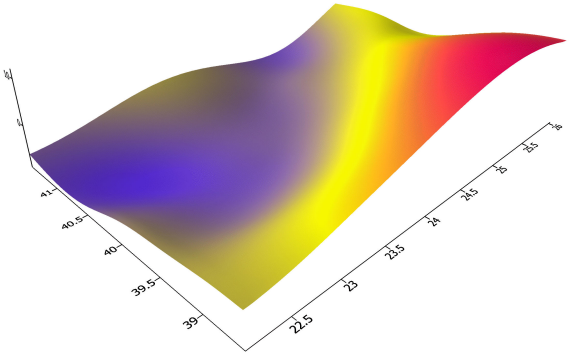

f) Correlation length d = 110 km.

Figure 9.15: Impact of different correlation lengths d on the signal of N.

9.4.2 Error-variances-covariances

The error matrices E_{xx} of the unknown parameters, E_{ss} of the signal and E_{tt} of the entire signal can be calculated a priori and independent from real observations (chapter 9.2.1, Eqs. 9.20 to 9.22). They depend on the distribution of the reference stations as well as the covariance model and parameters applied. The analysis of the error matrices allows for an evaluation of the accuracy of the resulting geoid. In the following, the error matrices of N (E_{tt}(N)), ξ ($E_{tt}(\xi)$) and η ($E_{tt}(\eta)$) have been analyzed, more precisely the square roots of its diagonal error variances (=standard deviations).

Figs. 9.16***a)*** and 9.16***b)*** show the errors of the DOV-components (ξ, η), based on the analysis of 27 Astro stations. Furthermore, Fig. 9.17 represents the error of geoid undulation N.

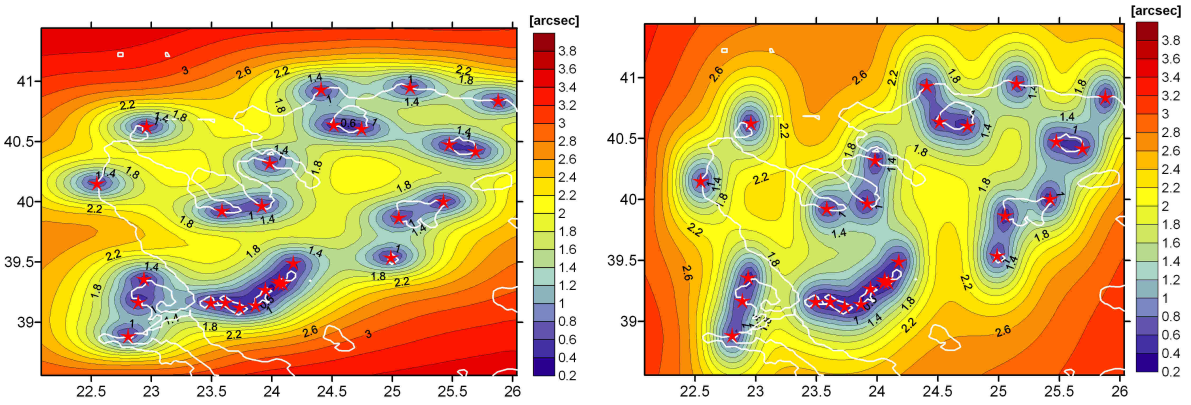

a) Error of ξ. ***b)*** Error of η.

Figure 9.16: Errors of ξ and η based on 27 DOV. The maximum accuracy is reached directly at the station. The accuracy decreases rapidly with increasing distance to the reference station.

The errors of ξ and η vary between 0.2 arcsec and 3.3 arcsec within the prediction area (plot area). The mean errors of ξ and η amount to 2.0 arcsec ($\pm$0.7 arcsec). It is clearly visible that the errors have a minimum at each Astro point and increase with increasing distance to the reference station.

The error of N varies between 0.31 m and 1.64 m within the prediction area. The mean error in the whole area amounts to 0.56 m, with a standard deviation of $\pm$0.22 m. In order to define a region of significance, a threshold of 0.6 m accuracy has been specified. This area is signalized by the red line (Fig. 9.17).

In statistical terms, the mean error within the region of significance amounts to 0.46 m with a standard deviation of $\pm$0.07 m. In contrast to ξ and η, the error of N decreases between the stations having a minimum in the region with the highest station density around. This is between Chalkidiki[2] and the Sporades islands.

[2]For geographic references see Figs. 7.1 and 7.12, respectively

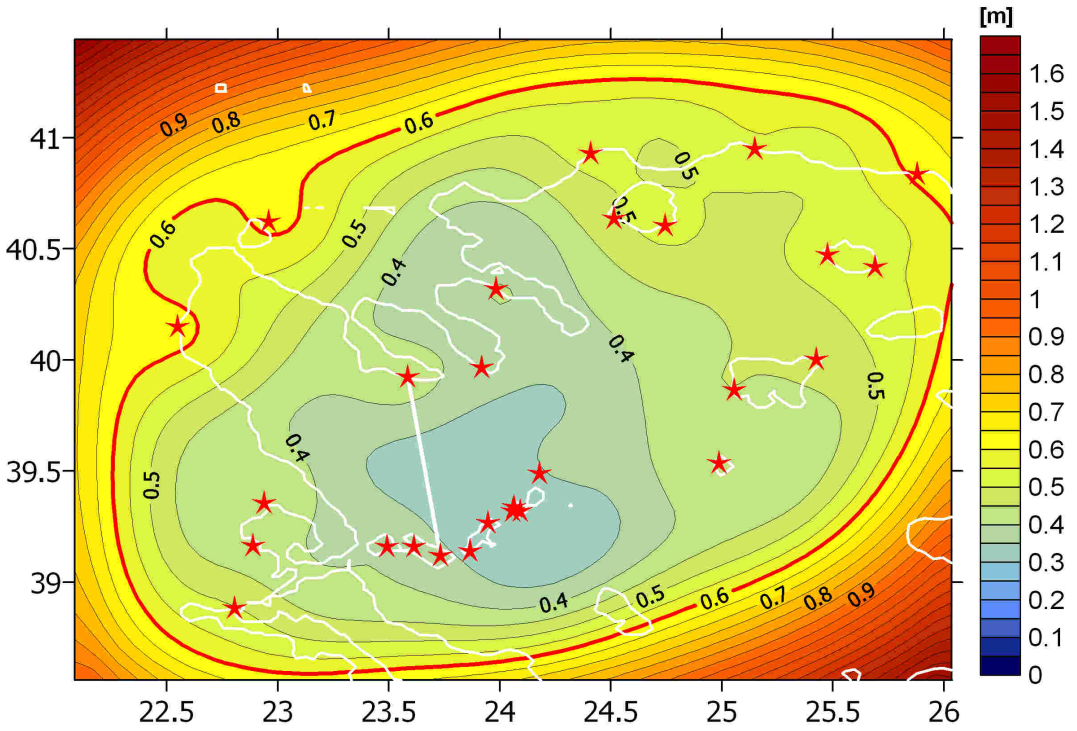

Figure 9.17: Error of geoid undulation N based on 27 DOV. The red line borders the region with an accuracy of better than 0.6 m. The best accuracy of 0.3 m is achieved at the eastern part of the Sporades islands. The error increases rapidly in outward direction. An interesting effect of the astrogeodetic method is the fact that the accuracy of N increases between the reference stations. This can be explained, on the one hand, by the distance dependence of relative geoid undulations and, on the other hand, by the characteristics of collocation. The method uses an averaged signal of all reference stations for the computation of the signal in an arbitrary interpolation point.

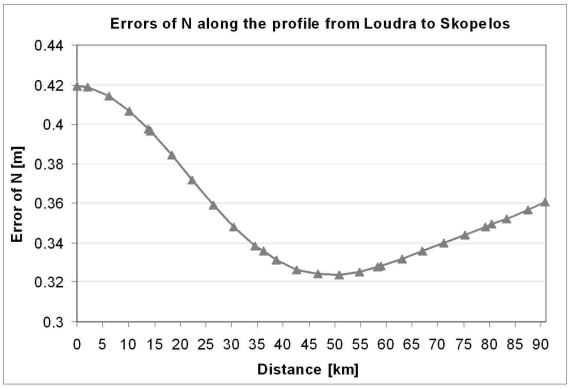

a) Error of geoid undulation N.

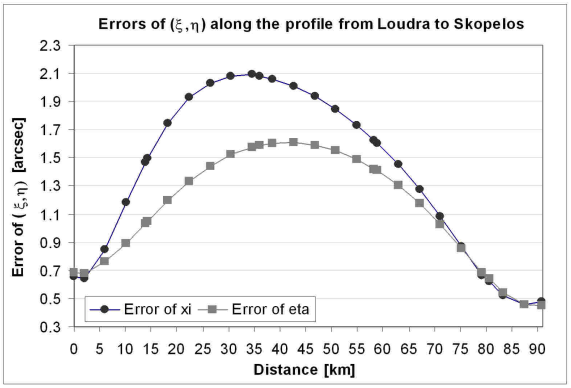

b) Error of DOV-components ξ and η.

Figure 9.18: Errors of N, ξ, η along the profile between Loudra (North) and Skopelos (South), see Fig. 9.17.

Fig. 9.17 shows an interesting effect of the astrogeodetic method: the accuracy of geoid undulation N increases between the reference stations. To illustrate this characteristic, a profile has been defined between Loudra (Chalkidiki) and Skopelos (see straight line

in Fig. 9.17). Figs. 9.18***a)*** and 9.18***b)*** show the course of the errors of N and ξ, η, respectively, along this profile. While the errors of ξ and η have their maximum ($\approx$2 arcsec) approximately in the middle between the two stations, those of N show a minimum (0.33 m) there. This can be explained, on the one hand, by the distance dependence of relative geoid undulations and, on the other hand, by the characteristics of collocation. There, the signal of all reference stations is averaged for the computation of the signal in an arbitrary interpolation point.

9.4.3 Impact of Astro station distribution

Relevance of each Astro station

In order to analyze the impact of the location of the Astro stations on the errors of N, the following investigation has been performed for each station: One Astro station has been excluded from the calculation of the error matrix $E_{tt}(N)$ (Eq. 9.22. The difference between the mean error including and excluding the respective station ($\Delta E_{tt}(N)$) can be regarded as a measure of its significance. The results of this investigation are plotted in Fig. 9.19, where the stations are classified by four groups: $\Delta E_{tt}(N)$ is...
red: $\geq$ 0.01 m, green: $\geq$0.005 m, yellow: $\geq$0.001 m, gray: $<$0.001 m

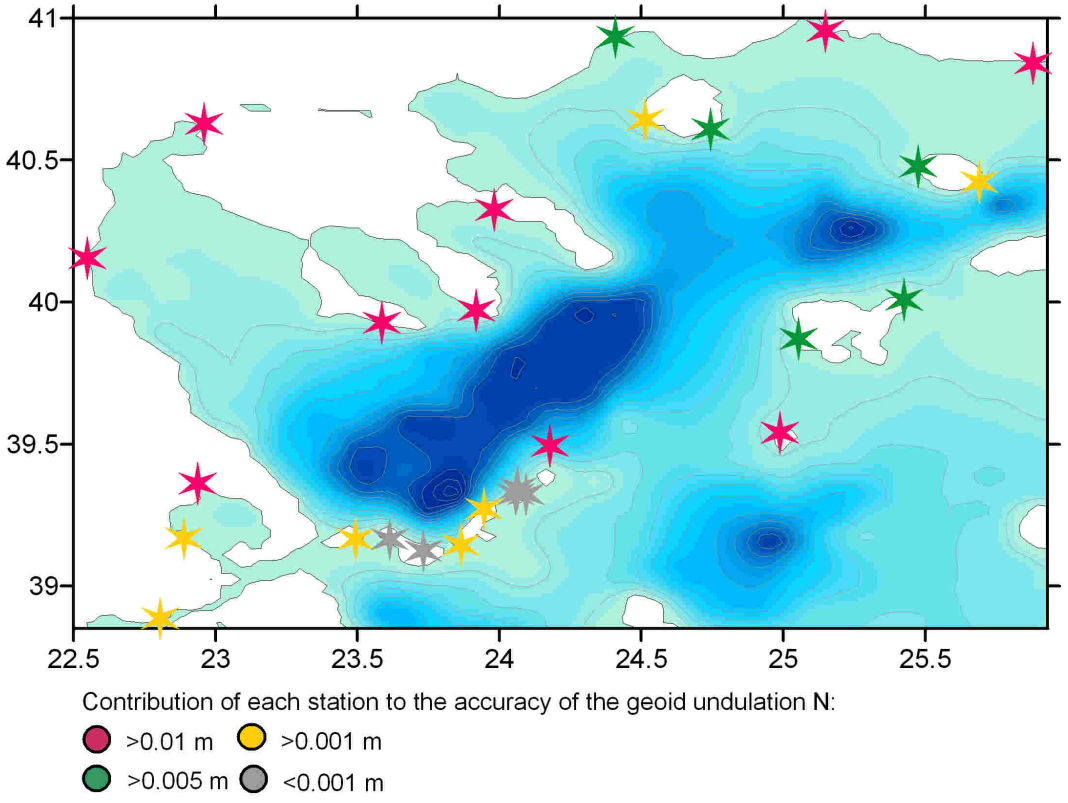

Figure 9.19: Impact of each Astro station on the mean error of N within the prediction area. The red stars signalize station, which are very important. Their removal produces a significant increase of the error for about 0.01 m. In contrast, the gray stars indicate stations, whose removal is less critical producing an increase of the error of $<$1 mm.

Stations marked by a red star induce the highest impact on the error of N within the prediction area. Hence, e.g. the three stations at Chalkidiki indicate values up to 3.5 cm. In contrast, stations marked by a yellow star (Sporades islands) have no significant impact. Based on these results, it is concluded that along the western and northern coastline, the station density is relatively low. Hence, if one of these stations is removed from the computation, the mean error of N increases significantly for more than 1 cm. In contrast, the station density on the Sporades islands is very high, hence, one single station can be excluded without a significant impact on the accuracy of N. This rating can be used to determine, where additional stations should be located in case of a densification of the Astro station network. As a consequence, it would be reasonable to measure additional stations along the western and northern coastline. Also an additional station at the island of Limnos might help to improve the accuracy of N.

Amount and distribution of Astro stations

Impact of a densification of the Astro station network. As analyzed in chapter 9.4.2, the accuracy of N averages to 0.56 m within the prediction area. This number shows that 27 Astro stations are not adequate for the relatively large area (W-E 370 km, N-S 220 km). The distances between the Astro stations vary between 2.5 km and 340 km, hence yielding a mean distance of about 130 km. The mean station density amounts to 1 station per 3015 km^2. One problem is the lack of stations in the marine area. An interesting question is now to what extent an increasing number of reference stations helps to improve the accuracy of N.

In order test the impact of additional stations, the existing Astro network has been arbitrarily densified along the coastline and at the islands. Therefore, totally 290 virtual stations have been defined (Fig. 9.20).

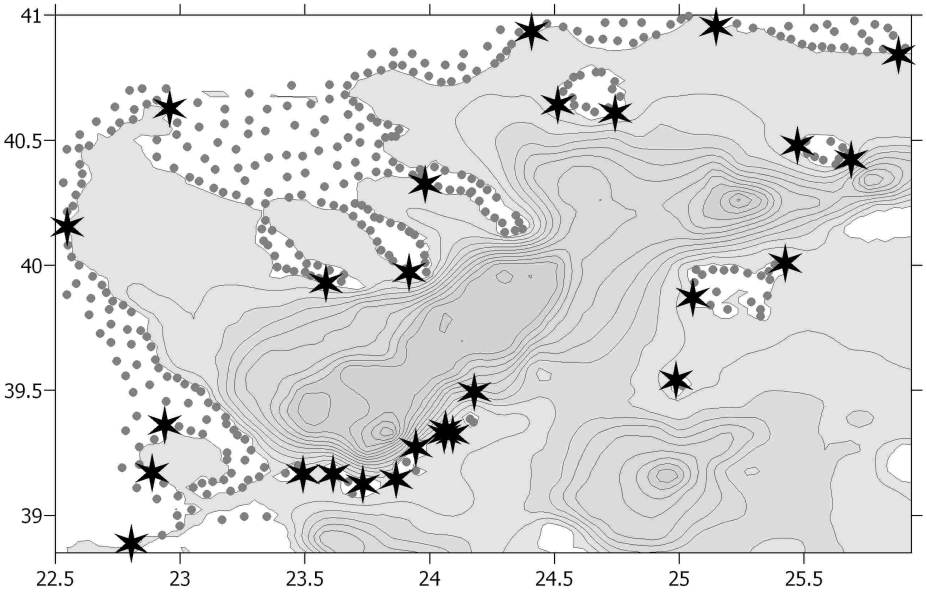

Figure 9.20: Location of 290 virtual Astro stations (gray points) and 27 original Astro stations (black stars).

The test started using all original (27) and additional stations (290) for the computation of $E_{tt}(N)$. As already mentioned in chapters 9.2.1 and 9.4.2, respectively, this matrix can

be computed a priori without any "real" observations. In the following, the additional stations have been thinned out stepwise for 10 stations. The corresponding mean errors of N (within the prediction area) depending on the number of additional stations are plotted in Fig. 9.21.

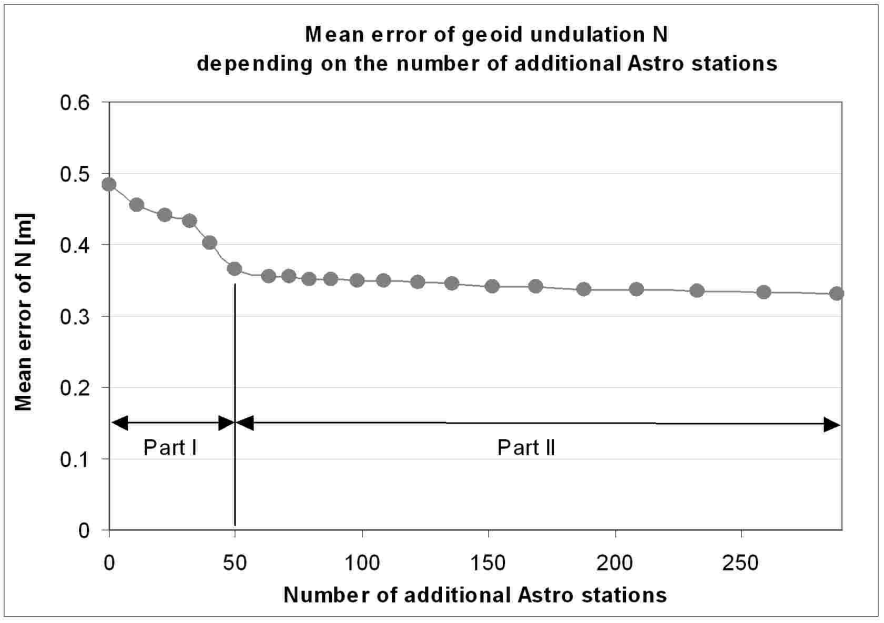

Figure 9.21: Mean errors of N depending on the number of additional Astro stations. A number of 50 additional station yields a reduction of the mean error for about 12 cm. After that, the contribution of additional stations is less significant.

It is clearly visible that an adding of about 50 stations yields a reduction of the mean error for about 12 cm (from 48 cm to 36 cm). A further densification of the network does not improve the accuracy anymore. By splitting the graph into two parts, the two charts shown in Figs. 9.22***a)*** and 9.22***b)*** can be generated.

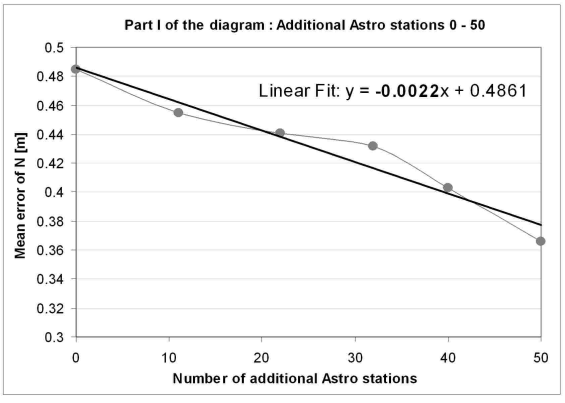

a) Part I: 0 - 50 additional stations. One additional station yields an error reduction for about 0.2 cm.

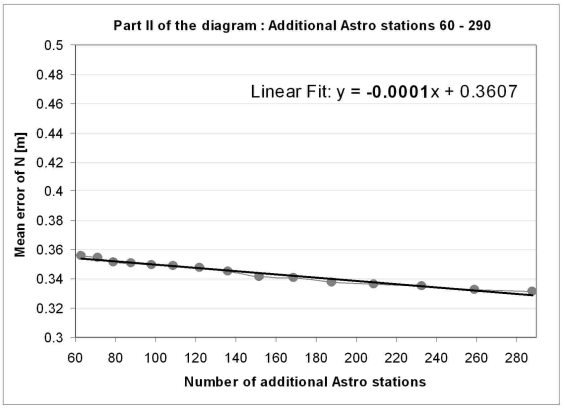

b) Part II: 60 - 290 additional stations. One additional station yields an error reduction for about 0.01 cm.

Figure 9.22: Part I and II of Fig. 9.21.

Up to a number of 50 additional stations, the impact of one station on the mean error of N amounts to about 0.2 cm (Fig. 9.22***a)***). Beyond, the impact approaches zero (Fig. 9.22***b)***).

A further test analyzed the location of additional stations. Therefore, two different networks have been defined:
- Network 1: 10 stations along the coastline and
- Network 2: 10 stations at the islands

Based on the results presented above, significant differences concerning the impact of each network on the mean error of N can be expected. A densification of the stations along the coastline (network 1) should have a higher impact than a densification at the islands (network 2). The results of the test are plotted in Fig. 9.23.

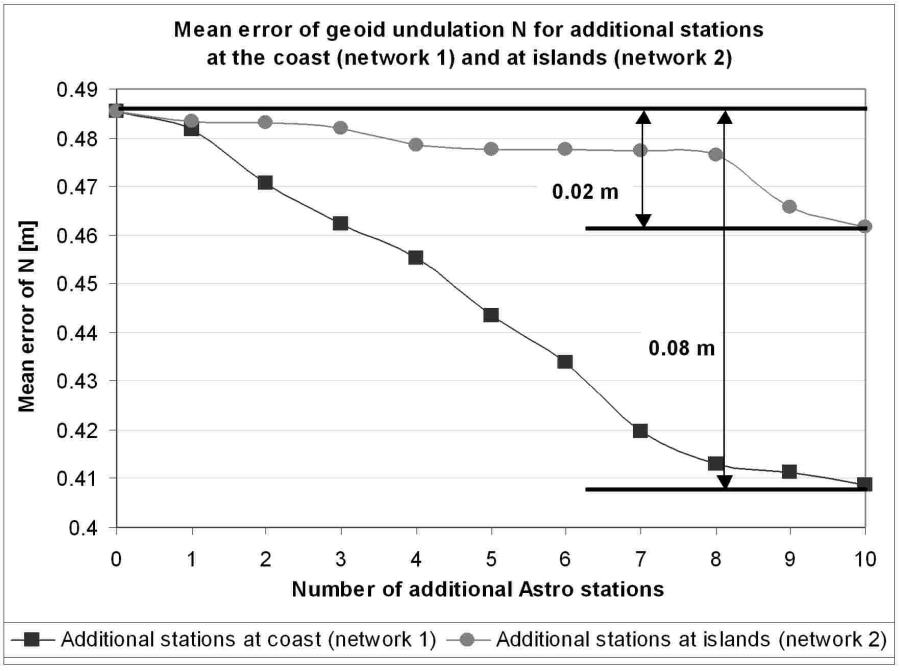

Figure 9.23: Comparison between network 1 (squares) and network 2 (points). Network 1: 10 additional stations at the coastline, network 2: 10 additional stations at the islands. Network 1 produces a significant reduction of the mean error for about 8 cm, while network 2 only achieves an improvement of about 2 cm.

As recognizable, network 1 (coastline) yields a significantly decreased mean error (0.08 m), while network 2 (island) causes a clearly smaller reduction of the mean error (0.02 m). This proves again the importance of a careful selection of the location of additional stations.

In order to determine the optimal distance between additional and existing stations, a similar test as described in the first section has been performed: One station has been excluded from the computation of the error of N. However, instead of performing the computation at regular interpolation points, the 27 Astro stations have been used. Afterwards, the differences between the errors at each Astro station including and excluding the respective test station have been calculated. These differences have been sorted depending on the distance between test station and all other Astro stations.

Finally, the error differences per distance have been assigned to dedicated distance groups. These results are presented in Fig. 9.24.

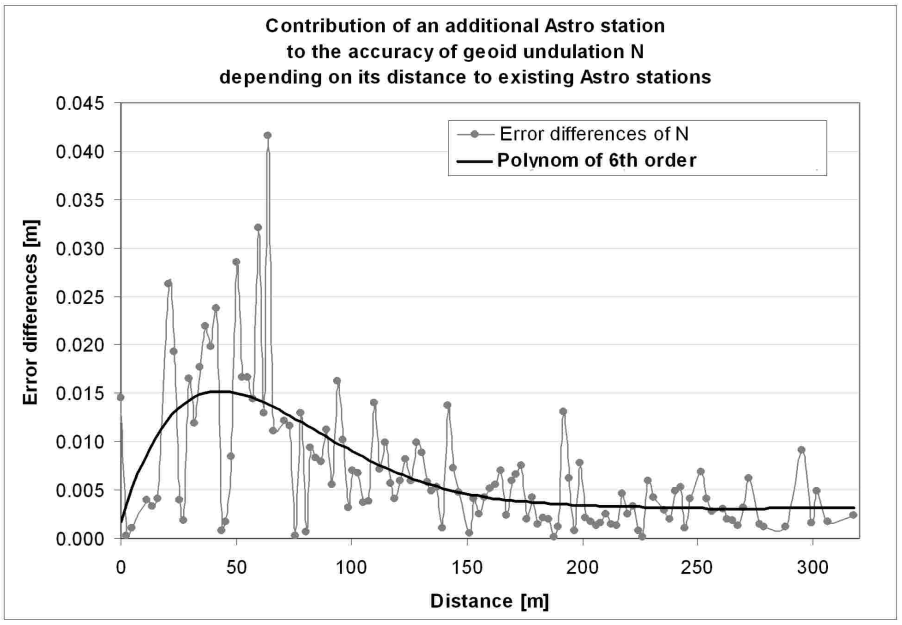

Figure 9.24: Dependence of the errors of N on the distance of a station.

Based on the analysis of Fig. 9.24, the following can be concluded: In order to achieve the best possible reduction of the error of N, the mean distance between additional and existing stations should not exceed 150 km. The best results are obtained for mean distances ranging between 20 km to 60 km.

In summary, it can be said that additional stations improve the accuracy of N considerably, if their location is well chosen. Hence, e.g. five additional stations at the Sporades islands will not have an obvious impact. However, in case they are located at the northern coastline, the improvement might reach a level of about 1 cm. About 50 stations at coast and islands allow to increase the accuracy of N for about 0.15 m, hence reaching a mean accuracy of about 0.35 m. An improvement by further additional stations is not expectable, unless the stations would be located in the marine area bridging the lack of reference stations there. This forms, of course, an unrealistic approach for Astro observations. Therefore, the next section analyzes the impact of an additional introduction of marine data by means of Sea Surface Heights (SSH).

Combination with Sea Surface Heights. As assumed in the section before, an implementation of marine data should increase the accuracy of the geoid undulations considerably. Therefore, 240 SSH corrected for tidal effects and the Mean Dynamic Ocean Topography (chapter 7.4.2) have been used together with 27 DOV for a common calculation of $E_{tt}(N)$. The resulting error plot is represented in Fig. 9.25.

As expected, a combination of both data sets causes a significant increase in the accuracy of N, especially within the marine area. Hence, the error of N ranges now between 0.05 m and 1.59 m within the whole prediction area, with a mean error of 0.41 m and a standard deviation of ± 0.31 m. This represents an improvement for about 0.15 m compared to the pure Astro geoid (see Tab. 9.2).

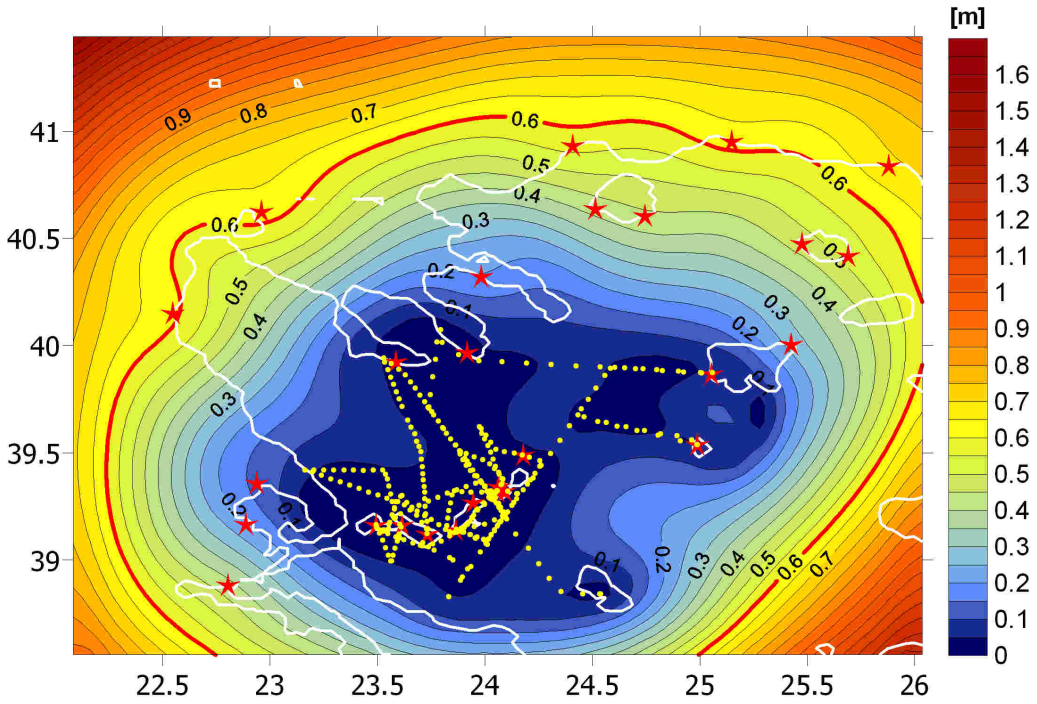

Figure 9.25: Errors of N based on 240 corrected SSH and 27 DOV. The maximum accuracy is achieved between Chalkidiki and the Sporades islands amounting to 0.05 m. It decreases rapidly in outward direction. An interesting effect of the application of SSH is recognizable within $39° \leq \varphi \leq 39.5°$ and $24.5° \leq \lambda \leq 25°$. In contrast to the purely astrogeodetic solution (Fig. 9.17), the isolines show a converse behavior there. This can be attributed to the fact that SSH provide direct information about the geoid undulations, while DOV represent their gradients.

	Prediction area				Area with acc. $\leq$ 0.6 m	
Input data	min [m]	max [m]	mean [m]	sigma [m]	mean [m]	sigma [m]
DOV	0.31	1.64	0.56	0.22	0.46	0.07
DOV + SSH	0.05	1.59	0.41	0.31	0.27	0.19

Table 9.2: Statistical comparison between geoid solution based on DOV and on DOV+SSH, respectively, concerning the obtainable accuracy of geoid undulation N. It is differentiated between the whole prediction area and the defined area of significance (error $\leq$0.6 m).

The position of the isoline representing an accuracy of 0.6 m is not obviously shifted in comparison to the Astro solution (compare Fig. 9.17 and 9.25). It coincides approximately with the most outlying Astro stations. This shows that the positive effect of SSH data is very local and largely restricted to the location of observational data. An interesting effect of the application of SSH is recognizable within $39° \leq \varphi \leq 39.5°$ and $24.5° \leq \lambda \leq 25°$. In contrast to the purely astrogeodetic solution (Fig. 9.17), the isolines show a converse behavior there. This can be attributed to the fact that SSH provide direct information about the geoid undulations, while the DOV represent their gradients.

Within the 0.6 m-area, the mean error of N amounts to 0.27 m, with a standard deviation of $\pm$0.19 m. A comparison of the mean accuracies within this area shows that the

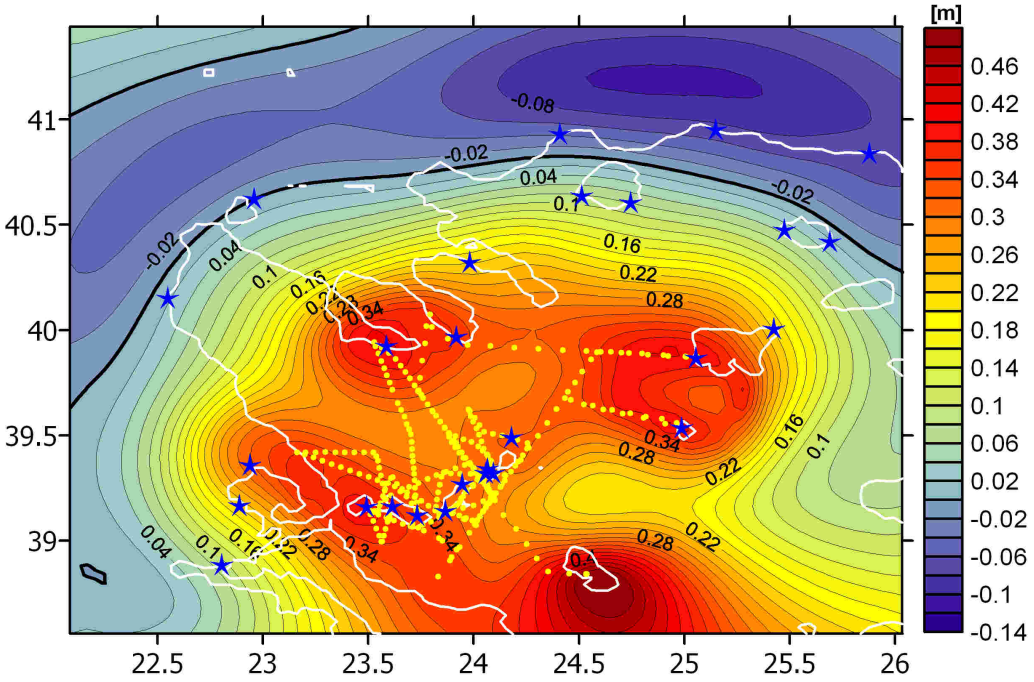

Figure 9.26: Differences between the errors of N using DOV (Fig. 9.17) and DOV+SSH (Fig. 9.25), respectively. In some regions, the improvement amounts to about 0.4 m.

accuracy of the combined solution increased for about 0.19 m. If analyzing the error difference plot between Astro and combined solution (Fig. 9.26), it is remarkable that the improvement amounts to about 0.4 m in some regions. These regions are characterized by the availability of information from both data sources (e.g. Sporades islands, western side of the island of Limnos, and Chalkidiki). The results presented emphasize the importance of a combined introduction of DOV and corrected SSH for the computation of the geoid. This ensures the achievement of a mean accuracy of better than 0.3 m. The DOVSSH07 geoid computed from a combination of 27 DOV and 240 SSH is presented in chapter 9.3.4.

9.4.4 Cross-validation method

In order to evaluate the prediction quality, the so called *cross-validation method* has been applied: Each time, one Astro station has been excluded from the least-squares-collocation (chapter 9.2), while the prediction has been performed at all 27 Astro stations. In that way, a comparison between original and predicted DOV is possible. Furthermore, in order to analyze the relevance of data reduction (see chapter 8), DOV reduced for different mass impacts have been introduced into the test.

Figs. 9.27 and 9.28 show the comparisons between following data reductions: DOV reduced to the geoid (black), DOV reduced for topography = T (dark gray), DOV reduced for topography and bathymetry = TB (light gray) and DOV reduced for topography, bathymetry and isostasy after Airy-Heiskanen = TBAH (white). The plots show the prediction errors at each station representing the difference between original and predicted ξ- and η-components, respectively. The catchment area has been set to 30 km.

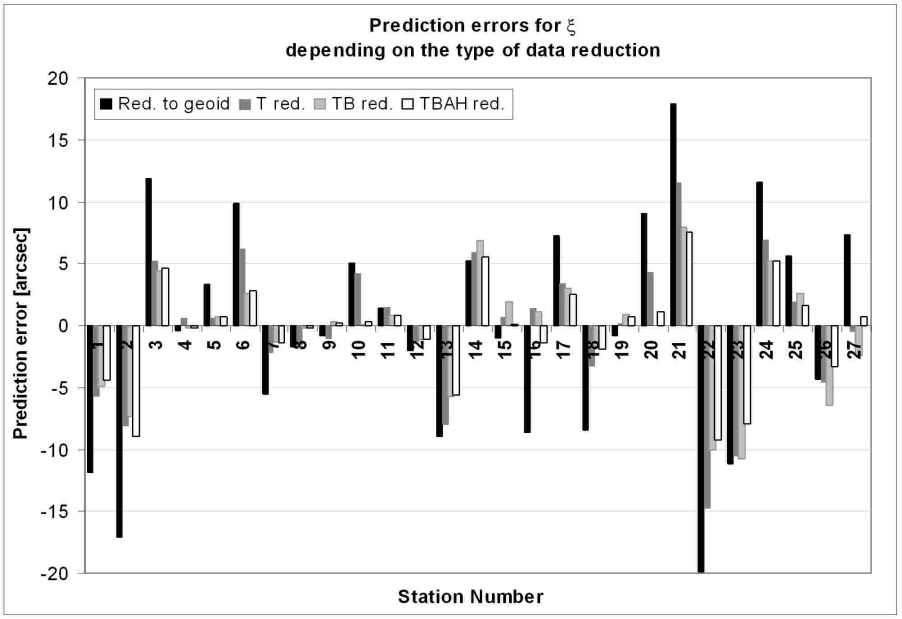

Figure 9.27: Prediction errors of ξ depending on the masses reduced. *Red. to geoid*: DOV have been reduced from surface to geoid, *T red.*: DOV reduced for topography, *TB red.*: DOV reduced for topography and bathymetry, *T red.*: DOV reduced for topography, bathymetry and isostasy after Airy-Heiskanen. The best prediction accuracy is achieved for TBAH reduced DOV.

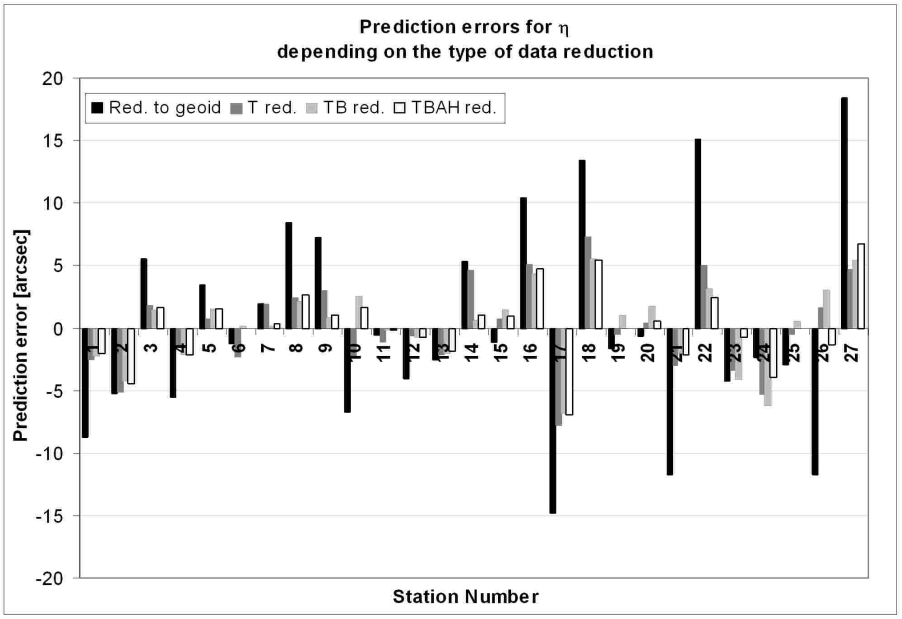

Figure 9.28: Prediction errors of η depending on the masses reduced. Also for the η-component, the TBAH reduced DOV enable the best prediction accuracy.

Data reduction	Pred.err.in ξ [arcsec]	Pred.err.in η [arcsec]
DOV red. to geoid	7.3	6.5
DOV red. for T	4.3	2.9
DOV red. for TB	3.3	2.5
DOV red. for TBAH	2.9	2.1

Table 9.3: Mean prediction errors (averaged for all Astro stations) for different types of data reduction.

It is recognizable that the data reduction has a significant impact on the prediction accuracy. If the DOV are reduced for the curvature of the plumb line only, the mean prediction error is about 7.3 arcsec for ξ and 6.5 arcsec for η. However, if the data are reduced for topography (T), hence eliminating high-frequency mass impacts, the mean prediction errors decrease by about 3 arcsec for both components (see Tab. 9.3)! The additional consideration of bathymetry (TB) yields a reduction of the mean prediction errors of 1 arcsec and 0.4 arcsec, respectively. Finally, the removal of long-wavelengths influences caused by isostatic masses (TBAH) causes a further improvement for about 0.4 arcsec in both components. Hence, the TBAH reduced DOV produce a significant smaller prediction error of 2.9 arcsec and 2.1 arcsec, respectively, than the raw data. This suggests a complete data reduction in order to obtain the best possible prediction quality.

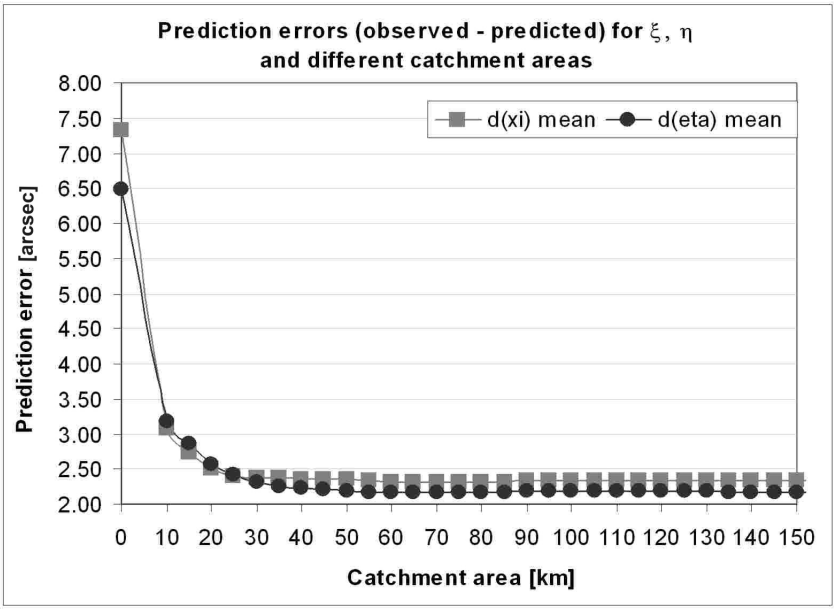

Figure 9.29: Prediction errors of ξ and η for different catchment areas (AoI). The difference between a AoI of 0 km (no reduction) and of 30 km amounts to about 4-5 arcsec. After that, the differences are negligible.

A further investigation analyzed the required dimension of the catchment area (AoI). Therefore, the DOV have been reduced for TBAH with varying AoI dimensions from 10 km to 200 km in 5 km steps. Fig. 9.29 shows the resulting mean prediction errors (averaged over 27 Astro stations).

It is obvious that the prediction error between 0 km (no reduction) and 10 km decreases for about 3-4 arcsec. There is also a considerable difference of about 0.7 arcsec between a AoI of 10 km and 25 km. However, from 30 km on, the prediction errors remain constantly at a level of about 2.4 arcsec. It means that the differences between two consecutive AoI are approximately zero, hence advising that a further extension of the AoI will not have a significant impact on the prediction quality. This corresponds also to the results presented in chapter 8.7.1, where the optimum AoI for a sufficient smoothing of the reduced data has been determined to be 30 km. It can be concluded that a complete data reduction for topography, bathymetry and isostasy (TBAH) within a AoI of about **30 km** is advisable. This ensures the attainability of the best possible prediction quality.

10 Discussion and conclusions

Enhancement of DIADEM in terms of hard- and software developments

The present state of DIADEM offers the possibility for a fully-automatic and PC controlled observation of the astronomical parameters (Φ, Λ). The system is equipped with CCD technology enabling a computer-operated processing of the digital images. The highly light-sensitive CCD sensor allows for the exposure of stars with a maximum magnitude of 14, which comprises 40 times brighter stars than with the old analog system TZK3. Two different pairs of high-resolution tiltmeters provide permanently information about the vertical alignment of DIADEM referring to the direction of the vertical. A GPS receiver allocates precise epoch information and approximate geodetic positions. Furthermore, several servo motors offer the conditions for an automatic leveling, focussing and turning of DIADEM. The whole process is controlled by a complex data acquisition software running on two industrial PCs. The Zenith Camera system including both computers can be operated via 12V car batteries. A subsequent data analysis is assured via a dedicated interface to the software package AURIGA developed at the University of Hannover (Hirt [2004]). All these conditions enable the provision of approximate deflections of the vertical (DOV) (ξ, η) in the field, hence allowing the instant verification of the data regarding their quality, accuracy and plausibility. Provided that parallel real-time DGPS measurements are performed, highly-precise DOV can be derived at once. Related to the fact that the system is completely operated via PC, the touching of the system and motions around the system are largely avoidable.

Besides, the time efficiency concerning data acquisition and analysis improved significantly in comparison to the old analog TZK3. The whole process takes now about 35 minutes (20 minutes observation, 15 minutes analysis) if applying the new tripod method. In contrast, the data acquisition and analysis with the TZK3 was very time-consuming needing about half a day labor input. This was mainly due to the extensive measuring of the analog photos.

Error investigation and calibration of DIADEM

The thorough investigation of the error budget of DIADEM constituted an important integral part of the instrumental evaluation. This includes errors in the determination of rotational direction, inclination data, observation epoch, azimuth calibration parameters and geodetic position. The total error budget has been specified for different measuring configurations (azimuth vs. tripod method, Wyler vs. Lippmann sensors). The analysis revealed that the Tripod/Lippmann configuration enables the best precision, which agrees well with conclusions based on an empirical analysis of long-term observations. It has been estimated that the standard deviations of (ξ, η) range between 0.08 arcsec and 0.32 arcsec. The largest part of this error is caused by the determination of the rotational

direction, while errors in the determination of the observation epoch are almost negligible (provided that the shutter delay is considered).

Furthermore, the instrument has been subject to thorough calibrations. This includes the determination of the focus-temperature-relation, which enables an automatic adaption of the focus depending on the temperature. Besides, the delay of the electronic blade shutter used in the CCD camera has been investigated. The knowledge of this value is essential for an instant correction of the exposure epoch during an observation. Furthermore, the celestial calibration developed at the University of Hannover (Hirt [2004]) has been conducted several times during the period of the project. It aims at the determination of the scales of the inclination sensors, the shearing angle between both sensors as well as the angle between CCD and inclination sensor coordinate system. The method allows for a fast and easy determination of the calibration parameters. An interesting result is the fact that the formerly applied azimuth calibration has become dispensable because of the introduction of the tripod method. The time-consuming method of azimuth calibration was necessary to consider the dependence of the astronomical parameters on the azimuthal alignment of DIADEM. However, this effect does not occur anymore if applying the tripod method. This yielded a great step forward concerning the achievable internal and external accuracy as well as regarding the expenditure of time and effort for an observation.

Verification of the field capability of DIADEM by dedicated field campaigns

In order to verify the field capability and accuracy potential of DIADEM, dedicated field campaigns have been performed. The first campaign with the newly developed digital system has been conducted in Switzerland in 2003 in the frame of the CHGeo2003 project. Besides, the campaign offered the possibility to perform first time simultaneous observations with a second digital Zenith Camera, the TZK2-D of Hannover. In total, 68 stations have been measured with both cameras within three weeks. DIADEM worked reliably, even under very harsh conditions like in mountainous regions and at temperatures of -15°. Repeated measurements during different nights at the reference station Zimmerwald allowed for the comparison of the respective night means, hence revealing the repeatability of the system. Furthermore, parallel measurements with TZK2-D enabled conclusions about the external accuracy of the instrument. Both comparisons yielded very satisfying results demonstrating the high potential of Zenith Cameras in general and of DIADEM in particular. The repeatability and the external accuracy of DIADEM was assessed at about 0.1 arcsec. The measurements formed a valuable contribution to the improvement of the Swiss geoid, which was the actual goal of the CHGeo2003 project.

In 2005, another interesting campaign has been conducted in Switzerland. There, long-time observations with two Zenith Cameras have been performed. The goal was to investigate the effect of anomalous refraction. Due to missing highly-precise reference values, the data were not suitable for the estimation of the absolute impact of refraction, but for the detection of potential refraction changes. Unfortunately, the weather conditions prevented the performance of long-time observations during more than two nights. Based on the limited quantity of data, it has been assumed that the maximum impact of refraction changes is within the obtainable accuracy range of DIADEM (0.1 arcsec). Further long-term observations will be necessary, most preferably at a station with highly-precise reference values. As regards the consistency between both

Zenith Cameras, the comparison of the respective night means revealed a very good agreement of better than 0.1 arcsec. Furthermore, the measurements demonstrated the importance of the inclination sensors. The respective standard deviations of the systems differed with 0.33 arcsec (DIADEM) and 0.21 arcsec (TZK2-D) for about 50%. These results initiated further hardware improvements of DIADEM by implementing two additional tiltmeters (Lippmann sensors) with a very high resolution in time and inclination.

Evaluation of the accuracy of DIADEM

The analysis of repeated observations during four years formed an important contribution to the evaluation of DIADEM. The measurements have been performed at the reference station of the institute. It has been demonstrated that the system features a very good repeatability within a range of 0.15 arcsec. The external accuracy (derived from the comparison between reference and actual coordinates of the reference station) amounted to better than 0.15 arcsec. These results are based on the analysis of data measured with the Azimuth/Wyler (AW) configuration and agree well with results from comparative observations with the TZK2-D. Since May 2007, the new tripod method using Lippmann sensors (TL) has been applied. The data derived from the comparison between new (TL) and old method (AW) denoted a considerable increase in accuracy. Hence, the TL method allowed for an improvement of about 33% for the internal and 59% for the external accuracy. It has to be noticed that the conclusions are based on a relatively small data set. Therefore, the method has to be verified by further measurements.

Deployment of DIADEM in the North Aegean Sea

After a thorough verification and evaluation of DIADEM, the system has been successfully deployed in the research area of the North Aegean Sea, Greece, in 2005. During about three weeks, totally 27 stations have been observed at several islands and along the coastline of the North Aegean Sea. The distribution of the Astro stations was mainly motivated by the intention to cover the area around the North Aegean Trough (NAT). The system worked reliably, although the conditions were very ambitious. A long journey from Switzerland to Greece and the travel between the stations, partly on pathless roads, implied great stress for the system. Furthermore, the transportation of the camera by sailing boat, associated with the loading and unloading into a dinghy for entering the islands, imposed high demands on the instrument.

In order to provide highly-precise astronomical parameters (Φ, Λ), about 80 to 120 single solutions have been observed at each station. Furthermore, parallel differential GPS measurements, analyzed in post-processing, enabled the determination of precise geodetic positions (φ, λ). The accuracies of the final DOV (ξ, η) ranged at the expected high level, hence providing the conditions for a high-quality geoid determination. The (ξ, η)-components clearly reflect the topography and bathymetry of the research area and, especially, the influence of the NAT representing a distinctive mass deficit with respect to the surrounding masses.

Computation of different cogeoid solutions and isostatic interpretation

The observed DOV have been reduced for dedicated mass models. The residual data served as input for the computation of different cogeoid solutions. These models formed the basis for two important goals of the Ph.D. thesis: astrogeodetic geoid determination and isostatic considerations. They have been realized by applying the Remove-Restore method and least-squares-collocation. Depending on the masses removed, a topographic-bathymetric (TB), a topographic-bathymetric-isostatic (TBAH) and a topographic-bathymetric-Moho (TBMoho) cogeoid have been computed.

The TBAH cogeoid shows a rising Moho along the NAT, hence allowing for the conclusion that this region is isostatically overcompensated. This characteristic can also be associated with extensional forces being active there. The main focus has been put on the interpretation of the Moho cogeoid. Therefore, the Moho model of Tsokas and Hansen [1997] applied for the reduction of the data has been analyzed thoroughly. Hence, it has been compared with other Moho models in the research area. This theoretical investigation already revealed substantial discrepancies of the model. The final Moho cogeoid largely confirmed these inconsistencies. It has been concluded that the Moho model is too deep along the NAT since the cogeoid shows a mass excess there. Furthermore, the model suggests a too shallow Moho beneath the peninsulas of Chalkidiki since the cogeoid indicates a depression there. These results agreed well with the conclusions based on the theoretical analysis.

Computation of an Astro geoid based on DOV

The cogeoid model represents a "geoid reduced for dedicated masses". In order to determine the geoid, the removed masses have been restored to the cogeoid solution (Remove-Restore method). The final astrogeodetic geoid reflects topographic and bathymetric features of the project area. The effect of the NAT is indicated by geoid variations, which reaches about 3 m. In order to validate the geoid solution, several investigations have been performed. The analysis of amount and distribution of reference stations as well as of the respective error-covariances revealed a disadvantage of the astrogeodetic method: the restriction of observations to the continental area and the related inhomogeneous distribution of Astro stations within the research area. These features influenced significantly the error of the predicted geoid undulations N. The mean error of N reached about 0.5 m showing a minimum of about 0.3 m. This is not sufficient. A theoretical investigation concerned with the impact of an increased number of Astro stations denoted a potential reduction of the mean error of N for about 15 cm if observing 50 additional stations. A higher number of stations does not have a significant impact on the accuracy unless they are located in the marine area. In order to obtain the best possible accuracy for the geoid solution, additional Sea Surface Heights (SSH) have been implemented, hence closing the lack of data in the marine area.

Combined geoid computation based on DOV and SSH

The combined geoid solution called DOVSSH07 geoid comprises of 27 DOV and 240 SSH, respectively. Beforehand, the SSH were corrected for tidal influences and the Mean Dynamic Ocean Topography (Limpach et al. [2006]). Concerning the accuracy of the geoid undulations, the combined solution represents a significant improvement. The mean error within the research area decreased for about 0.15 m. The most obvious

improvement has been obtained within the marine area along the NAT. There, the error of the combined solution amounts to better than 0.1 m in comparison to about 0.3 m to 0.4 m before (Astro geoid). Besides, the DOVSSH07 geoid better reproduces the location and SW-NE extension of the NAT. Due to these results, the DOVSSH07 geoid has been presented as final solution. It has been evaluated by comparing it with other geoid models available for the region of the North Aegean Sea.

Evaluation of the final geoid by comparing it with other gravity field models

The DOVSSH07 geoid has been evaluated by comparing it with the EGM96 as well as with local gravimetric and altimetric models. The comparison revealed significant discrepancies between the newly calculated geoid and other models. In the region of the NAT and, especially, north of the Sporades islands, the differences between DOVSSH07 and gravimetric geoid HGFFT98 reached values of about -1 m indicating a clear underestimation of the distinctive bathymetric features by the gravimetric solution. Another region of strong discrepancies is the bay of Thessaloniki, where differences of about -1.9 m have been detected. The evaluation by the altimetric geoid revealed similar results. The discrepancies can be mainly attributed to a deficiency of marine altimetric and gravimetric data used for the computation of the altimetric and gravimetric geoid, respectively.

Summary and Outlook

- From the instrumental point of view, the present work demonstrated the qualification of DIADEM for a completely automatic, observer-independent observation at a station. Theoretically, the system can be operated without any permanent personal control, also during long periods. However, further improvements of the instrumental design should consider the enhancement of the user-friendliness of the system. Partly long cables and a complicate current carrying hamper the preparation of a measurement, particularly for an untrained observer. Hence, a solution should be found that enables an easy and unambiguous handling of the system. This could be e.g. achieved by replacing the cables by a dedicated collector ring.
- Concerning the obtainable accuracy of the system, it has been demonstrated that the instrument provides internal and external accuracies at a very high range of better than 0.15 arcsec. However, two critical points remain in the error budget of a Zenith Camera observation, which have been already highlighted by Hirt [2004] in connection with the TZK2-D: First, a limited astrometric accuracy, and secondly, the unmodelled impact of zenithal refraction. The first problem depends on the fact that the Zenith Camera is a fixed instrument without any compensation of earth's rotation. Already an exposure time of about 0.5 s produces longish star images. This fact confines the obtainable astrometric accuracy to maximum 0.1 arcsec. Hirt [2004] suggested the use of a CCD sensor with drift-scanning-option, which allows for an electronically realized tracking of observations (Zaritsky and Shectman [1996]). The second limiting factor, the anomalous refraction, is relatively difficult to model. Its maximum influence has been estimated to 0.1 arcsec, which is within the obtainable accuracy range of DIADEM. The effect should be subject of further investigations. Hence, it would be interesting to analyze whether it is possible to determine the effect already from one night mean, e.g. by using additional weather information (Hirt [2006]).

* An interesting field of application of DIADEM is formed by local and regional geoid determinations, especially in mountainous regions. The high precision and efficiency of the determination of DOV as nowadays provided by the digital Zenith Camera DIADEM enables the high-resolution geoid determination along profiles or within networks (Hirt [2006]). With obtainable accuracies of better than 0.15 arcsec for the DOV, the course of the geoid can be determined within the sub-millimeter range over a distance of 2 km.
* Another field of application of DIADEM is its suitability for a precise and high-resolution determination of the gravity field. This advantage can be applied in geophysics and related tasks of interpretation. The sensitivity of DOV to local mass distributions on and inside the earth can be used for the appraisal of mass anomalies and the verification of mass models. The potential of a Zenith Camera for the detection of anomalous bodies has already been demonstrated in former times, e.g. by Bürki [1989]. In this work, the residual DOV resulting from a reduction of topographic, bathymetric and isostatic masses have been interpreted in terms of isostatic balance of the region. They allowed to determine the depth of the crust-mantle boundary (Moho) and to assess the state of isostasy.
* The astrogeodetic method is restricted to continental regions. This plays a role in research areas such as the North Aegean Sea in Greece, which is dominated by marine area. Within this work, the resulting lack of data was bridged by applying shipborne observations. Shipborne Zenith Camera observations carried out on marine platforms should move into the focus of future research work. A first approach might be a gimbal-mounted installation of DIADEM on a dedicated tripod.

Bibliography

Andritsanos, V. D. (2000). *Optimum combination of terrestrial and satellite data with the use of spectral methods for applications in geodesy and oceanography*. PhD thesis, School of Rural and Surveying Engineering, Faculty of Engineering, Department of Geodesy and Surveying, Aristotle University of Thessaloniki.

Andritsanos, V. D., Sideris, M. G., and Tziavos, I. N. (2001). A survey of gravity field modeling applications of the Input-Output System Theory (IOST). *IGES Bulletin*, 10:1–17.

Arabelos, D. N. (1980). *Untersuchungen zur gravimetrischen Geoidbestimmung dargestellt am Testgebiet Griechenland*. PhD thesis, Wiss. Arb. der Universität Hannover.

Arabelos, D. N., Asteriadis, G., Contadakis, M. E., Papazachariou, D., and Spatalas, S. D. (2007). Assessment of recent tidal models in the Mediterranean Sea. In *Dynamic Planet*, number 1, pages 57–62. Springer Verlag Berlin, Heidelberg.

Arabelos, D. N. and Tziavos, I. N. (1989). The Hellenic geoid - new considerations and experiences. *Miscellanea per il 70 di Guiseppe Biradi, CLUP, Milano, Ferdinando Sanso edn.*

Arabelos, D. N. and Tziavos, I. N. (1990). Sea Surface Heights in the Mediterranean Sea From Geosat Altimeter Data. *Journal of Geophysical Research*, 95:17947–17956.

Balodimos, D. D. (1972). *Geoidal Studies in Greece*. PhD thesis, Department of Surveying and Geodesy, University of Oxford.

Bangert, J. A. and Kaplan, G. H. (1998). NOVAS-C Naval Observatory Vector Astrometry Subroutines C Language version 2.0. Documentation of novas-c software libraries, United States Naval Observatory, Washington, D.C.

Bentz, F. (2006). Untersuchung des Verschlusses der CCD-Kamera der Zenitkamera DIADEM. Technical report, Institut für Geodäsie und Photogrammetrie, Geodäsie und Geodynamik Labor, ETH Zürich (unpublished).

Berry, R. and Burnell, J. (2000). *The Handbook of Astronomical Image Processing*. William Bell, Richmond, Virginia.

Bürki, B. (1989). *Integrale Schwerefeldbestimmung in der Ivrea-Zone und deren geophysikalische Interpretation*. Geodätisch-geophysikalische Arbeiten in der Schweiz Bd. 40, Schweizerisch Geodätische Kommission.

Bürki, B., Müller, A., and Hirt, C. (2005). Lotabweichungs- und Azimutmessungen für Alptransit. Technical report, Institut für Geodäsie und Photogrammetrie, Geodäsie und Geodynamik Labor, ETH Zürich.

Brockmann, E., Becker, M., Bürki, B., Gurtner, W., Haefele, P., Hirt, C., Marti, U., Müller, A., Richard, P., Schlatter, A., Schneider, D., and Wiget, A. (2004). Realization of a Swiss Combined Geodetic Network (CH-CGN). In *EUREF04 Symposium of the IAG Commission 1 - Reference Frames, Subcommission 1-3a Europe (EUREF), Bratislava, Slovakia*.

Casten, U. and Snopek, K. (2006). Gravity modelling of the Hellenic subduction zone - a regional study. *Tectonophysics*, 417:183–200.

Chesi, G. (1984). *Entwicklung einer tragbaren Zenitkammer und ihr Einsatz im 47. Parallel*. PhD thesis, Fakultät für Bauingenieurwesen, Technische Universität Graz.

Doufexopoulou-Patsada, M. (1985). *Study to the local gravity field for geoid approximation*. PhD thesis, Athens.

DTA (2008a). CHROMA User Manual. Technical report, DTA - Scientific instruments.

DTA (2008b). Full-Frame CCD Image Sensor - Performance Specification of KAF- 3200E and KAF- 3200ME. Technical report, DTA - Scientific instruments.

Ebbing, J. (2002). *3-D Dichteverteilung und isostatisches Verhalten der Lithosphäre in den Ostalpen*. PhD thesis, Freie Universtät Berlin, Fachbereich Geowissenschaften.

Elmiger, A. (1969). *Studien über Berechnung von Lotabweichungen aus Massen, Interpolation von Lotabweichungen und Geoidbestimmung in der Schweiz*. PhD thesis, Institut für Geodäsie und Photogrammetrie, ETH Zürich, No. 4210.

Farr, T., Rosen, P., Caro, E., Crippen, R., Duren, R., Hensley, S., Kobrick, M., Paller, M., Rodriguez, E., Roth, L., Seal, D., Shaffer, S., Shimada, J., Umland, J., Werner, M., Oskin, M., Burbank, D., and Alsdorf, D. (2007). The Shuttle Radar Topography Mission. *Rev. Geophys., RG2004*, 45.

Flury, J. (2002). *Schwerefeldfunktionale im Gebirge: Modellierungsgenauigkeit, Messpunktdichte und Darstellungsfehler am Beispiel des Testnetzes Estergebirge*. PhD thesis, Fakultät für Bauingenieur- und Vermessungswesen, Institut für Astronomische und Physikalische Geodäsie, Technische Universität München.

Forsberg, R. and Tscherning, C. (1981). The Use of Height Data in Gravity Field Approximation by Collocation. *Journal of Geophysical Research*, 86:7843–7854.

Fosu, C. (1999). *Astrogeodetic Levelling by the Combination of GPS and CCD Zenith Camera*. PhD thesis, Schriftenreihe Studiengang Vermessungswesen, Universität der Bundeswehr München, Heft 63.

Fotiou, A., Livieratos, E., and Tziavos, I. N. (1986). Comparisons of the various representations of the geoid for the Hellenic area. *Boll. Geod. Sci. Aff.*, 3:273–291.

Ganz, M. (2007). Geoidbestimmung am Sustenpass. Master's thesis, Geodesy and Geodynamics Laboratory of ETH Zurich.

Gerstbach, G. (1999). CCD und Astrogeodäsie. Unterwegs zur automatischen Lotrichtungsbestimmung. *Geowissenschaftliche Mitteilungen*, 50:45–58.

Gerthsen, C. (1966). *Physik*. Springer-Verlag.

Gessler, J. (1975). *Entwicklung und Erprobung einer transportablen Zenitkamera für astronomisch-geodätische Ortsbestimmungen.* PhD thesis, Wissenschaftliche Arbeiten der Lehrstühle für Geodäsie, Photogrammetrie und Kartographie an der TU Hannover, Nr. 60.

Grüninger, W. (1990). *Zur topographisch-isostatischen Reduktion der Schwere.* PhD thesis, Fakultät für Bauingenieur- und Vermessungswesen der Technischen Hochschule Karlsruhe.

Groth, E. J. (1986). A Pattern-Matching Algorithm For Two-Dimension Coordinate Lists. *Astronomical Journal*, 91:1244–1248.

Gurtner, W. (1978). *Das Geoid in der Schweiz.* Astronomisch-geodätische Arbeiten in der Schweiz Nr. 32, Schweizerischen Geodätischen Kommission.

Hatzfeld, D., Ziazia, M., Kementzetzidou, D., Hatzidimitriou, P., Panagiotopoulos, D., Markorpoulos, K., Papadimitriou, P., and Deschamps, A. (1999). Microseismicity and focal mechanisms at the western termination of the North Anatolian Fault and their implications for continental tectonics. *Geophysical Journal International*, 137:891–908.

Heiskanen, W. A. and Moritz, H. (1967). *Physical geodesy.* W.H. Freeman, San Francisco.

Høg, E., F. C., Makarov, V., Urban, S., Corbin, T., Wycoff, G., Bastian, U., Schwekendiek, P., and Wicenec, A. (2000). The Tycho-2 Catalogue of the 2.5 Million Brightest Stars. *Astronomy and Astrophysics*, 355:27–30.

Hirt, C. (2004). *Entwicklung und Erprobung eines digitalen Zenitkamerasystems für die hochpräzise Lotabweichungsbestimmung.* Nr. 253, Universität Hannover, Wissenschaftliche Arbeiten der Fachrichtung Vermessungswesen der Universität Hannover, Nr. 253.

Hirt, C. (2006). Monitoring and analysis of anomalous refraction using a digital Zenith Camera system. *Astronomy & Astrophysics*, 459:283–290.

Hirt, C. and Bürki, B. (2002). The Digital Zenith Camera - A New High-Precision and Economic Astrogeodetic Observation System for Real-Time Measurement of Deflections of the Vertical. In Tziavos, I.N., editor, *3rd Meeting of the International Gravity and Geoid Commission of the International Association of Geodesy, Thessaloniki*, pages 161–166.

Hirt, C. and Flury, J. (2007). Astronomical-topographic levelling using high-precision astrogeodetic vertical deflections and digtial terrain model data. *Journal of Geodesy.*

Hirt, C. and Seeber, G. (2007a). Accuracy analysis of vertical deflection data observed with the Hannover Digital Zenith Camera System TZK2-D. *Journal of Geodesy.*

Hirt, C. and Seeber, G. (2007b). High-Resolution Local Gravity Field Determination at the Sub-Millimeter Level using a Digital Zenith Camera. In *Dynamic Planet, Monitoring and Understanding a Dynamic Planet with Geodetic and Oceanographic Tools. IAG Symposium Cairns, Australia.*

Hollenstein, C. (2006). *GPS deformation field and geodynamic implications for the Hellenic plate boundary region.* PhD thesis, Institut für Geodäsie und Photogrammetrie, ETH Zürich, No. 16593.

Ingensand, H. (1985). Ein Beitrag zur Entwicklung und Untersuchung hochgenauer elektronischer Neigungsmesssysteme für kontinuierliche Messungen. *Veröffentlichung der Deutschen Geodätischen Kommission bei der Bayerischen Akademie der Wissenschaften, Reihe C, Heft Nr. 308.*

Kahle, H.-G. (2001). *Einführung in die Höhere Geodäsie.* Skript zur Vorlesung, Geodäsie und Geodynamik Labor, ETH Zürich.

Kahle, H.-G., Cocard, M., Peter, Y., Geiger, A., Reilinger, R., McClusky, S., King, R., Barka, A., and Veis, G. (1999). The GPS strain rate field in the Aegean Sea and western Anatolia. *Geophysical Research Letters*, 26(16):2513–2516.

Kahle, H.-G. and Müller, S. (1998). Structure and dynamics of the Eurasian-African/Arabian plate boundary system: Objectives, tasks and resources of the Wegener group. *Journal of Geodynamics*, 25(3/4):303–325.

Kahlmann, T. (2003). Untersuchungen zur hochpräzisen Neigungsmessung mit elektronischen Pendelsystemen. Master's thesis, Institut für Erdmessung, Universität Hannover.

Kaplan, G. H., Hughes, J. A., Seidelmann, P. K., Smith, C. A., and Yallop, B. D. (1989). Mean and apparent place computations in the new IAU System. III. Apparent, Topocentric, and Astrometric Places of Planets and Stars. *Astronomical Journal*, 97:1197–1210.

Karakaisis, G. F. and Papazachos, C. B. (2002). Seismology in Greece: a report.

Käker, R. (2003). Instrumentelle Untersuchung des Zenitkamerasystems. Master's thesis, Institut für Erdmessung, Universität Hannover.

Klinge, K., Kroner, C., and Zürn, W. (2002). Broadband seismic noise at stations of the GRSN. In Korn, M., editor, *Ten years of German Regional Seismic Network (GRSN).* Wiley-VCH, Weinheim.

Le Pichon, X. and Angelier, J. (1979). The Hellenic arc and trench system: A key to the neotectonic evolution of the eastern Mediterranean area. *Tectonophysics*, 60:1–42.

Lemoine, F., Kenyon, S., Factor, J., Trimmer, R., Pavlis, N., Chinn, D., Cox, C., Klosko, S., Luthcke, S., Torrence, M., Wang, Y., Williamson, R., Pavlis, E., Rapp, R., and Olso, T. (1998). The Development of the joint NASA GSFC and the National Imagery and Mapping Agency (NIMA) Geopotential Model EGM96.

Limpach, P., Geiger, A., and Kahle, H.-G. (2006). Sea Surface Topography by Airborne Laser Altimetry and Offshore GPS Buoys in the Eastern Mediterranean: Comparison with JASON-1 Radar Altimeter Data and GRACE Gravity Field. *Proceedings of the 1st International Symposium of the International Gravity Field Service (IGFS).*

Lippmann (2005). Datenblatt Tiltmeter. Technical report, Fa. Lippmann - Geophysikalische Instrumente.

Mader, K. (1951). *Das Newtonsche Raumpotential prismatischer Körper und seine Ableitungen bis zur dritten Ordnung.* Sonderheft 11 der Österreichischen Zeitschrift für Vermessungswesen, Österreichische Kommission für Internationale Erdmessung, Wien 1951.

Marti, U. (1997). *Geoid der Schweiz 1997.* Geodätisch-geophysikalische Arbeiten in der Schweiz Nr. 56, Schweizerische Geodätische Kommission.

Marti, U. (2002). Modelling of Differences of Height Systems in Switzerland. In *3rd Meeting of the International Gravity and Geoid Commission of the International Association of Geodesy, Thessaloniki: p. 378-383.*

Marti, U. (2004). High Precision combined geoid determination in Switzerland. In *IAG International Symposium in Porto, Portugal.*

Mascle, J. and Martin, L. (1990). Shallow structure and recent evolution of the Aegean Sea: A synthesis based on continuous reflection profiles. *Marine Geology, Elsevier Science Publishers B.V., Amsterdam*, 94:271–299.

McCarthy, D. (1996). IERS Conventions (1996). Technical report, IERS Technical Note 21. International Earth Rotation Service, Observatoire de Paris.

McClusky, S., Balassanian, S., Barka, A., Demir, C., Ergintav, S., Georgiev, I., Gurkan, O., Hamburger, M., Hurst, K., Kahle, H., Kastens, K., Kekelidze, G., King, R., Kotzev, V., Lenk, O., Mahmoud, S., Mishin, A., Nadariya, M., Ouzounis, A., Paradissis, D., Peter, Y., Prilepin, M., Reilinger, R., Sanli, I., Seeger, H., Tealeb, A., Toksöz, M., and Veis, G. (2000). Global Positioning System constraints on plate kinematics and dynamics in the eastern Mediterranean and Caucasus. *Journal of Geophysical Research*, 105(B3):5695–5719.

McKenzie, D. (1972). Active tectonics of the Mediterranean region. *Geophysical Journal of the Royal Astronomical Society*, 30:109–185.

Meeus, J. (1992). *Astronomische Algorithmen.* Verlag J. A. Barth, Leipzig, Berlin, Heidelberg.

Meyer, M. (2000). *Signalverarbeitung.* Vieweg Verlagsgesellschaft, Braunschweig/Wiesbaden.

Müller, A. (2002). Umbau des bestehenden Zenitkamera-Messsystems auf digitale Bildtechnik. Master's thesis, Institut für Photogrammetrie, Technische Universtität Dresden.

Müller, A., Bürki, B., Hirt, C., Marti, U., and Kahle, H.-G. (2004). First Results from new High-precision Measurements of Deflections of the Vertical in Switzerland. In *Proceedings of the IAG International Symposium in Porto, Portugal*, volume 129, pages 143–148. Springer Verlag.

Müller, A., Bürki, B., Limpach, P., Kahle, H.-G., Grigoriadis, V. N., Vergos, G. S., and Tziavos, I. N. (2006). Validation of marine geoid models in the North Aegean Sea using satellite altimetry, marine GPS data and astrogeodetic measurements. In *Proceedings of the 1st International Symposium of the International Gravity Field Service (IGFS), Istanbul, Turkey*, pages 90–95.

Münch, S. (2006). Beitrag zur Beschleunigung des automatischen Horizontiervorgangs beim Zenitkamera-Messsystem DIADEM. Master's thesis.

Moritz, H. (1980). *Advanced Physical Geodesy.* H. Wichmann Verlag, Karlsruhe.

Moritz, H. (1990). The inverse Vening Meinesz problem in isostasy. *Geophysical Journal International*, 102:733–738.

Naval Intelligence Division (1944). *Geographical Handbook Series B. R.516*, pages Greece, Vol. 1: Physical geography, history, administration and peoples.

Nyst, M. and Thatcher, W. (2004). New constraints on the active tectonic deformation of the Aegean. *Journal of Geophysical Reseach, B11406*, 109.

Papazachos, C. B., Hatzidimitriou, P. M., Panagiotopoulos, D. G., and Tsokas, G. N. (1995). Tomography of the crust and upper mantle in southeast europe. *Journal of Geophysical Research*, 100:12405–12422.

Pier, J. R., Mun, J. A., Hindsley, R. B., Hennessy, G. S., and Kent, S. M. (2003). Astrometric Calibration of the Sloan Digital Sky Survey. *The Astronomical Journal*, 125:1559–1579.

Ramsayer, K. (1970). *Handbuch der Vermessungskunde Band IIa-Geodätische Astronomie*. Metzlersche Verlagsbuchhandlung, Stuttgart.

Rio, M.-H. (2004). A mean dynamic topography of the Mediterranean Sea estimated from the combined use of altimetry, in-situ measurements and a general circulation model. *Geophysical Research Letter*, 6-03626.

Rodriguez, E., Morris, C., Belz, J., Chapin, E., Martin, J., Daffer, W., and Hensley, S. (2005). An Assessment of the SRTM Topographic Products. JPL D-31639.

Röösli, C. (2006). Untersuchungen zur Fokussierung der digitalen Zenitkamera DIADEM. Bachelor thesis, Institut für Geodäsie und Photogrammetrie, ETH Zurich.

Rummel, R. (2005). *Erdmessung Teil 1, 2 und 3*. Vorlesungsskript des Instituts für Astronomische und Physikalische Geodäsie der TU München.

Schöbel, R. and Eissfeller, B. (2000). Renaissance of Astrogeodetic Levelling Using GPS/CCD Zenith Camera. In *IAIN World Congress, U.S. ION Annual Meeting Receipt, San Diego, CA, USA*.

Schödelbauer, A. (2000). *Geodätische Astronomie - Grundlagen und Konzepte*. W. de Gruyter, Berlin, New York.

Schlatter, A. (2007). *Das neue Landeshöhennetz der Schweiz LHN95*. Geodätisch-geophysikalische Arbeiten in der Schweiz Bd. 72, Schweizerisch Geodätische Kommission.

Schwarz, K. P., Sideris, M. G., and Forsberg, R. (1990). The use of FFT techniques in physical geodesy. *Geophysical Journal International*, 100:485–514.

Seeber, G. (1972). Über das stochastische Verhalten von photographisch bestimmten Stern- und Satellitenkoordinaten. *Deutsche Geodätische Kommission bei der Bayerischen Akademie der Wissenschaften, Reihe C*, 178.

Seeber, G. (2003). *Satellite Geodesy*. W. de Gruyter: Berlin, New York. Second edition.

Seidelmann, P. (1992). *Explanatory supplement to the Astronomical Almanac*. University Science Books, Mill Valley, CA.

Shaw, L., Paul, I., and Henrikson, P. (1969). Statistical Models for the Vertical Deflection from Gravity-Anomaly Models. *Journal of Geophysical Research*, 74-17:4259–4265.

Sigl, R. (1991). *Geodätische Astronomie*. Wichmann, 4. Auflage.

Snopek, K., Meier, T., Endrun, B., Bohnhoff, M., and Casten, U. (2007). Comparison of gravimetric and seismic constraints on the structure of the Aegean lithosphere in the forearc of the Hellenic subduction zone in the area of Crete. *Journal of Geodynamics*, 44:173–185.

Sodoudi, F., Kind, R., Hatzfeld, D., Priestley, K., and Greece working group (2006). Lithospheric structure of the Aegean obtained from P and S reveiver functions. *Journal of Geophysical Research*, 111.

Stearns, S. and Hush, D. (1999). *Digitale Verarbeitung analoger Signale*. R. Oldenbourg Verlag, München, Wien.

Stone, R. C., Monet, D. G., Monet, A. K. B., Walker, R. L., Ables, H. D., Bird, A. R., and Harris, F. H. (1996). The Flagstaff Astrometric Scanning Transit Telescope (FASTT) and Stars Position determined in the Extragalactic Reference Frame. *The Astronomical Journal*, 111(4):1721–1742.

Tapley, B., Ries, J., Bettadpur, S., Chambers, D., Cheng, M., Condi, F., Gunter, B., Kang, Z., Nagel, P., Pastor, R., Pekker, T., Poole, S., and Wang, F. (2005). GGM02 - An Improved Earth Gravity Field Model from GRACE. *Journal of Geodesy*.

Tirel, C., Gueydan, F., Tiberi, C., and Brun, J.-P. (2004). Aegean crustal thickness inferred from gravity inversion. Geodynamical implications. *Earth and Planetary Science Letters*, 228:267–280.

Torge, W. (2001). *Geodesy*. Berlin: Walter de Gruyter, 3rd comp. rev. and ext. ed.

Torge, W. (2003). *Geodäsie*. W. de Gruyter Berlin, New York, 2. Auflage.

Tsokas, G. N. and Hansen, R. O. (1997). Study of the crustal thickness and the subducting lithosphere in Greece from gravity data. *Journal of Geophysical Research*, 102:20585–20597.

Tziavos, I. N. (1984). *Study of the Optimal Combination of Heterogenous Data on Geoid Determination with Application for the Area of Greece*. PhD thesis, Department of Geodesy and Surveying, School of Rural and Survey Engineering, University of Thessaloniki.

Tziavos, I. N. and Andritsanos, V. D. (1999). Recent Geoid Computations for the Hellenic Area. *Chemical Earth (A)*, 24(1):91–96.

Tziavos, I. N., Kotzev, V., Vergos, G. S., and Pashova, L. (2005). Mean sea level and sea surface topography studies in the Black Sea and the Aegean. In Jekeli, C., Bastos, L., and Fernandes, J., editors, *Gravity Geoid and Space Missions 2004*, volume 129, pages 254–259. International Association of Geodesy Symposia, Springer-Verlag Berlin, Heidelberg.

u-blox AG (2003). SBR-LS Sensor Based GPS Receiver Board - Data Sheet. Technical report, u-blox AG.

Valdes, F. G., Campusano, L. E., Velásquez, J. D., and Stetson, P. B. (1995). FOCAS Automatic Catalog Matching Algorithms. *PASP*, 107:1119–1128.

Vergos, G. S., Tziavos, I. N., and Andritsanos, V. D. (2005). On the Determination of Marine Geoid Models by Least-Squares Collocation and Spectral Methods Using Heterogeneous Data. In *A Window on the Future of Geodesy*, volume 128F, pages 332–337. International Association of Geodesy Symposia, Springer Verlag Berlin, Heidelberg.

Wild, U., Grünig, S., Hug, R., and Kummer, P. (2004). SWIPOS - Positionierungsdienste auf der Basis von Differentiellen GPS (DGPS) für Navigation, GIS-Datenerfassung und Vermessung. Technical report, Bundesamt für Landestopographie.

Wildermann, E. (1988). Untersuchungen zur lokalen Schwerefeldbestimmung aus heterogenen Daten dargestellt am Beispiel der Geotraverse venezolanische Anden.

Winter, L. (1999). *Wide-Field-Astrometrie mit CCD-Detektoren am Hamburger Zonenastrographen*. PhD thesis, Fachbereich Physik, Universität Hamburg.

Wirth, B. (1990). *Höhensysteme, Schwerepotentiale und Niveauflächen*. Geodätisch-geophysikalische Arbeiten in der Schweiz Bd. 42, Schweizerisch Geodätische Kommission.

Wirth, B. and Marti, U. (1986). Lotrichtungs- und Schweremessungen in der Ivrea-Zone, Messkampagnen 1985/1986, Bericht Nr. 114. Technical report, Institut für Geodäsie und Photogrammetrie, ETH Zürich.

Wissel, H. (1982). Zur Leistungsfähigkeit von transportablen Zenitkameras zur Lotabweichungsbestimmung. Technical report, Wissenschaftliche Arbeiten der Fachrichtung Vermessungswesen, Universität Hannover, Nr. 107.

Wyler (2007). Spezifikationen der Wyler Produkte. Technical report, Wyler AG.

Zacharias, N. (1996). Measuring the Atmospheric Influence on Differential Astrometry: a Simple Method Applied to Wide Field CCD Frames. *PASP*, 108:1135–1138.

Zacharias, N., Urban, S. E., Zacharias, M. I., Wycoff, G. L., Hall, D. M., Monet, D. G., and Rafferty, T. J. (2004). The second US Naval Observatory CCD Astrograph Catalog (UCAC2). *The Astronomical Journal*, 127:3043–3059.

Zacharias, N., Zacharias, M. I., and Urban, S. E. (2000). Comparing Tycho-2 Astrometry with UCAC1. *The Astronomical Journal*, 120:1148–1152.

Zaritsky, D. and Shectman, S. A. (1996). The Great Circle Camera: A New Drift-Scanning Instrument. *Publications of the Astronomical Society of the Pacific*, 108:104–109.

Zimmermann, H. and Weigert, A. (1995). *ABC-Lexikon Astronomie*. Spektrum Akademischer Verlag, Heidelberg, Berlin, Oxford.

A Mathematical background

A.1 Variations of star positions

Transformation of mean into apparent star positions:

$$\begin{pmatrix} \alpha_{Topo} \\ \delta_{Topo} \end{pmatrix} = N(t) \cdot P(t) \cdot \begin{pmatrix} \alpha_0 + \Delta\alpha_{pm} + \Delta\alpha_r + \Delta\alpha_{aa} \\ \delta_0 + \Delta\delta_{pm} + \Delta\delta_r + \Delta\delta_{aa} \end{pmatrix} + \begin{pmatrix} \Delta\alpha_{da} \\ \Delta\delta_{da} \end{pmatrix} \tag{A.1}$$

$(\alpha, \delta)_0$...	Mean star position at catalog epoch T_0
$(\Delta\alpha, \Delta\delta)_{pm}$...	Correction of proper motion during time interval $t = T - T_0$
$(\Delta\alpha, \Delta\delta)_r$...	Correction of relativistic light diversion at exposure epoch T
$(\Delta\alpha, \Delta\delta)_{aa}$...	Correction of annual abberation at T
$N(t) \cdot P(t)$...	Correction of precession and nutation during t
$(\Delta\alpha, \Delta\delta)_{da}$...	Correction of daily abberation at T

Proper motion after Høg et al. [2000]**:**

$$\mu_\alpha = \frac{\Delta\alpha}{\Delta t} \qquad \mu_\delta = \frac{\Delta\delta}{\Delta t} \tag{A.2}$$

(μ_α, μ_δ)...	Proper motion components
$(\Delta\alpha, \Delta\delta)$...	Difference between star positions at two different epochs
Δt...	Time interval elapsed since the astrometric observation of the star

Daily abberation after Sigl [1991]**:**

$$\begin{aligned} \Delta\alpha_{da} &= k \cdot \cos tt \cdot \sec\delta \\ \Delta\delta_{da} &= k \cdot \sin tt \cdot \sin\delta \end{aligned} \tag{A.3}$$

$(\Delta\alpha, \Delta\delta)_{da}$...	Daily abberation
(α, δ)...	Equatorial coordinates of star position
tt...	Hour angle of the star
k...	Daily abberation constant

with:

$$k = \rho \cdot \frac{v}{c} = 0.32[arcsec] \cdot \cos\Phi$$
$$v = \omega \cdot r \cdot \cos\Phi = 0.46 \left[\frac{km}{s}\right] \cdot \cos\Phi \tag{A.4}$$

v...	Velocity of the observation point
c...	Speed of light
$\omega = 2\pi/86164\,s$...	Angular velocity of the earth
$\rho = \frac{180 \cdot 3600}{\pi}$...	Conversion factor [rad] to [arcsec]
$r = 3670\,km$...	Earth's radius

For the observation of a zenithal star field, it is $tt = 0$ and $\Phi = \delta$ and, therefore:

$$\Delta\alpha_{da} = 0.32\ arcsec$$
$$\Delta\delta_{da} = 0.00\ arcsec \tag{A.5}$$

Annual abberation after Meeus [1992]**:**

$$\begin{aligned}\Delta\alpha_{aa} &= -k \cdot (\cos\alpha \cdot \cos L \cdot \cos\varepsilon + \sin\alpha \cdot \sin L)\sec\delta \\ &\quad +e \cdot \kappa \cdot (\cos\alpha \cdot \cos\pi \cdot \cos\varepsilon + \sin\alpha \cdot \sin\pi)sec\delta \\ \Delta\delta_{aa} &= -k \cdot ([\tan\varepsilon \cdot \cos\delta - \sin\alpha \cdot \sin\delta] \cdot \cos L \cdot \cos\varepsilon + \cos\alpha \cdot \sin\delta \cdot \sin L) \\ &\quad +e \cdot \kappa \cdot ([\tan\varepsilon \cdot \cos\delta - \sin\alpha \cdot \sin\delta] \cdot \cos\pi \cdot \cos\varepsilon + \cos\alpha \cdot \sin\delta \cdot \sin\pi)\end{aligned} \tag{A.6}$$

$(\Delta\alpha, \Delta\delta)_{aa}$...	Annual abberation
$v = 29.8\ km/s$...	Velocity of the earth around the sun
$k = 20.495\ arcsec$...	Annual abberation constant
ε...	Mean obliquity of ecliptic
e...	Eccentricity of the earth's orbit around the sun
π...	Longitude of perihel
M...	Mean anomaly
L_0...	Mean longitude of sun
L...	Apparent longitude of sun

A.2 Mass reduction

Gravitational potential after Mader [1951]**:**

Instead of V (Eq. (8.2)), the antiderivative W is treated:

$$W = \int dx \int dy \int \frac{dz}{r} \tag{A.7}$$

The integration of **W with respect to x** results in:

$$W = \int dy \int dz \cdot \log(x + r) \tag{A.8}$$

and further to **y**:

$$W = \underbrace{y \int dz \cdot \log(x + r)}_{A} \underbrace{- \int dy \cdot y^2 \int \frac{dz}{(x + r)r}}_{B} = A + B \tag{A.9}$$

For an integration of **W with respect to z**, the terms A and B have to be treated separately. The partial integration of **A to z** yields:

$$A = y \cdot z \cdot \log(x + r) + x \cdot y \cdot \log(z + r) - y^2 \cdot \arctan\left(\frac{x \cdot z}{y \cdot r}\right) \tag{A.10}$$

and the partial integration of **B to z**:

$$B = \frac{y^2}{2} \cdot \arctan\left(\frac{x \cdot z}{y \cdot r}\right) + x \cdot z \cdot \log(y + r) - \frac{x^2}{2} \cdot \arctan\left(\frac{y \cdot z}{x \cdot r}\right) - \frac{z^2}{2} \cdot \arctan\left(\frac{x \cdot y}{z \cdot r}\right) \tag{A.11}$$

The sum of A and B as well as the introduction of the integration limits results the gravitational potential V (Eq. (8.3)).

Gravitational attraction after Mader [1951]**:**

Instead of V_x (Eq. (8.4)), the antiderivative W_x is treated:

$$W_x = -\int dy \int dz \int dx \frac{x}{r^3} \tag{A.12}$$

The integration of W_x **to x** yields:

$$W_x = \int dy \int \frac{dz}{r} \tag{A.13}$$

further to **y**:

$$W_x = \int dz \cdot \log(y + r) \tag{A.14}$$

and to **z**:

$$W_x = z \cdot \log(y + r) + y \cdot \log(z + r) - x \cdot \arctan\left(\frac{y \cdot z}{x \cdot r}\right) \tag{A.15}$$

By introducing integration limits, the gravitational effect V in x-direction is obtained (Eq. (8.5)).

A.3 Geoid determination

The shape of C_{ss} and C_{nn} matrices, respectively, is as follows (Wirth [1990]):

$$C_{ss} =$$

	ξ_1	...	ξ_n	η_1	...	η_n	g_1	...	g_n	N_1	...	N_n
ξ_1	$\Phi_{\xi 1 \xi 1}$	...	$\Phi_{\xi 1 \xi n}$	$\Phi_{\xi 1 \eta 1}$	...	$\Phi_{\xi 1 \eta n}$	$\Phi_{\xi 1 g 1}$	...	$\Phi_{\xi 1 g n}$	$\Phi_{\xi 1 N 1}$	...	$\Phi_{\xi 1 N n}$
...	...	...	...	...	...	...	...	...	...	...	...	...
ξ_n	$\Phi_{\xi n \xi 1}$	...	$\Phi_{\xi n \xi n}$	$\Phi_{\xi n \eta 1}$	...	$\Phi_{\xi n \eta n}$	$\Phi_{\xi n g 1}$	...	$\Phi_{\xi n g n}$	$\Phi_{\xi n N 1}$	...	$\Phi_{\xi n N n}$
η_1	$\Phi_{\eta 1 \xi 1}$	...	$\Phi_{\eta 1 \xi n}$	$\Phi_{\eta 1 \eta 1}$	...	$\Phi_{\eta 1 \eta n}$	$\Phi_{\eta 1 g 1}$	...	$\Phi_{\eta 1 g n}$	$\Phi_{\eta 1 N 1}$	...	$\Phi_{\eta 1 N n}$
...	...	...	...	...	...	...	...	...	...	...	...	...
η_n	$\Phi_{\eta n \xi 1}$	...	$\Phi_{\eta n \xi n}$	$\Phi_{\eta n \eta 1}$	...	$\Phi_{\eta n \eta n}$	$\Phi_{\eta n g n}$	...	$\Phi_{\eta n g n}$	$\Phi_{\eta n N 1}$	...	$\Phi_{\eta n N n}$
g_1	$\Phi_{g 1 \xi 1}$	...	$\Phi_{g 1 \xi n}$	$\Phi_{g 1 \eta 1}$	...	$\Phi_{g 1 \eta n}$	$\Phi_{g 1 g 1}$	...	$\Phi_{g 1 g n}$	$\Phi_{g 1 N 1}$	...	$\Phi_{g 1 N n}$
...	...	...	...	...	...	...	...	...	...	...	...	...
g_n	$\Phi_{g n \xi 1}$	...	$\Phi_{g n \xi n}$	$\Phi_{g n \eta 1}$	...	$\Phi_{g n \eta n}$	$\Phi_{g n g 1}$	...	$\Phi_{g n g n}$	$\Phi_{g n N 1}$	...	$\Phi_{g n N n}$
N_1	$\Phi_{N 1 \xi 1}$	...	$\Phi_{N 1 \xi n}$	$\Phi_{N 1 \eta 1}$	...	$\Phi_{N 1 \eta n}$	$\Phi_{N 1 g 1}$	...	$\Phi_{N 1 g n}$	$\Phi_{N 1 N 1}$	...	$\Phi_{N 1 N n}$
...	...	...	...	...	...	...	...	...	...	...	...	...
N_n	$\Phi_{N n \xi 1}$	...	$\Phi_{N n \xi n}$	$\Phi_{N n \eta 1}$	...	$\Phi_{N n \eta n}$	$\Phi_{N n g 1}$	...	$\Phi_{N n g n}$	$\Phi_{N n N 1}$	...	$\Phi_{N n N n}$

(A.16)

The covariance functions Φ_{ij} have to be calculated for the distances (Δx_{ij}, Δy_{ij},) between station i and station j.

$$C_{nn} =$$

	ξ_1	...	ξ_n	η_1	...	η_n	g_1	...	g_n	N_1	...	N_n
ξ_1	$\sigma^2_{\xi 1}$	0	0	0	0	0	0	0	0	0	0	0
...	0	...	...	...	...	...	...	...	...	...	...	...
ξ_n	0	...	$\sigma^2_{\xi n}$	...	...	...	...	...	...	...	...	...
η_1	0	...	...	$\sigma^2_{\eta 1}$	...	...	...	...	...	...	...	...
...	0	...	...	...	...	...	...	...	...	...	...	...
η_n	0	...	...	...	...	$\sigma^2_{\eta n}$	...	...	...	...	...	...
g_1	0	...	...	...	...	...	$\sigma^2_{g 1}$	...	...	...	...	...
...	0	...	...	...	...	...	...	...	...	...	...	...
g_n	0	...	...	...	...	...	...	...	$\sigma^2_{g n}$	...	...	...
N_1	0	...	...	...	...	...	...	...	...	$\sigma^2_{N 1}$	...	...
...	0	...	...	...	...	...	...	...	...	...	...	...
N_n	0	...	...	...	...	...	...	...	...	...	...	$\sigma^2_{N n}$

(A.17)

Please note: the positions in Eq. (A.17) represented by dots have to be filled with "0".